Optoelectrical studies of ZnO

Martin J. H. Henseler

A thesis submitted in partial fulfillment
of the requirements for the Degree of
Doctor of Philosophy
in
Physics
at the
University of Canterbury,
Christchurch, New Zealand

· September 2009 ·

Abstract

The temperature dependence of the band structure of ZnO has been studied on epitaxial films and bulk crystals with the methods of temperature dependent photoluminescence, photoconductivity, reflectivity and transmission spectroscopy. A major question investigated was the intriguing detail that could be resolved in band edge photoconductivity spectra of both high quality ZnO bulk crystals as well as epitaxial films. The connection of these spectral details in photoconductivity to the excitonic band structure of ZnO was made by comparison to the other spectroscopic methods which have a better understood relation to the semiconductor band structure.

Photoluminescence spectroscopy enabled us to get a direct and reliable feedback about the energy fine structure of emitting levels in ZnO. Comparison of the emitting levels of epitaxial films with the emitting levels of high quality bulk material allowed the identification of dominating defect structures and impurities in the epitaxial films. The investigation of the effect of annealing on these emission lines finally allowed us to get a better understanding of the effects of annealing on the crystal and electric structure of epitaxially grown heterostructural films and allowed the determination of the optimum temperature range to be used for improved crystal quality.

It has been investigated if temperature dependent reflectivity can serve as a simple tool for the examination of the temperature dependence of the band structure of ZnO. The appeal of reflectivity is its enhanced sensitivity only to free excitonic transitions. This proved a valuable simplification compared to the methods of photoluminescence and photoconductivity: Photoluminescence is limited by phonon-broadening of the multitude of emission levels in the band gap region of ZnO, and photoconductivity has a multitude of processes that are potentially contributing to its spectra, making the identification of their relation to the band structure less reliable. Therefore the applicability of reflectivity for the deduction of the temperature dependence of the band structure has been investigated, by measuring the temperature dependence of the energy positions of the characteristic reflectivity features, with particular focus on the effect of phonon broadening and interaction of close lying resonator levels.

The investigation of the temperature dependence of photoconductive centres was enabled through the resulting possibility of directly relating the purely excitonic reflectivity spectra to the complex features in photoconductivity. The temperature dependent evolution of the spectra obtained by photoconductivity then revealed that there are at least two types of photoconductive processes that have to be distinguished: features in photoconductivity that are directly related

to the band structure proved to be distinguishable from slow defect related processes in terms of their response speed. For the samples of bulk ZnO as well as epitaxial films, the peaks in photoconductivity only had a meaningful position in regard to the band structure for the cases of spectra that are dominated by fast processes. The spectra dominated by slow processes showed a meaningful temperature dependence of respective dips in the spectra. The strong response of fast photoconductive levels in bulk ZnO allowed us to directly observe the A- and B-free excitons by photoconductivity. Additional fine structure could be observed that is likely to be related to the narrow photo emission lines of neutral as well as ionized donor bound excitons and the upper polariton branch of the A-free exciton. These findings agree with the temperature dependence of related Anti-Stokes phonon replica levels that allow a first estimate of the activation energies of the zero-phonon lines.

The energy and temperature dependent lateral transport properties of ZnO are expected to be of importance in ZnO device technology.

Acknowledgments

First and foremost I want to thank my supervisor Professor Roger Reeves for the boundless support, trust, patience and advice he gave me throughout the entire progress of my PhD-studies. Despite his busy schedule he was always there for me to share his profound insight into physics and give invaluable advice whenever needed.

Secondly I want to thank my Co-supervisor Professor Steve Durbin for his enthusiasm for my research as well as the support he gave. His honest involvement always inspired me to go further by following his valuable advice in how to manage the next step.

Financially, these studies would not have been possible without the University of Canterbury Doctoral Scholarship Program, which enabled me to do my studies without financial worries and was a good motivation to do the step of coming to New Zealand to do my PhD abroad.

The research as well as trips to numerous conferences were funded by the MacDiarmid Institute as well as the Department of Physics, whom I am truly grateful to for the wide ranging network of Colleagues I was able to connect to. Due to these crucial trips, an integration into the research field with a personal connection to its questions that are being investigated across the globe was a wonderful part of my PhD-studies. Combined with the numerous visitors from

overseas universities that came to Canterbury, studying in New Zealand has not been an isolating experience at all, but has inspired me throughout with many valuable bonds I was able to create with inspired and thus inspiring great people.

The work would have been impossible and unbearable without the social and scientific support of the colleagues in our research group, each of whom were always there with a helping hand and advice whenever needed. This type of teamwork made all the difference in creating such a pleasant and energizing curiosity in the lab and in the office. Therefore I want to thank Martin Allen and William Lee for the fruitful collaboration we had, and their kind support with the preparation of samples. I want to thank Joon Scott Choi, particularly for his skilled help in the lab, Paul Miller for his encouraging advice and enthusiastic discussions about ZnO, Ian Farrell for all the good discussions and laughter and Chito Kendrick for his helping hand in the clean-room as well as Young-Wook Song for his support. For several years I had to share my office with Rueben Mendelsberg, whom I want to thank for such a great time studying, which was rarely boring and filled with countless truly helpful discussions as well as lots of lessons in sailor's English.

The biggest price to pay for studying so far away from home was that I had to leave my dear family and friends behind for several years. Although being on the other side of the planet they still changed the world by giving endless support, understanding and love, whether things went well or the going got tough.

Contents

List of Figures

List of Tables

Chapter 1

Introduction

1.1 Background

Light and optical phenomena have always drawn great religious, philosophical and later scientific interest. This might be due to the fact that vision is arguably the most enlightening of our senses, or because light has many rather distinct properties. What makes light so interesting in semiconductor physics is that photons interact with the semiconductor electrons in a very simple manner. Planck's quantum hypothesis states that 'in emission and absorption of electromagnetic radiation by atoms, the energy may be exchanged only in definite amounts (quanta)' [2]. This process is at heart of almost all semiconductor-light interactions and offers a convenient key to a better understanding of the electron states and their related electron transitions in semiconductors. In this thesis the semiconductor light-interaction is used to work towards a better understanding of ZnO, a material that has a great scope of possible applications, many of them optical.

The interaction of semiconductors with light is not only interesting for their analysis, but directly leads to a number of increasingly important applications. Solar cells already are established solutions for the power supply of remote devices such as water pumps, parking meters or satellites and space stations. LEDs are in the exciting process of becoming more reliable, more versatile and most importantly more energy-efficient replacements of conventional light sources, with their application extending from traffic lights to large-scale video screens.

The engineering of semiconductor devices which have particular electron states and transitions is confined by the intrinsic properties of the semiconductor materials used, with the band gap of the material being of particular interest for optical applications. For the generation of visible light across the whole spectrum, a band gap of more than 3eV is desirable.

For a semiconductor to be an efficient optical material, the band gap has to

be direct, and the exciton binding energy has to be large, at least large enough for stable operation at room temperature. The current technology leap of high power LEDs for applications such as white torches or traffic lights is relying on (In)GaN. ZnO has very similar opto-electronic properties to GaN but exceeds its specific advantages by having an even larger exciton binding energy. Other decisive factors are cost and toxicity. With several hundred tonnes of ZnO used for applications such as car-tires, cement and sun-screen, the availability has proven to be no problem, whereas the price for Indium is rising dramatically, mainly due to its application in LCD-displays.

With the large scope of possible applications a ZnO-based range of semiconductor devices would mean a brighter future in a world with the social challenges of growing human population, the pressuring ecological challenges of a quickly growing industrialization and the knowledge of limited fossil fuels. The semiconductor industry already is the biggest single industry of the world, but there are strong incentives besides the economical rewards to widen the scope of possibilities of solid state devices. Recent history shows us that the range of applications of new solid-state technology has most often exceeded expectations dramatically.

1.2 History of ZnO as a semiconductor

The potential electronic and optoelectronic capabilities of ZnO were recognized and led to the first period of intensive research on ZnO by groups in the USA, Germany (Mollwo(Erlangen), Heiland(Aachen), Broser(Berlin)) and Japan in the 1950s [3]. The first commercial application of ZnO thin films for surface acoustic wave devices took advantage of the good piezoelectric properties for ZnO that were discovered in 1960 [4]. Interest died down in the 1980s, since studies failed to get past a major obstacle that still has not been tackled till today: the achievement of reliable p-type doping of ZnO.

A lot of interesting studies have been done in this early period of ZnO research, including reflection, absorption and polarity-studies that form the basis of our knowledge about the material system today. The goal has to be to broaden the knowledge about ZnO on the basis of these early findings with the help of improved materials and techniques available today.

Renewed interest in ZnO as a semiconductor came with the realization that ZnO might be complementary to the advances made with GaN. ZnO has very similar optoelectronic properties and is lattice matched to In(x)Ga(1-x)N at an In concentration of $\approx$22%. This creates hope for an integrated GaN-ZnO technology, promising enhanced functionality for both materials [5]. Additional interest in ZnO stems from the tendency of ZnO to grow in structures of low dimensionality (nanostructures) if grown by growth techniques such as Molecular Beam Epitaxy (MBE) and Pulsed Laser Deposition (PLD). Recent investigation techniques

such as AFM, STM, EBM and nano-scale electron beam lithography allow the investigation and modification of these exciting nanoscale structures.Currently, the ZnO related research activity is remarkable, with more than 3000 ZnO relevant publications per year (see figure 1.1).

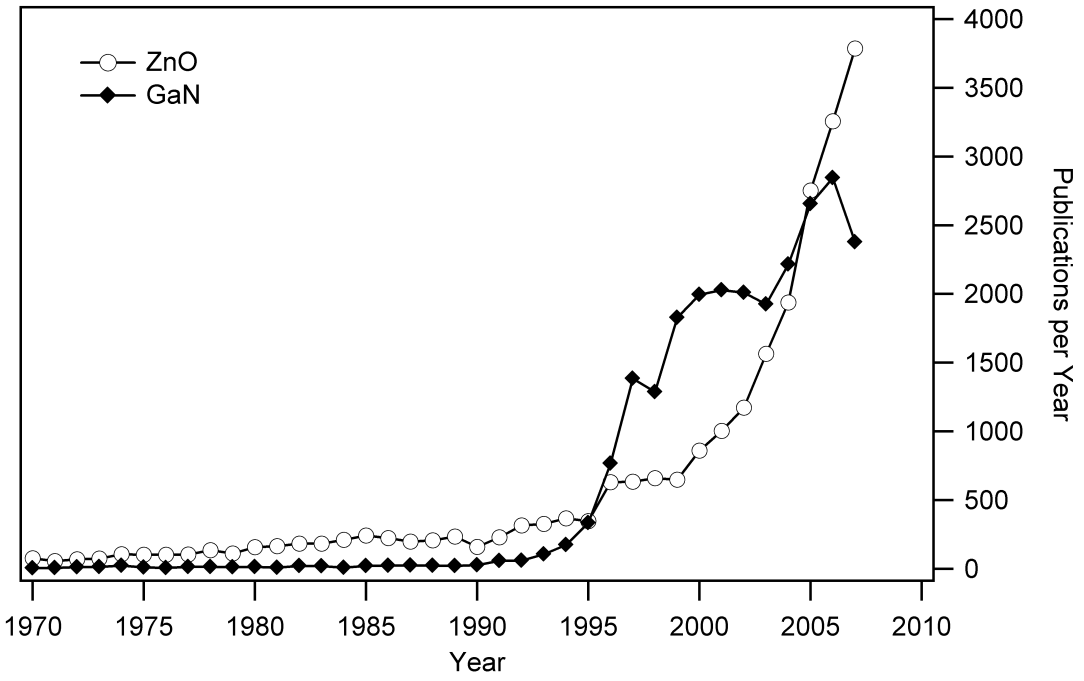

Figure 1.1: Papers published per year concerning ZnO or GaN, according to the online research literature database Scopus

1.3 Crystal structure

Binary II-VI compounds such as ZnSe, ZnTe, CdS and ZnO are known for their high degree of ionic bonding as well as their high band gaps. The ionic bonding in ZnO is nearly on par with the usually dominating covalent bonding and leads to a particularly strong overall crystal strength, which is exemplified by the high melting point of 1975 °C. When separated, the components of ZnO therefore have a very volatile nature and cause difficulties in melt growth. But for modern epitaxial growth methods such as PLD and MBE, the strong bonding tendency has particular advantages, allowing a highly stoichiometric recombination and high growth rates [6].

Depending on its environment, ZnO can crystallize in the hexagonal wurtzite, cubic zinc blende and rocksalt (NaCl) structure. At ambient conditions, the wurtzite structure is prevalent. This gives proof that covalent bonding is dominating, since the tetrahedral coordination of the wurtzite structure is typical for

the sp^3 covalent bonding between the atoms. Experiments investigating pressure-induced phase transitions in ZnO beautifully demonstrate how closely the ionic and covalent bonding is balanced. ZnO can be transformed into the rocksalt structure by compressing it with 10-15 GPa external pressure. The volume decreases by 17% and the lattice dimensions are reduced sufficiently to allow the Coulomb interaction between the Zn- and O-ions to dominate over the covalent bonding. The atoms rearrange into the sixfold NaCl structure, which is partly retained even after the pressure is reduced back to zero [7] [8–10].

The wurtzite crystal structure has two atoms per unit cell. It is formed by two hexagonal close packed diatomic sub-lattices, which are layered in the ABAB configuration along the c-axis, which is the major difference to the cubic zinc-blende structure, where the layers are arranged in a ABCABC configuration. In both cases each atom of one kind is tetragonally surrounded by 4 atoms of the other kind (see figure 1.2). All three crystal structures of ZnO do not have a centre of inversion, but a crystallographic polarity [7]. The crystallographic polarity is of major importance since it influences the crystal properties in many ways. For example it is known to affect growth, as well as defect generation, plasticity and piezoelectricity [7].

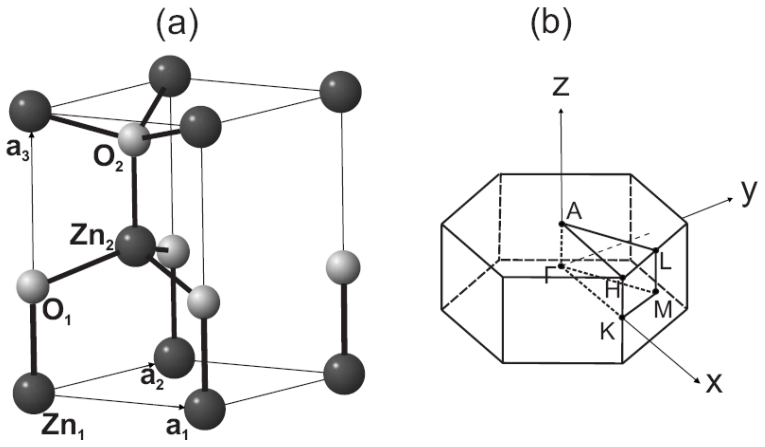

Figure 1.2: Representation of the polar wurtzite crystal structure of ZnO, with the c-axis in vertical direction (from [11]). $a_0 = 3.25$ Å, $c_0 = 5.205$ Å

1.4 The electronic structure and its relation to temperature

The electric band structure is defining the electrical properties of semiconductors and is closely related to the long range translational order of crystals. In the reciprocal lattice description, the Brillouin zone incorporates all possible k-values

an electron can have within the regular lattice, since the reciprocal lattice vectors have the property

$$e^{i\boldsymbol{G}\cdot(\boldsymbol{r}+\boldsymbol{T})} = e^{i\boldsymbol{G}\cdot\boldsymbol{r}}. \tag{1.1}$$

The Brillouin zone of ZnO is shown in figure 1.2. To calculate the band structure of bulk semiconductors across the Brillouin zone, a local-density approximation (LDA) of the density-functional theory (DFT) is a preferred method of calculation [12]. Since ZnO semiconductors have highly localized and strongly bound cationic d-electrons, the atomic self-interaction as well as the electronic relaxation inside the crystals atoms have to be taken into account when calculating the band-structure. Dirk Vogel et al. successfully used the LDA with Self-Interaction Corrections-Pseudo Potentials (SIC-PP) to achieve a very good agreement between the calculated and experimentally investigated band-structure [12]. This band structure for ZnO is shown in figure 1.3, with the vertical axis showing the energy of the electrons in relation to the highest valence band energy, and on the x-axis are the indices of the k-vector of the Brillouin zone (see figure 1.2).

Photons carry only very little momentum ($p = h/\lambda$). In order for a semiconductor to be an efficient optical emitter, it is crucial that the electron-photon interaction can take place without a third body, such as a phonon, to take account of momentum-transitions. Therefore the lowest energy of the conduction band must lie at the same k-value as the highest energy of the valence band in order for a semiconductor to efficiently emit light. Semiconductors that fulfill this condition are called direct. Silicon is an example for an indirect semiconductor. ZnO, as can be seen in its band-structure, is a direct semiconductor, such as GaN.

As the band structure of a semiconductor is closely related to its crystal structure, the regularity of a given crystal influences its optical response such as photoluminescence (PL). PL therefore is a good indicator of crystal quality, since crystal irregularities result in less defined and weaker optical transitions. Also, impurities and defects of different kinds each have their particular 'fingerprint' in terms of their spacing to other transitions, width and behaviour with variation of measurement parameters, that often is distinguishable from other impurities and defects. This is where the true strength of optical experiments lies, but also the source of its greatest challenges, as the particular responses to various defects and conditions are often not fully understood or leave room for interpretation.

Defects and impurities play a very important role in ZnO research. One major aspect is that most defects and impurities cause ZnO to get more n-type. To be able to dope ZnO n- and p-type (bipolar), it would help to understand why shallow acceptor levels do not like to form in ZnO, especially not without the creation of a compensating amount of shallow or activated donor levels. Even doping with elements such as nitrogen, phosphorous and arsenic releases more free electrons into the crystals via defects than the material is provided with positive carriers. To get p-type material, a dominance of holes for conduction is needed. It is the hope that through the understanding of defects an appropriate

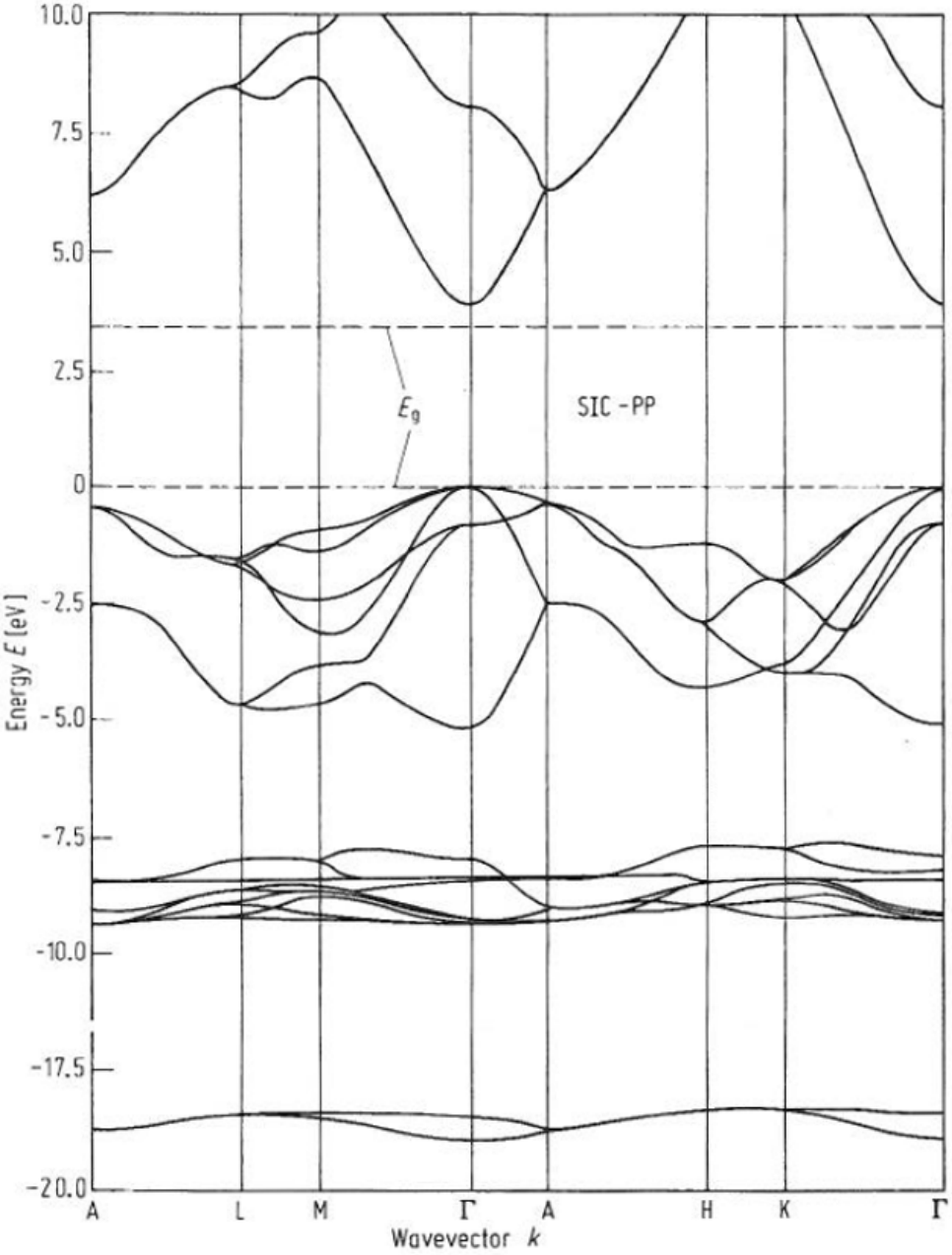

Figure 1.3: Band structure of ZnO, calculated by DFT with the LDA approximation and SIC-PP corrections. Energies are referred to the top of the valence band. The dashed lines indicate the experimental band gap. From D. Vogel et al. [12]

way of p-type doping can be found.

The optical properties that are related to the electronic structure of ZnO have been studied in detail for low temperatures around 10 Kelvin, giving more detailed results as time goes on, since the available material quality has been improved considerably. More knowledge has also been obtained step by step in the identification of optical features of ZnO and their relation to the band structure [1, 13–18].

To take ZnO and its promising material properties into applications requires a good understanding of its energy levels at room temperature. But even such elementary band structure parameters as the band gap itself are not well understood for room-temperature conditions [19]. At 10 K, phonons do not play a dominant role in the broadening of energy levels, and the fine structure of the electronic bands can be resolved with methods such as photoluminescence spectroscopy. But with rising temperatures, phonons do become more prevalent and influence the band structure in many ways. In ZnO, the role of phonons is particularly dominant: Although excitons do have a very large binding energy of 60 meV, the energy of longitudinal optical (LO) phonons is even larger with about 72 meV. According to the Froehlich interaction, excitons interact more strongly with longitudinal optical (LO) phonons than transverse phonons [20]. The strong interaction is enabled by the electric field the LO-phonons create in the ionic crystal lattice, which couples well with charge carriers and excitons [20]. Thus in ZnO, with all its potential room temperature applications, the band-structure at elevated temperatures is strongly influenced by phonons and has to be analyzed carefully. This is crucial to make it possible to take advantage of the material properties in the conditions that the material will be applied the most.

This motivated us to do temperature dependent analysis with several optical spectroscopic techniques, in particular photoluminescence, reflectivity and photoconductivity. Studies were carried out on epitaxially grown ZnO films as well as newly available bulk crystals with a strongly improved level of crystal quality [21]. This allowed us to relate findings published about epitaxially grown films by other groups with our growth products, helping in the optimization of growth parameters. Most importantly, the comparison of epitaxially grown films with high quality bulk crystals enabled us to distinguish properties that are due to reduced crystal quality with properties that are intrinsically connected with the material system ZnO.

Reduced crystal and optical quality of epitaxially grown films is often related to strain, impurities and defects which are hard to avoid for the growth on non-ZnO substrates at non-perfect conditions. The intrinsic properties of strain free, low defect and low impurity ZnO bulk crystals are therefore a handy benchmark. This benchmark can also be used for a better understanding of the spectra obtained with complex techniques such as reflectivity and photoconductivity. Using

the highest quality material available allows us to get closer to the intrinsic optical response of perfect ZnO for these less well known methods, to then relate them to less perfect crystals, giving insight into defects and their relation to optical properties.

Temperature dependent measurements are a great tool to extend the understanding of physical processes causing features in optical material response spectra. Naturally, this technique is a great way to display the interaction of energy levels with phonons. Through the interaction, the levels shows characteristic energy shifts [22], broadening [23] and dissociation of energy levels [14]. The broadening as well as energy shift-related overlap of several spectroscopic features into one makes it important to trace features apparent at room temperature back to lower temperatures, where they deconvolve into separate peaks and reveal which processes might play a dominant role in its existence.

In this context it is surprising how little is known about the temperature dependence of the spectral reflectivity properties of ZnO [24], although this method might be very interesting for the investigation of the temperature dependence of the free excitons. For example in photoluminescence spectra, the temperature dependent broadening and overlap of many well defined features into one broad feature at temperatures above 150 K is the reason why it is so hard to precisely determine the electronic structure of ZnO at room temperature.

To get a detailed insight into the effect that increased phonon interaction has on energy levels, the temperature has to be varied at fine enough intervals between scans, allowing to track a particular spectroscopic feature as it changes its intensity and energy gradually from its low temperature appearance. The fine structure due to energy levels with small localization or binding energies drastically loses its intensity at the temperature that is equivalent to its dissociation energy.

In photoluminescence, high quality bulk ZnO crystals have paved the way for the resolution of a plenitude of features in the band edge emission spectrum [14, 17]. The multitude of peaks that can be observed at low temperature shows that it can be misleading to simply identify a transition by its apparent energy in the optical response spectrum. The peaks are sometimes spaced at such small energy intervals that they are close to the reproducibility limit of most spectrometers. This plethora of transitions at the band edge makes it all the more crucial to investigate the temperature dependence of transitions that need to be understood better.

For the understanding of the spectra obtained by photoconductivity, not only this multitude of known transitions can play a role in creating spectral features, but the relation between peaks or dips and physical processes can be much more complicated as in fast and purely electronic level related processes such as photoluminescence. This is due to the more complex nature of the photoconductive process itself, as it involves a lateral charge transfer between contacts that can

be influenced by a number of factors: trapping, electron-phonon interaction and surface band bending effects to name a few, which can lead to a variation in charge carrier lifetimes and resulting photosensitivity. Also, photonductivity is more vulnerable to slow processes such as chemical photodesorption processes from the surface. This makes it insufficient to just analyze the temperature dependence of photoconductivity spectra by themselves. Due to their more complicated nature, PC-spectra have to be compared to response spectra obtained by other methods. We directly compare the temperature dependent photoconductive response to simultaneously recorded reflectivity spectra, as reflectivity spectra are nearly exclusively sensitive to free excitonic transitions. This avoids confusion with defect and phonon replica related features that can play an important role in photoconductivity spectra.

1.5 Surface properties

In the wurtzite structure, the ZnO crystal is polar along the c-axis, which has effects on the c-plane surfaces. Due to the tetragonal bonding character, all atoms of each plane perpendicular to the c-axis have three bonds on one side and only one bond on the other side of the plane (see figure 1.2). When cleaving the wurtzite crystal perpendicular to the c-axis, this imbalance of the tetrahegonal bonding leads to the formation of a Zn-polar and O-polar surface at the two different basal planes that cut off the crystal in the [0001] direction, since only the singular bonds break up, terminating the crystal with atoms that are connected to the next layer by triple-bonds only. By convention, the [0001] axis is defined as pointing from the Zn- to the O-polar face, therefore the O-polar face is the (0001) basal plane and the Zn-polar face is the $(000\bar{1})$ basal plane. These polar Zn- and O-surfaces each have different chemical and physical properties, making their understanding very important for device preparation, especially since ZnO is generally grown c-plane.

The effect of polarity on the etching-characteristic of ZnO is strong. As a result, etching can be used as a simple, although destructive method to identify the polarity of a given wurtzite c-plane surface. The spontaneous-polarization induced surface energy is also responsible for the formation of nanorings and nanohelics [25]. Since nearly all III−V and II−VI device layers are grown on the (100) surface of zinc-blende compound substrates, this is a very important semiconductor surface structure to be understood, not only for ZnO.

An effect of the polarity that will be investigated closer is the resulting spontaneous polarization and its effects on the surface properties. Spontaneous polarization is defined as the electric polarization that a substance possesses in the absence of an external electric field. In the case of ZnO it occurs as a direct result of the polarity of the wurtzite crystal structure and the ionic nature of the Zn-O bond. For purely covalent bonding, the ideal value for the ratio of c/a in

the wurtzite structure is $\sqrt{8/3} = 1.633$, resulting in equal distances between the atoms. In ZnO this value is 1.60, showing that the ZnO bond is of ionic nature, which is due to the differing electron negativity of the Zn- and O-ions.

There also is fundamental interest in how the evidentially stable and non-reconstructed polar Zn- and O- surfaces form, even though they have a non-ideal non-zero dipole moment perpendicular to them. Their resulting electrostatic instability can only be overcome by the introduction of compensating charges in the outer planes, i.e. on the surface or in the outermost layers, of the crystal [26]. There are several ways to achieve this, and there currently exists no agreement as to which exact process is responsible for the surface stabilization under a certain set of circumstances [7]. Since the structural and electronic properties of the polar surfaces is influenced differently by the different compensation methods, this is an interesting area of research that is important for many applications of ZnO [27].

In general, the introduction of compensating charges into the outer planes is necessary to overcome the electrostatic instability. The surface charge has to be reduced by a factor of $\approx 1/4$, to cancel out the crystal-polarity induced dipole along the c-axis [27]. Three charge compensation methods can be distinguished [26]:

(1) A deep modification of the surface electronic structure is possible by total or partial filling of surface states. This can lead to surface metallization.

(2) Alternatively, compensating charges can be introduced into the outer planes e.g. by strong changes in the surface stoichiometry. Processes that have been observed are faceting as well as an ordering of vacancies in the surface region via large-cell reconstructions.

(3) The charge compensation processes that will be investigated closer in this thesis involve the introduction of compensating charges into the outer planes via a spontaneous desorption of surface atoms as well as the adsorption of impurities such as H. Detailed studies have been carried out on the effects that hydrogen adsorption has on the (0001) zinc-terminated [28] and $(000\bar{1})$ oxygen-terminated [29] ZnO surfaces. With photoconductivity studies, the introduction of compensating charges into the outer planes via spontaneous surface-desorption and adsorption of atoms can potentially be investigated, since photoconductivity is well known to involve optically activated surface gas effects [30].

Persistent photoconductivity and the formation of surface conducting layers might also be of crucial importance in understanding the disturbing persistence of n-type conductivity in ZnO [31]: The existence of a near surface conducting channel in bulk ZnO suggests the maybe crucial involvement of persistent photoconductivity in the creation of free carriers. The thickness of this conducting layer varies strongly from 28 nm to 1.5 nm without a significant change in carrier concentration of the material.

As part of the internal effects that disturb the electrical state of the surface and surface region in a semiconductor, the inhomogeneous electric field of a space charge generated in the surface region due to the localisation of charge carriers at the surface is decisive in optical and photoelectrical processes. For an understanding of many phenomena associated with contacting, optical properties, and indeed, photoconductivity, this is crucial.

As mentioned above, the photoconductive response can be influenced by many different processes, each with characteristic response times. It has been observed that for ZnO the transitions related to free excitons are the fastest (in the order of 0.1 ms), whereas defect related transitions can be slower by several orders of magnitude [19]. The slowest transitions involve chemical desorption or adsorption of ambient molecules, a process that can happen with a response time of seconds, minutes or even hours. Between these two extremes lie the response times that are connected to defect levels. All photoconductive response processes can be slowed down if trapping of the charge carriers occurs [30]

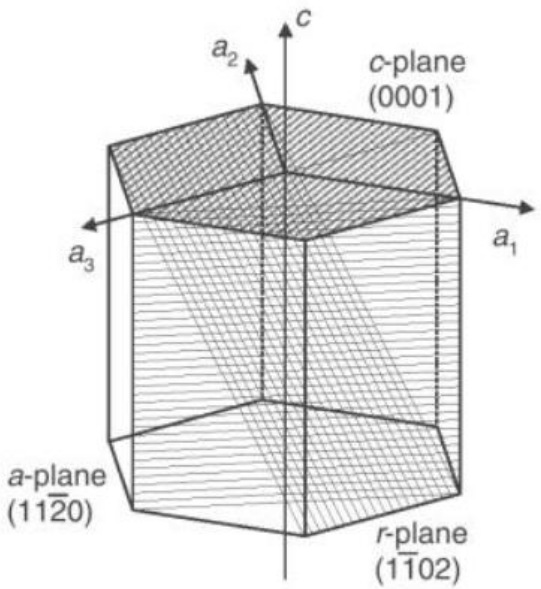

Figure 1.4: Schematic of the most common low-index planes along which a hexagonal wurtzite ZnO crystal can be cut [4]

The photoconductive response can be separated into fast and slowly responding parts. Typically, processes that are connected to electric band structure level-transitions can be very fast, with a response time of less than 0.1ms in ZnO [32], but if carriers become trapped, the response can be slowed down considerably [30]. Also, extrinsic deep level response is typically a lot slower than intrinsic band edge transitions [33].

Trapping of charge carriers can be described as a fundamental process of

energy storage [34]: A trapped charge carrier is spatially localized and requires thermal or optical energy to become mobile again. Charge carriers stay mobile until they recombine or become captured by another trap. The trap itself is a region in the crystal that is able to trap a charge carrier.

Figure 1.4 shows a schematic drawing of the different crystallographic orientations of surfaces of a hexagonal single crystal. The c-plane, a-plane and r-plane surfaces are marked. The six prismatic faces on the side of the hexagonal structure are called m-plane [35]. ZnO strongly prefers to grow along the c-axis and forms in a c-plane orientation when grown on (0001) c- or $(11\bar{2}0)$ a-plane sapphire substrates. It is possible though to grow $(01\bar{1}0)$ m- and $(\bar{2}110)$ r-plane ZnO on m-plane and r-plane sapphire substrates respectively [36]. Therefore most epitaxially grown films are c-plane and either have Zn- or O-polar surfaces. But an easy way to select unstrained crystallographic planes of ZnO is to cut bulk material along a chosen crystal direction. In this study, ZnO-surfaces in the c-plane, m-plane and a-plane orientation will be investigated.

1.6 Excitons and Polaritons

The interaction of photons, lattice polarization, electrons and holes in semiconductors is much easier to describe and understand with the help of quasi-particles such as excitons, polaritons, phonons, polarons and plasmons. Quasiparticles are called quasi, since they only can exist in crystalline matter, not on their own. Their quasi-momentum $\hbar\boldsymbol{k}$ is defined as being unaffected by integer multiplications with elementary translation vectors of the reciprocal crystal lattice. The most important aspect of the quasi-particle concept though is that they are mixed states of more than one constituent, with a quantization of the resulting mixed state, not its constituents [37].

Excitons are used to describe the behaviour of Coulomb-attracted electron hole pairs in a crystalline environment. They have been first postulated in 1931 [38, 39], when Frenkel investigated the absorption of light into crystals as a transformation of light into heat oscillations of the crystal. He described the excited state of the crystal that is created in one crystal cell by the energy injected by a photon. Due to the translation symmetry of a crystal with identical cells, the excited state can then spread all over the crystal, resulting in a slightly different vibrational state of the whole crystal. Wannier and Mott established the idea of a hydrogen like exciton within semiconductors, that consists of an electron bound to a hole via Coulomb interaction. Due to the high dielectric constant of semiconductor crystals, the Coulomb interaction is weakened by factor ϵ_r, causing the size of the electron hole pair to increase dramatically, beyond the lattice constant [40].

Although there were earlier experimental proofs of the existence of excitons

in the electronic structure of semiconductors before 1952, as e.g. in an absorption spectrum of a thin layer of ZnO on glass, published by Mollwo in 1943 [41], excitons were experimentally unrecognized until 1952, when E.F. Gross discovered and identified a series of narrow lines at the absorption edge of a thin plate of cuprous oxide at liquid nitrogen temperature as the hydrogen series of excitons [42]. He correctly associated these with the hydrogen like series of energy states of an exciton: To calculate the total energy required to create an exciton at $\boldsymbol{k} = 0$, one has to take into account the energy required to create an electron hole pair at the band gap (E_G) and subtract the binding energies involved in the formation of the exciton state:

$$E_n = E_G - E_{ex}(n) - E_b. \tag{1.2}$$

E_n is the resulting energy from the top of the valence band to the exciton state n. E_G the band gap energy, $E_{ex}(n)$ the exciton binding energy, E_b the binding energy released when the exciton binds to defects etc, a process which will be investigated later.

Excitons are created when a photon excites an electron from the valence band into the conduction band, and the excited electron as well as the newly created hole are positioned at a close by point in space. This enables the electron and hole to bind together via Coulomb interaction, resulting in a hydrogenic system in which the electron and hole have very similar masses and are orbiting each other within the crystal. The potential energy from the Coulomb interaction of a Wannier-Mott type exciton as shown in figure 1.5 can be calculated like that of a hydrogen atom, with two bodies moving around a common centre of mass [43]:

$$V_{ex}(|\boldsymbol{r}_e - \boldsymbol{r}_h|) = \frac{e^2}{4\pi\epsilon_0\epsilon_r\,|\boldsymbol{r}_e - \boldsymbol{r}_h|}, \tag{1.3}$$

with $\boldsymbol{r}_e$ and $\boldsymbol{r}_h$ being the position of the electron and hole.

Analogue to a hydrogen atom, the electron and hole can be excited into higher states of integer numbers ($n = 1, 2, 3, \ldots$) with increasing radii, reducing the Coulomb interaction $E_{ex}(n)$ towards 0 at the ionization limit. The Rydberg constant of the exciton, R_{exc}, is the exciton binding energy at n=1:

$$E_{ex}(n) = R_{exc} \cdot \frac{1}{n^2} \tag{1.4}$$

The Schroedinger equation following from the potential energy of the Wannier Mott Exciton in eq. 1.3 gives the eigenenergy values $E_{n,\boldsymbol{K}}$. The contribution of the centre of mass of the exciton, which is dependent on the momentum $\boldsymbol{K}$ of the exciton, can be expressed separately from the relative movement of the

electron and hole and is represented by the third part of the equation

$$E_{n,\boldsymbol{K}} = E_g - \frac{1}{2}\frac{\mu e^4}{\left(4\pi\epsilon_0\epsilon_r\right)^2\hbar^2}\frac{1}{n^2} + \frac{\hbar^2\left|\boldsymbol{K}\right|^2}{2\left(m_e+m_h\right)} - E_b, \tag{1.5}$$

with $\frac{1}{\mu} = \frac{1}{m_e} + \frac{1}{m_h}$ being the effective reduced mass of the electron and hole system.

The binding energy and radius of excitons strongly varies between different materials. The more the crystal lattice deforms due to the excitonic charge carriers moving through, the more tightly bound the exciton becomes by the crystal, resulting in a higher effective mass of electron and hole. Therefore the dielectric constant ϵ_r of the material determines the exciton binding energy. Excitons that are free 'Wannier-Mott' excitons with radii much larger than the inter atomic spacing are formed by materials with a large dielectric constant. Tightly bound 'Frenkel excitons', smaller than the inter atomic spacing are formed in case the dielectric constant is small and bound to one particular atom. The mathematical description of excitons as a hydrogenic system is based on the approximation that the dielectric background is uniform. This only is valid for the large, 'Wannier-Mott' type exciton, that encompasses a large number of atoms between the electron and hole.

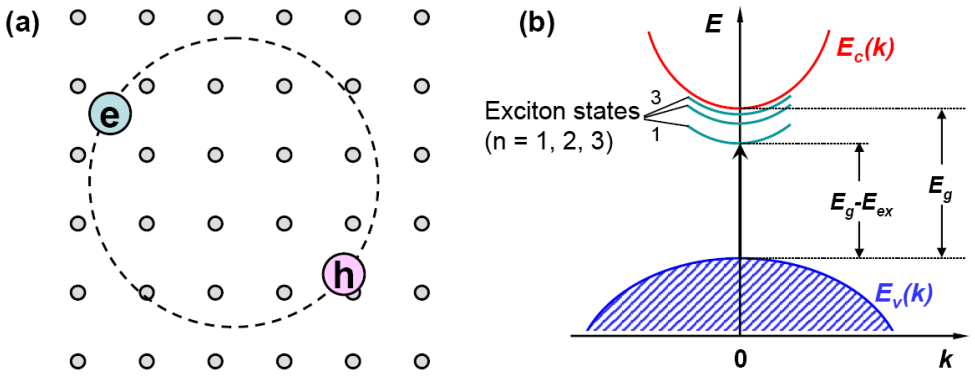

Figure 1.5: The energy levels of a Wannier-Mott exciton [43]

In general, for direct semiconductor compounds, the exciton binding energy increases and the exciton Bohr radius decreases with increasing band gap energies. For example, GaAs [6] has a band gap E_G of 1.42 eV, an exciton Bohr radius a_x of 14.2 nm and an exciton binding energy R_X of 4.2 meV. For GaN [6], $E_G = 3.5$ eV, $a_x = 3.1$ nm and $R_X = 23$ meV. The outstanding research interest into ZnO is strongly based on its very favorable and frequently quoted excitonic binding energy [44] of $R_X = 59$ meV with $E_G = 3.44$ eV and $a_x = 1.4$ nm. In order for the excitons to be stable, it has to withstand the collision with phonons. The maximum phonon energy at temperature T is given by the Boltzmann con-

stant $k_B = 8.617343 \times 10^{-5}$ eV/K, which means that a minimum binding energy of 25 meV is required in order for excitons to be stable at room-temperature. ZnO-excitons are therefore theoretically stable up to 412℃, allowing applications of the material in less than ideal environments. Also due to the high binding energy, the position of the band-gap in relation to the energy of the free excitons in ZnO does not change noticeably from low temperatures up to well above room temperature, making it stable for applications using excitonic energy levels. The exciton binding energy in ZnO is actually at the upper limit of what is desirable, since its exciton radius is close to the threshold of Frenkel excitonic behaviour. But only excitons that can move freely through the crystal lattice allow all the positive optical applications that make ZnO so interesting.

At low temperatures, free excitons can bind to donors or acceptors within the crystal that are due to defects or dopants. As a result their overall binding energy is characteristically altered. There are several different types of energies associated with excitons. Here is a short overview of the terms used in the literature and this thesis:

- Exciton binding energy: Dissociation energy of the electron hole pair which is due to the electron-hole Coulomb interaction. In case of ZnO it is 59meV.
- Localization energy: Binding energy of the exciton to a defect (unfortunately called exciton binding energy in some sources)
- Donor (acceptor) binding energy: The binding energy of an exciton to a neutral donor E_{Db} (acceptor E_{Ab}). It can be determined optically via the two electron satellite emission (TES) in PL.

Excitons can only form if an electron in the conduction band and a hole in a valence band are existing closely together in the crystal with very similar group velocities. Otherwise the electron and hole cannot stay together and form a pair. In the band structure as depicted in figure 1.3, the group velocity is proportional to the derivative of the respective bands:

$$v_g = \frac{1}{\hbar}\frac{\partial E}{\partial \boldsymbol{k}}. \tag{1.6}$$

Due to the small momentum of photons and the unlikeliness of a third-particle interaction by a phonon, the gradient of the valence and conduction band have to be similar at the point of the Brillouin zone where an electron is photo-excited from the valence into the conduction band, to allow the formation of a stable exciton. Around the centre Γ of the Brillouin zone, the momentum as well as the group velocity are small by definition. This is the reason why direct band gap semiconductors with the direct transition at Γ have a high likeliness of excitons to form at the fundamental band gap E_G, causing excitons to play a dominant role in their optoelectronic behaviour.

Excitons in ZnO have been found to have a lifetime of ≈ 300 ps, with smaller values for strained crystals [18], resulting in diffusion lengths of ≈ 100 nm. The lifetime and diffusion length of the excitons can vary strongly though, and many excitonic processes such as photoluminescence and in particular excitonic effects in photoconductivity are only possible through the polaritonic interaction of excitons with photons: A polariton is the quantization of the mixed state of the electromagnetic radiation and the excitation of the medium. An exciton polariton is a special form, where the excitation of the medium is in form of excitons [37].

1.7 Valence band ordering

ZnO has three valence bands at the Γ-point of the reciprocal lattice. This is due to the fact that the orbital angular momentum quantum number of the conduction band in hexagonal ZnO is 's', whereas that of the valence band is 'p'. The splitting of the p-type valence band into three sub bands creates free-exciton transitions from the conduction band to the valence band that are denoted as, from lowest to highest transition energy, A, B and C-free excitons. The *A*-exciton is also related to as the heavy hole, the *B*-exciton as the light hole and the C-free exciton as the crystal field-split band [7]. Figure 1.6 shows how the originally sixfold degenerate valence band is influenced by spin-orbit coupling and crystal field splitting: Negative spin-orbit coupling alone would lift the sixfold degeneracy of the valence band and split it into a high energy fourfold band with j=1/2 as well as a twofold degenerate band with j=3/2, with an energy spacing of the spin-orbit coupling, $|\Delta_{SO}|$, between the two levels. The asymmetric electric field of the wurtzite crystal by itself would reduce the sixfold valence band degeneracy as well, splitting the p-states into Γ_5 and Γ_1 states. Crystal field and spin-orbit coupling exist together, resulting in the formation of three twofold degenerate valence band maxima of the A, B and C-free exciton at Γ. Whereas the conduction band is expected to have Γ_7 symmetry, the energetic ordering of the three valence bands of the symmetries Γ_9 and two times Γ_7 is under controversy [13, 46, 47].

The valence band ordering as shown in figure 1.6 is according to the proposal of Thomas et al.. In 1960 they published the first paper to discuss the exciton spectrum of ZnO, investigating the reflection and absorption response. The paper concludes that the ordering of the symmetries of the A and B-valence bands surprisingly is reversed in comparison to most other wurtzite II-VI structures, including GaN [13]. Park, Litton et al. interpreted the spectral line that was identified as the intrinsic ground state *A*-exciton transition by Thomas et al. as an extrinsic, ionized donor-bound exciton complex transition [48]. Later, Reynolds, Litton et al. also investigated the PL-response of these excitonic transitions as they are splitted by an applied magnetic field. Also the binding energies of the excitons from the A and B-band were derived from PL-studies of their first three

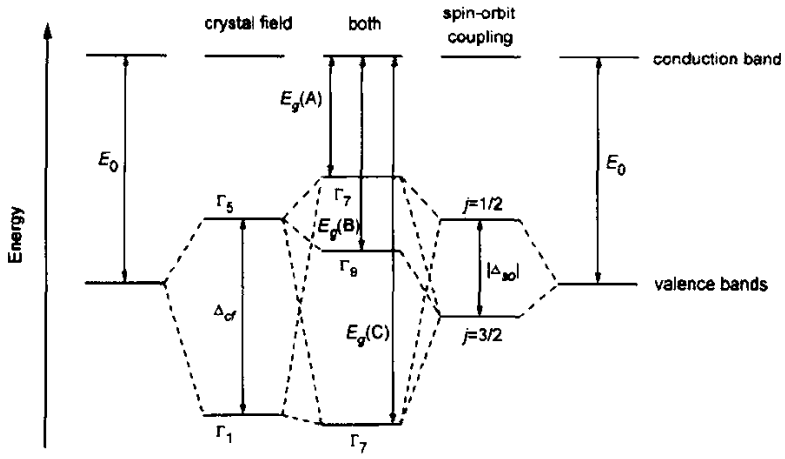

Figure 1.6: Crystal field and spin-orbit coupling related splitting of the valence band of hexagonal ZnO (not to scale) (from Mang et al. [45])

excited states n=1,2,3 [47].

1.8 Approach

The ability to control the type of the majority of free carriers in a semiconductor, i.e. vary the doping to achieve p-type and n-type material, is essential for almost any electronic application of semiconductor homostructures. The existence of photoconductivity related surface conducting layers might be part of the problem of unreliable p-type doping in ZnO [31].

Excitons already had been theoretically predicted for quite some time when the first experimental hints of their existence were measured. Although they were not recognized at the time, absorption spectra of ZnO taken by Mollowo in 1943 [41] show a characteristic peak at the onset of absorption [3]. In 1959, D.G. Thomas at Bell Labs in New Jersey published a paper about the exciton structure of ZnO. Until today this paper forms the basis of our understanding of the exciton structure of ZnO.

The incentive of this thesis is to broaden the knowledge about optical properties and their related electronic properties in ZnO.

In our group, the epitaxial growth of ZnO films is done by Plasma-Assisted Molecular Beam Epitaxy (PAMBE) as well as Pulsed Laser Deposition (PLD). To gain in-depth knowledge about the quality of newly grown samples, Photoluminescence (PL) experiments are a great tool. The existence, position, line-width and intensity of luminescence peaks originating from excitons bound to defects as well as free excitons reveals detailed information about impurities, defects

and crystal quality of the samples. This helps in the determination of optimum growth conditions.

But besides acting as a quality indicator, the electron transitions involved in interactions with photons of certain energies are of research interest themselves. Photoluminescence is strongly related to bound excitons, which are hydrogen-atom like configurations of electron-hole pairs in the semiconductor that are bound to various defects. Depending on the defect, they have slightly differing binding energies and therefore slightly differing associated photon-energies. By doing high-resolution photoluminescence spectroscopy these energies can be resolved. There is considerable effort to get a comprehensive idea about the exciton states involved in the photo emission of ZnO. [14, 17] A welcome reference point was recently given by the newly available commercial high quality bulk ZnO from sources such as Cermet and Tokyo Denpa. Albeit being far too expensive for the application in commercial devices, they offer unparalleled crystalline quality and chemical purity, a chance to gain better understanding of the material system ZnO itself, unperturbed by special conditions connected with the epitaxial growth of ZnO.

Since PL is mostly limited to emissions stemming from bound-exciton states, other analysation methods such as absorption and reflection spectroscopy have to be used to optically investigate the underlying valence-band structure. There has been a controversy about the valence band ordering in ZnO for quite some time [13, 17, 45–48].

Spectral Photoconductivity is a measurement technique commonly used to investigate the band-edge energy of novel semiconductors, since the onset of Photoconductivity is closely related with the semiconductor band gap. Thanks to the very sensitive photoresponse of MBE-grown ZnO thin films and later bulk ZnO investigated, the spectral resolution of the setup could be fine tuned to resolve spectral features far more detailed than the pure onset of photoconductivity.

1.9 Thesis outline

Details about the various experimental setups used, as well as experimental considerations necessary for the realization of the experimental work in this thesis, are presented in chapter 2.

Chapter 3 begins with the photoluminescence (PL) study of the annealing response of molecular beam epitaxially grown ZnO films, concluding with the detailed temperature dependent PL study of the best epitaxial film that was identified in this study, relating it to high quality commercial bulk ZnO.

Chapter 4 then focuses on the temperature dependence of the band structure of intrinsic ZnO by investigating the temperature dependent transmission and

reflectivity response of bulk ZnO. The chapter concludes with the investigation of the temperature dependent reflectivity response of PLD-grown epitaxial films, showing the applicability of reflectivity measurements for the investigation of crystal quality.

Chapter 5 investigates the complex structure that can be observed in the band edge region of photoresponse spectra of high quality ZnO crystals. The temperature dependence of this structure is related to the temperature dependent band structure as determined by the methods introduced in chapters 4 and 3. Chapter 5 concludes with a relation of the band structural photoresponse details in bulk ZnO with the temperature dependent photoconductivity spectra of the epitaxial films that were investigated in chapter 3.

Chapter 6 concludes with a summary and suggestions for further work.

Chapter 2

Experimental techniques

In this chapter the experimental techniques, devices and processes applied in the opto-electrical study of large band gap semiconductors will be outlined. The processes described are presented in the typical order in which a sample would be investigated.

2.1 Sample creation

Although the growth of samples was not part of this study, samples from a variety of fabrication methods were investigated in this thesis. Growth-techniques range from the MBE and PLD systems being run by groups in the Physics and Engineering departments at Canterbury University, to hydrothermal and melt growth that is used by commercial providers that grow the commercially acquired bulk ZnO crystals. Providers of ZnO bulk crystals were Tokyo Denpa, MTI and Cermet.

2.1.1 Plasma Assisted Molecular Beam Epitaxy

Molecular beam epitaxy relies on the high temperature evaporation of constituent elements of the desired film by effusion cells in a UHV-chamber. A schematic overview of the growth chamber used is shown in figure 2.1. A molecular beam is emitted out of the high-temperature effusion cells and directed towards the substrate, where the atoms deposit and ideally reach stoichiometric and epitaxial ordering with the help of an elevated substrate temperature. The elevated substrate temperature allows the deposited atoms to move along the surface more easily to achieve Frank-Van der Merwe growth of smooth films. In comparison to PLD, the growth process is very steady and, in order to avoid Vollmer-Weber (VW) type growth, in general demands higher substrate temperatures than are

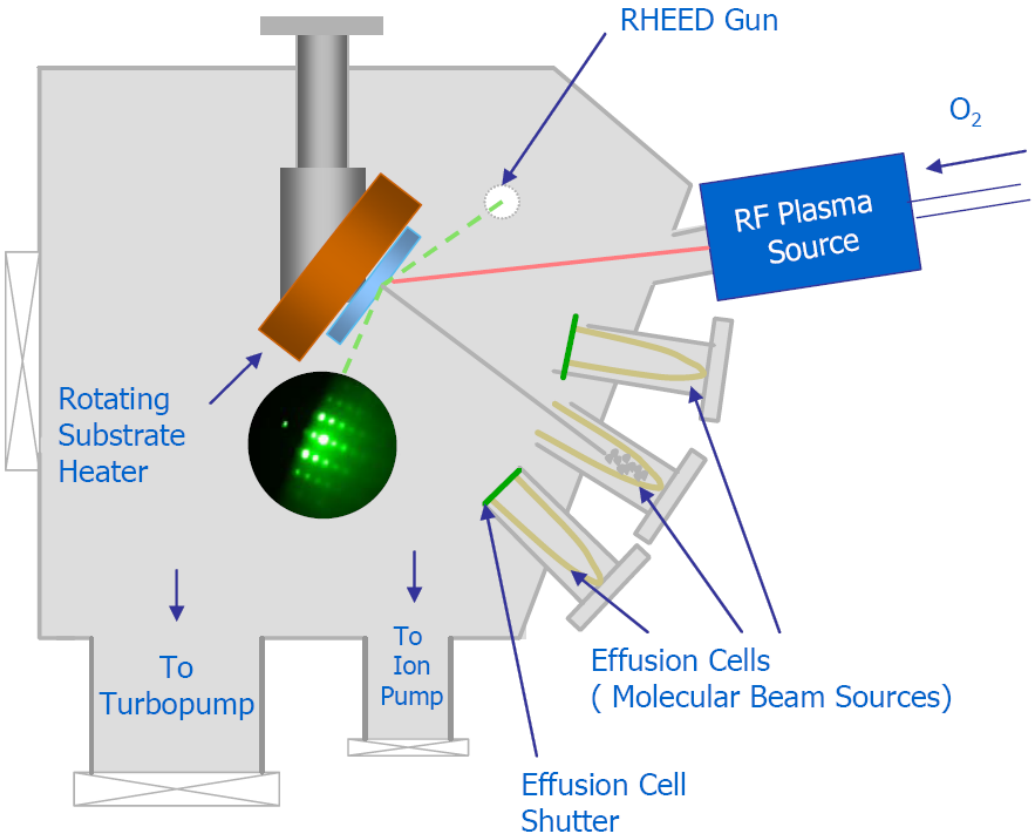

Figure 2.1: The MBE-setup at Canterbury University (from W.C.T. Lee [49])

needed in PLD. Figure 2.1 shows a schematic overview of the chamber setup used to grow the MBE-films analyzed in this study.

A special property of the setup used here is the plasma assisted growth technique. A plasma source activates oxygen atoms into a plasma to increase their ability to interact with the Zinc-flux towards the sample surface. The goal is to reach better oxygen implementation at lower ambient growth pressures, allowing a more stoichiometric and faster growth than with plain ambient oxygen in the chamber. Further detail about the PAMBE setup used can be found elsewhere [49, 50].

2.1.2 Pulsed Laser Deposition

A high vacuum chamber with a base pressure of 10^{-5} Torr was used for the pulsed laser deposition (PLD) of ZnO samples. The PLD-growth process is based on very short laser pulses of very high power hitting a target in a low-pressure environment. The samples investigated here were grown by a KrF excimer laser with the wavelength of $\lambda = 248$nm at a fluence of 3.2 ± 0.5 $mathrmJ/\mathrm{cm}^2$ per

laser pulse. The extreme amount of energy of each pulse causes atoms of the surface of the target to shed their electrons and form a plasma, which is ejected towards the growth substrate that is situated in front of the target. Zn targets were used and the oxidization to ZnO was achieved via an oxygen partial pressure of 8.2×10^{-5} Torr during growth. For more details about the growth setup see papers by Mendelsberg et al. [51, 52].

The nature of PLD-growth significantly differs from the process PAMBE-growth described in section 2.1.1. The PLD laser pulses only last 25 nanoseconds. And although the samples are grown at repetition rate of just 5 Hz, resulting in a deposition process that takes place only for a fraction of the growth time, i.e. for the duration of the plasma lifetime, the overall growth speed is comparable to that achieved by PAMBE. In MBE monomers, at higher substrate temperatures even dimers and trimers have time to move around on the surface and form islands of each new layer, promoting Frank-van der Merwe growth. In PLD, many atoms arrive on the substrate at the same time, adding enough atoms at once that instantly all newly deposited atoms can form multimers. Multimers are not able to move around as easily as single atoms. This makes the achievement of Frank-van der Merwe growth much harder for PLD and, especially for the case of ZnO, promotes the growth of nanostructures. Therefore the substrate temperature in PAMBE is much more critical than in PLD growth.

2.2 Commercially acquired bulk ZnO

Recent advantages in the growth of bulk ZnO made bulk material interesting for the analysis of the intrinsic properties of ZnO. High quality ZnO in this thesis is referred to as the bulk crystals of particularly low carrier concentration and defect density as they were commercially purchased by Cermet, Tokyo Denpa and MTI. These crystals have created great interest in the basic physical material properties of ZnO itself, aiming at a better understanding to what happens to the material when it is grown in thin films, nanocrystals, epi-layers, etc. by the various growth methods available for ZnO growth. Reports of experiments involving crystals very similar to the ones used in this thesis can be found in many publications published recently [14, 15, 17, 21, 23, 31, 53–61]. It is important to note though that we experienced that the difference of the optical qualities between crystals from consecutive shipments of the same order from the same supplier was often significant. Therefore the crystals investigated were carefully named and comparisons between different crystals were done taking into account potential changes in the crystal quality. Overall a steady improvement of crystal quality was observed in the course of this work from 2004-2008, as it became possible to resolve more and more excitonic features with smaller linewidths at the band edge by photoconductivity and photoluminescence. Also the carrier concentration went down, the mobility of the carriers went up as could be seen in Hall measurements. As a consequence, the samples became more and more

surface sensitive.

Commercial samples were delivered as pieces of clear crystal with a typical thickness of about 0.5 mm. Some samples came as pieces of 7×5 mm, whereas larger wafers were cleaved to pieces of about 5×5 mm. A diamond scribe was used to establish a line of preferential breaking, before the crystal was cleaved over a metal edge.

2.3 Non-optical characterisation

2.3.1 RHEED

Reflection high-energy electron diffraction (RHEED) scans are used in situ in the MBE-chamber to characterize the surface properties of grown, and even growing crystalline films. RHEED relies on a high energy beam of electrons between 10 and 100keV, that hit the investigated surface at a grazing angle of 3 to 5°. In case the surface has a regular crystalline structure, the electrons are diffracted into a pattern that can be detected via a fluorescent screen that is mounted opposite to the RHEED electron gun. The setup of the RHEED-system in the PAMBE growth chamber can be seen in figure 2.1, showing a very nice sharp diffraction pattern of a sample after growth. The diffraction is based on elastic scattering of electrons of the investigated surface, and therefore is closely related to the surface reciprocal lattice. Its inverse transformation reveals the surface periodicity in real space.

A streaky pattern is a sign that the investigated surface has no 3-dimensional structure but is very planar, as would be the case for a finalized layer of a smooth, layer by layer grown film (see figure 2.2). It is very hard to observe sharp diffraction spots as shown in figure 2.1, since the diameter of the Ewald sphere is much greater than the reciprocal lattice vector. Therefore the reciprocal lattice rods are cut at a grazing angle, causing the diffraction pattern to become streaky. Actually, in case of crystalline islands or droplets on the surface, bulk scattering can lead to a very detailed and non-streaky spotty pattern that is a clear indicator of very poor surface properties.

RHEED is the standard technique for obtaining in-situ information of the structural properties of surfaces. As it can be used during growth, RHEED can also detect growth rate and strain relaxation effects. The biggest drawback of RHEED for the investigation of crystallinity is the limited coherence in the RHEED electron beam, which limits the degree of long-range order on the surface that can be detected.

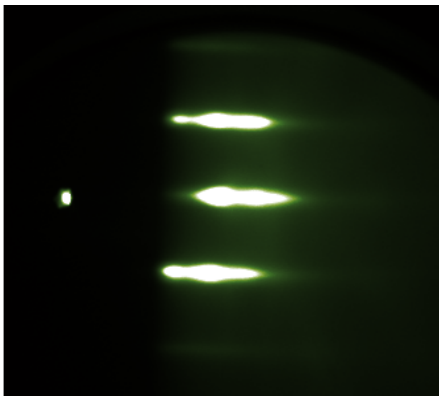

Figure 2.2: Streaky RHEED-pattern of a PAMBE grown ZnO film

2.4 Sample preparation for analysis

2.4.1 Cleaning regime

Most optical experiments described in this thesis have a high sensitivity to surface contamination. Especially photoconductivity and reflection experiments are undertaken to investigate surface effects. Therefore great care had to be taken in ensuring the cleanliness of sample surfaces, as grease and dirt could significantly alter the surface responses and properties investigated. The major sources of sample contamination were by handling errors during mounting and cleaning of the samples as well as by the oil-diffusion pumps used, as described below. In most cases the standard solvent cleaning procedure with the use of an ultrasonic bath was applied. First the sample is rinsed with acetone, then put, immersed in acetone, in an ultrasonic bath for additional mechanical removal of attached dirt. Then the sample would be rinsed with methanol to wash of the acetone. Finally a rinse with isopropyl alcohol washes off the methanol and allows, due to its low surface tension, a residue-free blow drying of the sample with nitrogen gas. In more severe cases of contamination cotton swabs were used and the solvent cleaning procedure repeated.

2.4.2 Sample handling

Storage is not expected to play a role in the quality of ZnO films, since any oxidization that is expected to change the surface properties is expected to happen rather quickly. Unfortunately we did not have the chance to investigate surface properties of films in situ before their first exposure to air nor did we investigate the long-term effect the exposure to air can have in terms of a further oxidisation of ZnO surfaces.

Identification of sample identity, for example when measuring multiple sam-

ples in the PL cryostat, was crucial. It relied on the careful sketching of their individual shape that resulted from their initial cleaving of the waver. In the cleaving procedure, only one side of the sample was scratched by the diamond-scribe tool, therefore it was easy to distinguish the two different sides of the samples.

For the mounting on the cold finger of the respective cryostat, silver paste was used. Silver paste essentially is a glue with a high proportion of colloid silver particles that provide good heat conduction properties, crucial to allow measurements at temperatures down to 4 °C. A welcome property of the glue in the silver paste used was its tendency to get very brittle after having been cooled down to low temperatures and heated back up to room-temperature. This allowed very easy removal of investigated samples from the cold finger but also resulted in a higher likeliness of samples to drop off the holder once they were cooled down. Particularly with very smooth double-sided bulk samples it was rather difficult to achieve a good adhesion of the samples to the cold-finger at low temperatures. Careful application of pressure onto the edges of the sample surface when sticking the sample on the cold finger as well as thorough drying of the silver paste at elevated temperatures prevented the silver paste from developing bubbles under the sample while evacuating the chamber.

The mounting of bulk ZnO samples for photoconductivity measurements proved a little more complicated, since it had to be prevented that the resistance measurements would be affected by conduction channels from the sample contacts on top of the sample through the sample into the copper cold finger underneath and then back through the sample under the other sample contact. Therefore the sample could not just be attached to the copper cold finger of the cryostat with silver paste. A solution was found by attaching bulk samples to a ceramic plate with the help of dried photoresist. The ceramic plate prevented external paths of conduction and itself could be attached to the cold-finger with silver paste.

2.4.3 Electrical contacting

For the electrical characterization of ZnO, probe-contact related measurement errors can have significant impact. Using two contacts to measure the conductivity of wavers is problematic, as it incurs measurement errors from current flowing through the contacts: The measured conductivity is influenced by the probes resistance, the resistance due to the spreading of the current out of each probe, as well as the contact behaviour between the probes and the material investigated. These errors can be completely avoided, as voltage measurements can be performed nearly current free with a high-impedance voltmeter. Therefore for the four-point probe technique, four contacts are placed in a line. The outer two contacts are used to source current into the sample whereas the inner two are used for voltage measurement. In the theoretically most straightforward

case of equal spacing S between four equally sized contacts that are placed at a sufficient spacing away from the edge of the sample, the resistivity of a sample then can be measured with high accuracy and calculated with [62]

$$\rho = 2\pi S \frac{V}{I}. \tag{2.1}$$

Most important when using two contacts is a very careful selection of the material used for the probes to secure ohmic instead of rectifying contacting. We used a 50nm thick Titanium layer followed by a 150nm thick Silver layer for all contacting. The contacts were deposited via e-beam evaporation. Due to the typical sample size of 0.5 × 0.5mm, four-point contacts were deposited via a mask fabricated by e-beam lithography. Wires were attached to the silver-contacts either via Indium-bonding in case of large contacts, or via ultrasonic wire-bonding if the contacts were too small for indium bonding. Indium bonding was chosen over the attachment of the wires with silver paste due to the tendency of silver paste to get brittle at cold temperatures that was mentioned earlier. In combination with the vibration of the closed cycle-cryostat used for monochromator experiments, silver paste proved not stable enough. The problem of a loose contact was that a wire would start shaking on and off the contact pad, causing the measurement to suddenly become extremely noisy after measuring at cold temperatures for some time. Indium had a smaller tendency to fail at low temperatures than silverpaste, but the most stable, although most inconvenient choice, was ultrasonic wire-bonding. It provided very reliable wiring of the sample, that did not tend to come off due to the vibrations of the closed-cycle cryostat at all. This is due to the low weight of the wires used for wire-bonding, as well as the fact that the bonding of the wires is not affected in its stability at low temperatures. Another advantage of wire bonding was that it allowed the use of very small contact pads, as they were necessary when the four-point contacting geometry was applied.

2.5 Optical and opto-electrical characterization

The optical investigation of semiconductors can potentially be of outstanding energetic accuracy and reveal a lot about the nature of the effects involved in the optical interaction of the semiconductor. But optical experiments are rarely absolute measurements. Calibration and variation of parameters play a key role in attaining in depth knowledge about the materials investigated. The two most important parameters that are subject to systematic variation in the optical experiments presented here are the measured photon energy and sample temperature. This is achieved by the use of spectrometers and cryostats. Normalization and calibration also play a key role in optical experiments. In this section the experimental devices used shall be illustrated.

2.5.1 Spectrometers

Spectrometers are used for two purposes in this work: To analyze the intensity distribution across a wavelength spectrum of an unknown emitter, i.e. luminescent ZnO, and as a monochromator that selects a variable but narrow wavelength section from a broad band light source, allowing the detection of the wavelength-dependent response function of the sample. For some experiments, such as photoconductivity, monochromated light is the only way to investigate the wavelength-dependent sample response. But for reflectivity and transmission experiments, both variations of spectroscopy can potentially be used. The advantage of exposing the sample with light of the measured wavelength only, is that the property of the sample does not get influenced by photons of other energies than the one measured. The analysis of the intensity distribution of the emitted light from a sample irradiated with a white light source can often be done at higher spectrometer resolution, since most white light sources are hard to collimate, causing a broadening of the line-width of the monochromator output.

Due to their outstanding spectral resolving power and light throughout, Czerny-Turner spectrometers (CTS) (see figure 2.4) were used for most spectrally resolved measurements. CTS is based on a turnable diffraction grating and two focusing mirrors mounted inside a light-proof box, that has finely adjustable entrance and exit slits. Light coming from the entrance slit gets collimated and directed onto the turnable diffraction grating by the first mirror. The grating has a size of about $10 \times 10cm$ and can be exchanged with gratings of different specifications. An important property of grating monochromators compared to prism-spectrometers is their ability to diffract in higher orders, since the diffraction of the grating is governed by the well known diffraction relationship

$$n\lambda = d\,(\sin\theta)\,, \tag{2.2}$$

(n: order of diffraction, d: spacing between the grating lines, θ: angle between the normal to the grating and the incoming light). An important property following from the diffraction equation is that larger wavelengths λ refracted at angles θ overlap with shorter wavelengths λ/n being refracted at higher orders n. This has to be considered experimentally by the use of appropriate filters.

For transmission measurements in air, a 'Cary 14 recording spectrophotometer' was used. It relies on the optical dispersion in a prism for the selection of light wavelengths the sample gets exposed to. Contrary to grating spectrometers, prism spectrometers have the strong advantage of a lack of higher orders in the emission spectrum.

An Ocean Optics CCD Spectrometer of type 'HR 4000 CG-UV-NIR' was used for reflection measurements at room temperature at ambient conditions. The spectrometer has no moving parts, but achieves a step size of ≈ 0.18 nm from IR

to UV. The minimum step size of 0.18 nm is given by the number of pixels on the CCD-chip of the system. The light sensitivity of the small spectrometer can be improved substantially by integrating over many measurement cycles. This is a significant advantage of CCD-systems, made possible by the CCD chip being able to take several thousand measurements at once, one for each pixel. This often allows us to measure the whole spectral range of interest at once, making time consuming step by step scanning procedures unnecessary. Therefore the only real drawback of the small Ocean Optics spectrometer is its resolution, which is limited to a minimum of ≈ 2 nm. Light is directed into the stationary grating spectrometer via optical fibres allowing to take reflection measurements at angles ($\alpha \leq 2$ °) very close to normal incidence ($\alpha = 0$ °).

2.5.2 The Lock-In technique

The Lock-In technique allows the detection of signals that are embedded within noise that is several times larger than the signal itself. The technique involves the use of a modulator, influencing the signal with a controlled reference frequency. In this case we used a mechanical chopper wheel to modulate the light exposure of the sample with a frequency of 5-5000Hz. The basic operating principle of the Lock-In Amplifier (LIA) can be understood in four steps:

1. Input Gain Stage: The LIA first amplifies the incoming signal with a pre-amplifier. The amount of amplification is controlled via setting the sensitivity of the LIA. To relate the LIA output with the signal measured, the sensitivity has to be taken into account.

2. Reference Circuit: The reference signal that is fed into the LIA from the chopper wheel is a on/off Voltage curve. The LIA determines the phase and frequency of the reference by measuring the time when the reference signal crosses a given voltage and generates an internal sine reference wave with the same phase and frequency. The phase shift between the internal sine wave and the reference signal from the chopper can be shifted with the phase shifter.

3. Demodulator: The heart of a LIA is a multiplier stage. It multiplies the internal sine reference wave with the signal from the experiment. The result of multiplying two sets of sine waves together are waves with frequencies of the sum and difference frequencies of the two waves. The signal from the experiment is not a perfect sine wave, since it contains noise and background offset. Only the part of the signal that has exactly the same frequency as the reference signal gives a DC output when multiplied with the reference signal though. Noise has a random frequency which therefore mostly is different to the reference frequency. Noise, as well as other components that are not triggered by the chopper result in components in the output with frequencies $f > 0$.

4. Low Pass Filter: Unwanted components including noise therefore can be filtered out simply by applying a strong low-pass filter. Integration over longer time constants allows the detection of weaker signals by filtering out the AC components more efficiently.

The time constant TC is a value in seconds that determines the low pass filter bandwidth:

$$TC = \frac{1}{2\pi f_{\mathrm{ro}}} \tag{2.3}$$

f_{ro} is the roll off frequency at which the low pass filter reaches a $-3dB$ filtering of the unwanted components in the signal output. The time constant TC therefore is closely linked to the noise level in the LIA output. Especially for scanning experiments, it is crucial to take into account that a higher time constant results in a slower response of the LIA and therefore has to result in a longer waiting time between steps. The time the LIA needs to settle to accomplish 95% of the change to its new value from the last output value it had before the current experimental conditions were set, is the waiting time W

$$W = k * TC \tag{2.4}$$

The waiting time W therefore states how much time has to pass once the experimental conditions have stabilized. After the waiting time W has passed, the LIA-output is mostly governed by the experimental state that is intended to be measured, without the signal reaching the LIA before the current condition were achieved influencing the LI-output. Unfortunately this assumes that the value measured in the experiment is not time-dependent, i.e. does not change during the waiting time. Therefore an increase in waiting time is not always a good way to reduce noise, since the decrease of noise is limited by the stability of the signal coming from the sample. W can be compared to an integration time, since it is related to the time-interval the LI averages over. Especially for scanning experiments it is important to keep W small, as it applies at each step of the scanning experiment, resulting in lengthy scans if too large. The factor k by which the time constant has to be multiplied depends on the steepness of the roll off of the low-pass filter, which can be adjusted to levels between $3 - 24\frac{\mathrm{dB}}{\mathrm{Octave}}$. For $12\frac{dB}{Octave}$, $k \approx 4$.

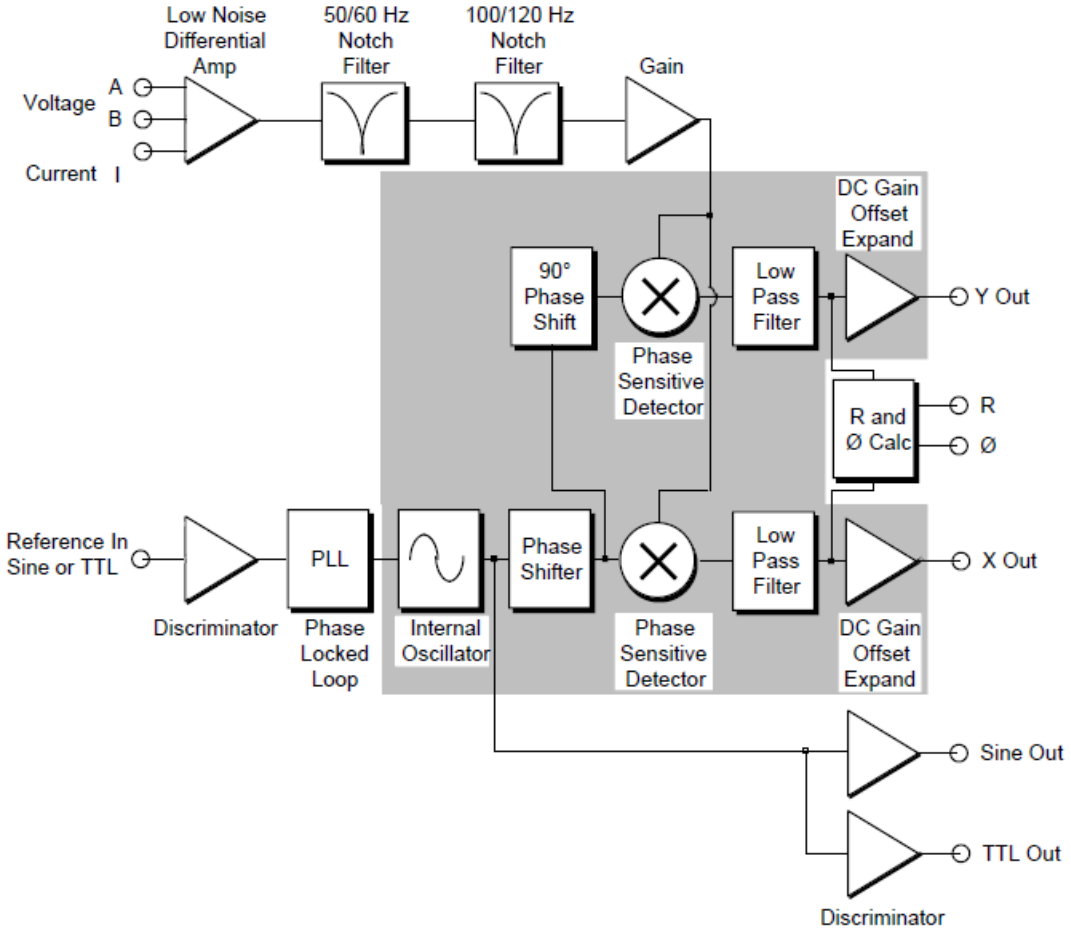

Figure 2.3: Functional block diagram of the digital signal processor Lock-In Amplifier of Stanford Research Systems that was used for most of the modulated experiments [63]

In a standard single phase LIA, the phase of the reference θ_{ref} has to be matched carefully to the phase of the signal θ_{sig}, in order to get maximum output X, since:

$$X = V_{\text{sig}}\cos(\theta_{\text{sig}} - \theta_{\text{ref}}). \tag{2.5}$$

is the strongest with

$$\theta = \theta_{\text{sig}} - \theta_{\text{ref}} = 0 \tag{2.6}$$

The advantage of a dual-phase LIA, as shown in figure 2.3, is that it is possible to measure the response of the signal Y to a 90° phase-shifted reference signal at the same time:

$$Y = V_{\text{sig}}\cos(\theta_{\text{sig}} - \theta_{\text{ref}+90^\circ}). \tag{2.7}$$

This allows us to treat X and Y as oscillating vectors at 0° and 90° relative to the lock-in reference signal, out of which the LIA calculates the absolute length

of the resulting signal vector R:

$$R = \sqrt{X^2 + Y^2} \tag{2.8}$$

with the phase shift between signal and reference being

$$\theta = \tan^{-1}(\frac{X}{Y}). \tag{2.9}$$

In summary, the LIA input consists of the measured sample signal (in Volts) as well as the reference frequency and phase. To understand the LIA's output R, the modulated input signal has to be considered in the frequency domain. Of the Fourier transformed sample signal, the LIA filters out everything but the sine component that is exactly frequency matched to the reference. The amplitude of the LIA-output is the RMS-value of the filtered-out sine component

$$V_{\mathrm{RMS}} = \sqrt{\frac{1}{T_2 - T_1}\int_{T_1}^{T_2} [V(t)]^2\, dt} = \frac{V_{\mathrm{peak}}}{\sqrt{2}}. \tag{2.10}$$

2.5.3 Photoluminescence

The layout of the photoluminescence setup is shown in figure 2.4. The samples were placed onto the copper cold-finger of an Oxford Instruments Microstat 2000 liquid helium flow cooled cryostat, which allowed rapid cooling from room temperature down to 3.9K. The air in the cryostat was evacuated by an oil-diffusion pump. The valve to the pump was closed before cooling, to avoid cryopumping of oil-particles onto the coldfinger and samples. Temperature control was achieved via a thermostat controlled electric heating stage in the cryostat, that was heating parallel to the liquid helium cooling, creating a stable balance. According to the temperature controller, the temperature sensors at the top of the cold finger could be held at steady temperatures ranging from 320K to 3.9K, with a precision of ± 0.15 Kelvin. The samples were glued onto the copper sample holder in the cryostat with highly heat-conducting sliver paste. To take account for delayed heat conduction to the samples, a minimum of 10 minutes was waited after the temperature sensor in the cryostat stabilized on the desired temperature.

For the optical excitation of ZnO ($E_G \approx 365$ nm), the 333 nm line of an Ar^+-Laser was used between 7 and 18 mW. Due to the relative closeness of the mounted samples on the cold finger to the cryostat window, the laser-light could be directed onto the samples at a low angle. This reduced laser scattering and reflected light getting into the spectrometer. The large diameter cryostat window allowed up to 9 samples of the size of 4×4 mm to be fitted onto the cold finger at once, enabling comparative measurements between a wide range of samples. The laser was focused to a spot size of ≈ 0.8 mm. The exposition of the samples to the laser causes the samples to emit photoluminescent light into all directions.

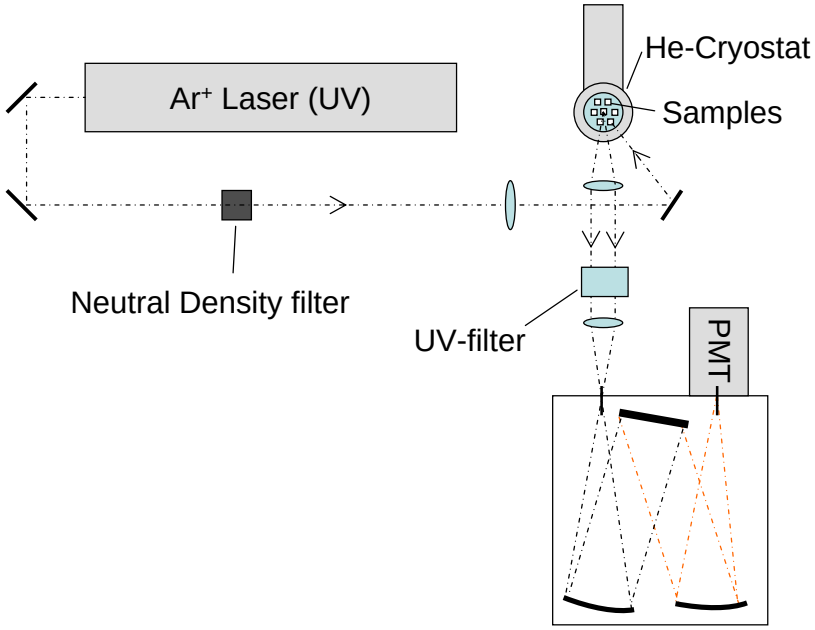

Figure 2.4: Schematic of the PL-setup

Therefore a collimating lens is required close to the cryostat to collect a large proportion of the emitted light.

The alignment of the collimated beam with the optical axis of the spectrometer is essential for accurate measurements and a high intensity yield and therefore was done with great care. The first step was to place the spectrometer focusing lens at a focal length's distance from the spectrometer entrance slit. The collimating lens and excitation laser spot on the sample then were adjusted accordingly. The f-number of the spectrometer focusing lens has to be matched with the f-number of the spectrometer. This is essential since only then the light hitting the grating is collimated, as indicated in Figure 2.4, minimizing the systematic error.

For the strongly UV-emitting ZnO, a clear Plexiglas UV-filter was used in the optical path of the PL-emission, to measure the relatively weak photoluminescence in the visible region of the spectrum while blocking the strong UV-emission that would overlap the signal in the visible range due to 2nd order diffraction on the grating.

The monochromated output of the spectrometer was directed into a Peltier-cooled photomultiplier tube (PMT), which was read-out by photon-counting electronics. The PMT was normally operated at 1800V. The dynamic range of the photo-counter setup allowed measuring in a wide range, from the dark background at $\approx$ 20 photons/second to $\approx 4 \times 10^6$ photons/second. It therefore is possible to record PL-emission lines that are very weak in comparison to the dominating emission lines in a single scan at the correct relative intensity. For

strongly emitting samples, the PMT-voltage was reduced to 1500V and the excitation laser power limited with the help of neutral density filters.

Only highly UV-transparent quartz lenses and windows were used in the setup. The response curve of the spectrometer grating and PMT are not fully constant, therefore care has to be taken in the comparison of absolute intensities of PL-lines of strongly differing wavelengths.

2.5.4 Spectral Photoconductivity

The layout of the photoconductivity setup is shown in figure 2.5. A Xe-arc lamp in conjunction with a monochromator is used to produce narrow-band light of selectable wavelength. The light gets collimated, chopped, and then focused to cover the area between the contacts on the sample that is mounted on the cryostat cold finger. The light spot could be focused to a width of 1mm. The cryostat was sitting on a fine-adjustable x,y-translating stage, allowing the optimization of the position of the light spot on the sample by maximizing the signal strength. Due to thermal contraction of the cold finger with changing temperature, the position of the light spot had to be optimized at each temperature step. Otherwise a sufficiently large uniform light spot had to be used, so that the sample would be under the same optical conditions at all temperatures. Since the cold-finger would contract by more than 2mm when being cooled from room-temperature to 10K, this requires substantial defocussing of the light spot and comes at the cost of less intense light and therefore can only be done if the signal is sufficiently strong.

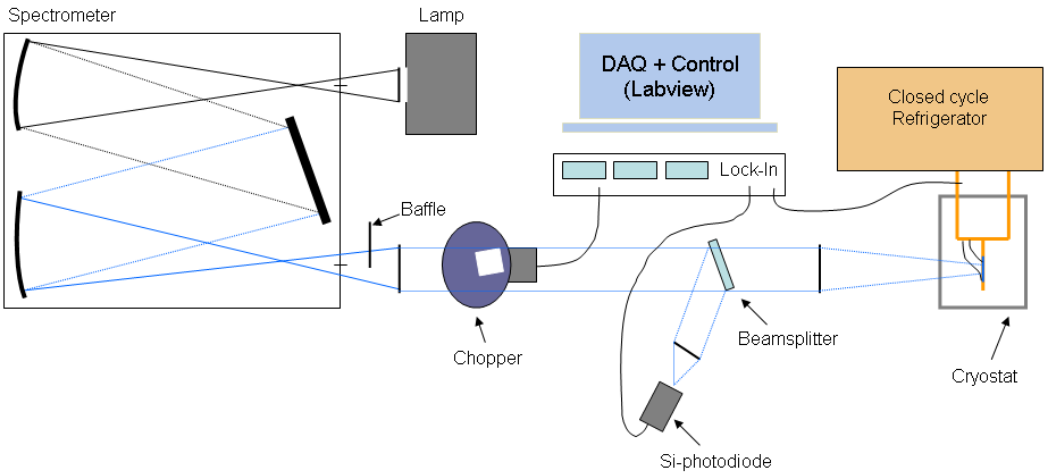

Figure 2.5: Schematic of the PC-setup

For cooling, a two-stage closed cycle CTI-Cryogenics Model21 He-refrigerator

was used. For variable temperature control, a temperature sensor and a pair of heating resistors were mounted to the cold-finger. In conjunction with a purpose-built temperature controller, the temperature could be adjusted with a precision of less than ±0.5 K from a minimum of 10 K up to a maximum of no more than 320 K, to avoid the melting of indium used for thermal contacting within the cryostat. The cryostat atmosphere was evacuated by an oil-diffusion pump. The operating pressures were below 1×10^{-4} Torr. To avoid oil-contamination of the sample-surface, a liquid nitrogen cold-trap was inserted into the vacuum-lines connecting the pump to the cryostat. At low temperatures, the cryostat valve was closed to avoid cryo-pumping.

To filter out slow changes in the sample's conductivity, the Lock-in technique was used in most experiments. It is based on the measurement of the phase locked sample response to the periodically chopped light exposure. As a Lock-In (LI), the 'Stanford Research Systems Model SR830 Digital Signal Processing Lock-In Amplifier' was used, since it allowed us to read out the phase-locked sample response independently of its phase-lag to the reference signal. The sample response and its phase difference to the chopped light were read out and recorded by the data acquisition (DAQ) system described below. The Si-photodiode was read out by a second LI of the same type. To chop the light and supply the reference signal to the Lock-Ins, the Princeton Applied Research Model 192 variable speed chopper was used. By the use of various blades the chopper could be operated at frequencies ranging from 5Hz to 4kHz. All chopping wheels used had a light/no light ratio of 1:1, which works best with the Lock-In technique. The driving current for the photoconductivity measurements was supplied by a Keithley 2400 Sourcemeter. Various contacting and wiring configurations were used to read out the photoconductivity response, as will be detailed out in the results chapters. Since the Lock-in effectively was limited to reading a change in sample voltage, the samples had to be supplied with a constant current. To avoid transient effects in the generation of a constant current by the Sourcemeter, for measurements involving high chopping speeds, a constant voltage was applied across a load-resistor. The Lock-In technique allowed the measurements of changes in the sample voltage down to $\Delta U = \mu V$ at frequencies up to several MHz. Therefore special care had to be taken to minimize the capacitance of the wiring between sample, Lock-in and sourcemeter. This was achieved by keeping the involved BNC-cables at a total length of less than 30 cm.

Most of the photoconductivity spectra in this work are presented as the photoconductive responsivity (PCR) of the investigated material, with

$$[PCR] = k \times \frac{V}{W} \tag{2.11}$$

V is the voltage that the Lock-In amplifier measures, i.e. the change in voltage due to the modulated light exposure of the sample that is under an applied constant current I. W is the intensity of the incident light as measured by the

referencing photodiode. k is an arbitrary factor that takes account of parameters of the setup that are hard to determine with meaningful precision and that can vary over time or between samples:

(a) The absolute power of the incident light on the sample, as the response of the referencing diode is only known as a relative response curve.

(b) The irradiated area of the sample that contributes most to the change in photoconduction. Investigation of the intensity of the sample response in relation to the irradiated sample area show that different parts of the sample show different sensitivity to the incident light. This sensitivity is closely related to the shape and alignment of the contacts on the sample.

(c) The resistivity ρ of the sample is not constant, as it is changed by slow photoconductive effects during the measurement. This results in a gradual change of the response of the sample to the modulated light.

(d) The contacting geometry used, including the size and separation of the contacts

(e) The ohmic quality of the Titanium contacts on the sample surface. This depends on the state of oxidization that the surface is at when the contacts are electron-beam deposited, as well as the parameters used for the electron-beam deposition of the contacts.

Monochromator setup

Due to its strong light output in the UV-range, a Cermax xenon arc lamp of type PE300BUV was chosen as broad-band light source (for the Xe-lamp spectrum see figure 2.10). It was operated at a current of 12 Ampere to avoid premature blackening of the reflective coating in the light bulb. Maximum light output of the monochromator was achieved by focusing the only roughly collimated broad-band light coming out of the lamp into the Spex 500M monochromator by a lens matching the spectrometers f-number. A high-precision CCD spectrometer (Spex Triax 320-Spectrum One) was used for the investigation of the monochromator linewidth. The FWHM and line shape of the spectrometer output can be seen in figure 2.6, indicating slightly uncollimated light hitting the spectrometer grating. The intensity dip in the middle of the output spectrum relates to the particular design of the lamp with the electrodes blocking the centre of the lamp-output. The best way to maintain high intensity output in combination with significantly improved linewidth was to block part of the monochromator light output with a baffle that was placed in front of the exit-slit (see figure 2.5, reducing the FWHM of the monochromator output at 0.4mm slit-width from 3nm to 0.6nm (see figure 2.6)). For the setup used, the resulting FWHM roughly was dependent on the

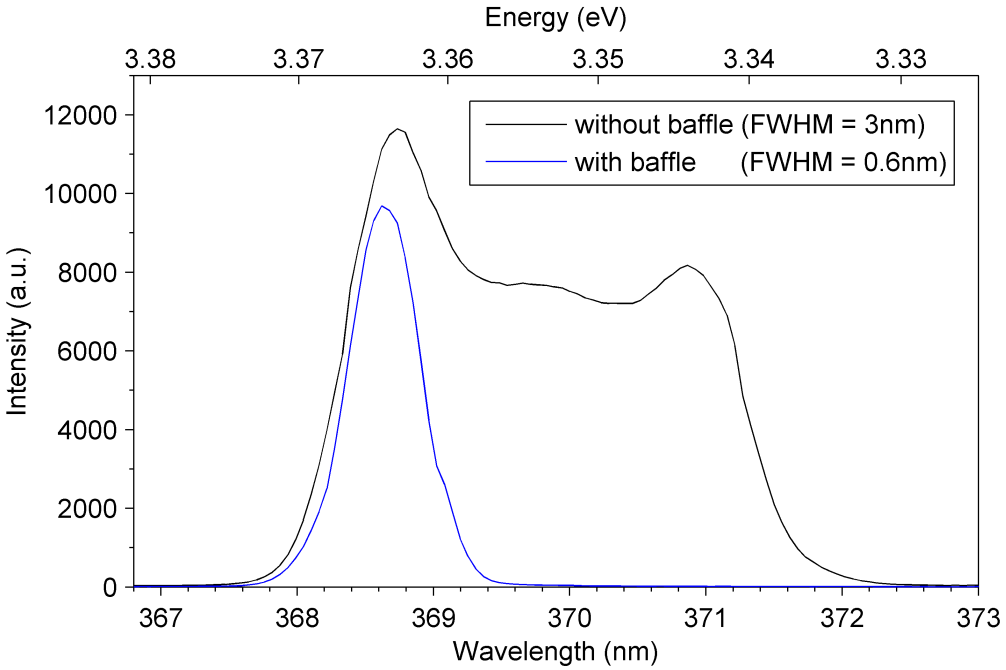

Figure 2.6: Monochromator output with 0.4mm slits, with and without baffle in front of exit-slit

slit width (W) by the linear relationship

$$FWHM \cong W \times 10^{-6}. \tag{2.12}$$

The intensity (I) of the light output of the spectrometer though was dependent on the slit-width by

$$I \propto \frac{1}{W^2}. \tag{2.13}$$

The achieved intensity of the light coming out of the spectrometer therefore was limited by the desired $FWHM$. Therefore careful balancing of the slit width was needed to gain optimum spectral information about the samples. The aim was to achieve a signal that is just strong enough for the features of interest to be clearly above noise level. To enhance the intensity of the diffracted light in the UV-range, the grating used had a blazing angle (θ_b), resulting in a maximized reflection efficiency at wavelength around $\lambda_b = 350$ nm, according to the relationship

$$n\lambda_b = 2dsin\theta_b. \tag{2.14}$$

Calibration of spectrometers

Electronvolts (eV) are the preferred unit to describe the energy of states in the electronic structure of matter. Experimentally, the energy of photons can be controlled at high precision with the use of reflection grating spectrometers,

which use the wave character of photons to separate them by interference. The wavelength of photons is directly related to their energy through:

$$E = \frac{hc}{en\lambda} = \frac{k}{\lambda}, \tag{2.15}$$

with Planck's quantum of action h, the speed of light in vacuum c, the elementary charge e and the refractive index of the medium the light is travelling through n. k is the factor that is used to swap between energy and wavelength.

A mercury lamp was chosen for calibration because it emits a spectrum with only a few lines of very well defined energy across the wavelength range between 300 nm and 410 nm. That makes it possible to identify each one of them out of its intensity relation and spacing to its neighbouring lines. The identification of each mercury-line would be much harder for the case of many lines in the spectral region of interest.

The spectrometer used for photoluminescence was calibrated by scanning the output of a mercury lamp aligned with the entrance slit at a distance of 1.5 m.

All experiments were calibrated at the end of each set of scans. Although experiments were carried out in air-conditioned laboratories this was particularly important when the spectrometer was used as a monochromator: for maximum light-efficiency, the Xe-arc light source was installed very close to the spectrometer entrance slit, causing significant and inhomogeneous heating of the spectrometer box. To achieve stable operating conditions, calibration sensitive measurements were only carried out after the equipment had had ample time to reach thermal equilibrium, i.e. at least after a running time two hours.

To take into account the particular alignment of Xe-lamp, monochromator and baffle, as well as thermal influences, the monochromator had to be calibrated under running conditions, too. A separate CCD-spectrometer therefore was used to calibrate the monochromator in conjunction with a mercury calibration lamp. This was done by precisely adjusting the monochromator to the positions of selected well known mercury lines and reading the according wavelength shown by the spectrometer display. The resulting calibration of the monochromator is shown in figure 2.7. Fitting the measured offset by a linear equation results in an error of less than ± 0.4 Åacross the spectral range investigated here.

By using a second CCD-spectrometer to set the SPEX-monochromator wavelength $\lambda_{\mathrm{SPEX(CCD)}}$ to a wavelength that is very close to the measured wavelength $\lambda_{\mathrm{Hg(CCD)}}$ of a mercury(Hg)-line with λ_{Hg}, the real wavelength of the light emitted by the monochromator λ_{real} can be determined as follows:

$$\lambda_{\mathrm{real}} = \lambda_{\mathrm{Hg}} - \lambda_{\mathrm{Hg(CCD)}} + \lambda_{\mathrm{SPEX(CCD)}} \tag{2.16}$$

As shown in figure 2.7, the output wavelength λ_{real} (=calibrated lambda) is in a linear relationship with the wavelength indicated on the display of the SPEX-

monochromator:

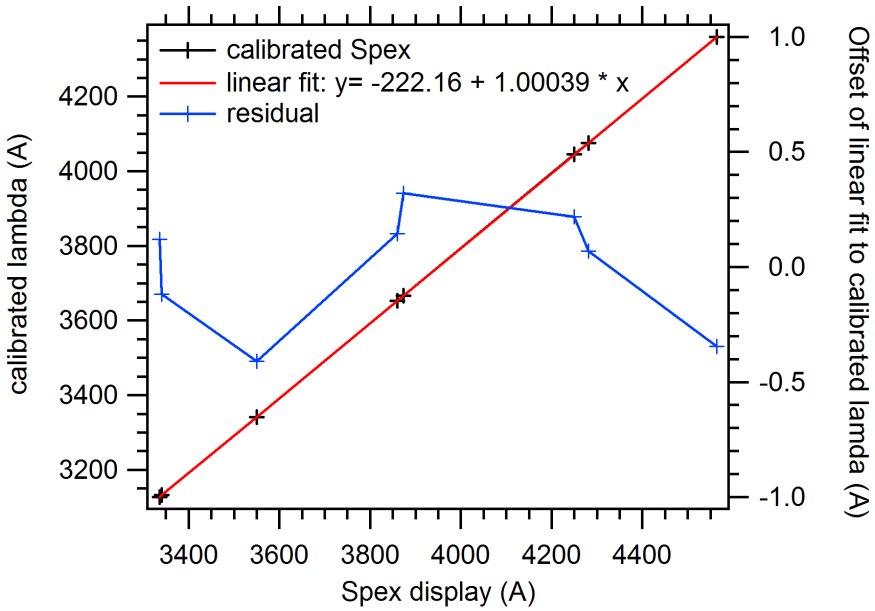

Figure 2.7: Typical Calibration of SPEX500M Monochromator with mercury lamp. The offset between monochromator and output wavelength could be accounted for by a linear fit.

It is important to notice that the mercury emission lines are extremely well defined in regard to their energy, but that their actual wavelength is dependent on the refractive index of the medium the light travels through, as described in equation 2.15. Since the selection of single wavelengths through interference only takes place directly at the surface of the diffraction grating, only the refractive index of the air at the surface of the grating is of importance for the selection of wavelengths by the spectrometers. The refractive index of air is $\neq 1$ and depends on humidity, pressure and temperature:

$$n \sim 1.0002 - 1.0003, \tag{2.17}$$

The resulting energy shift due to the variation of the calibration of the spectrometer that results from a change of the refractive index of air is plotted in figure 2.8. The variation of the refractive index due to extreme temperature and pressure variations, i.e. between 15°C at 104 kPa and 100°C at 101 kPa at the surface of the grating, only alter the spectrometer calibration by up to 0.3 meV in the energy range covered here. Note that the light-intensity of the light on the grating was very high, leading to a heating above 40°C of the grating itself. It is important to measure at fairly stable running conditions, then the changes of the refractive index during measurements should not play a significant role.

It is significant though to consider the refractive index of air, as it results in a total shift of ≈ 1 meV against using $n = 1$ in equation 2.15, see figure 2.8. The refractive index of air is best taken into account through the literature values

of the energy of the transitions investigated. A handbook by CRC was used for reference [64]. By using the same value for n as the reference

$$n = 1.00028, \tag{2.18}$$

the correct energy value can be obtained, independent of the refractive index the measurements were conducted under. The actual wavelength during the measurements is of little importance, as in the literature the spectral information is communicated in electronvolts.

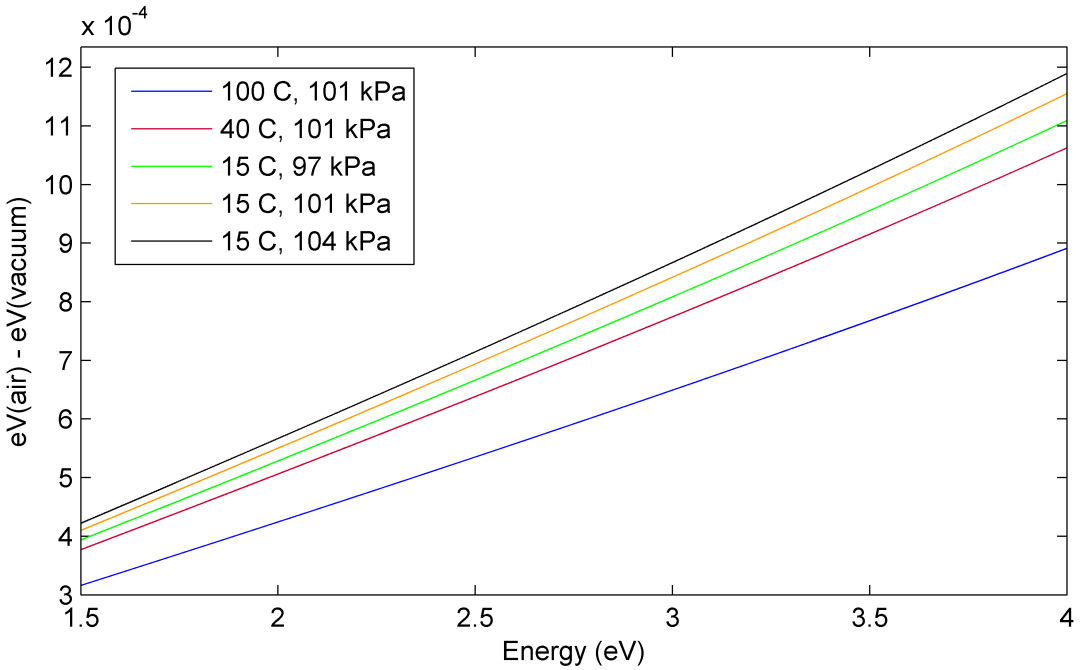

Figure 2.8: The refractive index of air and its influence on the spectrometers calibration, depending on temperature, humidity and pressure vs photon energy (dispersion). Note that the energies on the vertical axis are the apparently measured shift in energy that results from ignoring the refractive index of air: 'eV(air)'=$\frac{hc}{en\lambda_{\mathrm{air}}}$, 'eV(vac)'= $\frac{hc}{en\lambda_{\mathrm{vac}}}$. The real energy of the photons of course stays unaffected.

Normalisation of Intensity

The measurement of sample response spectra requires the knowledge of the intensity of the incident light across the investigated spectrum. The output of the monochromator is measured with the silicon photodiode as the reference signal (R):

$$R = L \times S \times P, \tag{2.19}$$

with the output spectrum of the xenon-lamp (L), the response spectrum of the spectrometer (S) and the photodiode response curve (P). As the same detector was used for referencing and detection of transmitted or reflected light ($Signal$), the detector response curve (P) (see figure 2.9) does not have to be known for normalization:

$$Signal = \frac{Signal_{raw}}{L \times S \times P} = \frac{Signal_{raw}}{R} \tag{2.20}$$

For photoconductivity, the sample's photoresponse (PC) can only be derived from the as-measured response spectrum (PC_{raw}) with the knowledge of the monochromator output ($M = R/P$):

$$PC_{real} = \frac{PC_{raw}}{L \times S} = \frac{PC_{raw}}{R} \times P = \frac{PC_{raw}}{M} \tag{2.21}$$

Figure 2.9 shows the respective spectra used for normalization. The strongly rising intensity of (M) for energies above 3.3 eV is due to the UV-blazing of the grating used.

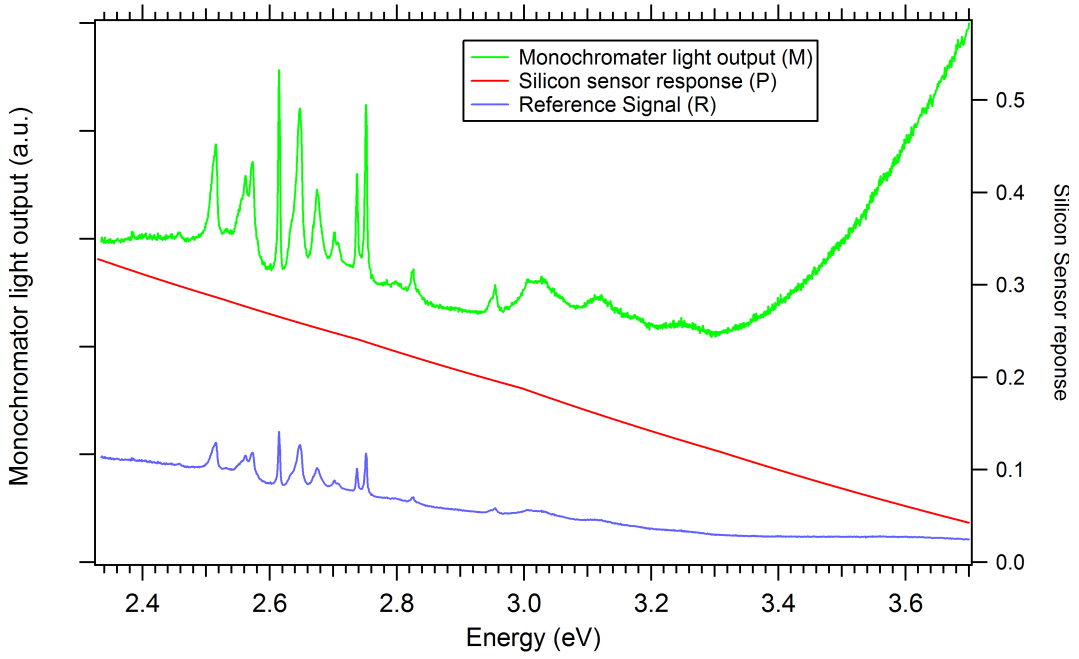

Figure 2.9: Spectra of 'reference signal' (R) and 'silicon sensor response' (P), resulting in the 'monochromator light output spectrum' (M)

Since lamp fluctuations do happen over time, it is a good practice to always measure the intensity of the incident light simultaneously with the sample response. This is done with the use of a beam-splitter, as shown in figure 2.5. To take account of the cryostat windows, the use of a mirror mounted next to the

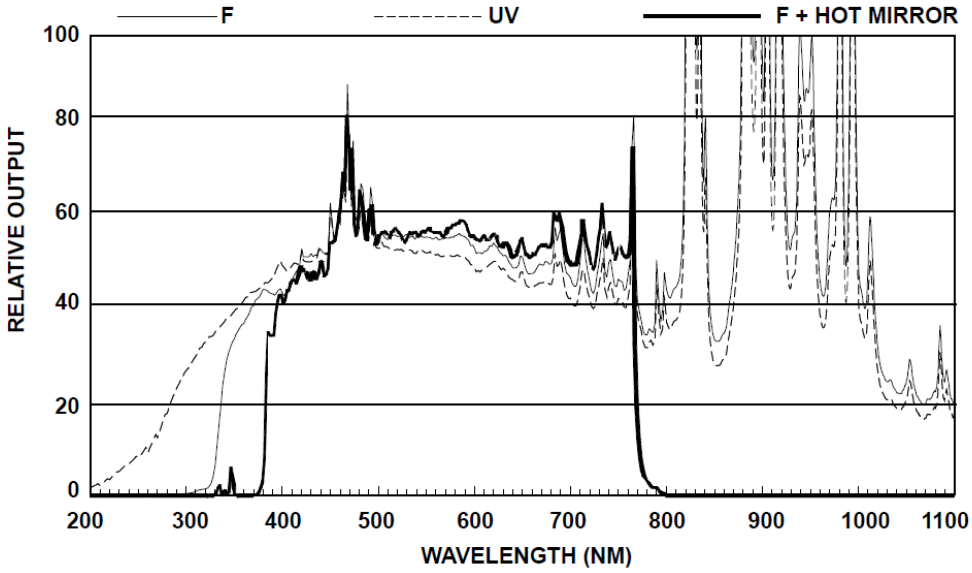

Figure 2.10: The dashed 'UV'-line shows the Output spectrum of the Xermax Xe-arc lamp PE300BUV used here

samples in the cryostat was considered, but proved to be an impractical solution since the reflectivity of the mirror is temperature dependent.

Care was also taken to minimize lamp fluctuations over time when series of measurements e.g. at a range of temperatures were taken, sometimes lasting many hours. The Cermax xenon arc lamp 'PE300BUV' has an operational current of 10-22 A (DC) [65]. Currents above 16 A resulted in a premature blackening of the reflection coating of the internal focusing mirror in the lamp. It is expected that this blackening is due to excessive temperatures caused by insufficient cooling at high operating currents. Therefore running the lamp at currents of more than 15 A proved counterproductive, the initial increase in light output was soon counterbalanced by a reduction of output intensity due to damage to the mirror. At currents below 12 A, the lamp output was unstable too, presumably due to an unstable arc due to a too low voltage. To maximize lamp-life and minimize intensity fluctuations, the lamp was run at an operating current of 12 A.

Neutral density (ND) filters are a reliable tool to reduce the intensity of a light beam by a well defined factor across a wide spectrum. We used filters by Newport, which essentially are quartz-slides coated with a thin film of aluminium, achieving a certain optical density (OD). The amount of optical power (T) transmitted through the filter is given by:

$$T = 10^{-\mathrm{OD}} \tag{2.22}$$

For $\mathrm{OD} = 0.5 \Rightarrow T \cong 0.32$. The measured transmission spectrum of the neutral

density filter indeed is very even across the full spectrum used, only varying from 0.33 at 2.4 eV to 0.35 at 3.7 eV (see figure 2.11).

For light-polarization dependent studies of the sample response, a standard transmission polarization filter was used. Figure 2.11 shows the transmission spectrum as measured by a Cary transmission spectrometer, showing strong variation across the whole spectral range. Since the Cary spectrometer relies on a prism for the spectral resolution and its light path also contains several mirrors, care has to be taken when determining the transmission spectrum of the polarizer, since the measured transmission spectrum depends on the orientation of the polarizer in the spectrometer. Therefore the transmission spectrum used for normalization was determined by averaging the spectra taken with the polarizer in vertical and horizontal rotation.

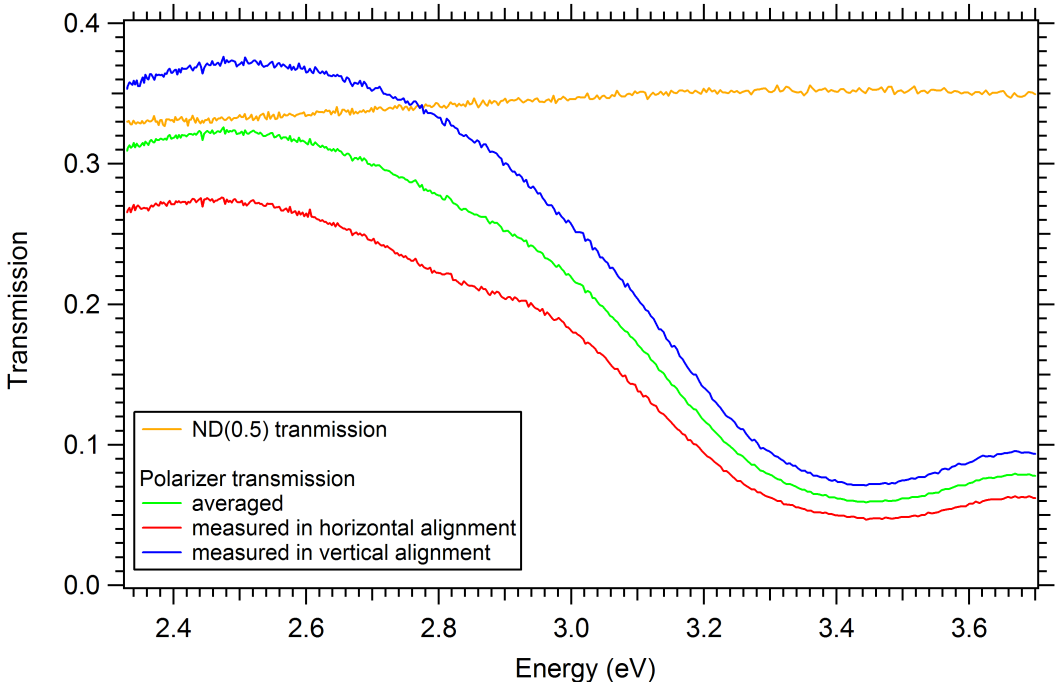

Figure 2.11: The transparency of the neutral density and polarization filters, as determined by a 'Cary Transmission Spectrometer'

2.5.5 Temperature dependent Reflection and Transmission experiments

The photoconductivity setup described above was modified to allow the spectral investigation of the temperature-dependent reflectivity behaviour of ZnO. Since the cryostat had windows on four of its sides, light could be directed onto the sample at an incoming angle of 45°. The reflected light was directed out of the

upper cryostat window and guided through vertically mounted collimating and focusing lenses into the detector that also was mounted vertically above the cold-finger. Due to the high overall light intensity, the same silicon photodiode that was used for normalization was the preferred option over a PMT to record the intensity of the reflected light. The photodiode was read out with the use of the Lock-in technique too, allowing a much better resolution of fine changes in light intensity. A limiting factor for the noise reduction in reflectivity therefore is the time constant of the Lock-in. The time constant typically used was 1 $\frac{second}{step}$, allowing a good compromise between step size, noise and the time needed to complete a scan.

The setup for the temperature dependent transmission experiments is very similar to the reflection setup. The main differences are that the detector is mounted behind the sample, and that the sample is mounted on a cold-finger with a hole under the centre of the sample, to allow transmitted light to be emitted out of the cryostat window behind the cold-finger. The Silicon-diode was also used as a detector for the transmission measurements.

The fast response speed of the silicon detector used allowed the reflectivity and transmission measurements to be taken with the Lock-in technique.

2.5.6 Software for Parameter Control and Data Acquisition

Programs for the control of experimental parameters as well as for data acquisition were custom written in Labview, for each experimental application. This way, many aspects of the measurement became automated, such as:

- Variable sized stepping of the spectrometer
- Monitoring and when necessary the adjustment of the sensitivity of the Lock-In amplifiers (LIA) for the sample and the referencing diode
- Continuous recording and control of the sample temperature
- Control of chopping speed
- Control of applied current and recording of sample voltage
- Recording of the phase and intensity measured by the LIAs.

The individual customization of the measurement software became necessary for the creation of scanning routines that allowed meaningful measurement conditions. Since a LIA was used, it was important to include waiting times into the scanning routine that are necessary as a consequence of the used LIA time constant. The sensitivity of the LIA had to be monitored and changed during

scans, in case the measured voltage dropped below 2% or above 90% of the used sensitivity range. This allowed for a high-definition measurement across many orders of magnitude, as necessary for example for the measurement of the onset of photoconductivity.

Chapter 3

Light emitting centres in Zinc Oxide

3.1 Introduction

The interest in ZnO largely stems from its potential applicability as an opto-electronic semiconductor. One direct way to analyze its optical properties is to excite the material with intense light of photons with energies above the band-gap and investigate the photoluminescence spectrum. Photoluminescence is a key technique used to get a thorough idea about the band structure of a given semiconductor. Spectral Photoluminescence (PL) is based on the precise measurement of the intensity and energy of photons emitted from optically excited states. The method offers key advantages for the investigation of semiconductors. Not only are the experimental requirements on the samples small, but the PL measurement is non-destructive and can give precise information about various aspects of the electronic structure. For the optical excitation, a laser beam with more than 10 mW of power was focused on a spot of less than ≈ 1 mm^2 at the wavelength of 333 nm. The laser-wavelength is equivalent to a photon-energy of 3.72 eV, sufficiently more than the band gap energy of ZnO, therefore large enough to excite the ZnO semiconductor electrons from the valence into higher levels of the conduction band creating electron-hole pairs. Thanks to large grating spectrometers the photoluminescence spectrum can be recorded at resolutions of ≈ 1 meV FWHM, allowing an in depth study of energy-transitions involved. Photoluminescence studies therefore form an important basis for our studies.

In this chapter the optimization of growth conditions via optical analysis will be demonstrated by an annealing study on PAMBE-grown films of ZnO on sapphire [66]. The study of temperature dependent photoluminescence spectra enables the identification of optimum growth conditions and gives information about the nature of defects and dopants that are present in the crystal structure of the material.

3.1.1 Linewidth in photoluminescence and its relation to crystal parameters

Due to Heisenberg's uncertainty principle $\Delta E \Delta t \geq \frac{\hbar}{2}$, there is an absolute minimum linewidth associated with the lifetime of the electron transition of each optical band. With $\Delta\nu$ being the FWHM of the emitted photon frequency distribution and Δt being the lifetime of the excited state associated with the transition, this homogeneous broadening leads to a Lorentzian lineshape, given by [67]:

$$g(\nu) = \frac{\Delta\nu/2\pi}{\left((\nu - \nu_0)^2 + (\Delta\nu/2)^2\right.} \tag{3.1}$$

The lineshape is Lorentzian, because all emitting states are assumed to be identical, therefore each contributing the same line-shape emission. In the crystal environment this even is the case for peaks broadened due to distortions of the crystalline environment by lattice phonons.

Inhomogeneous broadening is caused by a spread of static conditions as it can be found in the lattice environments of active centres. If several of these identical optical centres with a variety of static crystal environments overlap to one emission, their combination of slightly altered emission lineshapes results in the convolution of a Gaussian and a Lorentzian lineshape into a Voigt-profile.

3.1.2 Phonon replicas

Phonon replicas are evident in most of the PL-scans taken. They originate from lattice vibration modes in the crystal that interact with electrons, changing the electrons energy. Phonons can get created or absorbed, causing a Stokes/anti-Stokes shift of the photon energy associated with the electron transition.

Acoustic phonons can be distinguished from optical phonons in semiconductor crystals. Acoustic phonons are similar to soundwaves in the way they travel through the lattice, with two points in the unit cell moving with nearly the same amplitude, direction and phase. Optical phonons correspond to standing wave vibrations between two points in the lattice of positive and negative ions, therefore are prevalent especially in ionic crystals like ZnO. Because of the ions involved, they represent a time varying dipole moment, making optical phonons very easily excited by light. The characteristic minimum frequency of vibration of optical phonons is about 71.3 meV in the case of ZnO [17]. It is important to note that through Raman scattering, optical phonons can also interact indirectly with light.

The identification of phonon replicas is facilitated since most often more than just the first phonon replica of a certain transition is evident in photoluminescence spectra. At low temperatures (here we used 4 K), the interaction of n

phonons with the transition causes PL-features at energies of

$$E = E_0 - n \times E_{phonon}. \tag{3.2}$$

3.1.3 Donor-acceptor pair radiative recombination

A Donor-Acceptor Pair (DAP) recombination is often observed in the photoluminescence spectra. At low temperatures, when donor and acceptor ionization energies fulfill the condition $kT \ll E_D, E_A$, charge carrying free holes and electrons get trapped by the charged donors or acceptors. When these two trapped charges recombine, the characteristic energy of emitted photons is dependent on the distance between the two ions, since the recombination of the donors and acceptors causes them to be ionized and interact with the Coulomb-interaction [68] (page 302):

$$\hbar\omega = E_G - E_A - E_D + \frac{e^2}{4\pi\epsilon_0\epsilon_r R} + \Delta E \tag{3.3}$$

Additionally, the ionized impurities at a distance R undergo van der Waals interaction, which is taken into account by ΔE:

$$\Delta E = -\frac{e^2 b^5}{4\pi\epsilon_0\epsilon_r R^6} \tag{3.4}$$

The constant b is related to the dipole-dipole interaction between the radiative recombination centres. The influence of this interaction on the recombining carrier is dependent on the carriers Bohr's radius a_B around the localization centre with

$$b \approx (6.5)^{1/5}\, a_B. \tag{3.5}$$

3.2 Photoluminescence study of growth parameters for Zinc Oxide thin films

The goal of this study is to identify the right growth conditions for low carrier concentration epitaxial ZnO thin films grown by plasma-assisted molecular beam epitaxy. Especially in the quest for p-type doping, the ability to grow films with good crystal quality, low carrier concentration is an important step. ZnO has a strong tendency to be n-type. A high defect density results in a high n-type carrier concentration. Even p-type dopants of ZnO tend to exhibit a self-compensating effect: a high amount of n-type carriers is released due to defects that are associated with doping. These outnumber the p-type carriers released. The growth of ZnO thin films instead of bulk crystals is essential for the development of the material for commercial use, since only epitaxially grown films enable the technological realization of the large variety of applications that

ZnO offers. Film epitaxy allows complex growths, such as multilayer structures, homo and heteroepitaxial p-n junctions, Schottky diodes, nanostructures, quantum dots, etc.. A large number of studies on different ways of synthesizing ZnO thin films has been carried out by many different groups, such as thermal oxidation [3,4], MOCVD [5,6], and MBE [7,8]. Molecular beam epitaxy is particularly interesting since it allows very precise fine tuning of intentional dopant concentrations. This can be done by controlling the properties of the background gas. The most obvious parameters of the background gas that can easily be controlled are mixture and pressure. In this case extra focus was laid on the reactivity of the background gas. The reactivity can be controlled by exciting the background gas into a plasma with a radio frequency plasma source that is installed in the MBE-chamber. During the growth process, only oxygen atoms that do properly oxidize the depositing Zn atoms will contribute to the build-up of a regular epitaxial layer. To oxidize a sufficient proportion of the Zn-atoms, an inefficiently high oxygen growth pressure is needed due to a lack of reactivity of molecular oxygen. Besides slowing the growth process, the high oxygen pressure causes a high rate of incorporated oxygen that is not properly integrated in the lattice. This motivates the use of a plasma source to increases the oxidization rate via active oxygen and therefore allowing growth at lower oxygen pressures. The plasma source produces various oxygen species including atomic oxygen, neutral and excited molecular oxygen as well atomic oxygen ions. It has been found that not only the active oxygen, but several of these oxygen species created by the plasma-source play a role in improving the oxygen incorporation rate during MBE-growth [49, 50].

Sample resistivity is not a good indicator of sample quality, since carriers associated with defects tend to have low mobility. Hall analysis is able to distinguish between the case of a high defect related concentration of low mobility carriers from the case of a high quality crystal with a small number of carriers with high mobility. The disadvantage of standard Hall measurements is that it can give only averaged results for electron and hole concentrations in a certain semiconductor layer. Variable magnetic field Hall measurements are an option to get a more detailed idea about the carriers in a semiconductor film, even allowing to distinguish between different layers within the film [69]. Photoluminescence is only sensitive to the upper layers of the investigated film and gives direct, more simple feedback about the defect density via the peak intensity and peak FWHM.

The MBE-grown ZnO films, whose optical properties are investigated within this chapter for their response to thermal annealing, were deposited on epi-ready hexagonal (0001) sapphire substrates using a modified Perkin-Elmer 430 MBE system. The system was operated at a typical base pressure of about 1×10^{-10} Torr. High purity 6N (99.9999%) Zn was evaporated using an effusion cell, heated to provide a Zn flux of $2 - 7 \times 10^{14} \frac{\text{atoms}}{\text{cm}^2\text{s}}$ on the substrate surface. Oxygen of 5N purity, filtered by an Aeronex reactive gas filter, was excited by an Oxford Applied Research MPD21 inductively coupled plasma source. The substrate was

mounted on molybdenum growth blocks by indium bonding and outgassed at 650° C under vacuum prior to growth. ZnO was then deposited directly onto the substrate at a temperature of 550−800° C, with the plasma source operated at an RF power of 300 W. The typical oxygen flow rate is around 1.25 sccm (Standard Cubic Centimetres per Minute), which gives a process pressure of 1×10^5 Torr. These conditions result in a growth rate of approximately 300 nm/h, giving an approximately 1 μm thick film over a growth period of 3 hours. In-situ characterisation of as-grown samples with Reflection High Energy Electron Diffraction (RHEED) confirms that the growth follows a 2D (Frank-Van der Merwe) process, resulting in epitaxial films with a smooth surface. The smoothness was measured by AFM, with a typical root mean square roughness of 2.0(±0.5)nm.

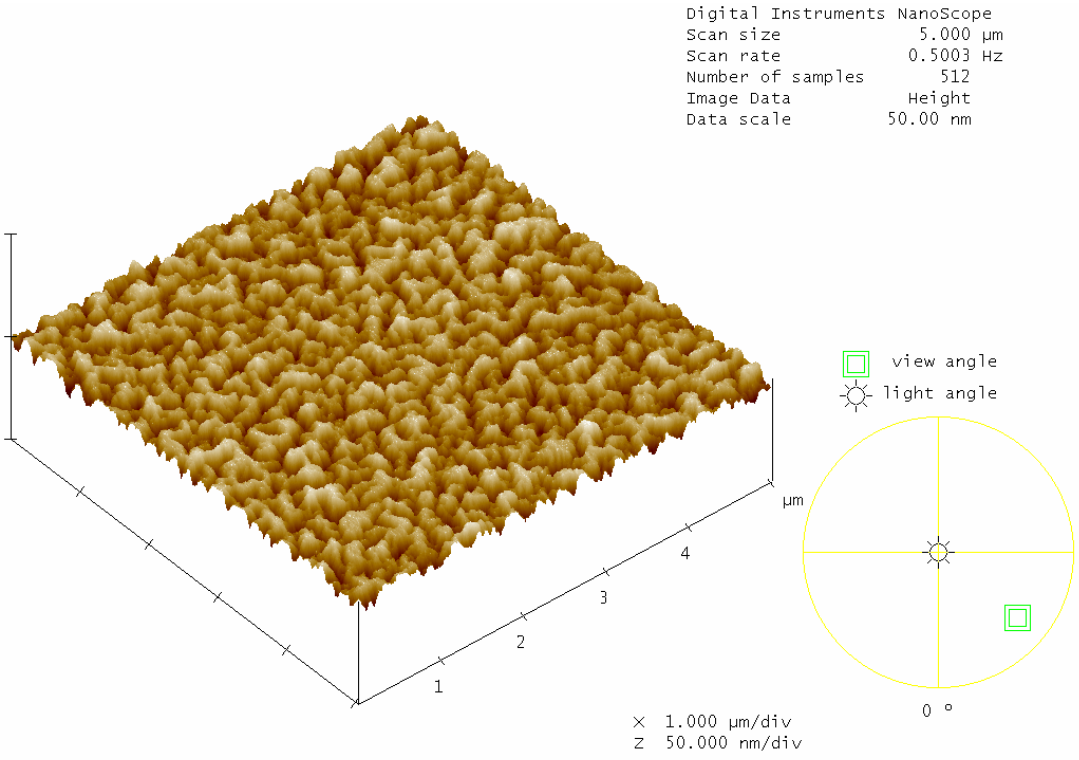

Figure 3.1: AFM scan of the MBE-sample, as-grown

3.3 Effects of annealing

Theoretically PAMBE allows the growth of epitaxial films with very well defined properties. But the growth setup also contains ample factors that can vary the growth conditions. A large number of parameters are involved in a growth: The substrate temperature, oxygen-plasma condition, parameters effecting the stoichiometry of the growth elements (like effusion cell temperature), geometry of the flux, buffer layers, etc., all affect the growth rate and film quality of the final

film. The desired film properties in this study are an epitaxial smooth film with low defect density, low impurity concentration and low n-type carrier concentration. Beside the AFM and RHEED scans, which give valuable information about the surface and crystal quality of the film, these high quality film properties typically all correlate with a strong PL emission intensity with narrow linewidth of the band gap features. Therefore it makes sense to take the photoluminescence properties as a strong guide towards the desired growth parameters.

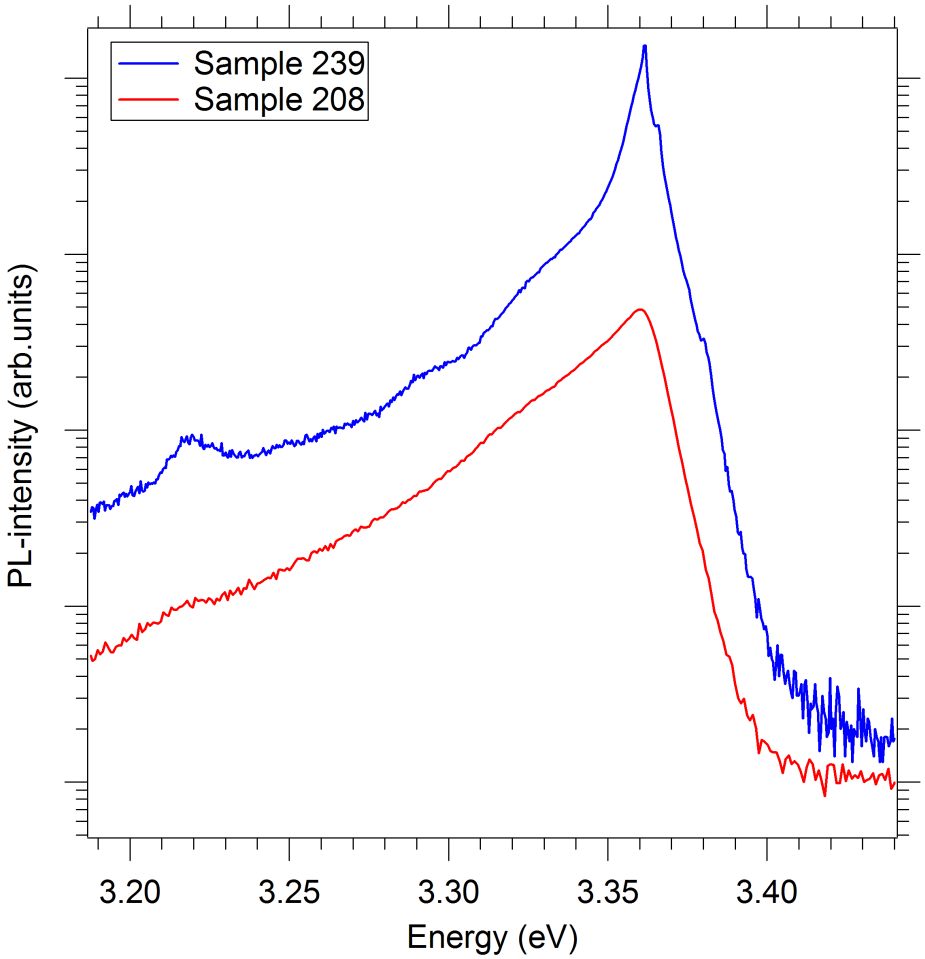

Figure 3.2: Photoluminescence spectra of sample 208 vs. sample 239. The spectra are offset for clarity. The absolute intensity was not investigated here.

Figure 3.2 shows the PL response of two samples grown with two selected differences in growth conditions. Sample 208 was grown with a substrate temperature of 550 °C, straight onto a sapphire substrate without a buffer layer. Sample 239 is grown with a substrate temperature of 650 °C, onto a low temperature ZnO buffer layer that was grown at a substrate temperature of 300 °C. Both were grown with a Zn cell temperature of 350 °C resulting in a measured flux of 6.77×10^{14} and 7.02×10^{14} $\frac{\text{atoms}}{\text{cm}^2 \times \text{s}}$ respectively. The oxygen pressure was kept at 1×10^{-5} Torr, with a growth time of 10,800 seconds.

Although sample 208 shows better single-crystalline behaviour in the RHEED scan and exhibits a lower roughness of 2.5 nm RMS in the AFM scan, compared to the 21 nm RMS of sample 239, it is clear from the PL spectra that the sample grown at 650 °C has better optical properties. Its optical spectrum features a detailed bound exciton structure at the band edge as well as longitudinal optical (LO) phonon replicas at energy steps of 72 meV, which are clearly resolved. In contrast the sample grown at 550 °C only shows one very broad peak of low intensity across the whole band edge region.

Annealing is one of the most common methods for post-growth processing and has been used in many previous studies [70, 71], to improve optical and electrical characteristics of ZnO thin films. By annealing film 208, the crystal improving potential of post growth heat treatment can be investigated. Therefore in this study, the film grown at 550 °C was broken into several pieces, which were then separately annealed under an oxygen atmosphere at ambient pressure, in an oxidation furnace, for 1 hour. The pieces were annealed at temperature steps of 50 °, ranging from the low growth temperature of 550 °C up to 1200 °C.

Figure 3.3 shows the PL-spectra of the band edge emission of the samples annealed at the various temperatures. It is evident that annealing strongly improves the linewidth and detail of the band edge PL in the same temperature range that results in gain of absolute PL-intensity in this spectral region. For annealing temperatures between 750 °C and 950 °C, the broad unstructured PL-response of the unannealed film turns into a spectrum with much greater detail, the band edge structure between 3.34 eV and 3.38 eV becomes more pronounced. For annealing temperatures of 850 °C and 950 °C, two close by bound exciton band edge peaks labelled 'A' and 'B' can clearly be distinguished at 3.358 eV and 3.362 eV respectively. A first identification of these peaks via their energies suggests that peak 'A' is associated with the I9 and peak 'B' is associated with the I4 bound exciton recombinations [14]. The I9 recombination is related to excitons bound to a neutral Indium impurity complex, whereas the I4 line is related to excitons bound to a neutral hydrogen donor complex. The two excitonic peaks can be clearly resolved although they have a spacing of just 3.6 meV. A very good lattice homogeneity is necessary to allow the emission of such narrow peaks.

The prevalence of either peak A at 3.358 eV or peak B at 3.362 eV is in direct relation to the annealing temperature. For the unannealed sample and the 550 °C sample, the B peak is strongly dominating. At 750 °C the A peak takes over the spectrum, to then step by step lose intensity relative to the B peak for annealing temperatures above 750, before only the B peak is visible in the sample annealed at 1050. For 950 °C, the A and B peaks are of comparable strength. If peak A indeed is linked to the I9 (Indium) transition and peak B is lined to I4 (hydrogen), this behaviour suggests that either the indium impurity gets activated by annealing at 750, or that the hydrogen complex is driven out by annealing at 750. A reduction of hydrogen complexes is expected to correlate

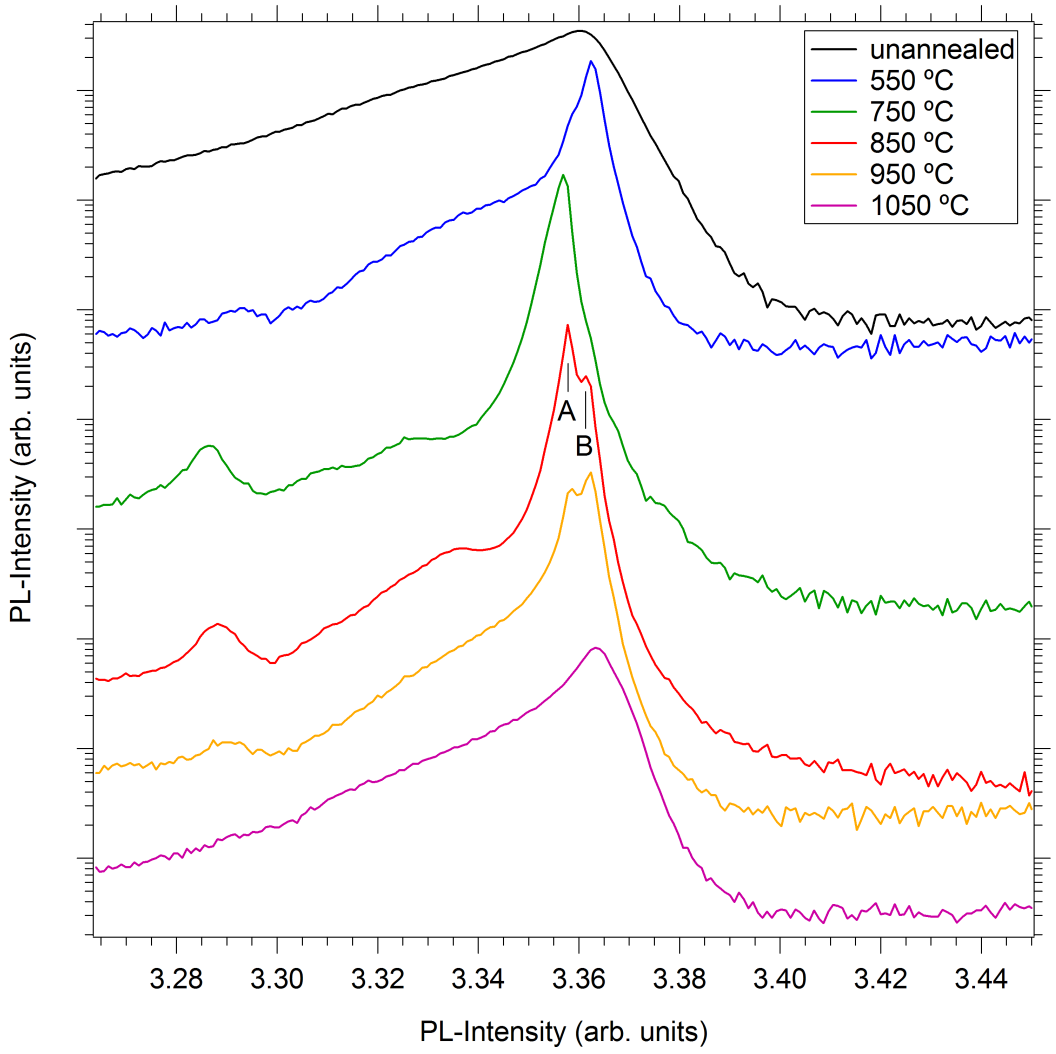

Figure 3.3: The 4 Kelvin band edge PL response of the MBE-film 208 annealed at a range of temperatures in ambient O_2. The plots are offset for clarity. At 3.45eV the spectra consist practically only of background noise, therefore the respective PL-intensity of each scan at 3.45 eV can be used as zero PL-intensity reference point. It can be seen that annealing at temperatures between 750 °C and 950 °C strongly improves the PL-signal, sharpening the excitonic features, and resulting in the appearance of the LO phonon replica at 3.29 eV.

with an improved sample quality and reduced number of carriers.

There is a broad shoulder to the bound exciton transition at about 3.335 eV for all annealed films, shifted to the slightly lower energy of 3.325 eV for the film annealed at 750 °C. Broad photoluminescence features at this energy range are frequently reported in the literature and related to a wide variety of origins [14]. A study by Alves et al., aimed at the optical investigation of excitons bound to impurities and dislocations in ZnO, investigates this energy region with spatially resolved cathodoluminescence experiments at low temperature. In these studies, the 3.335 eV emission is detected to be emitted only in distributed localized spots across the area of the material. Comparison of the spatially resolved cathodoluminescence scan with SEM-scans shows that the 3.335 eV emission spots are correlated with irregularities in the film structure that can be seen in the SEM scan. This is in contrast to e.g. the donor-bound exciton recombination emission lines, which show a homogeneous distribution across the sample [60]. Therefore the emission at 3.335 eV is expected to be due to excitons bound to structural defects.

Another frequently observed feature in this energy range is the Two Electron Satellite emission (TES). TES results from a complex process involving the exciton quasiparticle: An exciton recombines and gives part of the gained energy $h\upsilon = (E_G - E_B)$ to a neutral donor's additional electron, which gets elevated into a higher state. The resulting photoluminescence energy $h\upsilon = E_G - E_B - \frac{E_{Db}}{n^2}$ from the exciton therefore is lower than the energy that is normally emitted from a recombining exciton by $\frac{E_{Db}}{n^2}$.

According to other studies by Reynolds et al. and Thonke et al., lines at slightly lower energy around 3.31 and 3.33 eV, as featured for the sample annealed at 750 °C, belong to TES of the neutral donor bound exciton recombinations [72, 73]. This suggests that there might be an inherent difference in the origin of the broad shoulder in the sample annealed at 750 °C compared to the samples annealed at other temperatures. It hints towards the sample annealed at 750 °C not featuring an as high impurity concentration, causing a much weaker emission of excitons bound to structural defects.

The sample annealed at 750 therefore is unique in two of it's band edge PL characteristics. For one the A peak is strongly dominating the spectrum, the B peak being barely visible as a shoulder. The other difference for the sample annealed at 750 is that the defect related bound exciton structure is not showing at the expected energy, but a broad peak at the position of the TES complex. The TES complex might be part of the spectra of the other annealing temperatures, but only for the sample annealed at 750 it is not drowned out by the defect related donor bound exciton recombination peak.

The spectrum of the film annealed at the apparently excessive annealing temperature of 1050 strongly resembles the spectrum of the unannealed film. This shows that the healing effect that the annealing procedure has on the crystal

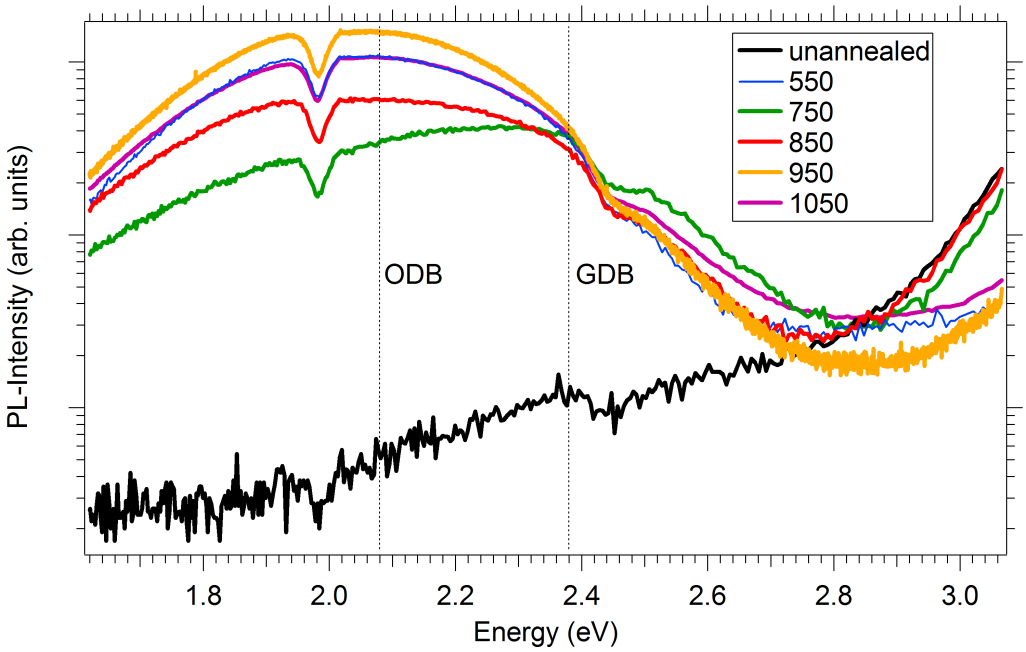

Figure 3.4: 4 Kelvin green defect band PL response of the MBE-film 208 annealed at a range of temperatures in ambient O_2. The plots are not offset. The dip just below 2 eV is due to a defect of the grating used for the measurement. The dotted lines indicate the central energy positions of the orange defect band (ODB) at 2.08 eV as well as the green defect band (GDB) at 2.38 eV.

structure is strongly dependent on the temperature, and that the crystal quality strongly degrades when a critical annealing temperature is exceeded. For very high temperatures of 1100 °C and more, the photoluminescence of the film completely dies, suggesting a destruction of the film by melting. The melting temperature of bulk ZnO is 1975 °C, but it is expected to be significantly lower for epitaxial films, due to the surface effects involved.

Figure 3.4 shows the spectra of the deep level emission of sample 208 for the various annealing temperatures. Besides the near band-edge emission, the deep-level emission of ZnO can give additional information about the film quality. It covers the visible spectrum and ranges from about 1.6-2.8 eV. When doing photoluminescence experiments, one can often see that each sample shines at its own characteristic colour, more or less brightly, ranging from deep red up to blue. These deep level emissions are associated with defects.

For the unannealed sample, the deep level emission consists only of a barely detectable feature at 2.38 eV, the green defect band. But annealing drastically changes the deep level spectrum. For all the annealed samples a strong broad emission peak cantered around 2.08 eV, the orange defect band, emerges, additionally to the rise of the green defect emission to a significant level. There are many reports about the association of deep level emission energies with different

types of defects [5,74–77]. There seems to be an abundance of reasons as to what can cause the orange as well as the green emission bands. For example a rise of the intensity of the green luminescence band at about 2.4 eV due to annealing has been reported earlier, both for annealing in a vacuum and in an oxygen atmosphere at 800 °C [75]. It has been associated with transitions involving doubly ionized zinc vacancies and an interstitial Zn^+ ion, forming self-activated centres, as well as oxygen vacancies, impurity acceptor related donor-acceptor pair recombinations, and, in several reports it has been associated with interstitial oxygen [5]. The orange defect band is also related to defect states, but it is not observed as frequently as the green defect band. Therefore it is interesting that the orange defect band dominates our defect related emission band for all annealing temperatures besides 750 °C.

Peculiar about our measurement is that the green and orange defect bands respond differently to the variation of annealing temperature. The logarithmic plot in figure 3.5 shows the effect annealing of sample 208 has on the intensity of three spectral regions of the PL-emission. The absolute intensity of photolu-

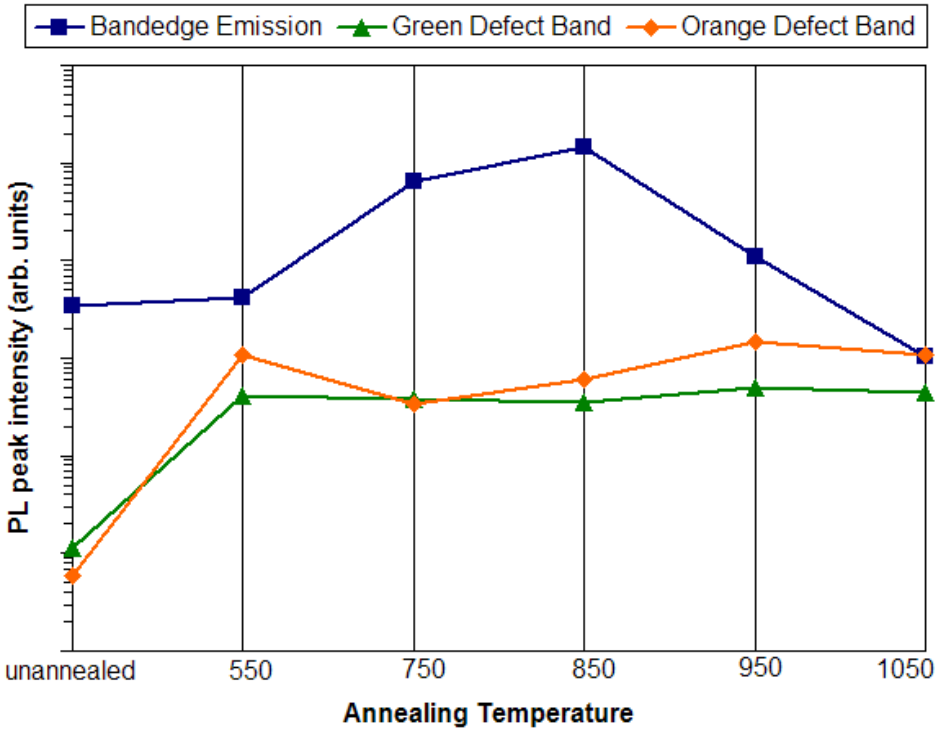

Figure 3.5: The influence of the annealing temperature on the PL-intensity of 3 distinctive energy-regions in the ZnO emission spectrum of the MBE film 208 grown at 550 °C

minescence is rarely quoted in the PL analysis of semiconductor energy levels, as it is hard to quantify it independently of the PL-setup. But by ensuring the same experimental conditions for all scans in one experiment, a comparative

measurement of the PL-intensity can reveal a strong relationship between the photoluminescence efficiency of the band gap and the annealing temperature. Together with improving the linewidth of the PL-features, annealing in oxygen gas does significantly enhance the band edge photoluminescence intensity. The strongest emission is achieved for 750 °C and 850 °C. At temperatures of 950 °C and higher, the emission intensity falls rapidly, reaching lower levels than that of the unannealed sample for annealing temperatures of 1050 °C and higher.

The intensity of the green PL of all the annealed samples up to the one annealed at 1050 °C is about 100 times stronger than the background noise of the unannealed sample, for which only the green defect band could be detected as a very weak feature located at 2.38 eV. The orange defect band is not detectable in the background noise for the unannealed sample. As the band edge PL intensity also increases by about the factor of 100 after annealing, there is the possibility that the orange PL just cannot be seen in the unannealed sample because it is drowned in the background noise. Therefore it is interesting to see that the defect band emission intensity behaves quite independent of the intensity at the band edge for the range of annealing temperatures. In fact there seems to be no correlation between the deep-level PL-emission intensity and the band edge PL-intensity. This makes us assume that the defect band is actually created by the annealing process itself, and its appearance is not a side effect of the improved emissivity of the annealed films.

To investigate the effect the specific annealing conditions we used has on the sample properties without the effect elevated temperatures have on the healing of defects in the crystal structure, we annealed some samples at the same temperature the films were grown at, 550 °C. And indeed, annealing at 550 °C, the same temperature the sample was grown at, has a very strong effect on the defect band emission intensity. This in particular gives the impression that the conditions the sample was annealed in are responsible for the orange defect band. Since the annealing was done in an oxygen atmosphere, the orange defect band may thus be evoked by the effect of the oxygen gas on the crystal surface. Another explanation is that the films were exposed to some unwanted impurity doping in the annealing chamber. Depth dependent time-of flight experiments would be a great tool to find out about the diffusion of dopants into the crystal from the surface. Of course, another possible reason for the orange defect band is the exposure of the samples to air in-between the growth and annealing process. This might lead to the thermally activated diffusion of surface layers of adsorbed gases. In this regard it is interesting that once the thermal effect of the annealing kicks in at 750 °C, the intensity of the orange defect band actually is decreased down to the intensity of the green defect band. Studies with a larger number of samples would be necessary to get an estimate of the uncertainties involved. The trend observed here shows that defect density associated with the doping effect of our annealing procedure, may it be adsorbed gases or impurities present in the annealing chamber, is reduced at the optimum annealing temperatures, where the surface stays intact and the PL-emission is maximized. At temper-

atures that high enough to cause a substantial melting of the films, the orange emission intensity rises again and becomes substantially stronger then the green band emission. This correlation lets us assume that the orange defect band at 2.08 eV is related to surface doping with impurities related to adsorbed water molecules, whereas the green defect band at 2.36 eV is expected not to be related to the band edge emission, but associated with other defects such as oxygen vacancies that create transitions from deep donor levels to the valence band, as the behaviour of the green defect band is similar to the ones observed by other groups [75].

ZnO is a polar semiconductor. Due to the ionic nature of its bonds in the longitudinal direction, lattice vibrations cause electric polarizations in the longitudinal direction, with in turn create electric fields. The interaction of these electric fields with moving charges cause polar longitudinal optical (LO)-phonon scattering. The resulting LO-phonon replicas in the PL spectrum are situated at 71-73 meV below the original peak energy [7]. The phonon replica in thin films typically are related to LO-phonon interaction with bound exciton states. It has been reported that for nanostructures, the LO-phonons strongly interact with free excitons rather than with bound excitons [78]. The energy transition the phonon replica is linked to typically is tracked down by the constant offset energy of the phonon replica. Also, the intensity of the phonon replica is related to the intensity of the peak it is coupled to. In general, the intensity of the LO-phonon replica is expected to be about two orders of magnitude below the PL-intensity of the coupled donor bound exciton line [7,18]. Second- and higher-order LO-phonon replicas can be observed for strong peaks at further energy steps of 71-73 meV.

The rise of the bound exciton band edge photoluminescence signal with improved annealing conditions correlates with a more defined phonon replica, which becomes resolved at about 3.29 eV for all annealing temperatures besides 1050 °C. Even the 2nd and 3rd order phonon replicas become clearly resolved for the annealing temperatures of 750 °C and 850 °C. As expected for a ZnO thin film, the phonon replica's energy distance to the bound exciton peaks indicate that they are coupled to the bound exciton transition that is dominating the spectrum [78]. This explains the shift of the phonon replica peak between the sample annealed at 550 and 750. Since the dominating bound exciton transition shifts from the I4 to the I9 line, the phonon replica shifts accordingly. For the sample annealed at 850, the phonon replica peak at 3.288 eV has a FWHM of about 10 meV. With a spacing of the bound exciton peaks at the band edge of just 4 meV from peak to peak, the phonon replica at this annealing temperature is assumed to be a combination of phonon replicas coupled to each of the two peaks.

3.3.1 Annealing and its effects on the surface topography

AFM scans taken for each of the annealing temperatures graphically display the strong effect annealing can have on the surface topography of epitaxial films. The AFM scans of samples annealed at 800 °C or less show no significant change in their surface topography when compared to the as-grown sample (see figure 3.6 in comparison to figure 3.1). But the AFM scan of the sample annealed at 850 °C clearly shows the formation of droplets on the sample surface. AFM-analysis shows they have a mean diameter of 35 nm and an average height of 6 nm with a standard deviation σ of 41 nm in diameter and 2.8 nm in height. A maximum diameter of 370 nm and a maximum height of 28 nm was detected for this film.

Most important is the fact that for 850 °C annealing temperature, the film has not yet entirely converged into droplets: in between the droplets a film structure similar to the structure of the unannealed samples is still evident in the surface AFM scan. The sample annealed at 1000 °C in figure 3.7 shows a different scenario: the film appears to have completely converged into big droplets with a mean diameter of 287 nm ($\sigma = 120$ nm) and a mean height of 59 nm ($\sigma = 21$ nm), without any apparent residue of the ZnO film topography in-between. Investigation of all the annealed films by AFM shows that the film only starts to melt when annealed at more than 800 °C. Up to an annealing temperature of 900 °C the AFM clearly shows a residual film between the droplets, which is a little less obvious for films annealed at 950 °C. At 1000 °C, the film seems to have been completely molten and resolidified into droplets, with no ZnO coverage on the substrate besides the large droplets. In general, the size and number of droplets is closely related to the annealing temperature and most likely duration of annealing, which was not investigated here. The size distribution of the droplets converges to larger diameters with higher temperatures. In the photoluminescence spectra, a slight blue shift in the spectral position of the excitonic peaks can be observed for higher annealing temperatures. This blue shift can be explained as a relaxation of stress due to annealing. The AFM scans reveal that this relaxation of stress seems to be achieved at the expense of a degraded surface morphology via the formation of droplets.

Droplet formation is not wanted in the growth of ZnO epitaxial films for several topographic reasons, such as the detrimental effect of the irregular structure on the growth of multilayer structures as well as lithography. But photoluminescence intensity and peak width degrade rapidly for annealing temperatures above 950 °C, correlating strongly with the disintegration of the film coverage. This clearly shows that the integrity of the electrical structure and epitaxial nature of the deposited ZnO is only granted within the continuous film, since the optical properties of the samples without a continuous film coverage are strongly deteriorated. The droplets have a strongly degraded electrical and crystal structure of ZnO, most likely not being of epitaxial crystal nature any more. This suggests that the droplets are not responsible for the improved intense photoluminescence with narrow peak width that is achieved by annealing at 850 °C, compared to

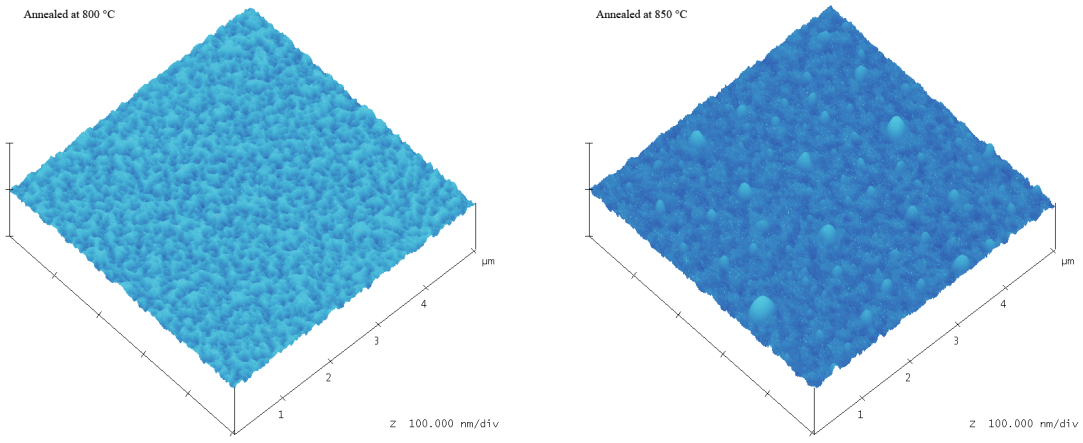

Figure 3.6: Comparison of AFM scans of MBE-films annealed at 800 °C and 850 °C. The samples have been annealed for 1 hour under an oxygen atmosphere at ambient pressure. It is evident that the film topography does start to be influenced by the annealing at temperatures of 850 °C and more. For temperatures of 800 °C and less, the surface topography shows no significant change in the AFM scans, compared to the surface of unannealed sample shown in figure 3.1

the PL-spectrum of the film annealed at 750 °C.

In conclusion, annealing at the right temperature can strongly improve the optical response of ZnO films. The annealing seems to be beneficent for the optical properties of the remaining epitaxial film even at temperatures that cause partial melting and droplet formation. Methods to avoid the conflicting scenario of improved annealing and partial melting of the film could be a prolonged annealing duration at temperatures of below 850 °C, as no droplet formation is recorded for 800 °C. When comparing the annealed sample to a film grown at superior conditions, the similarity of the PL-spectrum of the sample grown at the superior growth conditions with the sample grown at inferior growth conditions annealed at 750 °C is striking. It is important to note that an unexpected change of growth conditions can always occur due to unstable growth parameters such as the oxygen plasma condition, Zn-flux, etc.. Therefore this comparison shows that annealing can be great tool not only to improve films grown at below-optimum growth conditions, but to smooth out sample irregularities between growths.

3.4 Photoluminescence study of films annealed at optimum annealing conditions

The sample annealed at 850 °C shows the most intense and detailed photoluminescence spectrum of all the annealed samples from MBE film 208. An analysis of the light emitting properties of this semiconductor film can help in the closer

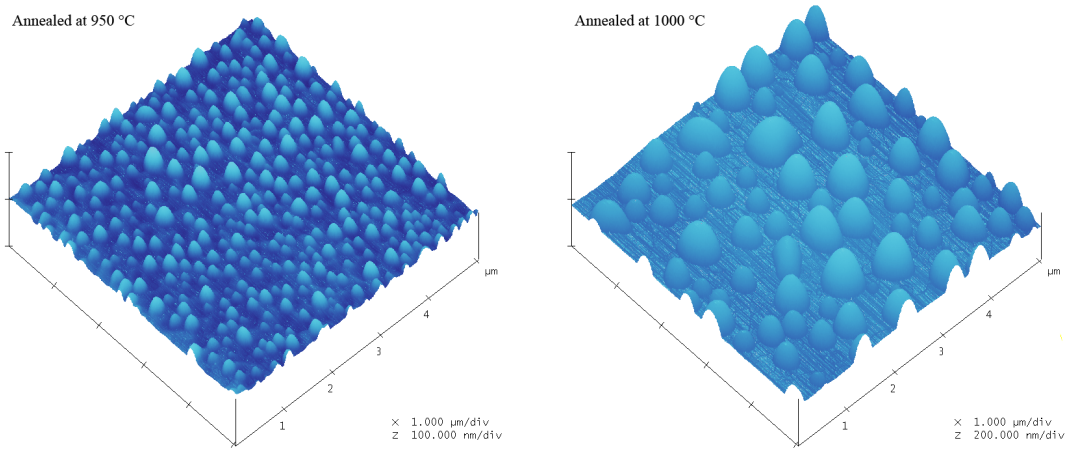

Figure 3.7: Comparison of AFM scans of MBE-films annealed at 950 °C and 1000 °C. The film annealed at 950 °C shows a last residue of film topography between the droplets. In contrast, the film annealed at 1000 °C solely consists of large droplets, with no signs of a residual film remaining in-between. This is in correlation with the optical analysis that shows a rapid degradation of optical properties for films annealed at more than 950 °C

identification of the sample's structural imperfections and impurities. One of the main challenges therefore is to dependably identify the physical process related to features of the PL spectrum.

A first sensible step for the identification of the transitions observed in the spectrum of the MBE-sample 208 annealed at 850 °C is a comparison of its PL-spectrum to the PL-spectrum of a very high quality ZnO crystal that can serve as a reference. In recent years, the fabrication of hydrothermal and pressurized melt bulk ZnO has been improved greatly. The resulting bulk ZnO crystals show remarkable detail in their photoluminescence spectrum. Figure 3.8 shows the emission spectrum of the MBE-grown film on sapphire substrate in comparison with the photoluminescence spectrum of hydrothermally grown bulk ZnO purchased from Tokyo Denpa Co. Ltd. The wafers are double side polished, hydrothermally grown m- and c-axis wavers (HT-1) having a carrier concentration of just $1.2\times10^{14}\ \frac{\text{carriers}}{\text{cm}^3}$, compared to the carrier concentration of the MBE-film of $4\times10^{19}\ \frac{\text{carriers}}{\text{cm}^3}$. By plotting the emission spectra on a logarithmic intensity scale, peaks at strongly different intensity levels can be shown on one single graph. Although the bulk ZnO spectrum has a much more detailed spectrum, the spectra of the bulk and MBE films have many common features. The light emission of both samples is dominated by a strong band edge emission around 3.36 eV. For the MBE-film this emission consists of two distinguishable peaks labelled here as peak A and B. At intervals of 72 meV below the intense and narrow band edge emission peaks are the broad longitudinal optical phonon replica peaks, which can be identified by their equidistant spacing of $n \times 72$ meV and are labelled

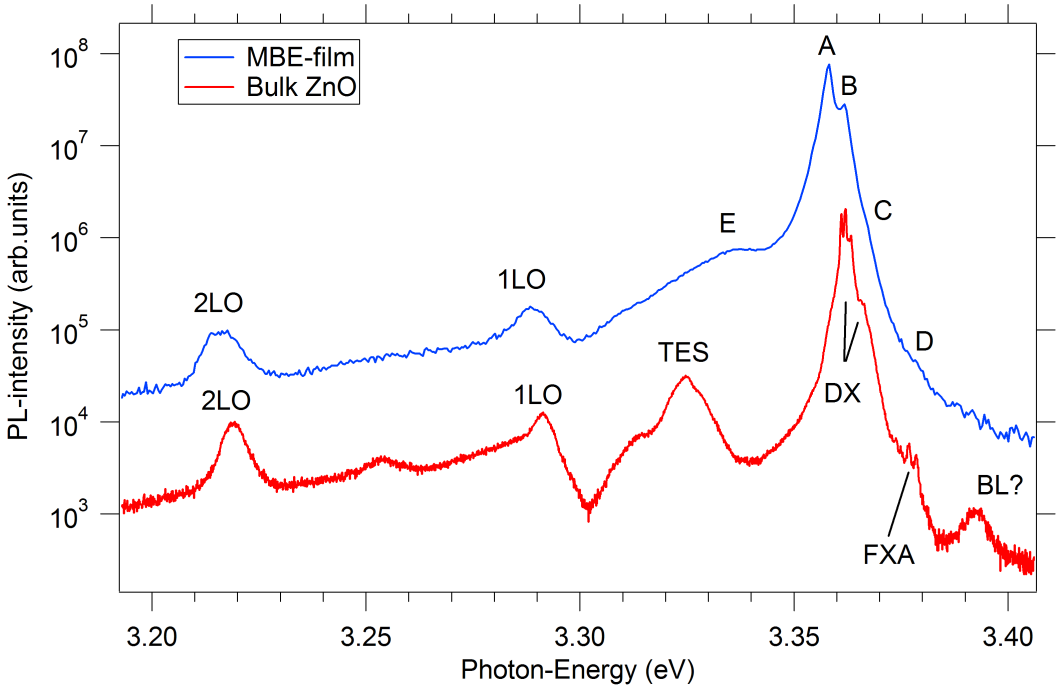

Figure 3.8: Comparison of the 4 Kelvin UV-PL spectrum of high quality bulk ZnO grown by the hydrothermal method with an MBE grown film annealed at 850 °C. Explanation of the labels used: A, B, C, D, E stand for peaks of the MBE-film that are to be identified. 1LO and 2LO are the first and second phonon replica lines, which for both samples are linked to the bound A-excitonic transitions that dominate the spectrum at low temperature. TES is the two electron satellite, DX stands for donor bound excitons, FXA are the free A-exciton related peaks, BL stands for the longitudinal free B-exciton transition $B\omega_L$

here with nLO, standing for longitudinal optical phonon replica of order n. The phonon replica can not always be linked to a particular band edge emission peak since they are quite broad and situated at 71-73 meV below the original transition. For the MBE sample and the bulk sample, the phonon replica peaks show a spacing of 72 meV between 1LO and 2LO. Applying this same spacing places the zero phonon line in the middle between peak A and peak B for the MBE sample. For the bulk sample, the zero phonon line is located at the energy of the I4 peak (see figure 3.9).

As discussed earlier on page 55, peak E of the MBE-sample annealed at 850 °C is situated at a slightly higher energy than the typical energy of the TES as featured by the bulk ZnO spectrum. Therefore the low temperature emission causing peak E in this MBE-sample is expected to be associated with excitons bound to structural point defects.

The differences in crystal quality between the bulk ZnO crystal and the MBE grown film become more obvious when looking at the fine structure of the band

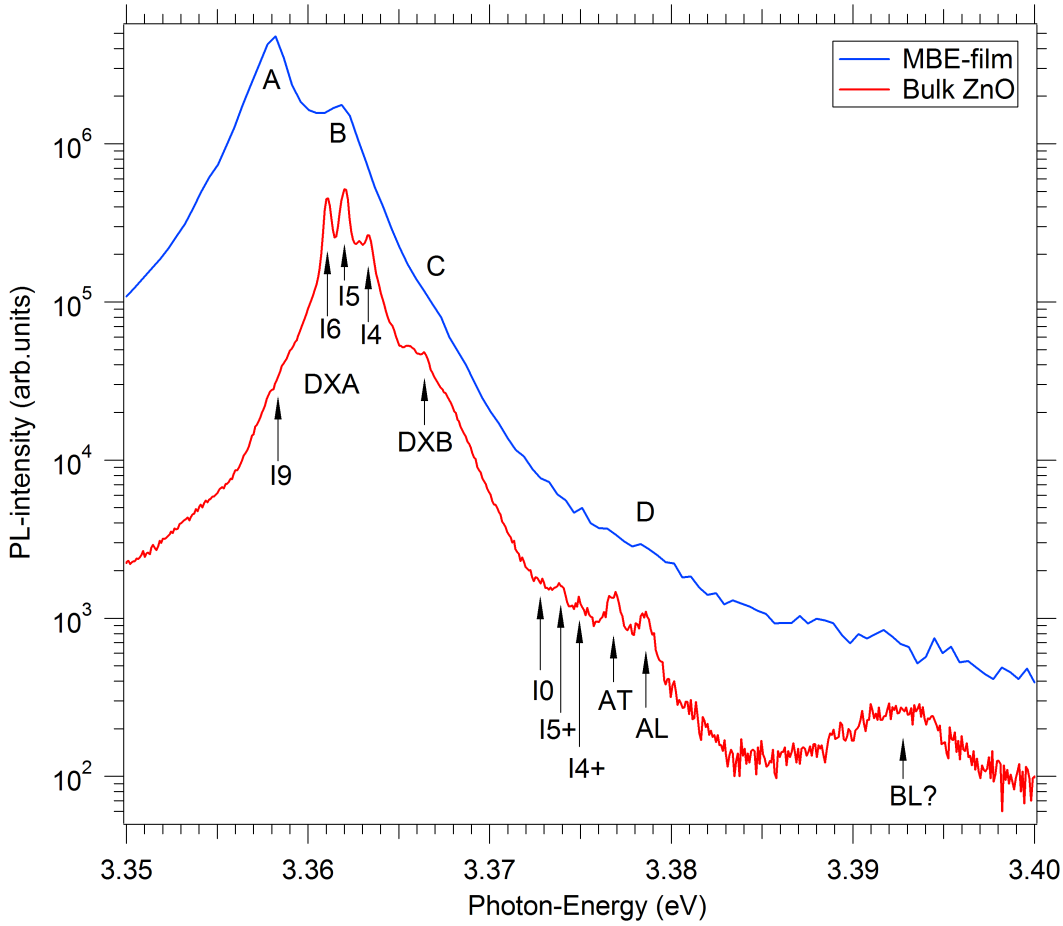

Figure 3.9: Closeup of the band edge PL-transitions of the bulk and MBE sample. Labels A, B, C, D are the MBE-film transitions to be investigated here. DXA stands for donor bound excitons in the A-valence band with the transitions I4, I5, I6 being linked to donor bound exciton recombinations linked to particular impurities. DXB stands for the donor bound excitons of the B-valence band. FXA are the free A-exciton transitions, BL is the longitudinal free B-exciton transition.

edge transition, which is displayed in figure 3.9. The spectrum of the bulk sample features donor bound A and B-excitons, marked as DXA and DXB, with a FWHM of less than 0.9 meV. The A-free exciton shows a clear splitting into its longitudinal and transverse symmetries, with A_T at 3.377 eV and A_L at 3.3785 eV. At this position the low temperature MBE spectrum only shows a weak shoulder, labelled here with D. Also only observable in the bulk spectrum, albeit only very weakly, is a fine structure at the position of the ionized donor bound excitons I_5^+ and I_4^+, just below the A-free exciton [14].

When comparing the spectrum of the MBE-sample annealed at 850 °C with the spectrum of bulk ZnO, it becomes clear that a closer investigation of peak B is necessary to know if it is possible to identify it with any particular donor bound exciton. The linewidth and uncertainty connected with peak B make it a candidate to be associated with I_6, I_5 and I_4, see also table 3.1. It is important to consider that lattice strain can cause a substantial shift of the position of the emission peaks. Due to the lattice mismatch between the sapphire substrate and the ZnO film in this epitaxially grown film, a certain amount of strain is expected. Therefore it is important to locate the energy-position of the A-free exciton to establish the relative spacing of the donor-bound transitions to the free exciton transition, giving an estimate about the localisation energy of the bound excitons. A better estimate of the position of the A-free exciton is only possible by investigating its temperature dependent behaviour, as presented in section 3.4.1. The A-excitonic transition can thus be positioned at 3.3779 eV $\pm$0.7 meV. Since the linewidth of the A-free excitonic PL-peak of the MBE-samples can be estimated to be greater than 3 meV, the longitudinal-transverse splitting of the A-free exciton can not be observed at any temperature for this MBE-film. Therefore the localisation energy of the donor bound transitions can only be specified with an uncertainty of at least the spacing between the longitudinal and transverse free excitons. But the energy of the mixed A-free excitonic transition is centred at 3.3779 eV, matching the position of the middle between the A_T and A_L-peak of the bulk that is located at 3.3777 eV with an offset of merely 0.2 meV. This is well within our expected limit of reproducibility of about 1 meV between separate scans on separate days. Thus we can derive that there is no significant shift of the spectral features due to lattice strain in the MBE-film annealed at 850 °C.

It is expected that the MBE-film does incorporate some hydrogen impurities, as it is very hard to avoid a certain amount of hydrogen contamination of the UHV-growth-environment. Hydrogen impurities in ZnO are associated with the donor-bound emission peak I_4 [14], and are a prominent feature in almost all high quality ZnO films observed. Thus Peak B is expected to be at least partly due to excitons bound to hydrogen donors [66, 79]. Since the centre of peak B is offset from the position of the peak associated with $I4$ in the bulk spectrum by about 1.5 meV, whereas the free excitonic transitions of both spectra match up very well, it is expected that the $I4$ transition is not the only constituent of peak B. The linewidth of peak B is sufficient to cover the position of $I6$, $I5$ and $I4$, therefore we conclude that peak B is a combination of those three. In

Table 3.1: PL summary

	Bulk		**MBE**		
Type	eV	± (meV)	Ident.	eV	± (meV)
2LO	3.2191	$5.3^{(x)}$	2LO	3.2156	$8.4^{(x)}$
1LO	3.2914	$4.4^{(x)}$	1LO	3.2884	$7.7^{(x)}$
TES	3.3247	$7.6^{(x)}$	E	3.3357	$9.4^{(x)}$
Donor bound A-excitons (DXA)					
I_9	3.3583	0.25	A	$3.3580^{(*)}$	1.18
I_6	3.3611	0.09	B	$3.3618^{(*)}$	1.51
I_5	3.3620	0.09	B	$3.3618^{(*)}$	1.51
I_4	3.3633	0.09	B	$3.3618^{(*)}$	1.51
DXB	3.3664	0.1	C	3.3669	0.46
Donor bound A-excitons (DXA)					
$I_0(=I_6^+)$	3.3738	0.11	–		
I_5^+	3.3749	0.13	–		
I_4^+	3.3755	0.12	–		
Free excitons					
A_T	3.3768	0.18	D	3.3779	$3^{(x)}$
A_L	3.3785	0.14	D	3.3779	$3^{(x)}$
B_L?	3.3926	1.4	–		

$^{(*)}$ Dominant Emission (fitted by lorentzian)
$^{(x)}$ FWHM

section 3.4.4 we will investigate if the temperature dependence of the intensity reveals different activation energies for the three components in peak B.

Peak A at 3.358 eV lines up very well with the shoulder of the bulk sample that is associated with excitons bound to indium-donors, a complex generally labelled as $I9$ [14]. The shoulder of the MBE-spectrum labelled with C is at the energy of the donor bound excitons of the B-valence band (DXB) in the bulk spectrum. The clearly resolved but very weak broad feature of the bulk spectrum at 3.393 eV is at the energy associated in the literature with the longitudinal B-free exciton [16] and is not resolved in the PL spectrum of the MBE film.

3.4.1 Temperature dependence of photoluminescence

Since the A-free exciton is drowned by the dominating donor bound emission lines for the low temperature MBE-spectrum, a better estimate of the position of the A-free exciton is only possible by investigating the temperature depen-

dence of the PL-emission spectrum. Figure 3.10 shows the PL-spectrum of the MBE-film annealed at 850 °C measured at temperatures ranging from 4-300 K. As expected from the linewidth considerations on page 71, towards room temperature all peaks join into one broad feature. Through consideration of the temperature dependent behaviour of the band edge, it is possible to estimate the positions of the A-free exciton and its first phonon replica in the broadened spectra towards room temperature. In figure 3.10, the resulting temperature dependent position of the A-free excitonic transition AX is marked by rectangles, whereas the position of the first LO-phonon replica of the A-free exciton is marked by circles. Elevating the sample temperature has a distinctive effect on the photon energy emitted from each type of process that leads to a photoluminescence peak. The characteristic temperature dependent behaviour of the various peaks allows us to get a better understanding of the nature of the various processes that are responsible for the different emission lines. The minimum temperature that could be realized with the liquid Helium flow cryostat in this study was 4 Kelvin. Besides a shift of the emitted photon-energy due to a temperature dependent shift of the band gap, elevating the sample temperature generally causes a phonon-related broadening of the line-width of the observed transitions as well as a drop off in intensity due to the activation of non-radiant relaxation paths for the excited states that can be linked to the activation energy of the states involved in the low-temperature PL-emission. Therefore the spectra at lowest temperatures show the most detail and usually are a good start to map most of the peaks and their transition energies.

There are some exceptions though: For samples with a weak emission peak of the free-exciton transition it pays off to locate it in scans done at higher temperatures. This is because the bound exciton transitions that strongly dominate the low-temperature spectrum typically decay faster with rising temperatures than the free exciton transitions, allowing a clearer identification of e.g. the free A-exciton shoulder of the MBE-film at temperatures above 4 Kelvin. The different behaviour of the bound and free excitonic transitions can be traced by investigating the evolution of the photoluminescence spectrum with temperature in figure 3.10: The temperature dependent position of the A-free excitonic transition AX is marked by rectangles, whereas the position of the first LO-phonon replica of the A-free exciton is marked by circles. As mentioned above, at 4 Kelvin the bound excitons marked as A and B dominate the spectrum. Accordingly, the phonon replica at 4 K are related to the bound excitonic transitions, as they are spaced at 72 meV from A and B. The A-free exciton and its phonon replica do not create strong features in the low-temperature spectrum. But between 60 and 150 K, the shoulder of the A-free exciton becomes much more pronounced, allowing a much more accurate estimate of its energy. With rising temperatures a broad peak associated with the first phonon replica of the free excitonic also becomes more and more distinguishable, whereas the phonon replica of the bound exciton transition die off rapidly towards temperatures of 80 K and above. In fact, a considerable part of the emission at room temperature

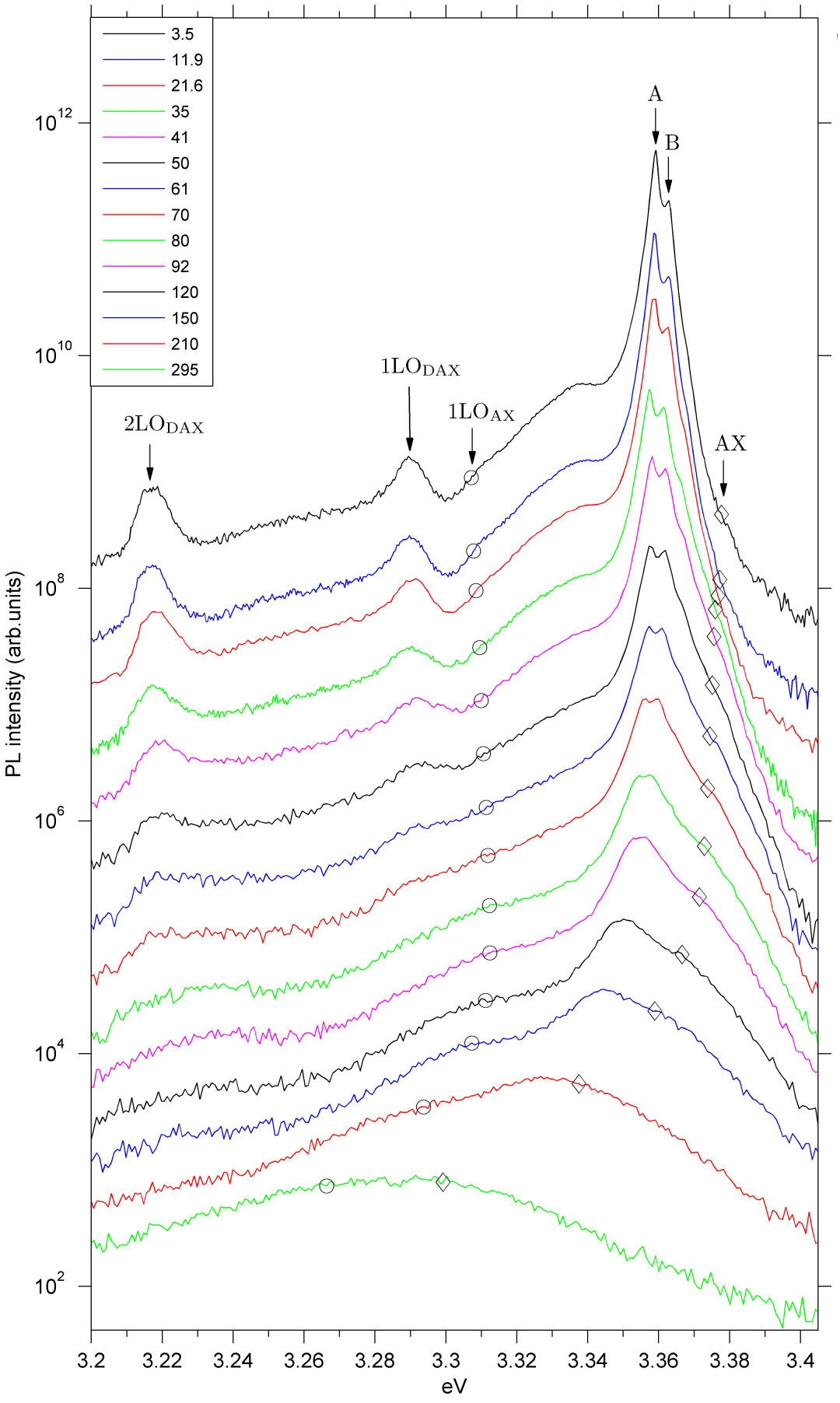

Figure 3.10: Temperature dependent PL-spectra of MBE-film annealed at 850 °C

seems to be related to the free exciton and its phonon replica. The emission from the bound excitons is still, though only just, dominating at 210 K. Thus it can be expected to also play a major role in creating the broad emission peak at room temperature that therefore is expected to be due to the overlap of mainly these three phonon broadened peaks.

The spacing between the position of the A-free exciton and its first phonon replica is not constant, but changes according to the theories of Permogorov [78] and Klingshirn [37]: The change of the spacing between the free excitonic emission and its phonon replica in polar semiconductors is connected with the temperature related rise of the kinetic energy of the free exciton. The transition probability of the excitons with higher kinetic energy is dependent on their interaction with phonons. In general, the resulting spacing between the energies of the emission lines of free excitons and their phonon replica is described by [37,80]

$$E_{AX} - E_{LO}^{n} = n\hbar\omega_{LO} - E_{\mathrm{kin}}, \tag{3.6}$$

with E_{LO}^{n} as the energy of the n-th phonon replica and E_{AX} as the energy of the free exciton at momentum $\boldsymbol{k} = 0$. $\hbar\omega_{LO}$ is the LO phonon energy, which is 72 meV for ZnO [7]. At elevated temperatures the free excitons are gas-like in the crystal, and E_{kin} is the kinetic energy of the free excitons that interact with phonons to recombine [37]. Their transition probability is proportional to $(E_{\mathrm{kin}})^{L}$ [78, 80]. Thus, the kinetic energy of the free excitons influences the energy of the resulting phonon replica and their spacing from the zero phonon-exciton emission line. The kinetic energy of the excitons is related to $\boldsymbol{k}$ via the dispersion relation $E_{\mathrm{kin}} = \frac{\hbar^2\boldsymbol{k}^2}{2M}$. Free excitons with an elevated kinetic energy require the help of a phonon of suitable momentum to recombine, since they have to recombine at $\boldsymbol{k} = 0$. The transition probability W of the excitons is related to their kinetic energy through $W \propto (E_{\mathrm{kin}})^{L}$. For single phonon-processes, the number of final states increases with E_{kin}, resulting in $L = 1$. For two-phonon processes the number of final states stays constant even as E_{kin} increases, as there are many different combinations of two phonon wave-vectors that can absorb the momentum $\boldsymbol{k}$ of the moving exciton [37]. This results in $L = 0$. Photoluminescence measurements of ZnO nanowires [78] and epitaxial thin films [80] in the temperature range from 0-300 K confirm the change of the spacing from the free exciton to their phonon replicas according to the kinetic energy of the excitons that are able to recombine due to a high transition probability:

$$E_{kin} = (L + 1/2)\, k_B T, \tag{3.7}$$

with $L = 1$ for the 1LO-phonon line of the free excitons and $L = 0$ for the spacing to the 2LO-phonons of the free excitons. The spacing of the phonon replica to the bound excitonic transitions shows a weaker coupling with temperature, since the binding energy of bound excitons is much smaller with $E_b < 10$ meV, and thus far from resonating with the LO phonon energy of 72 meV in ZnO [78].

The position of the first phonon replica of the free exciton is marked by circles in figure 3.10, which are spaced to the position of the A-free exciton that is marked by rectangles by the energy resulting from the relation expressed by equation 3.7, with $L = 1$. The position of the first phonon replica and its temperature dependent spacing to the A-free exciton is important, as it helps in locating the A-free excitonic transition at temperatures of 92 K and above. In a nutshell, the position of the A-free exciton is determined through several steps: first the A-free exciton has to be located through its position at temperatures where it is the most dominant in the spectrum, e.g. around 100 K in figure 3.10. The temperature dependent change of position is then made easier through the known relationship for the spacing to its first phonon replica of equation 3.7. With its help, the A-free excitonic shoulder and the broad peak of the first phonon replica can be located much better at higher temperatures. This helps to get a better tracking of the free exciton across a wide temperature range. Particularly at temperatures close to room temperature it is otherwise hard to distinguish between the strongly phonon-broadened bound excitonic transitions and the A-free excitonic shoulder.

Towards lower temperatures, the phonon replica of the A-free exciton becomes drowned by the emissions from excitons bound to structural defects marked as E in figure 3.8. Therefore the position of the A-free exciton at low temperatures, i.e. below 60 K can best be specified through modelling the temperature dependence of the band gap as shown in section 3.4.2.

The thermal broadening of a single excitonic transition in ZnO with temperature can be calculated as [81, 82]

$$\Gamma(T) = \Gamma_0 + \Gamma_{\mathrm{ph}} \left[\exp\left(\frac{E_{LO}}{k_B T}\right) - 1 \right]^{-1} + \Gamma_{\mathrm{imp}} \exp\left(-\frac{E_b}{k_B T}\right). \qquad (3.8)$$

A good fit to the linewidth of sol-gel derived ZnO films has been achieved with the following parameter-values: Γ_0=31 meV as the intrinsic linewidth at $T = 0$, the exciton-LO phonon coupling constant $\Gamma_{ph} = 230$ meV, the LO phonon energy $E_{LO} = 72$ meV, the linewidth due to the ionized impurity scattering $\Gamma_{imp} = 13.4$ meV and $E_b = 32$ meV as the average binding energy of the impurity-exciton complexes or the exciton localisation energy to donors [82]. According to this model, for ZnO a FWHM of about 54 meV can be expected at room temperature [81]. The good fit achieved by Kumar et al. shows that, although this model has been explicitly developed for quantum well structures [82, 83], it seems to be very applicable for ZnO films too.

One therefore has to consider that for the evaluation of the linewidth of peaks at elevated temperatures in photoluminescence spectra the resulting peak will consist of more than one single photoluminescence transition line at higher temperatures. This is due to the broadening of the individual transitions. The effect can be seen in the spectra recorded at elevated temperatures shown in figure 3.10.

The according approach is to convolute the sum of the excitonic PL and phonon replicas $I_n^{PL}(\hbar\omega)$ of the region covered by the FWHM of the entire investigated lineshape $I(\hbar\omega)$ with a Lorentzian L with a temperature dependent half width at half maximum $\Gamma(T)$ [23]:

$$I(\hbar\omega) \propto \left(\sum_n I_n^{PL}(\hbar\omega) \right) \times L, \tag{3.9}$$

with

$$L(x) = \frac{1}{\pi} \frac{\Gamma(T)}{(x - x_0) + \Gamma(T)^2} \tag{3.10}$$

This approach leads to a typical FWHM of the ZnO PL emission band at room temperature of about 95meV, a value that is comparable to the width of the room temperature emission line of the MBE-film annealed at 850 K as shown in figure 3.10.

An approach different to the model used by Kumar et al. as presented in equation 3.8 has been applied by Hauschild et al. [23]. Here the broadening of the excitonic PL-emission lines is modelled only through the exciton-phonon interaction, with

$$\Gamma(T) = \Gamma_0 + \alpha T + \frac{\beta}{e^{E_{LO}/k_B T} - 1}. \tag{3.11}$$

The purely excitonic PL-emission was obtained by deconvolving the broad PL-emission peak at higher temperatures into its constituents. Fitting the excitonic part with equation 3.11, an average phonon energy E_{LO} of 33 meV was found, a value that is in the correct range for ZnO. The fitted values of the other parameters are: the linewidth at zero temperature $\Gamma_0 = 0.65 \pm 0.60$ meV, as well as the fitting coefficients $\alpha = 0.016 \pm 0.013$ meV and $\beta = 47 \pm 12$ meV [23].

3.4.2 Modelling the temperature dependence of the band gap

Many models have been developed to describe the temperature dependent variation of the band gap of semiconductors [84–88]. These theoretical models can be fitted to the measured temperature dependent shift of the band gap. This is done by numerically adjusting the parameters of the models to achieve a minimum value of the χ^2-parameter used to describe the goodness of the fit:

$$\chi^2 = \sum \left(\frac{y - y_i}{w - I} \right)^2, \tag{3.12}$$

with y being the fitted value for a given point, y_i the original data value, and w_i the standard error for each point.

Ideally, the fitting-parameters of the model are related to physically meaningful material parameters that play a dominant role in creating the temperature dependent energy shift, i.e. the $T = 0$ K intercept, the Debye temperature Θ_D, the lattice dilatation U and the electron phonon interaction. But in all cases, the theoretical fit of the band gap describes the temperature dependent behaviour of spectral features and makes it possible to compare the temperature dependence of one feature with the temperature dependent behaviour of other features at different energies. The energy at temperatures outside the measurement range (e.g. zero temperature, high temperature) can also be estimated by using the theoretical fit to a limited temperature range. Most importantly, fitting the temperature dependent energy shift of a spectral feature of unknown origin allows us to investigate its relation to the material band gap, therefore giving clues for the identification of the nature of the process causing the spectral feature and its relation to the band gap.

An early attempt for a model by Varshni et el. [84]

$$E_G(T) = E_0 - \frac{\alpha T^2}{T + \beta} \tag{3.13}$$

with E_0 as the transition energy at 0 K, the temperature T combined with α and β as temperature coefficients has been widely adapted since it works surprisingly well within the limited temperature range of $T < 300$ K. But the temperature coefficients α and β cannot be brought into physically reasonable connection with actual features of phonon dispersion [87], making the parameters α and β somewhat meaningless, although β is expected to be comparable to the Debye temperature Θ_D in certain materials [89].

Since it has been shown numerously that the contributions of the individual phonon modes to the total shrinkage of the fundamental band gap is proportional to their average phonon occupation numbers, a fit based on the Bose-Einstein occupation factor [87]

$$E_g(0) - E_g(T) \propto \frac{1}{e^{\Theta/T} - 1} \tag{3.14}$$

gives much more meaningful fitting parameters. A model of Bose-Einstein type was rewritten by Paessler: [87]

$$E(T) = E_0 - \frac{2\alpha}{e^{\Theta/T} - 1}. \tag{3.15}$$

In this model, α represents the strength of the electron-phonon interaction and contains the entropy related limiting slope

$$\alpha_{\mathrm{LS}} = -dE(T)/dT|_{T\to\infty}, \tag{3.16}$$

with

$$\alpha = \alpha_{\mathrm{LS}}\Theta/2. \tag{3.17}$$

Θ is the average phonon temperature with $\Theta = \hbar\omega/k_B$, where ω is the average single 'phantom' phonon frequency in the lattice [87]. Thus it follows that

$$\Theta \approx 3/4\Theta_D. \tag{3.18}$$

The Manoogian and Wool

$$E = E_0 + UT^s + V\Theta\left(\coth(\Theta/2T) - 1\right) \tag{3.19}$$

is based on the Bose-Einstein fit in equation 3.15, but takes into account the semiconductor crystal's lattice dilatation with temperature through the additional term UT^s. Since the Manoogian equation 3.19 has more fitting parameters than the Bose-Einstein or the Varshni fit, it can offer a more precise representation of the actual physical processes that lead to the particular temperature dependent behaviour of the band gap. As expected it achieves a much lower χ^2-values for fits to the free excitons in ZnO than other models [22]. But it only makes sense to fit all the parameters of equation 3.19, in case a sufficient number (n) of measurements has been taken across the temperature scale [85]. Due to the physical significance of its fitting parameters though, the Manoogian procedure is chosen for most temperature dependent fits in this work, with the values for U and s set according to theoretical considerations [22], thus keeping the number of free parameters to a meaningful limit.

To show the relation of the MW-model to the Bose-Einstein model above and simplify comparisons between the two models, the MW-formula can be rewritten as

$$E = E_0 - UT^s - \frac{\alpha\Theta}{e^{\Theta/T} - 1}, \tag{3.20}$$

with $\alpha = 2V$ and the mathematical relation: $2\left(e^x - 1\right)^{-1} = \coth\left(\frac{x}{2}\right) - 1$.

3.4.3 Temperature dependence of the band gap of MBE-grown ZnO films

The electronic structure at room temperature is one of the most interesting for the actual application of devices made with ZnO. To get to know the temperature dependent electronic structure of newly grown ZnO structures, the free excitonic transitions are a good indicator, as they are expected to be at a constant spacing to the band gap at temperatures up to 300 K (equivalent to 25 meV) and above. But it has to be kept in mind that, although excitons in ZnO have a binding energy of 60 meV, that the energy of the longitudinal optical phonons in ZnO is even larger, with 72 meV. Therefore phonon-related effects can potentially change the electronic properties drastically as the temperature is increased [23], making the investigation of the bandstructure at elevated temperatures all the more interesting.

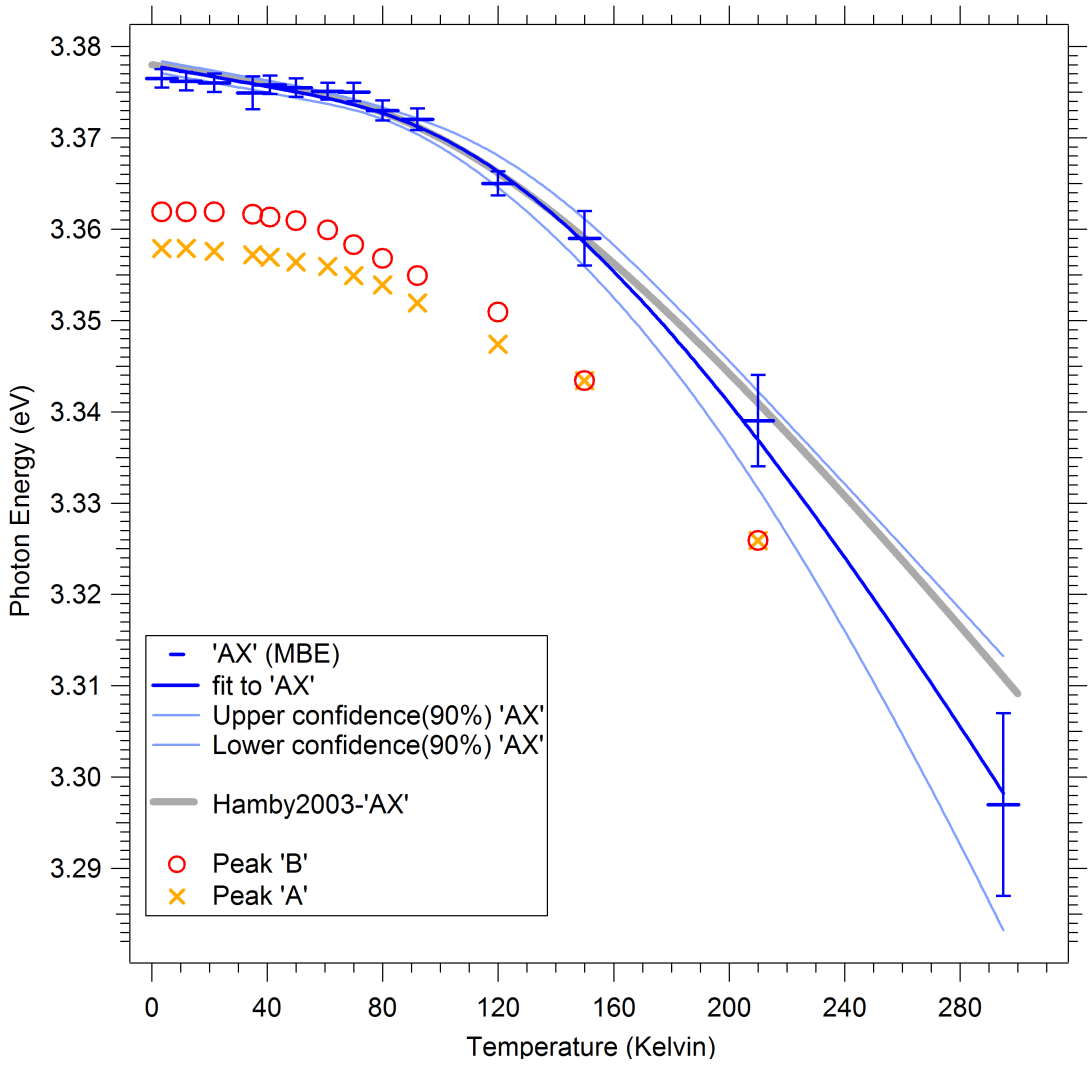

Figure 3.11: Temperature dependence of emission energy of bound and free exciton transitions in MBE-sample annealed at 850 °C. The temperature dependence of the free A-exciton ('AX') has been fitted with the MW-model [22]. For comparison, the MW-fit to the A free exciton of high quality bulk ZnO, as presented by Hamby et al. is shown [22]

Table 3.2: Fitting parameters of modified Manoogian-Woolley (MW) fitting procedure, see equation 3.20, for the A-free excitonic emission AX of the MBE-grown film annealed at 850 °C, compared to the MW-fit to the A free exciton of high quality bulk ZnO, as presented by Hamby et al. [22]:

	AX in MBE-film		***AX in bulk [22]***	
Parameter	Value	Uncertainty (±)	Value	Uncertainty (±)
E_0 $[eV]$	3.3779	0.656×10^{-3}	3.378	–
Θ [K]	483.87	122	398.4	–
α [eV/K]	-5.37×10^{-4}	2.4×10^{-4}	-3.68×10^{-4}	–
U^*[eV/K]	-5.5×10^{-5}	–	-5.5×10^{-5}	–
s^*	1.01	–	1.01	–

* Values set according to Hamby et al. [22]

Figure 3.11 shows the temperature dependent position of the A-free excitonic transition AX, according to the spectra in figure 3.10 of the MBE-film annealed at 850 °C. The fit to AX in figure 3.11 is done by using the Manoogian Woolley fitting model of equation 3.19 that is introduced in section 3.4.2. In table 3.2, the according fitting parameters are compared to the fitting parameters for the A-free exciton in high quality bulk ZnO as measured by Hamby et al. [22]. Hamby et al. only measured the position of the A-free excitonic photoluminescence line up to a temperature of 150 K, since the identification of the free exciton at higher temperatures becomes difficult. To obtain a fit that covers the whole temperature region up to room temperature, they used the literature value of the band gap of ZnO at room temperature of 3.37 eV, and subtracted the exciton binding energy of 60 meV. This is a valid approach since it is assumed that the energy spacing between the band gap and the free exciton is unaffected by the phonon interaction at room temperature [22]. Here we can show that by associating the A-free exciton with its first phonon replica and tracing the peak position of these two peaks up to room temperature, we get a good estimate of the temperature dependence of the band gap by measuring the free exciton directly up to room temperature.

The good match between our fit and the fit presented by Hamby et al. for temperatures below 150 K shows that the A-free exciton of our epitaxial film annealed at 850 °C has a very similar property compared to the A-free exciton of high quality bulk ZnO. This is a strong sign of good crystal quality and low strain of the epitaxial film.

The discrepancy between the fit to our data and Hamby's fit to the emission of the bulk material at temperatures above 150 K is within the 90% confidence band of our fit. The confidence bands show the region the model falls with a certainty

of 90% for the uncertainties of the fitting parameters presented in table 3.2 and the uncertainty of the data represented by error bars in figure 3.11. Combined with the uncertainty of Hamby's fit, that unfortunately is not known, the position of the two fits can be valued as a good overlap. But there is a clear tendency of our fit to show a stronger temperature dependence of the A-free exciton energy for temperature above 150 K. This either shows that the method of tracing the A-free exciton and its phonon replica can easily lead to a phonon-broadening related misjudgement of the positions of the two peaks. Other more unlikely explanations would be, that the spacing of the A-free exciton and the band gap of ZnO is indeed affected by phonon coupling at temperatures of 150 Kelvin and above, or that the band gap at room temperature is not 3.37 eV, as assumed by Hamby et al. More measurements of bulk materials would be necessary to evaluate the applicability of the method presented here, and achieve a smaller uncertainty of the measurements.

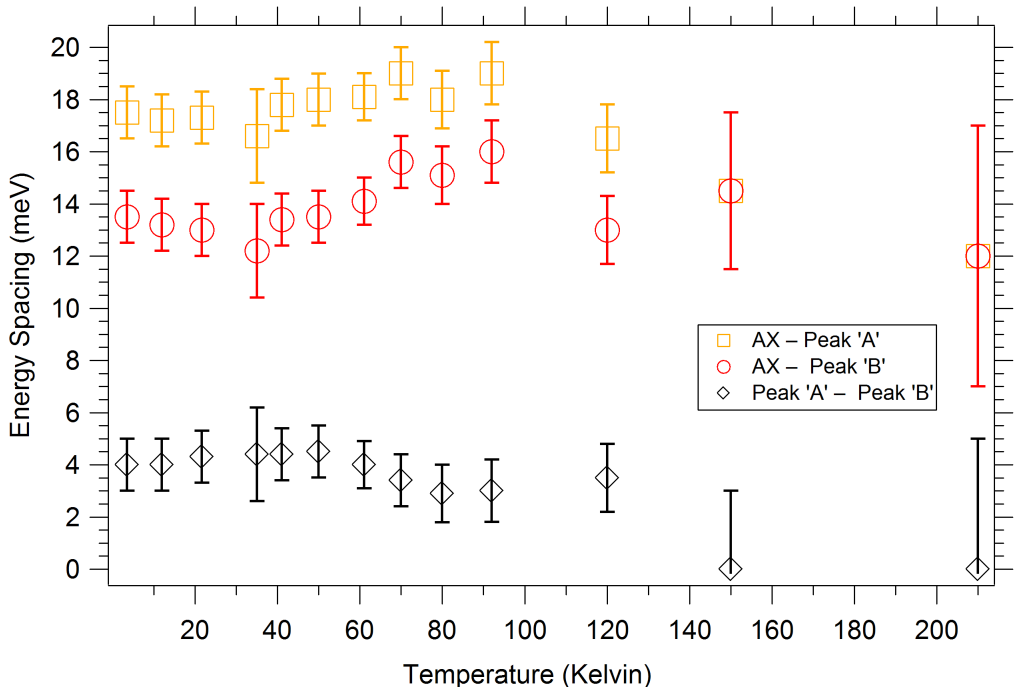

Figure 3.12: Temperature dependent peak spacing between the localized bound excitons as well as between the bound excitons and the free A-exciton in the MBE samples annealed at 850 °C

Figure 3.11 also shows the temperature dependent position of the two donor-bound exciton related peaks A and B. The position of these two emission lines can only by distinguished below the temperature of 150 Kelvin. The temperature dependent spacing between these donor bound exciton, as well as the spacing from each of the donor bound excitons to the free A-exciton AX is shown in figure 3.12. It demonstrates that the spacing between the two bound excitons as well as between the bound and free excitonic emission lines does not show a

clear sign of temperature dependence. The phonon-related broadening can be made responsible for the joining of the two bound exciton transitions at 150 K.

3.4.4 Intensity

At low temperatures, the photoluminescence spectrum presented in figure 3.10 is strongly dominated by two bound excitonic peaks, which are about two orders of magnitude stronger than the other emission lines in the spectrum. Therefore the y-axis is plotted on a logarithmic scale, enabling the display of peaks of such different intensities in a single graph. The PL-features are quite close together and broad enough to form a continuous spectrum. Thus, for the investigation of the temperature dependent change of photoluminescence intensity, the highest point of each transition within the spectrum had to be taken as the respective transition intensity. Alternatively, a peak fitting procedure could have been applied to investigate the underlying transitions separately. But due to the dominance of the more intense transitions, this has proven to be connected with great errors and not suitable to improve the precision of the measurement.

Figure 3.13 shows the temperature dependent intensity variation of the transitions of the MBE-film annealed at 850 °C for low temperatures that can be distinguished for temperatures below 100 K. Peak A is expected to be connected to I_9. Peak B is expected to be connected to $I4$, $I5$ and $I6$ (see section 3.4). Peak A is much more intense at temperatures below 60 K. In comparison to the highly temperature sensitive peak A, the intensity of peak B is barely influenced by temperatures up to 21 K. The difference in their sensitivity to temperature results in very similar intensities for both peaks at temperatures above 60 K. The two peaks can be separately identified on the energy scale up to temperatures of 120 K.

The emission rate of a semiconductor is a function of the electron population of the upper level, the availability of a free lower level, as well as the radiative lifetime τ_R versus the non radiative lifetime τ_{NR}. Within the conduction band, the electrons excited into high energy levels by the excitation laser can relax with enormously short time constants into lower energy levels via phonon coupling, with $\tau_{NR} \approx 10^{-13}s$. The radiative transition time in general is substantially slower, with $\tau_R \approx 10^{-9}s$. The luminescent efficiency η_R is the ratio of the radiative emission rate to the total de-excitation rate out of a certain state with the population N [90].

$$\eta_R = \frac{1}{1 + \tau_R/\tau_{NR}} \tag{3.21}$$

In short, the intensity of a photoluminescence peak of a certain electron transition is dependent on two factors. On one hand is the population of the radiant energy level. On the other hand the relation of the radiant time constant versus the time constant of non-radiative processes. [90]

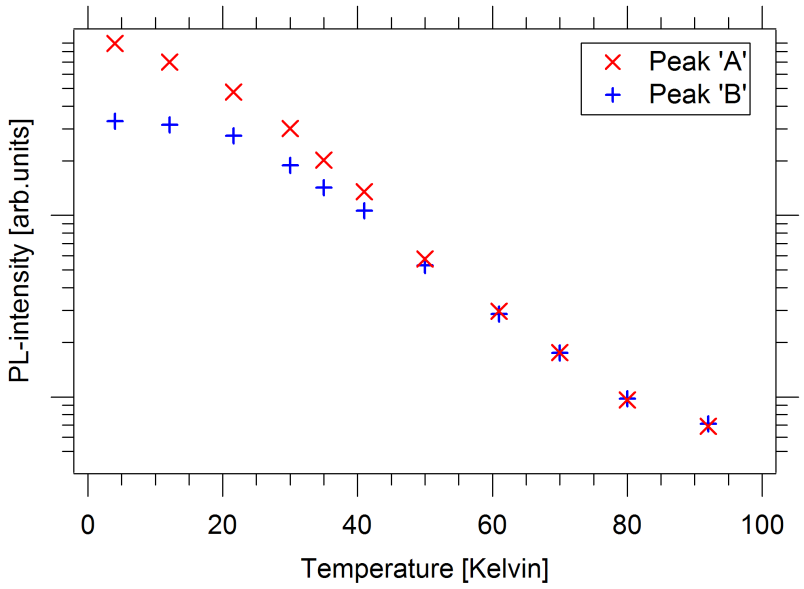

Figure 3.13: Temperature dependence of PL-intensity of peak 'A' and peak 'B' in figure 3.10

The temperature dependence of the non-radiative processes can be described by the standard Arrhenius rate equation. Two parameters are of importance for the rate equation: the process rate parameter C, and the activation energy E:

$$\frac{I(T)}{I_0} = \left(1 + C_1 e^{\frac{-E_{T1}}{k_B T}}\right)^{-1} \tag{3.22}$$

It has been found that the thermal dissociation of bound excitons from their ground state energy E_0 often happens via intermediate states, creating more than one channel of dissociation. These intermediate states can be described with the energies $E_{T1} = E_1 - E_0$ and $E_{T2} = E_2 - E_0$, by introducing a second part to the Arrhenius function [91]:

$$\frac{I(T)}{I_0} = \left(1 + C_1 e^{\frac{-E_{T1}}{k_B T}} + C_2 e^{\frac{-E_{T2}}{k_B T}}\right)^{-1}. \tag{3.23}$$

Figure 3.14 compares the applicability of both models to the temperature dependence of the two bound-excitonic peaks investigated here. Monteiro et al. have shown that the single Arrhenius function can be used to describe the decay of the Fe-related strong emission in Fe-implanted bulk ZnO [1], although only the temperature range of 10-70 K was investigated. By applying a strong weighting of the fitting procedure to the low temperature region, we could also achieve very good fits to the low temperature regions of both peaks using the single Arrhenius function.

Through this method it can be demonstrated nicely that the low-temperature sensitivities of the two peaks differ, as the single Arrhenius fit achieves good results for up to 60 K for peak B, but only up to 40 K for peak A.

Very good fits up to room temperature could be achieved for both peaks by using the double Arrhenius fit of equation 3.23, showing that the dissociation of the bound excitonic emission can be described by the combination of one low-temperature and one high-temperature process, with a lower activation energy for the low-temperature dissociation of peak A. This is also evident in the resulting fitting parameters which are presented in table 3.3 and 3.4.

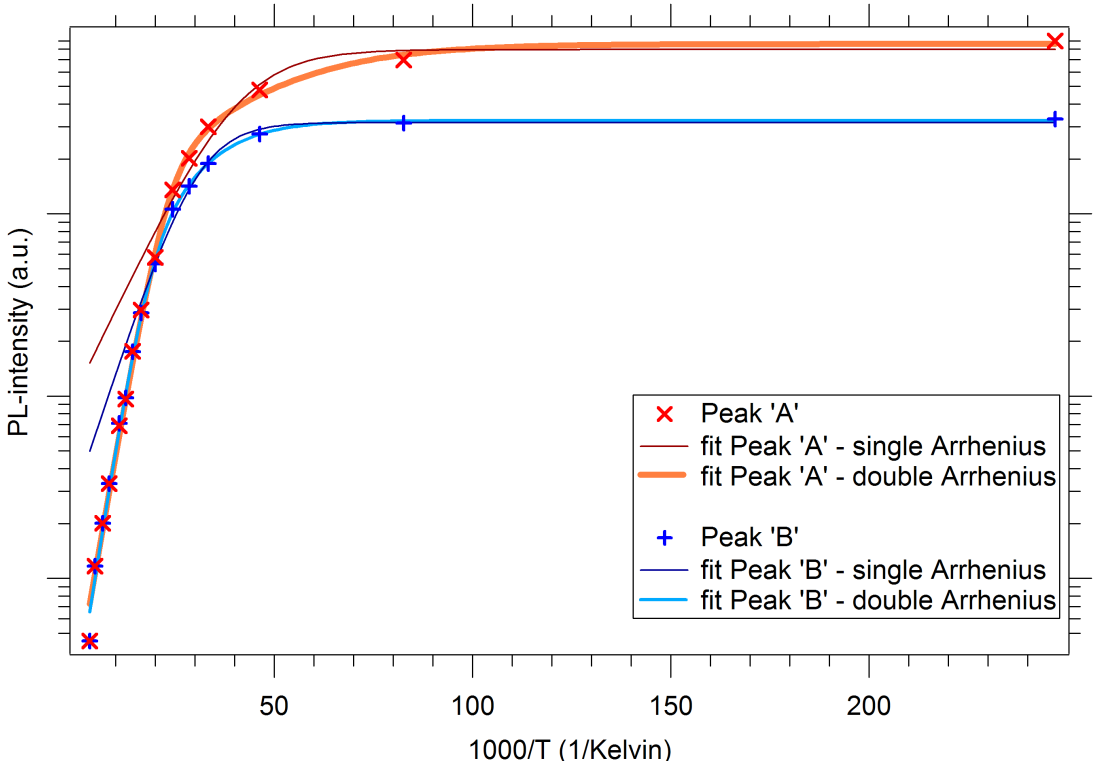

Figure 3.14: Arrhenius fit of the temperature dependent decay of intensity of photoluminescence for peaks A and B

Table 3.3: Fitting parameters, using single Arrhenius fit [1] for the intensity of the two dominant peaks in the low temperature PL-emission, as shown in figure 3.14

	***Peak** A*		***Peak** B*	
Parameter	Value	Uncertainty (±)	Value	Uncertainty (±)
I_0 [a.u.]	7.95×10^5	0.338×10^5	3.16×10^5	0.064×10^5
C_1 [a.u.]	73.6	35.1	105	30
E_{T1} [eV]	9.10×10^{-3}	1.21×10^{-3}	1.32×10^{-2}	0.092×10^{-2}

Table 3.4: Fitting parameters, using double Arrhenius fit [91] for the intensity of the two dominant peaks in the low temperature PL-emission, as shown in figure 3.14

	***Peak** A*		***Peak** B*	
Parameter	Value	Uncertainty (±)	Value	Uncertainty (±)
I_0 [a.u.]	8.54×10^5	0.01×10^5	3.24×10^5	0.03×10^5
C_1 [a.u.]	3135.2	6	1447	11
E_{T1} [eV]	2.506×10^{-2}	0.23×10^{-2}	2.8×10^{-2}	0.41×10^{-2}
C_2 [a.u.]	9.123	2.1	19.1	6.5
E_{T2} [eV]	4.305×10^{-3}	0.3×10^{-3}	8.6×10^{-3}	0.8×10^{-3}

Chapter 4

Optical studies of the band structure of ZnO

4.1 Temperature dependent transmission of thick bulk ZnO crystals

In the context of this work, the absorptive behaviour of bulk ZnO is of special interest since it plays an integral part of the photoconductive process. A detailed understanding of the spectra presented in chapter 5 requires the investigation of the absorptive behaviour across the respective energy range. Also, the absorptive behaviour of semiconductors gives basic clues about their band structure and its variation with external parameters such as temperature. The setup described in section 2.5.5 was used for temperature dependent transmission and reflection experiments of bulk ZnO crystals and epitaxially grown films. Contrary to setups that expose the sample with a broad light-spectrum and then measure the spectral distribution of the transmitted spectrum, this setup has the advantage that the sample gets irradiated with only one wavelength (more precisely a narrow wavelength-region, with FWHM ≈ 0.6 nm) at a time. This allows us to assume that the incident beam of light can only be reflected, absorbed or transmitted. Scattering is not expected to play a large role due to the quality of the investigated crystals and their polished surfaces. But photoluminescent processes that are caused by light of higher energies can otherwise easily distort the measured spectrum considerably [13]. Also, using only one wavelength to probe the semiconductor minimizes a potential distortion of the measured electronic structure by light of other wavelengths.

The Transmission T is defined as the transmitted light intensity, normalized with the incident light intensity:

$$T = I/I_0. \tag{4.1}$$

As is discussed in section 5.1.3, semiconductors show a strong change of transmitted light intensity in the energy region of the band gap of the semiconductor. The steepness of this change and the maximum transmittance and absorption levels are a good indicator of crystal quality, since defects and impurities represent a distortion of the crystal periodicity and lead to a widening of the energy range in which the transmission sets in. The spectrum of the absorption coefficient at the absorption edge of semiconductors is a combination of various absorption features. Defects and impurities lead to a weak absorption tail just below the exponential edge region of the onset of strong absorption. The exponential edge region itself is influenced by the structural irregularity of the investigated system, resulting in a more gentle rise for structurally less regular samples [92].

Figure 4.1 shows the room temperature transmission and absorption coefficient spectra of three bulk samples with a thickness of 460 μm. The samples were obtained from three different wafers purchased from Tokyo Denpa (c-plane and m-plane) and Cermet (a-plane). As expected, the transmission curve of these high quality bulk ZnO crystals shows a very sharp transition, switching from highly transparent with about 50% transparency below the band gap, to strongly absorbing, with no detectable light passing through the crystal for energies close to the band gap. This transition happens rapidly across a photon energy range of $\approx$ 100 meV. Due to the relatively large thickness of the samples (460 μm), the energy at which no transmitted light can be detected is slightly below the band gap, preventing the direct investigation of free excitons. But the room temperature transmission and absorption spectra show considerable differences in the response of the three bulk ZnO samples that are cut in three different orientations: The energy at which no transmitted light can be detected varies from 3.19 eV for the c-plane sample and 3.225 eV for the m-plane and a-plane sample. At energies well below the band gap (2.8 eV), the a-plane sample is not as transparent as the m-plane sample, which again is not as transparent as the c-plane sample. Most remarkably, between 2.8 eV and 3.05 eV, the transmission of the c- and m-plane sample do not show any significant variation but show a rather constant value of 0.55 for the m-plane sample and 0.63 for the c-plane sample. In contrast, the a-plane sample shows a continuous decrease in transmission from 0.45 at 2.8 eV to 0.34 at 3.05 eV across this same energy range. The exponential, band edge related onset of absorption starts at about 3.1 eV for all samples. The c-plane sample reaches a level of absorption high enough to block any light from reaching the detector behind the sample within 85 meV at 3.185 meV, whereas the m- and a-plane samples only achieve that same level of absorption at 3.225 eV, at an energy 40 meV above that of the c-plane sample, with a total energy range of 125 meV from low to high absorption. Therefore, although the bulk samples investigated here all show a similarly outstanding level of detail in their photoluminescence emission spectra, there is a considerable variation in the crystal quality of these high quality samples.

From the room-temperature transmission and absorption spectra alone, it can be assumed that, due to its less apparent absorption tail at energies below the

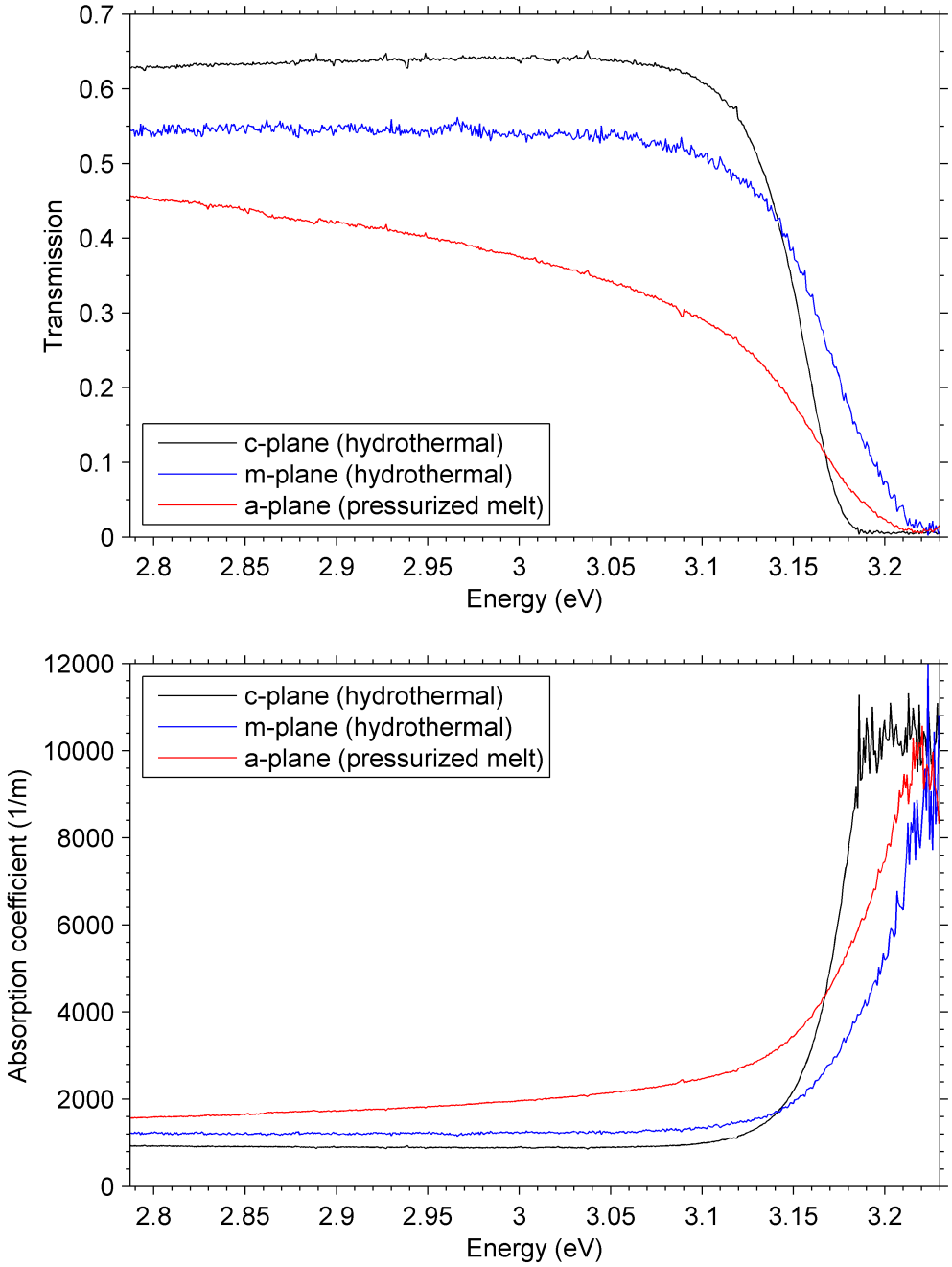

Figure 4.1: Room temperature transmission and absorption spectra of three different ZnO bulk crystals of equal thickness

exponential edge region of the onset of absorption, the c-plane sample has a lower defect and impurity density than the m- and a-plane samples [92], whereas the a-plane sample can be expected to have a higher defect and impurity concentration than the m-plane sample. But the steepness of the transition from transparent to highly absorbing is very similar for the a- and m-plane sample, indicating a comparable level of crystal regularity for the two samples. The c-plane sample, in contrast, shows a much steeper transition from transparent to absorbing, thus the c-plane sample can be expected to have a higher crystal regularity than the m- and a-plane samples, too.

In general, the high transmission rate below the band gap indicates a lack of energy states originating from impurities and defects. But for energies approaching E_G, energy states become abundant, allowing the absorption of photons according to the standard stimulated absorption process. Therefore temperature dependent transmission experiments are a good way to establish the behaviour of the band gap with temperature. Figure 4.2 shows the low-temperature (12 Kelvin) transmission, reflectivity and absorption coefficient spectra for the c- and m-plane sample. α is calculated using

$$T = (1 - R)^2 \exp(-\alpha d), \tag{4.2}$$

requiring the measurement of the transmittance (T), reflectance (R) and thickness (d) of the investigated crystal. Equation 4.2 takes into account that the transmitted light intensity is reduced by the amount of light that gets reflected at the front and rear interface of the crystal, including multiple internal reflections [93]. The reflection spectrum in figure 4.2(b) shows strong narrow features at energies between 3.34 eV and 3.47 eV. These features are due to excitonic resonances from the A, B and C-valence band to the conduction band and will be investigated closer in section 4.2. The transmission in figure 4.2(a) does reveal a similar scenario as the transmission spectra taken at room temperature: the c-plane sample shows a much more rapid decrease in transmission located at a substantially higher energy (offset by 50 meV), a higher transmittance at low energies (0.65 for the c-plane sample vs. 0.57 for the m-plane sample), and a complete absorption of the incident light at a lower energy (3.376 eV for the m-plane and 3.363 eV for the c-plane sample).

Most remarkable about the low temperature transmission curves of the m-plane vs. the c-plane sample is, that the c-plane sample exhibits a fully exponential fall of the transmission towards the band gap, whereas the transmission curve of the m-plane sample clearly shows some structure across the spectrum. This structure can be described as a dip at 3.237 eV and 3.338 eV. Also, the spectrum becomes significantly more flat after each dip, leading to the higher energy of full light absorption compared to the c-plane sample. The reflectivity spectrum shows that the excitonic resonators are at energies above the energy of full light absorption for each sample, therefore the excitonic transitions can not be resolved in the resulting calculated absorption coefficient spectra nor are they

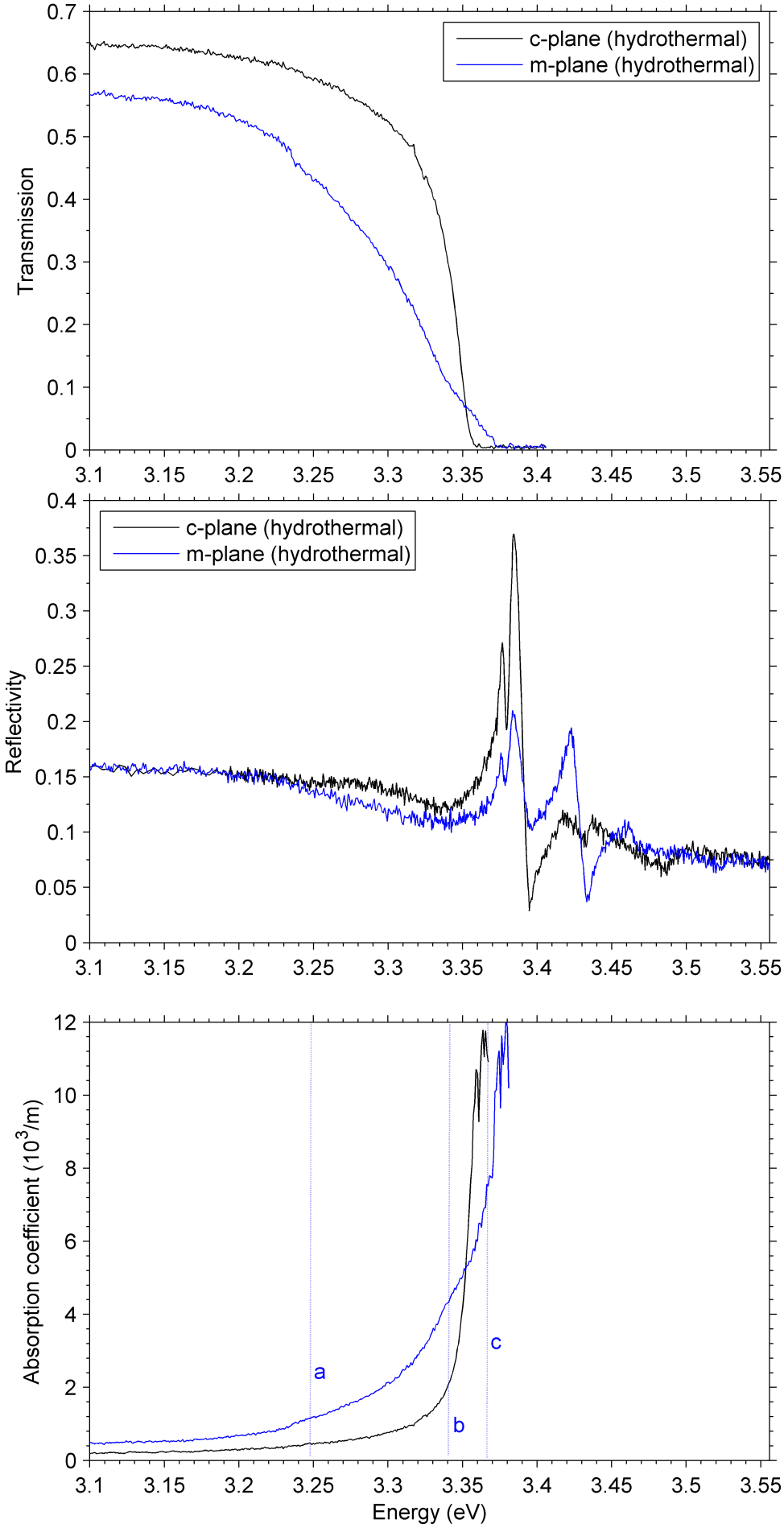

Figure 4.2: Transmission (a), Reflectivity (b) and Absorption coefficient (c) of m- and c-plane bulk ZnO at 12 Kelvin

directly responsible for the structure in the transmission spectrum of the m-plane sample. The spectrum of the absorption coefficient allows us to relate peaks to a heightened intensity of transitions across the energy range. The absorption coefficient of the c-plane sample is very smooth and exponential, as expected, and the m-plane sample shows three very broad and weak shoulders in the exponential onset of absorption: they are marked with lines named 'a' (at 3.249 eV), 'b' (at 3.342 eV) and 'c' (at 3.368 eV) in figure 4.2(c).

In the absorption spectrum, only the energy region above the band gap is suitable to determine the band gap of the system with the well-known Tauc relation for the absorption coefficient [92]:

$$\alpha = \frac{B\,(E - E_G)^p}{E} \tag{4.3}$$

E is the energy of the incident photons, B is the constant transition probability factor and p is related to the type of electron transition that causing the photoabsorption. Allowed direct, allowed indirect, forbidden direct and forbidden indirect transitions each have a characteristic associated exponent p of $2, 1/2, 3, 3/2$, respectively. Equation 4.3 can be applied to measure the band gap energy, since

$$(\alpha E)^{1/p} = B^{1/p}\,(E - E_G) \tag{4.4}$$

must be zero for $E = E_G$. Therefore, to establish the band gap energy out of the absorption coefficient, $\alpha E^{1/p}$ is plotted against energy with a value of p that results in a linear plot. The intercept with $y = 0$ of a line fitted to that plot reveals the band gap energy. However, due to the thickness of the investigated samples, this method can not be applied here. As can be seen in figure 4.2, the transmission and reflection spectra can be combined to reveal α, but the amount of light transmitted through the sample at energies of more than 3.9 eV is too small to be picked up by the photodetector used here, causing the absorption spectrum to be meaningless for this energy region. Since the Tauc-routine only relies on fitting a straight line to the spectrum of the absorption coefficient at energies higher than the band gap energy, absorption coefficient spectra as the one shown in figure 4.2(c) are not suitable for this method.

The temperature dependent band gap shift can be established in a way other than by the standard method according to equation 4.4. Figure 4.3 shows the transmission response spectrum of m-plane bulk ZnO at temperatures ranging from room temperature to 12 Kelvin: Hauschild et al. [23] show that the transmission spectra themselves can be used to establish the energy shift of the band gap in regard to changing parameters. Since the inflection point is a unique point in the transmission spectrum, it can be used as a reference point. The energy at which the tangent to the inflection point crosses the energy axis at *Transmittance* = 0 carries a systematic constant offset to the band gap. With a change in temperature it therefore shifts according to the shift of the band gap energy. Figure 4.3 shows the tangent to the inflection point of the Transmission

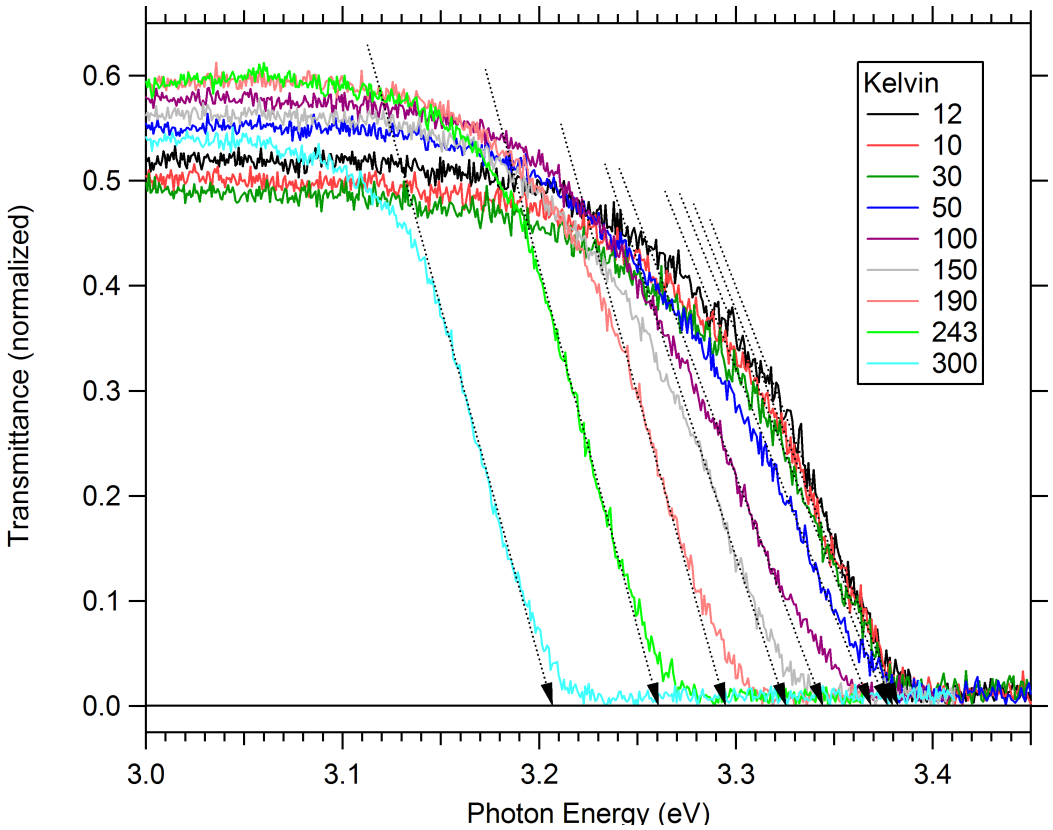

Figure 4.3: Normalized temperature dependent transmission spectra of bulk ZnO. The Arrows point at the energy of the intercept of the tangents to the inflection points with zero transmission

spectrum for each temperature. The arrows at the end of the tangents point at the energies of the intercept with *Transmittance* = 0. Figure 4.4 shows the temperature dependent band gap shift from its value at 10 Kelvin, obtained by this transmission method. Assuming the binding energy of the free exciton to be constant, the temperature dependent shift of the energy of the free *A*-exciton should be equivalent to that of the band gap. Therefore figure 4.4 also shows, in comparison, the measurement of the temperature dependent photon energy of the free *A*-exciton transition as measured by photoluminescence on the MBE-film investigated in section 3.4.3. The Manoogian fitting procedure introduced in section 3.4.2 is applied for both measurements, to investigate the applicability of the inflection method for the transmission measurement of rather thick bulk crystals and the resulting apparent differences in measured material parameters. These fits are shown as lines in figure 4.4. The fitting procedure was weighted by the standard deviations of the measurements as expressed by the error bars of *dE* of the values measured by transmission and PL in figure 4.4. The uncertainties of the resulting fitting parameters (see table 4.1) are expressed as the respective upper and lower confidence bands in figure 4.4. They indicate the region around the fitting curve where the actual fit should fall with a probability

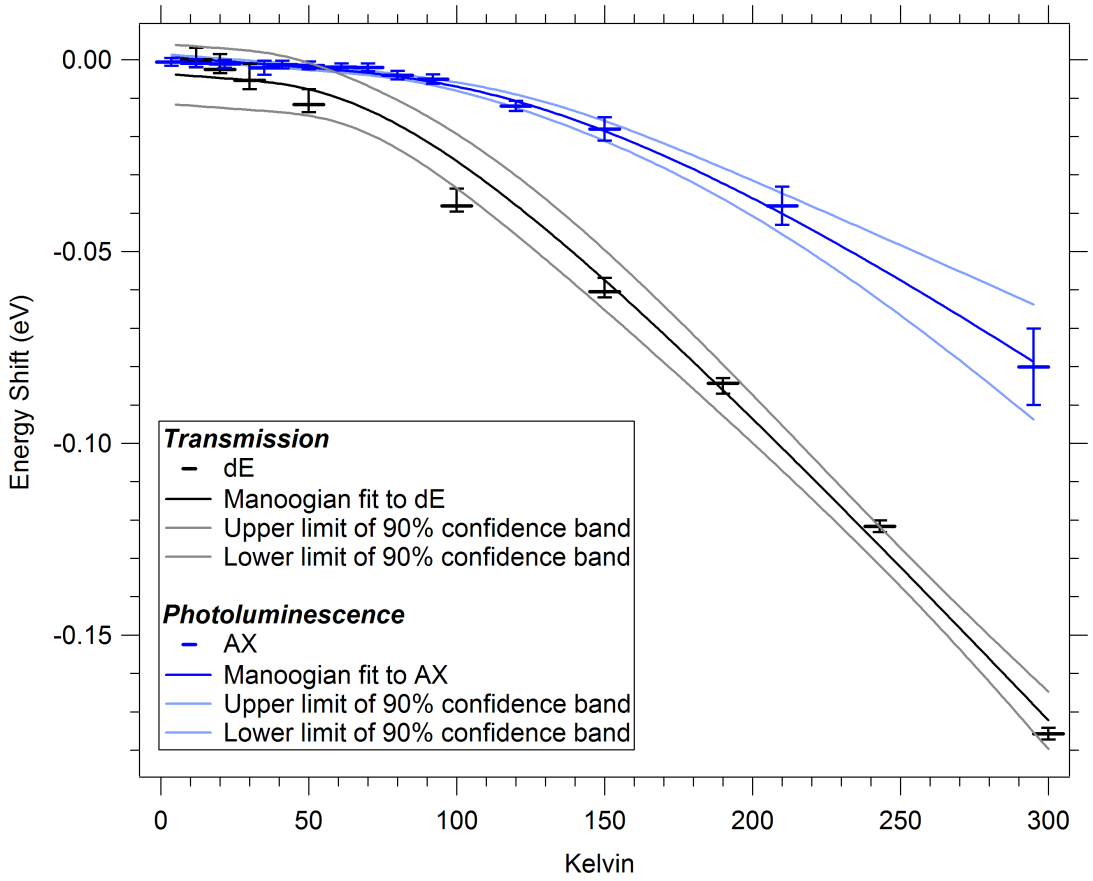

Figure 4.4: The energy shift of the band gap of m-plane hydrothermal bulk ZnO, according to the inflection point tangent measurement and the temperature dependent PL-measurement of the A-free exciton of an MBE-film (see figure 3.11). Both temperature dependent shifts are fitted by the Manoogian fitting procedure [22]

of 95%. Table 4.1 gives an overview of the resulting fitting parameters for the two methods.

As the thermal lattice dilatation parameter U can be related to the pressure coefficient of the band gap $\frac{\partial E_G}{\partial P}$, the bulk modulus B and the mean thermal expansion coefficient $\langle \alpha_L \rangle$ with the expression [94]

$$U \approx -3B \left(\frac{\partial E_G}{\partial P} \right) \langle \alpha_L \rangle \,, \tag{4.5}$$

for high quality ZnO we used the theoretical values of $\partial E_G/\partial P = 2.7 \times 10^{-6}$ eV/bar, $B = 157$ GPa and $\langle \alpha_L \rangle = 4.3 \times 10^{-6}$ 1/K, resulting in $U = 5.5 \times 10^{-5}$ eV/K, see Hamby et al. [22]. Since U was fixed, the value of s was also fixed to the expected value of 1.01. The motivation for using theoretical values for U and s is the limited number of data-points that is available for the

Table 4.1: Fitting parameters of Manoogian fitting procedure [85] for the energy gap shift measured by the inflection method, compared to the shift of the A-free exciton of MBE-grown ZnO film annealed at 850 K, measured by PL, see figure 3.11:

	Transmission		***AX in PL of MBE-film***	
Parameter	Value	Uncertainty (±)	Value	Uncertainty (±)
E_0 [eV]	-3.61×10^{-3}	7.78×10^{-3}	6.56×10^{-4}	6.56×10^{-4}
Θ [K]	256.05	99.5	483.87	122
α [eV/K]	-7.96×10^{-4}	1.56×10^{-4}	-5.37×10^{-4}	2.4×10^{-4}
U^*[eV/K]	-5.5×10^{-5}	–	-5.5×10^{-5}	–
s^*	1.01	–	1.01	–

* Values set according to Hamby et al. [22]

fits. Limiting the number of free fitting parameters, helps to get a more meaningful result for the remaining fitting parameters. For high quality bulk ZnO the crystal lattice dilatation is a reasonable material property to exclude from the fitting procedure.

The much smaller value for the energy shift of the A-free exciton measured by PL versus the shift of the band gap as measured by transmission shows that the method of inflection has to be applied with care, and phonon broadening might be responsible for an overestimate of the temperature dependent shift of the band gap with this method. Additionally, a unique point of inflection can only be specified for purely exponential spectra, as the transmission spectra of the c-plane sample in figure 4.1-(a). But, as discussed above, the m-plane sample actually exhibits an irregular structure at temperatures below 150 Kelvin, creating more than one point of inflection across the transmission spectrum. Due to this structure, the uncertainty in the measurement of the point of inflection of this sample actually becomes smaller with rising temperature, as the transmission curve becomes purely exponential only for temperatures above 150 Kelvin. At temperatures below 150 Kelvin, the measurement might carry a considerable systematic error due to these structures, as indicated by the confidence bands in figure 4.4.

There is a substantial difference in the effect that phonon interaction has on the room temperature spectra recorded with photoluminescence and transmission. Although the identification of the free excitonic peak in the photoluminescence spectrum becomes harder with higher temperatures, one can still estimate the centre of the free excitonic transition. The temperature dependence of the bandgap as derived from the inflection method in figure 4.4 suggests though, that the broadening of the energy levels results in the transmission curve to be

pushed to lower energies, thus appearing to be related to the low energy tail of the broadened transitions, and not to their centre. Although the onset of transmission becomes easier to be identified with elevated temperatures, phonon broadened energy levels therefore might obstruct its direct relation to the band gap. At room temperature, the resulting FWHM from the broadening of the PL-lines is about 95 meV, see section 3.4.1 and figure 3.10, which might be related to a shift of the transmission curve to lower energies at room temperature of ≈ 40 meV. The absolute distance between the room temperature shift determined by PL and transmission in figure 4.4 is 95 meV, showing that the method of inflection can not be applied on thick bulk ZnO crystals for the determination of the temperature dependent band-gap shift, as its inaccuracy goes beyond the possible effect of phonon-broadened energy levels.

4.2 Photoreflective properties of ZnO

Due to its sensitivity to resonances of oscillators like excitons and polaritons, spectral reflectivity is a powerful tool to analyse the electronic and crystal structure of ZnO [17, 95–97]. Since the reflection process happens at the material interface, reflectivity is sensitive to the behaviour of excitons in the surface area, considerably more than other methods such as absorption spectroscopy. Reflectivity allows us to gain valuable information about the nature of energy states of thin films [98, 99], plays an important role in the discussion of the ZnO valence band ordering via the polarization dependent study of excitons [13, 17, 47] and the behaviour of excitons inside the surface layer of bulk crystals [100–105]. Yet no studies of the temperature dependence of the reflectivity behaviour of high quality ZnO can be found in the literature. The temperature dependence of reflectivity though is particularly interesting as it allows the tracing of the free excitons without bound excitons, hot excitons or phonon replica of excitons making the identification of the free excitonic transitions difficult. The fact that reflectivity features are so clearly related to the free excitonic transitions in the surface area also makes reflectivity spectroscopy a great addition to photoconductive spectroscopy, as the relation of spectral features in photoconductivity to electric processes in the semiconductor surface is not straightforward at all, but very sensitive to phonon related processes like hot excitons [106, 107] and phonon replica [32, 108–113]. Also the response to electric fields varies between different classes of materials, excitonic features can be expressed as dips or peaks in the photoconductive spectrum [114, 115]. As was found in this study, this results in the fact that even the geometry of optical exposure can influence the photoconductive response spectrum. Therefore the comparison to photoreflectivity is a good way to establish the relative position of photoconductive features to the free excitons, particularly for temperature dependent studies.

The experimental advantage of reflectivity studies is that samples stay virtually untouched, since they do not have to be modified, electrically contacted or

exposed to high intensity laser radiation. The oblique geometry used here also allowed us to record the reflectivity spectrum simultaneously while measuring the temperature dependent photoconductivity response of various ZnO surfaces, under various optical conditions. The experimental setup used for the measurements of reflectivity spectra presented in this work are described in section 2.5.5.

4.2.1 Principles of photoreflection

Reflectivity (R) is defined as the ratio of the reflected light intensity to the intensity of the incident light [90]. The ratio at which light of a certain wavelength is reflected of an investigated material is determined by the boundary conditions at the interface causing the reflection. For thick samples, the interface at the surface of the sample as well as the material properties of the bulk near the surface play a role in the measured reflected light intensity. For thin films the interface to the substrate layer underneath the film can also play a significant role, causing thin film interference patterns in the spectrum. In terms of classical physics, the reflection of light is described by the Fresnel formulas, which are derived from Maxwell's equations of electrodynamics. For light at normal incidence the reflectivity is given by [2]

$$R(\omega) = \frac{I_r}{I_i} = \frac{(n(\omega)-1)^2 + \kappa^2(\omega)}{(n(\omega)+1)^2 + \kappa^2(\omega)}, \tag{4.6}$$

with the refractive index n and the extinction coefficient κ. n and κ are combined into the complex refractive index $\tilde{n}$:

$$\tilde{n}(\omega, \boldsymbol{k}) = n(\omega, \boldsymbol{k}) + i\kappa(\omega, \boldsymbol{k}). \tag{4.7}$$

The extinction coefficient κ is related to the absorption coefficient α by [116]

$$\kappa = \alpha/4\pi. \tag{4.8}$$

Since the refractive material properties described by n and the absorption properties described by κ are forming the real and imaginary part of the complex function $\tilde{n}$, the Kramers-Kronig relations can be used to relate them to each other. Thus for $\tilde{n}$ the Kramers-Kronig relations describe two important properties [37]: If $n(\omega, \boldsymbol{k}) \neq 1$ anywhere in the frequency range, there must be an absorption structure in the spectrum, with $\kappa(\omega) \neq 0$, and vice versa; the second property following from the mathematically derived Kramers-Kronig relations is that the knowledge of the wide spectral response of either n or κ allows the calculation of the other.

The conductivity only plays a small role in the optical properties of semiconductors. Only for heavily doped materials, the relatively high concentration of free charge carriers influences the optical properties. This influence can only be

seen in the low frequency, infrared spectral region. Therefore we can assume, especially for the UV-response of highly resistive ZnO, that [37]

$$|\boldsymbol{j}| = |\sigma \boldsymbol{E}| \ll |\dot{\boldsymbol{D}}| \tag{4.9}$$

From this assumption of no free charges at the interface, the boundary conditions of the Maxwellian electric displacement $\boldsymbol{D}$ and magnetic flux density $\boldsymbol{B}$ can be deduced: Their normal components have to be continuous across the interface. Through the Maxwell equations these conditions have the effect that the tangential components of the electric field strength $\boldsymbol{E}$ and magnetic field strength $\boldsymbol{H}$ also have to be continuous across the interface [37]. The Fresnel Formula then gives the separation of incident light into beams of transmitted and reflected light, as caused by an interface between regions with different refractive indices n_1, n_2. Although $\tilde{n}$ is defined classically in terms of electrical material properties, without any consideration of the atomic structure, the quantum structure of the material does become apparent in the dispersion related frequency dependency of $\tilde{n}(\omega, \boldsymbol{k})$ [117].

Semiconductor crystals, especially ionic crystals like ZnO, respond to an applied electric field from sources like a free charge carrier, exciton, or an external electromagnetic field, with a polarization $\boldsymbol{P}$ of the crystal lattice. High power laser radiation can result in a non-linear response of the lattice, but for light intensities used in this work, the interaction of the crystal lattice with electromagnetic radiation can be regarded as linear [2]:

$$\frac{1}{\epsilon_0}\boldsymbol{P} = \chi_e \boldsymbol{E} = (\epsilon - 1)\boldsymbol{E}. \tag{4.10}$$

The response of the crystal is measured by the electric susceptibility χ_e, or the dielectric function ϵ, describing the polarization response of the medium to the stimulation of an incident electric field [37]. ϵ is connected to the complex refractive index $\tilde{n}$ by the simple relation [118].

$$n = \sqrt{\epsilon \mu_r}. \tag{4.11}$$

With $\mu_r = 0$ for nonmagnetic materials follows:

$$\tilde{n}(\omega, \boldsymbol{k}) = \sqrt{\epsilon(\omega, \boldsymbol{k})} = \sqrt{\epsilon_1(\omega, \boldsymbol{k}) + i\epsilon_2(\omega, \boldsymbol{k})}. \tag{4.12}$$

The dielectric function ϵ (sometimes called relative permittivity) therefore is a material parameter of key importance, since it links the dielectric properties of nonmagnetic materials directly to their optical properties. The dependence of ϵ on the wave-vector $\boldsymbol{k}$ is called spatial dispersion $\epsilon(\boldsymbol{k})$ [37].

The wave equation for an electric field in vacuum, described by

$$\nabla^2 \boldsymbol{E} - \mu_0 \epsilon_0 \ddot{\boldsymbol{E}} = 0 \tag{4.13}$$

resulting in the solution for electric waves [37]

$$\boldsymbol{E}(\boldsymbol{r},t) = \boldsymbol{E}_0 f(\boldsymbol{kr} - \omega t) \tag{4.14}$$

gets extended, as a result of equation 4.10, into the wave equation for light traveling through matter as a combination of lattice polarization and electromagnetic wave

$$\nabla^2 \boldsymbol{E} - \mu_0 \epsilon_0 \ddot{\boldsymbol{E}} = \mu_0 \ddot{\boldsymbol{P}}. \tag{4.15}$$

Quantum-mechanically, the interaction of the lattice polarization with the electromagnetic wave results in the description of light travelling through matter in form of a quasiparticle called the polariton (see section 1.6).

An important result of the polarization of the crystal lattice is that electromagnetic radiation in matter is able to propagate with longitudinal polarization $\boldsymbol{E} \parallel \boldsymbol{k}$, a solution for equation 4.15 made possible by $\epsilon(\omega, \mathbf{k}) = \mathbf{0}$. The frequency at which $\epsilon = 0$ is therefore called longitudinal resonance frequency ω_L [37].

4.2.2 Excitonic resonances in Photoreflectivity

The resonance of oscillators like phonons and excitons, with resonance frequency ω_0, resonator strength f_j and damping γ is connected to the dielectric function of the semiconductor by the Helmholtz-Ketteler formula, that can be simplified to an expression for the spectral surroundings ω of ω_0 [37]

$$\epsilon_1(\omega) + i\epsilon_2(\omega) = \epsilon_b + \frac{f\left(\omega_0^2 - \omega^2\right)}{\left(\omega_0^2 - \omega^2\right)^2 + \omega^2\gamma^2} + i\frac{\omega\gamma f}{\left(\omega_0^2 - \omega^2\right)^2 + \omega^2\gamma^2} \tag{4.16}$$

This relation describes that resonances influence the polariton propagation modes within the crystal in a particular way, giving a characteristic shape to the dielectric spectrum, and therefore causing characteristic spectral features in the reflectivity spectrum in accordance with equation 4.6. Two frequencies play an important role: the resonance frequency ω_0, with $\epsilon(\omega_0) = \infty$, and the frequency of the longitudinal mode, the frequency for which a transverse electromagnetic wave is not allowed, $\omega_L = \omega(\epsilon = 0)$. For ω_L, the propagation mode therefore is a purely longitudinal polarization mode with $\epsilon_0 \boldsymbol{E} = -\boldsymbol{P}$.

Through equation 4.16, the oscillator strength is directly related to the spacing between ω_L and ω_T, with [37, 97]

$$\omega_L - \omega_T = \omega_{LT} = f/(2\omega_T \epsilon_b) \tag{4.17}$$

The longitudinal resonance frequency is always higher than the transverse resonance frequency since only the longitudinal electric field produced by the longitudinal polarization wave acts on the lattice as an additional restoring force, therefore increasing the resonance frequency. In contrast, for transversal waves,

the electric field caused by the lattice polarization does not influence the restoring force of the lattice in direction of the transverse polarization.

Below all resonance frequencies, ϵ is influenced by all higher lying resonances, resulting in ϵ_s. Above all resonance frequencies, ϵ is influenced by all lower resonances, resulting in ϵ_b. Through the Fresnel Formula in equation 4.6 and the relation of the complex refractive index to ϵ in equation 4.12, ϵ_s and ϵ_b define the reflectivity value at frequencies substantially above and below the main resonances to be a certain constant value, with [37]

$$\epsilon_s = \epsilon_b + f/\omega_0 \tag{4.18}$$

and the Lyddane-Sachs-Teller relation

$$\frac{\epsilon_s}{\epsilon_b} = \omega_L^2/\omega_0^2 > 1 \tag{4.19}$$

The reflectivity region between ω_0 and ω_L is called stop-band, as no propagating mode is available in case of no damping causing all light to be reflected [37]. For no damping the reflectivity is 1 between ω_0 and ω_L. Damping $\gamma > 0$ reduces the maximum reflectivity from 1 and shifts it to gradually higher frequencies within the stop-band $\omega_0 < \omega < \omega_L$. The amount of light that is not reflected from the stop-band therefore is an indication of the size of the damping γ of the resonance. The higher the damping, the more the peak in reflectivity is offset from ω_T. But independent of damping, the reflectivity rapidly drops to a minimum close to 0 just above ω_L, making it possible to read ω_L directly from the reflectivity spectrum.

4.3 Reflectivity spectra of ZnO at ambient conditions

The Ocean Optics system described in section 2.5.1 was used for reflection experiments with incident angles very close to normal incidence with ($\alpha \leq 2°$). The rather low resolution of the system of $\approx 2\ nm$ is sufficient for reflection measurements of ZnO at ambient conditions, i.e. at room temperature, in air. Figure 4.5 shows the reflection response of high quality bulk ZnO in comparison to two different areas of a MBE grown thin film on sapphire. Although the samples have different overall thicknesses, they were investigated with the same distance between the fibre-optic and the sample surface of about 1 cm. To avoid the unknown reflectivity of the sample holder to influence the reflection spectrum, the bulk sample was placed directly onto a mirror surface. The spectra were normalized against the light-intensity reflected at 2.9 eV.

The bulk sample is highly transmissive for energies below 3.046 eV (a), with

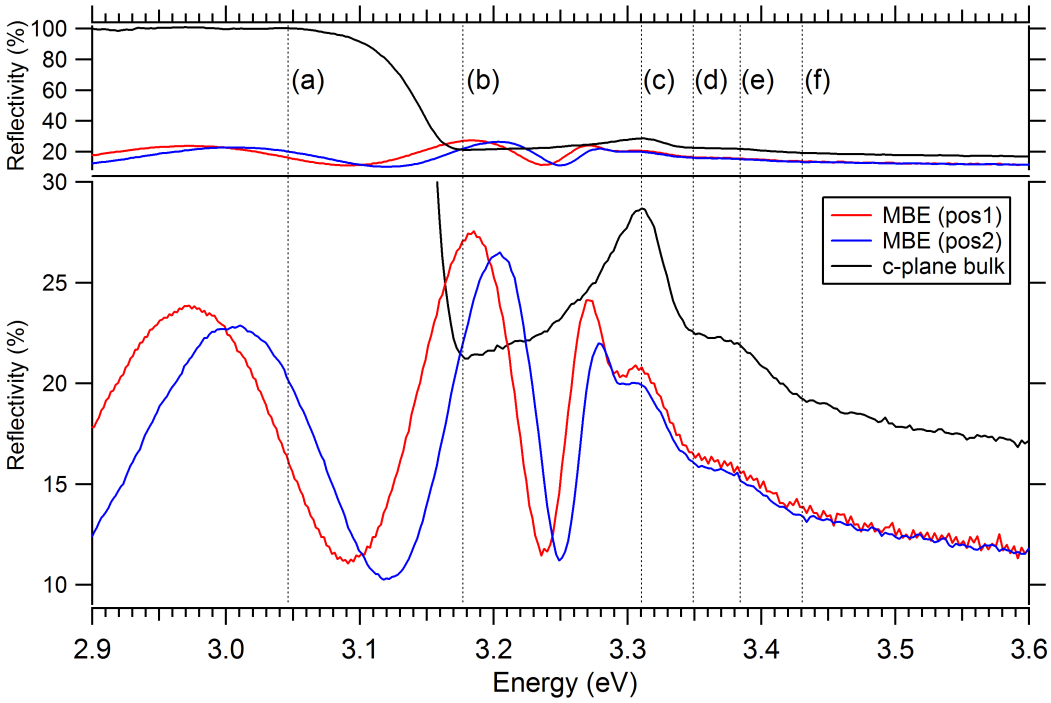

Figure 4.5: Reflectivity at normal incidence and room temperature, of bulk ZnO compared to two spots on the same MBE-grown film on sapphire. The bulk crystal was placed on a mirror, resulting in the onset of transmission between markers (a) and (b). For identification of features (a)-(f), see table 4.2.

the transmission setting across 131 meV, starting at 3.177 eV (b). The room-temperature reflectivity of the bulk ZnO and the MBE-grown film show a series of excitonic peaks and dips that line up perfectly, at least up to the resolution limit of the Ocean Optics spectrometer. Both samples show a clear excitonic peak at 3.310 eV (c), followed by a dip at 3.349 eV (d), a second peak at 3.384 eV (e) and a second dip at 3.431 eV (f). The orientation of the bulk sample is c-plane, and according to the selection rules outlined in section 4.3.1, the A and B free excitons are strongly preferred against the C free excitons under this geometry. This allows the assignment of the ground state and the first excited state of the A and B free excitons to the two peaks with their accompanying dips. The separation between the A and B free excitons in ZnO is, with a spacing of 4.9 meV at 1.6 Kelvin, too small in order to be resolved individually at room temperature where we expect a thermal broadening of about 54 meV. Therefore (c) is the reflectance peak of the B free exciton at $\hbar\omega_T$, with the reflectance feature of the A free exciton in its low energy shoulder, and (e) is the first excited state of the same transition. (d) and (f) are related to the ground and first excited states at $\hbar\omega_L$ of the B-free exciton.

The interference pattern of the MBE-film is due to interference of light reflected by the surface of the film with light reflected at the interface of the film and the sapphire substrate. The spacing of the energies of the interference max-

ima can be used to determine the thickness of the film. The reflectivity spectrum taken at two spots separated by about 1 cm on the MBE-film shows only a slight offset in the positions of the interference maxima, a good indication of an even film growth. The peak at (c) can be clearly identified as excitonic and not part of the interference pattern as it does not shift between the two positions on the sample. The interference pattern gradually decays between (b) and (c), representing the onset of absorption in the MBE film. The energy of strong absorption of the MBE film is thus positioned at a substantially higher energy compared to the bulk sample. It is offset by 133 meV, the distance between (b) and (c). Only above (c) the spectra recorded at the two thickness positions of the MBE film are equivalent, therefore the transmission to the substrate and back to the surface is possible up to the energy of (c).

4.3.1 Polarization studies of ZnO at an oblique incident angle of 45°

Besides measurements at ambient conditions, which for comparison were also carried out at normal incidence, all measurements of reflectivity were carried out at an incident angle of 45°. The primary reason for the choice of an oblique angle of incidence of 45° was to allow for the light-polarization dependent investigation of the reflectivity and photoconductivity response of samples with the c-axis normal to their surface (c-plane [0001] ZnO). At normal incidence, c-plane surfaces can only be investigated with the electromagnetic field of the incident light being perpendicular to the c-axis. At the geometry used here, the polarization of the light can be switched between fully perpendicular to the c-axis and with an angle of 45° to the c-axis. Although a fully parallel polarization is still beyond reach with this geometry, the 45° setup allowed us to investigate the reflectivity response to light not polarized fully perpendicular to the c-axis, for c-plane surfaces. At normal incidence, the study of the response to light polarised perpendicular or parallel to the c-axis is only possible for a-plane and m-plane cut surfaces. But the optical properties of the c-plane surfaces is particularly interesting, since ZnO is a polar semiconductor, with its polarity parallel to the c-axis. This polarity creates an inherent crystallographic difference between the two opposite c-plane surfaces, called the O-polar [000$\bar{1}$] and the Zn-polar [0001]-face (see section 1.5). The polarization dependent investigation of the optical properties of these polar surfaces only is possible for oblique angles of incidence. An additional advantage of taking reflectivity spectra at oblique incidence is an improved surface sensitivity compared to reflectivity at normal incidence [104]. The angle of 45° was also chosen because theoretical calculations show that at 45° incidence the reflectivity lineshape is not significantly changed by the exciton free surface layer [102], avoiding the so-called dead layer effect to additionally complicate the spectrum.

The measurements were carried out in a cryostat, allowing the alteration of

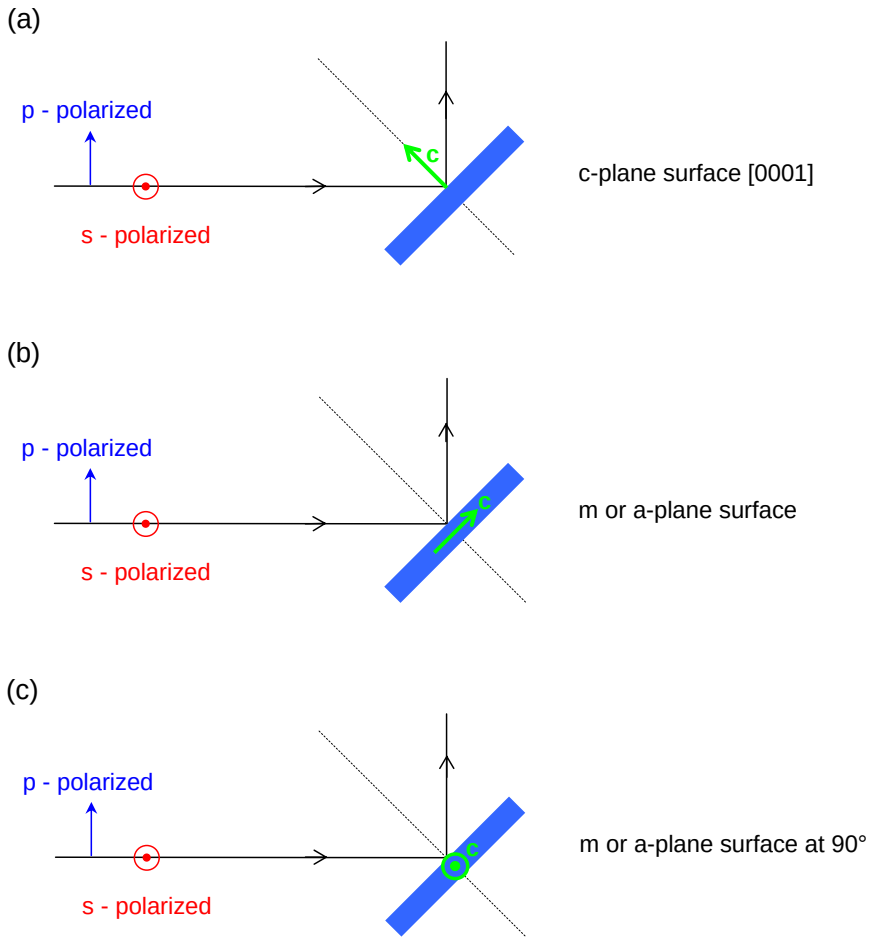

Figure 4.6: Polarization geometries at an incident angle of 45°. For c-plane samples (a), for samples with their c-axis in-plane as well as in the plane of incidence (b), and for samples with the c-axis in-plane as well as perpendicular to the plane of incidence (c)

the temperature and ambient gas conditions. The reflected beam of light was directed vertically through a window on top of the cryostat. Since the reflected beam did not have to be directed out of the same window as the incident beam, the relatively small size of the cryostat windows did not hinder the investigation of more than one sample with the same optical setup for this geometry. Shifting the cryostat along the x-axis allowed easy comparison at stable optical conditions. Figure 4.6 gives an overview of the possible polarization geometries at an oblique incident angle of 45°. The reflection of electric field amplitudes at an interface has to be treated as a combination of the reflection of light with two orientations: For light with the electric field $\boldsymbol{E}_i$ of the incident beam polarized parallel to the plane of incidence $E_\parallel$, and with the electric field $\boldsymbol{E}_i$ polarized perpendicular to the plane of incidence $E_\perp$. The plane of incidence is defined by the plane opened up by the wave vector of the incident light and the normal to the plane

interface [37]. For light that is interacting with the interface polarized differently than $E_{\parallel}$ or $E_{\perp}$, the reflected light intensity is a superposition of the reflected light of $E_{\parallel}$ and $E_{\perp}$. Here we polarize light in the direction of $E_{\parallel}$ and $E_{\perp}$ only, to keep the geometries simple, but for the case for unpolarized light, the reflected amplitudes are a superposition of the reflectivity light incident light decomposed into $E_{\parallel}$ and $E_{\perp}$ [37].

As outlined in section 1.7, the spin-orbit and crystal field splitting in ZnO results in three valence bands, two of symmetry Γ_7 and one of Γ_9. Group theoretical arguments show that the direct product of the band symmetries results in intrinsic exciton ground state symmetries for the transitions between the conduction band and a level of the valence band [17], as shown in figure 4.7.

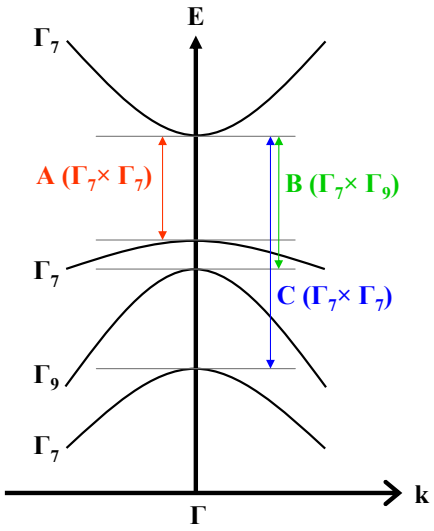

$$\Gamma_7 \times \Gamma_7 \rightarrow \Gamma_5 + \Gamma_1 + \Gamma_2 \qquad (4.20)$$

$$\Gamma_7 \times \Gamma_9 \rightarrow \Gamma_5 + \Gamma_6 \qquad (4.21)$$

Figure 4.7: Intrinsic exciton ground state symmetries [7]

According to these symmetries, each of the A- B- and C- free excitons can be observed in a longitudinal and transverse mode: Without a magnetic field, the Γ_2 transition is forbidden due to selection rules [47], and the Γ_5 transition has transverse orientation whereas the Γ_6 as well as the Γ_1 transitions have longitudinal orientation. One can picture the longitudinal free exciton as a quasiparticle that travels through the crystal lattice with its polarization vector $\boldsymbol{P}$ parallel to its wave vector $\boldsymbol{k}$, that points in its direction of propagation. The transverse exciton thus can be pictured as a quasiparticle with its polarization vector orientated perpendicular to its wave vector $\boldsymbol{k}$. The energy splitting between the longitudinal and transverse modes ω_{LT} is related to their oscillator strength [37], and makes it possible to resolve the two different modes energetically.

The symmetries of these transitions result in polarization dependent selection rules for the interaction of electromagnetic waves with free exciton polariton resonances in an ideal, strain free wurtzite crystal [7,17]: Three optical polarizations

can be used to get a distinguished response from the A, B or C free excitons in ZnO:

- In the $\boldsymbol{\sigma}$ polarization with $\boldsymbol{E} \perp \boldsymbol{c}$ and $\boldsymbol{k} \perp \boldsymbol{c}$, all three excitons are allowed, but the C-exciton is only very weakly observable.
- In the $\boldsymbol{\pi}$ polarization with $\boldsymbol{E} \parallel \boldsymbol{c}$ and $\boldsymbol{k} \perp \boldsymbol{c}$, the C-exciton is strongly allowed, whereas the A-exciton is forbidden and the B-exciton is only weakly observable.
- In the $\boldsymbol{\alpha}$ polarization with $\boldsymbol{E} \perp \boldsymbol{c}$ and $\boldsymbol{k} \parallel \boldsymbol{c}$, all three transitions can be observed clearly.

For normal incidence on a c-plane surface, only the $\boldsymbol{\alpha}$ polarization can be realized. For the case of an incident angle of 45° on a c-plane surface, as shown in figure 4.6(a), none of the $\boldsymbol{\sigma}$, $\boldsymbol{\pi}$ and $\boldsymbol{\alpha}$ polarizations can be achieved purely. But the three cases of polarization of the incident light (p-polarised, s-polarised and unpolarised) select a varying proportion of $\boldsymbol{\sigma}, \boldsymbol{\pi}$ and $\boldsymbol{\alpha}$. For all measurements taken at an incident angle of 45°, $\boldsymbol{k}$ is at an angle of 45° to $\boldsymbol{c}$, resulting in a combination of 50% $\boldsymbol{k} \perp \boldsymbol{c}$ and 50% $\boldsymbol{k} \parallel \boldsymbol{c}$. The electric field though can be switched from $\boldsymbol{E} \perp \boldsymbol{c}$ for s-polarized light to $\boldsymbol{E}$ at an angle of 45° to $\boldsymbol{c}$ for p-polarized light. This means that for p-polarized light, the C-exciton is more allowed through the $\boldsymbol{\pi}$ polarization than for s-polarized light, where $\boldsymbol{E} \perp \boldsymbol{c}$ and therefore the $\boldsymbol{\pi}$ polarization is not realized at all. Although it has to be considered that for the case of unpolarized light, the s-polarized light gets reflected much stronger than the p-polarized light [37], the portion of p-polarized light in the incident unpolarized light can cause the C-excitonic transition to show additionally to the A- and B-excitonic transitions for incident unpolarized light. Overall, for the case of unpolarized light, similar results are expected as for the s-polarized case, strongly preferring the A- and B-excitonic transitions.

As with normal incidence, when measuring at an incident angle of 45°, surfaces with the c-axis 'in-plane' can be analysed with the electric vector of the incident light being perpendicular or parallel to the c-axis. This is possible by arranging the sample in the way shown in figure 4.6(c), i.e. with the c-axis orientated horizontally. For the p-polarized incident light this results in $\boldsymbol{E} \perp \boldsymbol{c}$, for the s-polarized incident light in $\boldsymbol{E} \parallel \boldsymbol{c}$. For samples with the c-axis 'in-plane', the orientation shown in figure 4.6(c) therefore allows us to measure the, in regard to the electric field, purely $\boldsymbol{\sigma}$ and $\boldsymbol{\pi}$-polarization cases. One has to keep in mind though that there still is a difference to the polarizations available for measurements at normal incidence, since for the incident angle of 45°, $\boldsymbol{k}$ is always at an angle of 45° to $\boldsymbol{c}$.

One advantage of the oblique incidence for the case of 'in-plane' samples is, that by orientating the 'in-plane' sample with its $\boldsymbol{c}$-axis in the plane of incidence as shown in figure 4.6(b), the $\boldsymbol{\alpha}$-polarization can be partly realized by using s-polarized light. At normal incidence, the $\boldsymbol{\alpha}$-polarization can not be realized. The

other advantage of oblique incidence over normal incidence for in-plane samples is, that for p-polarized light, the geometries in figure 4.6(b) and in figure 4.6(a) are equivalent with $\boldsymbol{k}$ and $\boldsymbol{E}$ both at an angle of 45-degree to $\boldsymbol{c}$, allowing the direct comparison of 'in-plane' samples to c-plane samples. At normal incidence these two types of surfaces can not be directly compared, since there is no shared polarization geometry.

The measurement of the reflectivity of ZnO at an oblique incident angle of 45° is unconventional, most reflectivity spectra found in the literature are taken at close to normal incidence. The numerical calculation of reflectivity spectra is considerably more straightforward using the Fresnel equation for normal incidence (equation 4.6). A numerical calculation of the reflectivity spectrum at oblique angles requires the use of a more generalized Fresnel-approach and can be found e.g. in a publication by B. Harbecke, taking into consideration the thickness of the investigated sample as well as the refractive index of the backing [104]. Numerical calculations of the reflection spectra are beyond the scope of this work though, here reflectivity spectra are investigated comparatively. The direct comparison of measured reflectivity spectra to reflectivity spectra in the literature allows us to assign reflectivity features to the exciton resonances they are created by. From there, a comparison can be made between samples with different carrier concentrations, crystallographic faces, ambient conditions, etc. . Most importantly, the temperature dependent measurement of the reflectivity response allows us to track the energy of excitonic resonators across a wide temperature range. Particularly the B- and C-excitons can be distinguished up to room temperature, with the A-valence band being too close to the B-valence band to resolve the respective exciton transitions at elevated temperatures. The B- and C-excitons can easily be identified individually via the selection rules outlined above. Via the polarization dependence of the reflectivity response to the intrinsic exciton ground-state symmetries outlined above, a confusion between the close-lying C_{n1} and A_{n2}, B_{n2} levels can be avoided. The unambiguous relation of the reflectivity features to free excitonic resonances in ZnO allows us to use reflectivity measurements as a tracer of the free excitons when doing photoconductivity measurements that result in strongly phonon-related spectra, with phonon replicas and hot excitons dominating the spectrum. Since the reflectivity measurements were done at oblique incidence, a direct comparison with high spectral resolution of the reflectivity and photoconductivity response, with both spectra measured simultaneously, was possible without limitations to the optical conditions used for the photoconductive measurements (see chapter 5). This allows us to directly assign energies of photoconductive features to their energetic position in relation to excitonic resonances. Reflection spectroscopy is particularly sensitive to the longitudinal resonant frequency of the free A, B, and C-excitons, associated with a dip at slightly higher energies ($\Delta E \sim 1$ meV). Contrary to the position of the peak, the relative position of the dip in reflectivity is not influenced by resonator damping or angle of incidence [37].

Figure 4.8 shows room temperature reflectivity spectra taken at normal and

Marker in fig. 4.5	Marker in fig. 4.8	Related to	Energy
(c)	B1T	$B\omega_T(n1)$	3.310
(d)	B1L	$B\omega_L(n1)$	3.349
(e)	B2T	$B\omega_T(n2)$	3.384
(f)	B2L	$B\omega_L(n2)$	3.431
	C1T	$C\omega_T(n1)$	3.355
	C1L	$C\omega_L(n1)$	3.376
	C2T	$C\omega_T(n2)$	3.402
Onset of strong absorption:			
	c-plane	3.180	
	m-plane	3.222	

Table 4.2: Energies of peaks and dips in room temperature reflectivity of c- and m-plane bulk ZnO shown in figure 4.5 and 4.8

oblique incidence (45°) of c-plane and m-plane bulk crystals. The excitonic response of the c-plane sample does not show any change in its excitonic spectrum above 3.18 eV due to the change of the angle of incidence. This confirms that a change in the angle of incidence does not shift the energies of the features considerably. The spectrum of the m-plane sample changes considerably due to the change of angle of incidence: The ratio of the intensity of the B and C-excitonic features shifts towards a stronger C-exciton with oblique incidence of 45°. The m-plane sample was aligned horizontally, therefore with unpolarized light incident at an angle of 45°, the π-polarization was more dominant than at normal incidence, due to the stronger reflection of s-polarized over p-polarized light at that angle. Table 4.2 shows the energies of the marked spectral features.

Below energies of 3.180 eV for the c-plane crystal and 3.222 eV for the m-plane crystal, the reflectivity spectra taken at normal incidence show a strong increase in light-intensity. As shown in figure 4.1, the c-plane sample with a thickness of 460 μm does become so strongly absorbing for energies above 3.187 eV, that the detector is not able to pick up any transmitted light for energies above this threshold. For the m-plane material of comparable thickness ($\pm 15\mu$m), this threshold lies at ≈3.227 eV, offset towards higher energy by 40 meV compared to the c-plane material. Since the light reflected from the material behind the investigated ZnO crystal has to travel through the crystal twice in order to reach the photosensor, the onset of light reflected by the material behind the crystal is expected at slightly lower energies. For our samples the onset of this light reflected from the sample holder shows an onset of transmission at energies shifted by 7 meV and 5 meV to lower energies respectively when compared to the onset of the light transmitted directly. Between the samples these onsets also show a difference in energy of ≈ 40 meV. The slope of the transmission related rise in the reflectivity value is also considerably steeper for the c-plane material compared to

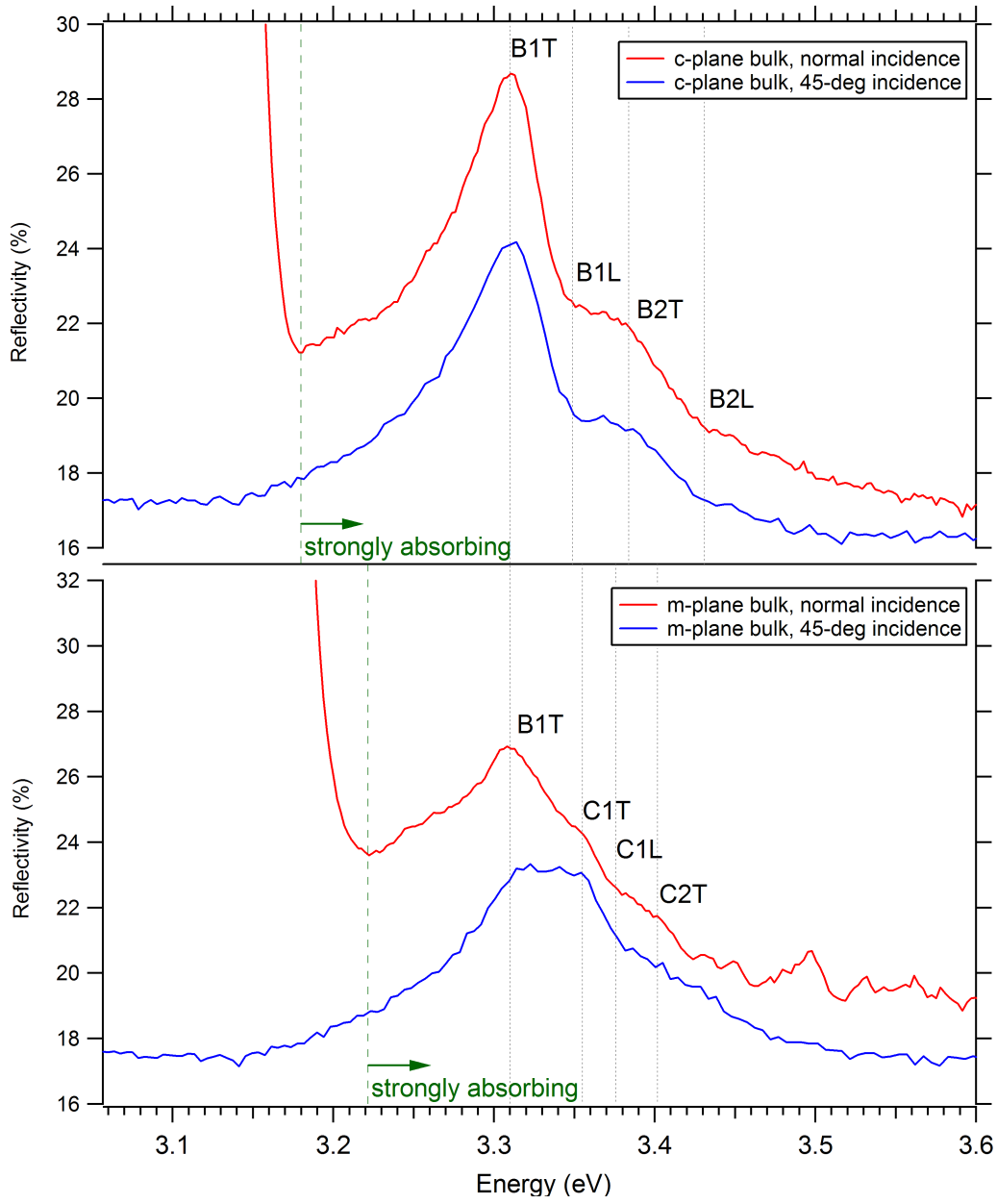

Figure 4.8: Room temperature reflectivity of c- and m-plane bulk ZnO. A comparison of spectra taken at normal incidence with spectra recorded at oblique incidence with an angle of 45°. The c-axis of the m-plane sample was horizontally aligned. For the energies of the markers, see table 4.2

the m-plane material. The reflection of the material behind the layer of interest (in this case the ZnO crystal) can accordingly be used for a rough estimation of the transmissive properties of the investigated material. Figure 4.8 shows that measurements at oblique incidence effectively allow the separation of the light reflected from the sample's front surface from light reflected from the material underneath the investigated ZnO-crystal. This was done by focusing only the surface related light spot onto the photosensor. The reflectivity curve recorded at 45° accordingly shows no rise in intensity for energies below the transmission threshold at 3.180 eV for the c-plane sample and 3.222 eV for the m-plane sample, enabling the measurement of reflectivity related to ϵ_b, which is expected to be constant for energies far below a resonance, i.e. for energies E with $|E - E_0| >> \Delta_{TL}$ [37].

4.4 Low temperature reflectivity of high quality bulk ZnO, at an incident angle of 45°

As expected, the reflection spectrum in figure 4.9 shows strong spectral features in the energy range of the free excitons. The downside of reflectivity measurements is, that energetic positions of the absolute peaks and dips in reflectivity are only roughly related to the energetic position of the transverse and longitudinal exciton resonances [37]. Line-fitting is a way to locate the absolute energies of the resonances that are responsible for the spectral feature in reflectivity with higher precision. Besides the uncertainty in the position of particularly the transverse resonance in relation to the peak in reflectivity, reflectivity is a very appealing method to investigate free excitons, since free excitonic transitions strongly dominate the reflectivity spectra.

When analyzing the spectra in figure 4.9 and the position of the excitonic energy values of recent high quality bulk ZnO as quoted in the literature [16,47,97], which are marked by vertical lines (see also table 5.1), the precision with which the spectral features of reflectivity spectra taken at 45 ° incident angle agree with the excitonic resonance energies can be estimated for low temperatures. Table 5.1 (see page 175) contains the literature values for ω_T and ω_L of the free A, B, and C-excitons in their ground and first excited states, determined with methods ranging from photoluminescence [16, 47], reflectivity [16] and photoreflectivity [97].

For the A-free exciton, our measurements strongly agree with the PL-values presented by Syrbu et al. in [16]. Spectra in figure 4.9 (a closeup of the A-excitonic region can be found in figure 5.5) show a very good agreement for the position of the energy of $A(\omega_L)$ between the literature PL-values, our PL-spectrum and the position of the dip in our reflectivity measurements. Also the spacing between the longitudinal and transverse excitons is measured to be

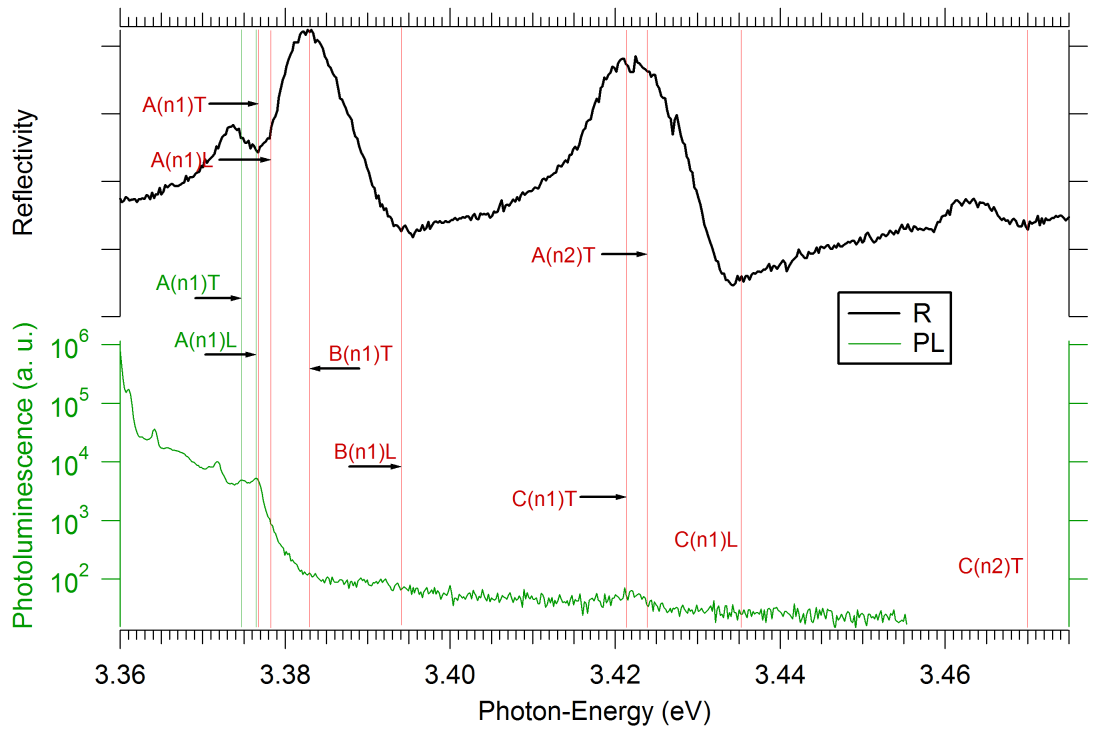

Figure 4.9: Low temperature (10K) spectra of photoluminescence and reflectivity of the a-plane surface of hydrothermally grown bulk ZnO. For orientation, the red lines show literature values for the ground (n=1) and 1st excited state (n=2) of the free A, B and C-exciton measured by photoreflectance (PR) of recent high quality bulk ZnO [97]. The green lines show literature values for the A-free exciton as attributed to peaks in photoluminescence-measurements [16]. An overview of these values can be found in table 5.1. 'L' stands for the longitudinal branch ω_L of the respective exciton, 'T' stands for its transverse branch ω_T

above 2 meV for our reflectivity measurement. The peaks that we associated with $A(\omega_T)$ and $A(\omega_L)$ in our photoluminescence measurements also show a spacing of more than 2 meV. The values obtained by photoreflectivity by Chichibu et al. [97] are shifted to higher energies, associating the energy we identify as $A(\omega_L)$ with $A(\omega_T)$, whereas the position we identify as $B(\omega_L)$ is associated with $A(\omega_L)$. Our measurements, although they are of lower resolution, do not agree with this position and the resulting small spacing of the transverse to the longitudinal resonance frequency, ω_{LT}, of just 1.5 meV. For a summary of the free excitonic transition energies, see table 5.1 (page 175).

For $B(\omega_T)$ and $B(\omega_L)$ as well as $C(\omega_T)$, the peaks and dips in our reflectivity measurements show a good match with the literature values determined by photoreflectivity by Chichibu at al. [97], that is well within the margin of error of our measurements ($< 1\ meV$). The reflectivity dip associated with $C(\omega_L)$ is shifted to lower energies by 1 meV. The match between our measurements and the values quoted is particularly interesting for the positions of the ω_T transitions and the associated positions of the absolute maxima of reflected light intensity for the reflectivity peaks, suggesting that these positions can also, besides the positions of the dips that are associated with ω_L [37], be taken as a good indication of the actual energy of the ω_T-resonance of the free excitons, at least for our measurements that were taken at an incident angle of 45 °.

Besides the ground states of the A, B, and C-free excitons, we see a further feature in the reflectivity spectrum of the a-plane material at 3.462 eV, resulting in a dip at 3.470 eV. Reflectivity measurements of Reynolds et al. [47] also detect a dip at 3.4700 eV, that they accordingly associate with $C(\omega_L^{n=2})$. Chichibu et al. also associate an energy between the energies of the $C^{n=2}$ peak and dip with the first excited state of the C-exciton, not specifying its longitudinal or transverse character.

Figure 4.9 also shows that the A-free exciton is the only excitonic resonance that can be measured rather well with photoluminescence spectroscopy. The B- and C-free excitons are at a too high energy, resulting in a lower emission probability and hence less intense PL-lines. For most PL-samples, the B-free exciton is completely drowned in the high-energy tail of the band edge emission. The spectrum in figure 4.9 for example shows only a very weak B-excitonic rise at the energy of 3.392 eV. The weak feature at 3.422 eV in the PL-spectrum might be associated with the first excited state of the A-free exciton, although its position matches with $C(\omega_T)$, as the sample is c-plane. It might also be associated with another high energy emission process.

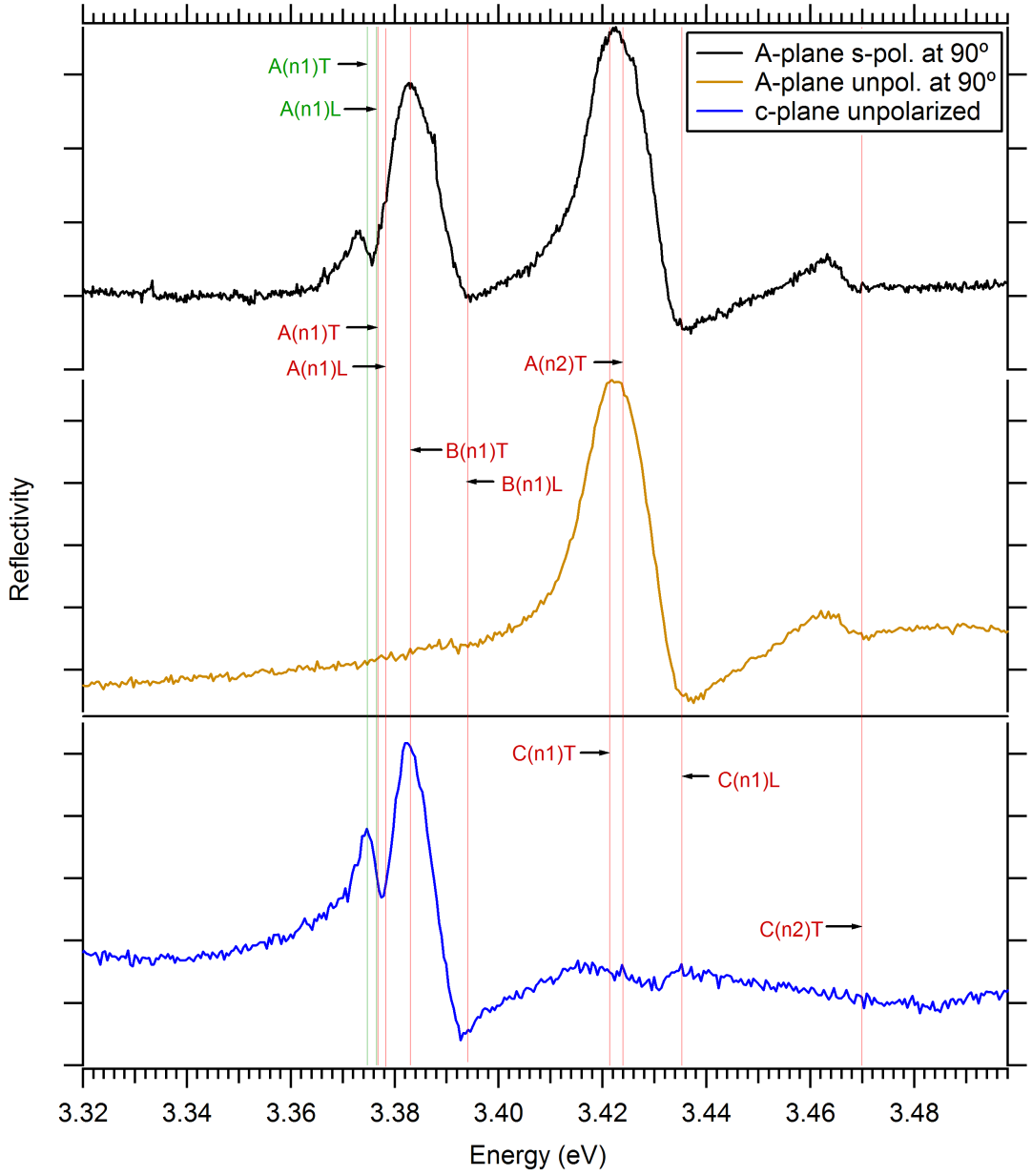

Figure 4.10: Comparison of the free excitonic reflectivity features under various polarizations, strongly illustrating the effectiveness of the selection rules introduced in section 4.3.1

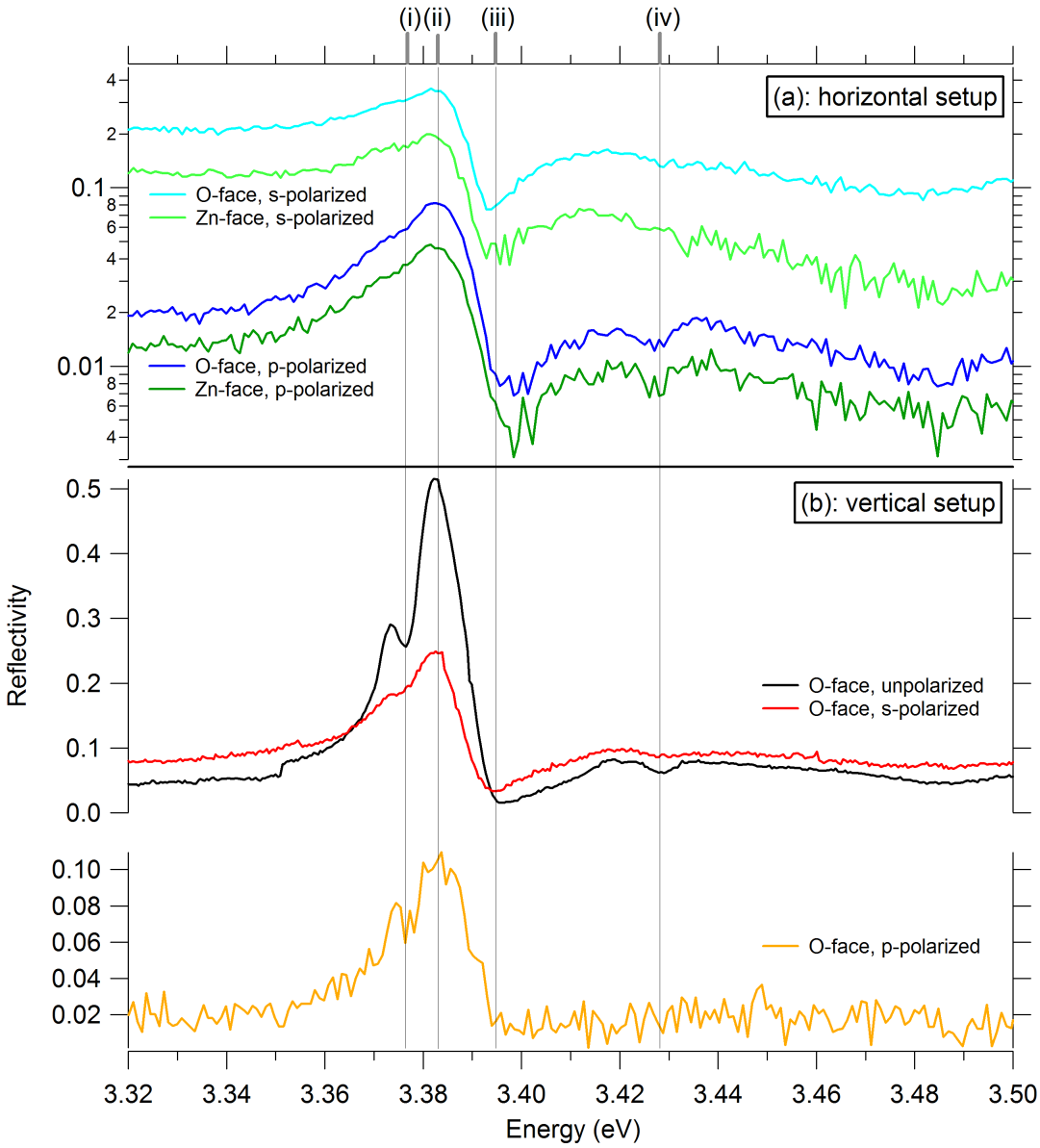

Figure 4.11: (a): Comparison of the polarization dependent reflectivity of the Zn- and O-faces of hydrothermal bulk ZnO at 10 K. The markers position is: (i) 3.377 eV, (ii) 3.383 eV, (iii) 3.394 eV, (iv) 3.428 eV. Part (b) shows the same polarization study of a different crystal of hydrothermal bulk ZnO, recorded with a different optical setup that offered better resolution. All measurements were taken at an angle of incidence of 45°

4.4.1 Face dependent reflectivity and the influence of mixed polarizations on reflectivity spectra

Figure 4.11 (a) shows face and polarisation dependent low temperature (10 K) reflectivity spectra of hydrothermal bulk ZnO. The spectra of the Zinc(Zn)- and oxygen(O)-faces of c-plane bulk ZnO were compared by cutting a c-plane crystal into two pieces, which were mounted next to each other in the cryostat, one with the O-face facing upwards and the other with the Zn-face facing upwards. This allowed a direct comparison of both faces with an emphasis on comparable conditions between scans.

The only remarkable difference that was evident between the O- and the Zn-face is a difference in their absolute reflectivity: Across the entire spectrum, the reflectivity of the O-face was more than 1.5 times stronger than that of the Zn-face for s-polarized and p-polarized incident light.

The difference in the overall reflectivity of the two polar faces is an indication of the face dependent influence of adsorbed gases on the electronic surface structure, resulting in band bending at the surface: The reduction of the reflectivity can be explained by high electric fields at the surface [119], and the high electric fields are interlinked with the band bending [114]. The difference between the two faces stems from a different susceptibility of the Zinc and oxygen faces to gases such as oxygen and hydrogen: A study by Hoffmann has shown that atomic hydrogen causes a reduced reflectivity only of the O-face, whereas the reflectivity of the Zn-face stays unchanged after exposure to hydrogen. Subsequent exposure to oxygen causes the reflectivity of both faces to rise [120]. This difference in the reflectivity response to the exposure with adsorbing gases is expected to play a role in differences we see for the reflective behaviour of the two faces. But we can not make a direct comparison to these controlled studies, as the exposure of our crystals to gases was not controlled. They certainly were exposed to atmospheric gases for an extended period of time though, as they were stocked in ambient conditions.

It is important to note that, besides the difference in intensity of reflectivity, the different faces do not exhibit a detectable change of the position of any reflectivity features nor the appearance of faint features in any of our reflectivity measurements (see e.g. figure 4.11). The face dependent change in reflectivity of similarly 'contaminated' surfaces to the ambient atmosphere was investigated at room temperature, by evacuating the cryostat and subsequently filling it with pure hydrogen, oxygen and nitrogen, as well as air. Reflectivity scans of the Zn- and O-face were recorded at each stage of the experiment, revealing no detectable changes in the recorded spectra. This shows that the faces are well covered with adsorbed ambient gases, shielding the surfaces from any further interaction with the atmosphere that could change the state of band-bending the samples were in. It is expected that there would be strong changes in reflectivity if we would have cleaned the sample surfaces of their ambient gases, by e.g. heating them to above

350 °C in vacuum [120]. This was beyond the capabilities of our experimental setup.

For both polarizations, the spectra recorded on the Zn-face show more noise due to the lower intensity of the reflected light, but there is a remarkable alignment of all features for both polarization geometries, as presented in figure 4.11. This is another sign that reflectivity is very selective in its response, with the variation of reflectivity across the spectrum being exclusively due to the resonances of ground and excited states of free excitons.

As outlined on page 98, due to a different proportion of the π-polarization, the C-exciton is more allowed for p-polarized light than it is for s-polarized light in the 45 ° geometry used here. The C-exciton related feature at 3.428 eV (*iv*), which is clearly evident for scans taken with p-polarized light in figure 4.11 (a) and unpolarized light in figure 4.11 (b), is only very faint for the spectra taken with s-polarized light. Since the dip at (*iv*) lines up very well with the literature value for the C-excitonic reflectivity feature, which lies in this region with a peak at 3.4219 eV and a dip at 3.4338 eV [16], this can be taken as a sign that the C-exciton is indeed observable of c-plane surfaces with the 45 ° geometry used here.

The scans in figure 4.11 were taken in an early stage of the experimental work of this thesis. The small shifts between the different reflectivity spectra could be related to calibration issues. Later scans were taken with an improved optical setup, i.e. with the use of a baffle at the exit slit of the spectrometer as well as a more reliable calibration procedure, as described in section 2.5.4. All the scans that were used to determine the exact position of spectral features were taken with the improved setup. This reduced the uncertainty from several meV to below 1 meV.

4.5 The temperature dependence of the free B- and C-excitons in ZnO

In section 4.4 we demonstrated that the spectral position of the peak and dip in the low temperature reflectivity spectra can be associated with the energy of the free excitonic ω_T and ω_L resonance of the *A*-, *B*- and *C*-free excitons, respectively. Here we want to investigate the influence of temperature related effects on the free excitonic resonances in ZnO, as the investigation of the temperature dependence of the band-gap as well as the broadening of the excitonic energy levels is of great relevance for ZnO as a material for room temperature optical applications [23]. Are temperature dependent reflectivity measurements a suitable method to get a direct estimate of the temperature related effects on excitons? Reflectivity is an interesting tool for the investigation of excitons, as they are the only resonance in ZnO that cause strong reflectivity features. This 'filtering' of the free excitonic

transitions avoids the overlap with other transitions at higher temperatures.

The band gap of semiconductors typically shifts to lower energies with rising temperature due to two dominating processes: the thermal expansion of the lattice as well as electron phonon interactions [37]. It has been shown though that existing models for the temperature dependence of semiconductor band gaps do not show satisfying results, particularly for wide band gap materials with $E_G(0\ K) > 2.5$ eV [87]. The result is a large scatter in the quoted empirical parameter values of the temperature dependence of the fundamental energy gap $E_G(T)$. One way to improve the accuracy of the obtained semiconductor parameters would be to measure at temperatures closer to the Debye temperature. This is difficult since it is far above room temperature for GaN and ZnO. But it also has been found that particularly a lack of precision of most data sets between 200 and 300 K is responsible for the large spread of quoted temperature dependent band gap properties [87]. This region close to room temperature is particularly important since the $E_G(T)$ dependence at these temperatures deviates significantly from the quadratic low temperature asymptotic behaviour [87]. The lack of reliable data points for the temperature region from 160 to 300 K is due to the fact that free excitons can not be resolved in photoluminescence (or transmission) above temperatures of 160 K [16, 121], due to the phonon-broadening related overlap of the excitonic emission with other photo-emitting transitions and their phonon-replica [7]. At heart of the unknown behaviour of the band gap with rising temperatures is the phonon dispersion coefficient, that has to be considered and well-known, to understand the temperature dependent effect of phonons on the band structure [87]

Due to the high exciton binding energy in ZnO, the free excitons are expected to keep a nearly constant energy-distance to the band gap and therefore shift in energy according to the shift of the band gap [22]. But besides following the shift of the band gap, the excitons are susceptible to the higher density of phonons at elevated temperatures themselves: The interaction of electrons with lattice vibrations has been theoretically described by Froehlich [20] and is one of the dominating processes leading to the shift of the band gap. But the Froehlich interaction has also been the basis of theoretical models that have been developed to describe the influence of lattice vibrations on excitons [88]: It has been found that the interaction of excitons with LO-phonons is the main cause for temperature related broadening effects. Besides this type of broadening , excitons also interact with acoustic phonons by coupling to the acoustical phonon related deformation potential [88]. Piezoelectric coupling is found to be less of an influence for most III-V and II-VI materials, although ZnO, which has strong piezoelectric properties, has not been considered in this study [88]. These theoretical considerations have been carried out in an attempt to create a meaningful understanding of temperature related broadening of exciton line widths in semiconductors as they were detected in transmission experiments.

It also has to be considered, that in ZnO the high exciton binding energy of

60 meV, which is making ZnO particularly interesting for the operation of excitonic processes at elevated processes, is confronted by an even higher energy of 72 meV for a single phonon in the ZnO lattice. This means that single phonons do carry sufficient energy to break up an exciton, potentially leading to strong phonon-related processes of excitons at elevated temperatures. This is an interesting aspect for exciton research, as most ZnO devices will be operated at room- or higher temperatures [23].

In PL only the A-free exciton is detectable at elevated temperatures [17]. But phonon related broadening of the free exciton transitions leads to a significant shift of the peak position of the PL-emission of the free A-exciton at temperatures above 160 Kelvin: the PL-emission of the A-free exciton becomes broad enough that it merges with its equally phonon-broadened phonon replica peaks, forming a single broad PL-emission peak across the whole UV-emission spectrum. At room temperature the resulting shift between the only remaining peak of the PL-spectrum at $\sim$3.28 eV to the expected energy of the A-free exciton is 30 meV (see figure 3.10): the band gap of strain-free ZnO is expected to be at 3.37 eV at room temperature [7], with a binding energy of 60 meV, the free exciton transition is therefore expected at 3.31 eV.

To the authors knowledge, there are also no published photoluminescence measurements of the C-free excitonic transitions, even of high quality bulk ZnO. This might be due to the prevalence of c-plane samples for the investigation of high quality bulk crystals [14,15,17,22]. It is expected though that the C-exciton is particularly hard to observe in PL [47]. Reflectivity related methods are responding very strongly to the C-exciton. Recently, for example, the effects of the isotopic mass on the A-, B- and C-excitonic band gaps in ZnO have been investigated with low-temperature wavelength modulated reflectivity measurements [122].

The study of the temperature dependent evolution of free excitons in ZnO is also important to get a better consensus about the origin of the numerous fine structured features in low temperature photoluminescence, particularly in high quality bulk ZnO, as they were observed in Figure 3.8 [7, 17]. Several studies have recently been published, investigating the temperature dependent evolution of the free excitons in ZnO by photoluminescence spectroscopy. This includes PL-studies of high quality bulk ZnO [17,23,61,123,124], ZnO thin films [125], as well as nanocrystalline ZnO thin films [124].

One way to get a direct relation between the absolute energy of exciton levels and the observed reflectivity response spectrum, is to record it with a modulation technique, as done by Tsoi et al. [122]. Here we want to use the more simple method of plain reflectivity spectroscopy, to see if the relative change of position of features in the reflectivity spectra is directly related to the effect that elevated temperatures have on the excitonic resonances. For more precise absolute values of the material parameters, the reflectivity spectra have to be modelled theoret-

ically. By achieving an optimum fit of the theoretically calculated spectra with the measured spectra, the values of the parameters of the model can be established. This procedure goes beyond the scope of this work though, since the fitting has to be done using a number of parameters, some of which themselves are temperature dependent [16]: For example the temperature dependence of the dielectric function for ZnO is not available in the literature [24]. The lack of a direct relation between the position of the reflectivity feature and the exciton resonance applies in particular to the ω_T resonance and its position relative to the reflectivity peak [37]. For the 45 ° geometry used here though, the positions of both the ω_T and ω_L resonance as observed by other groups [16] match with the position of the reflectivity dip and, surprisingly, also with the reflectivity peak. The deviation between peak and dip position and the literature values are well within the uncertainty of our measurements, as shown in section 4.4, which are limited by the resulting line-width from the applied spectrometer slit width, as well as calibration and signal-to-noise considerations.

Temperature dependent reflectivity studies of ZnO that are available in the literature have been used to investigate the temperature dependence of higher-order excitons up to 80 K [99] as well as to measure the temperature dependent refractive index of "low quality ZnO thin films" [24]. Temperature dependent reflectivity studies up to room temperature on epitaxial ZnO films have been proven difficult due to the limited response of the excitons at elevated temperatures, combined with the dominance of interference effects in relation to the excitonic spectral features [126]: It seems that the peaks and dips from the interference pattern of thin films, as it can typically be observed up to energies just below the excitonic transitions (see figure 4.5), have mistakenly been interpreted as excitonic features. It is interesting though, that there is a temperature dependence in peak position of the interference features, which we also observe for thin films (see figure 4.22). It is suggested to be due to a band gap related temperature dependent change of the refractive index close to the band gap.

The free excitons associated with all three valence bands, including some of their excited states, can be resolved sharply in low temperature reflectivity spectra (see figures 4.9). With the help of the selection rules, the first excited states of the A and B-free excitons can be distinguished from the very close-lying ground state of the *C*-exciton, as illustrated in figure 4.10. This allows us to distinguish the ground state and first excited state of the C-free exciton from the excited states of the A- and B-free excitons. The energetic proximity of the A-free exciton to the B-free exciton makes it hard to resolve it above temperatures of 120 Kelvin, but the B and C-free excitons can be resolved quite clearly up to 210 Kelvin and higher. Therefore reflectivity spectroscopy is a great tool to investigate the temperature dependence of the energy of the B- and C-free exciton resonances.

The reflectivity spectra of unpolarized light of a-plane bulk ZnO, recorded at sample temperatures ranging from 10 Kelvin to room temperature are shown

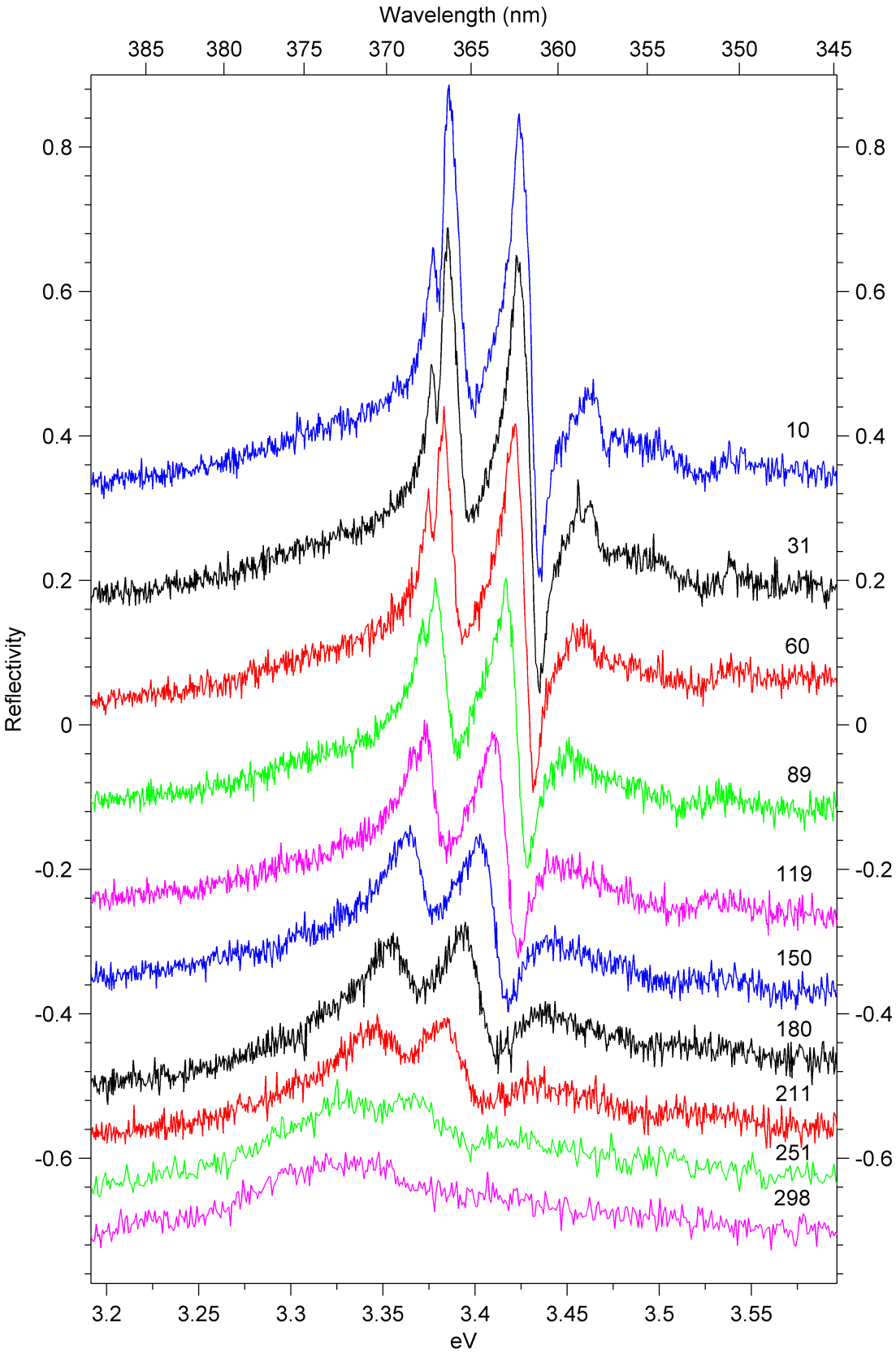

Figure 4.12: Reflectivity spectra of a-plane bulk ZnO, recorded at temperatures ranging from 10 Kelvin to room temperature, using unpolarized incident light. To avoid the spectra to overlap, the spectra at temperatures above 10 K are plotted with individual constant negative offsets. The absolute values of the reflectivity scale on the y-axis therefore is only valid for the spectrum at 10 Kelvin

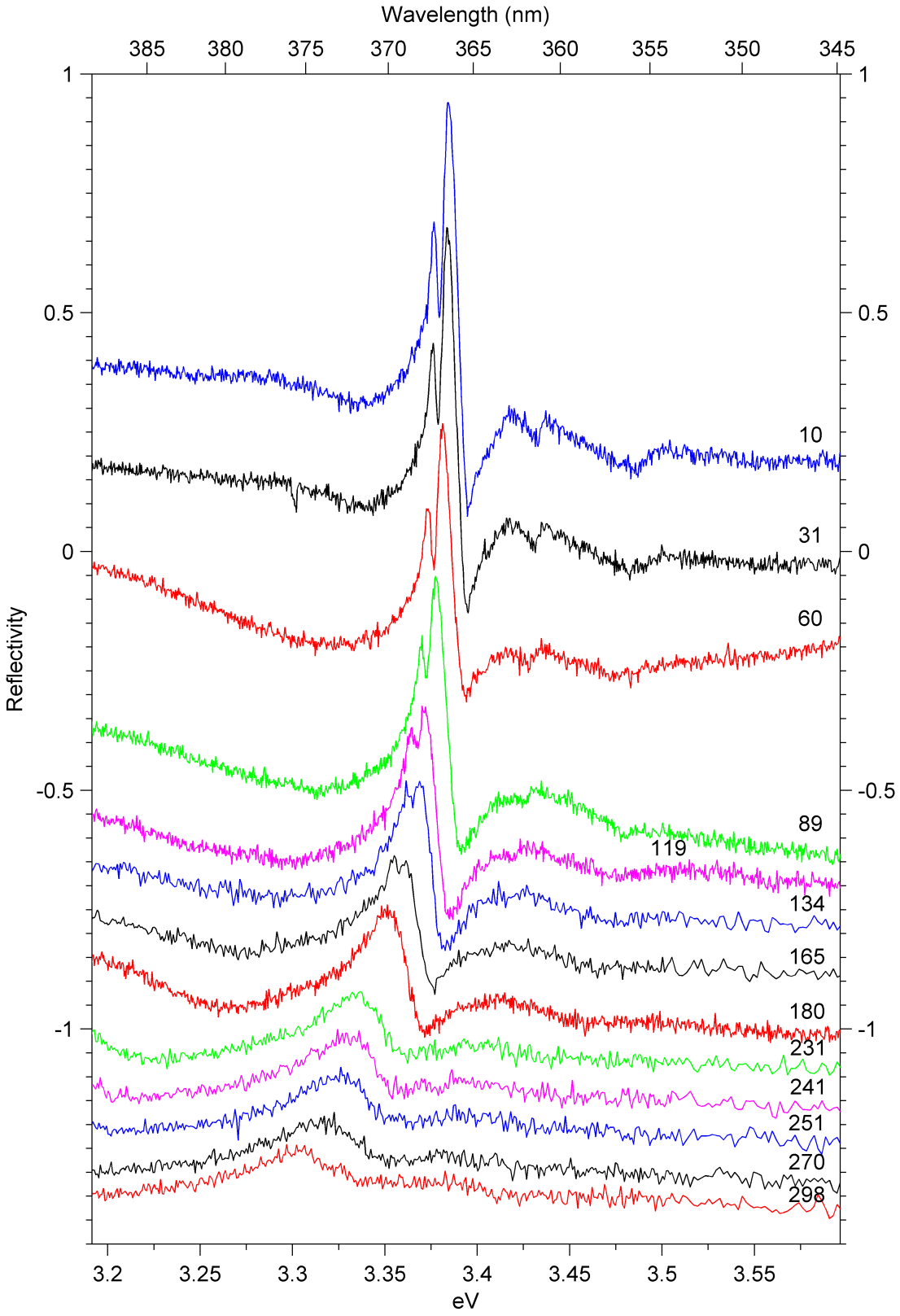

Figure 4.13: Reflectivity spectra of c-plane (O-face) bulk ZnO, recorded at temperatures ranging from 10 Kelvin to room temperature, using unpolarized incident light. To avoid the spectra to overlap, the spectra at temperatures above 10 K are plotted with individual constant negative offsets. The absolute values of the reflectivity scale on the y-axis therefore is only valid for the spectrum at 10 Kelvin

in figure 4.12. In comparison, figure 4.12 shows the temperature dependent reflectivity response of unpolarized light for c-plane bulk ZnO.

4.5.1 Fitting of temperature dependence of features in reflectivity

The selection rules offer the possibility to investigate the isolated C-free exciton in temperature dependent reflectivity. Thus we investigated a sample with its c-axis inplane. In the 45° geometry used here, the sample was mounted with its c-axis aligned horizontally. This allowed us to use s-polarized light. Since, as described by the Fresnel-formula, s-polarized light is reflected about 5 times stronger than p-polarized light at an incident angle of 45° [37], the possibility to use s-polarized light gives us a much better response and therefore allows us to measure with about half the slit-width, i.e. about half the FWHM at equal Signal to noise-level as with p-polarized light. The measured temperature dependent positions of the ω_T-related peak and ω_L-related dip of the C-free exciton are plotted in figure 4.14. The measured values for the peak and the dip of the C-free exciton of the a-plane of a melt-growth grown Cermet bulk ZnO crystal are marked as 'C(dip)' and 'C(peak)'. As expressed by error bars, these two positions could only be determined in the spectra with a certain degree of uncertainty, see section 4.5.2 below. The temperature dependent variation of the position of the peak and dip has been fitted with the modified 'Manoogian and Woolley' model [22], see equation 3.20, marked as 'fit' in figure 4.14. The fit was weighted with the absolute values of the uncertainty of each point.

As evident from figure 4.14, the fit to the reflectivity peak yields a result that is much more comparable to the temperature dependence of the band gap as deduced from photoluminescence by Hamby et al. [22]. Assuming that the temperature dependence of the bandstructure as presented by Hamby is right, this might give a clue about the effect of phonon-broadening on the reflectivity features. Assuming also that the spacing between ω_T and ω_L stays constant with temperature, this suggests that the phonon related broadening of the reflectivity features is centred at the reflectivity peak rather then reflectivity dip, causing the reflectivity dip to be pushed to higher energies by the phonon-interaction.

The phonon-relation of the difference between the fit of Hamby and the fit to the reflectivity-dip is underlined by figure 4.15. It shows a good match between the broadening of the zero-phonon line in PL, as described by Hauschild [23], to the change in spacing between Peak and Dip in the reflectivity spectra of the isolated C-free exciton.

Figure 4.16 shows fits to the temperature dependent change of the position of the *B*-excitonic reflectivity features. A similar scenario can be observed here, with the phonon broadening pushing the position of the reflectivity dip to higher energies, whereas the reflectivity peak follows the temperature dependence as

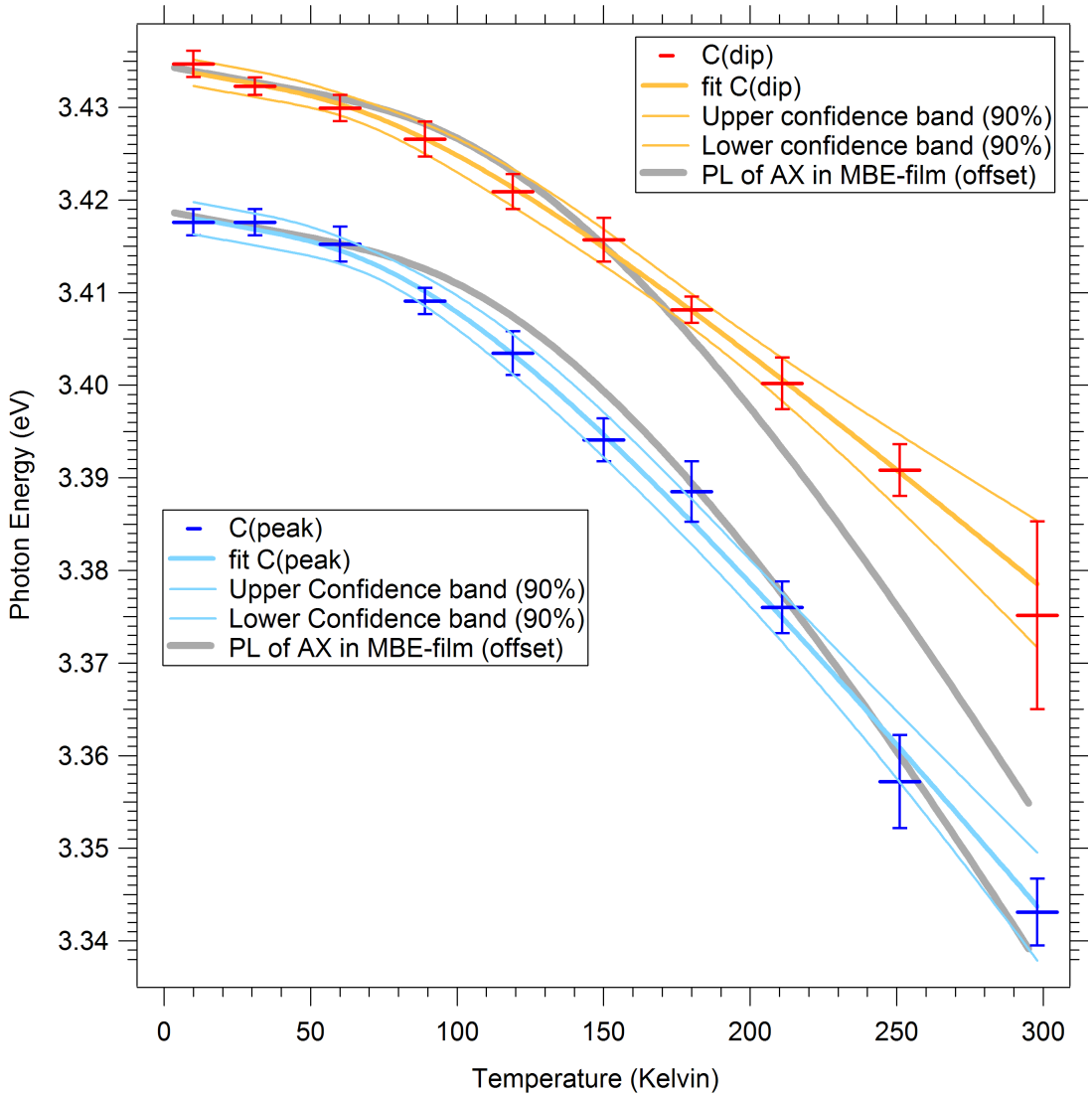

Figure 4.14: Manoogian [22] fitting to temperature dependence of peak and dip position in the reflectivity spectra of the isolated C-free exciton

derived from photoluminescence. In fact, the upper confidence band of our fit matches the temperature dependence described by Hamby astonishingly well, with a maximum deviation of 1.1 meV across the entire temperature range. Note that Hamby et al. did not have any PL-data points above 160 K, but used the expected room temperature band-gap energy to extend the fit beyond 160 K. The fact that the upper confidence band matches with Hamby's fit indicates that the B-excitonic peak position might be pulled to slightly lower energies by the close-lying A-excitonic resonance.

Figure 4.17 rounds up the temperature dependent behaviour of the free-excitonic peaks and dips that can be measured at 45 ° incidence by reflectivity. The phonon-broadening of the reflectivity feature results in a shift of the dip to higher energies for the B- and C-excitonic features. Note that the C-free excitonic

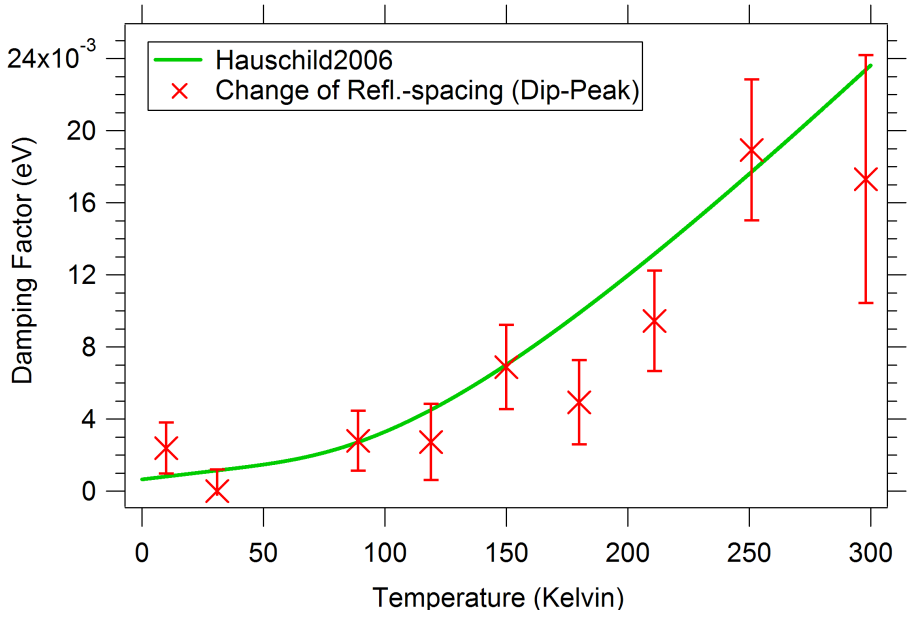

Figure 4.15: Temperature dependent change of the spacing between the reflectivity peak and dip in comparison to the temperature dependent exciton phonon-interaction related broadening of the zero-phonon line in PL as described by Hauschild [23].

peak should not be measured with unpolarized light, as it convolves with the B-excitonic dip at temperatures above 250 Kelvin. Due to the resulting necessity of using a polarization filter to measure the C-excitonic feature, the confidence intervals for the fits to the s-polarized scans are significantly larger than for the unpolarized scan of the B-free exciton, as the polarization filter reduces the intensity of the incident light considerably and thus reduces the signal-to-noise ratio of the measurement. Since the peak is the feature in the reflectivity spectrum that is not influenced in its energy-position by phonon broadening, it is the feature of choice for the investigation of the temperature dependent shift of the free exciton levels by reflectivity. The comparison of the B-excitonic peak-fit with the literature values (offset) suggests that the close lying A-exciton plays a role in shifting the B-excitonic peak to lower energies towards higher temperatures. It is expected that for higher temperatures, the convolution of the temperature broadened A- and B-excitonic features results in a broadening of the single resulting peak that leads to its apparent shift to lower energies due to the influence of the A-free exciton. This is suggested by a compelling overlap between the upper confidence band of the $B\omega_T$-excitonic fit with literature values.

As a conclusion, the B-excitonic peak in reflectivity is the feature of choice to investigate the temperature dependent shift of the band gap in, e.g. ZnO films with large lattice strains. The convolution with the close-lying A-free exciton results in an additional apparent shift to lower energies with rising temperatures. This maybe can be accounted for by analyzing the phonon-related broadening

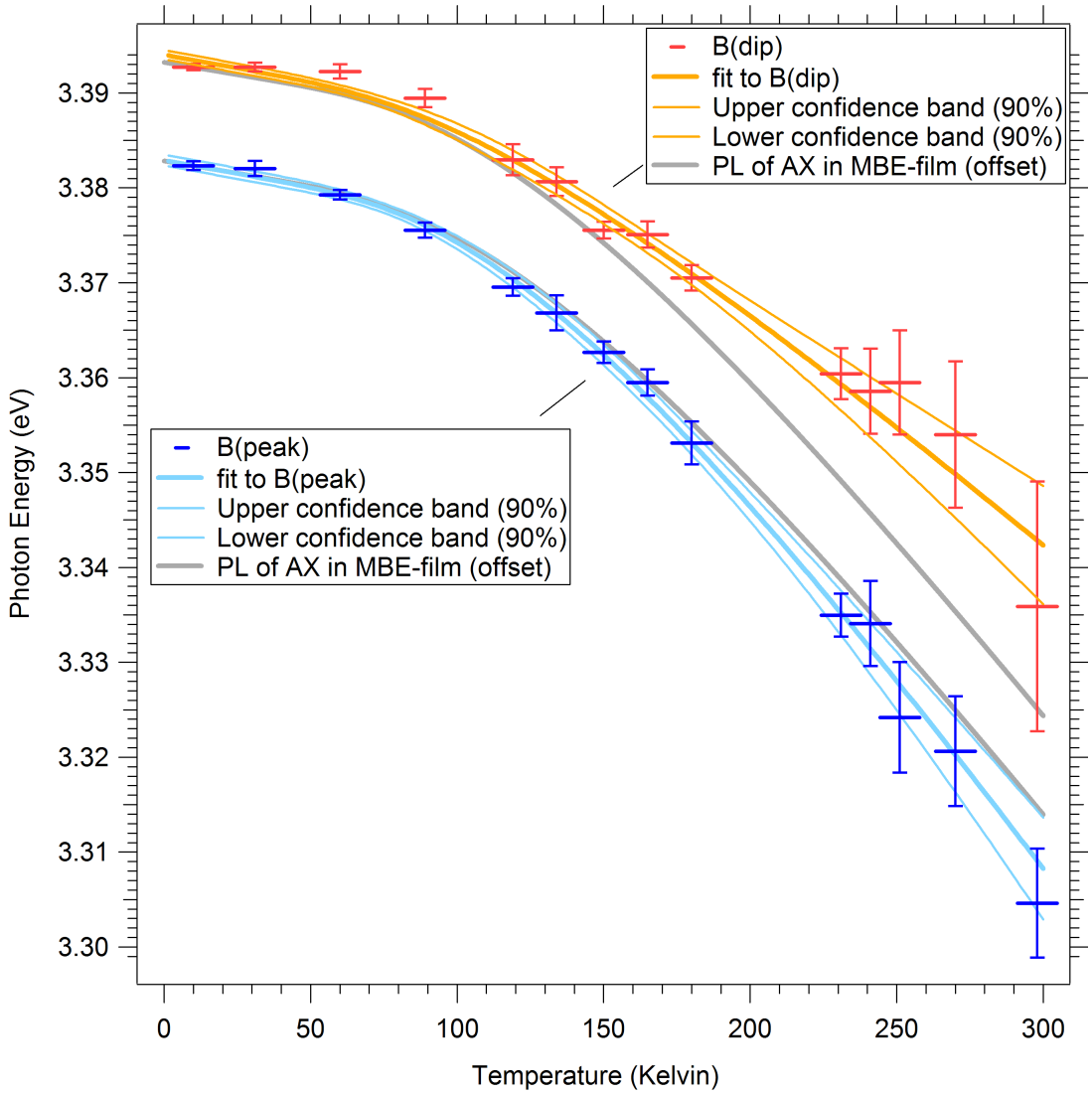

Figure 4.16: Manoogian [22] fitting to temperature dependence of peak and dip position in the reflectivity spectra of the B-excitonic peak and dip

of the excitonic reflectivity peaks and accounting for the additional apparent broadening caused by the overlap with the A-free exciton.

The fitting parameters for the fits presented here are summarized in table 4.3.

4.5.2 Uncertainty in determining the position of reflectivity features

The uncertainty in determining the position of the excitonic reflectivity features is expressed by the error bars e.g. in figure 4.14. The temperature dependent uncertainty in determining the energy position of the features related to the ground

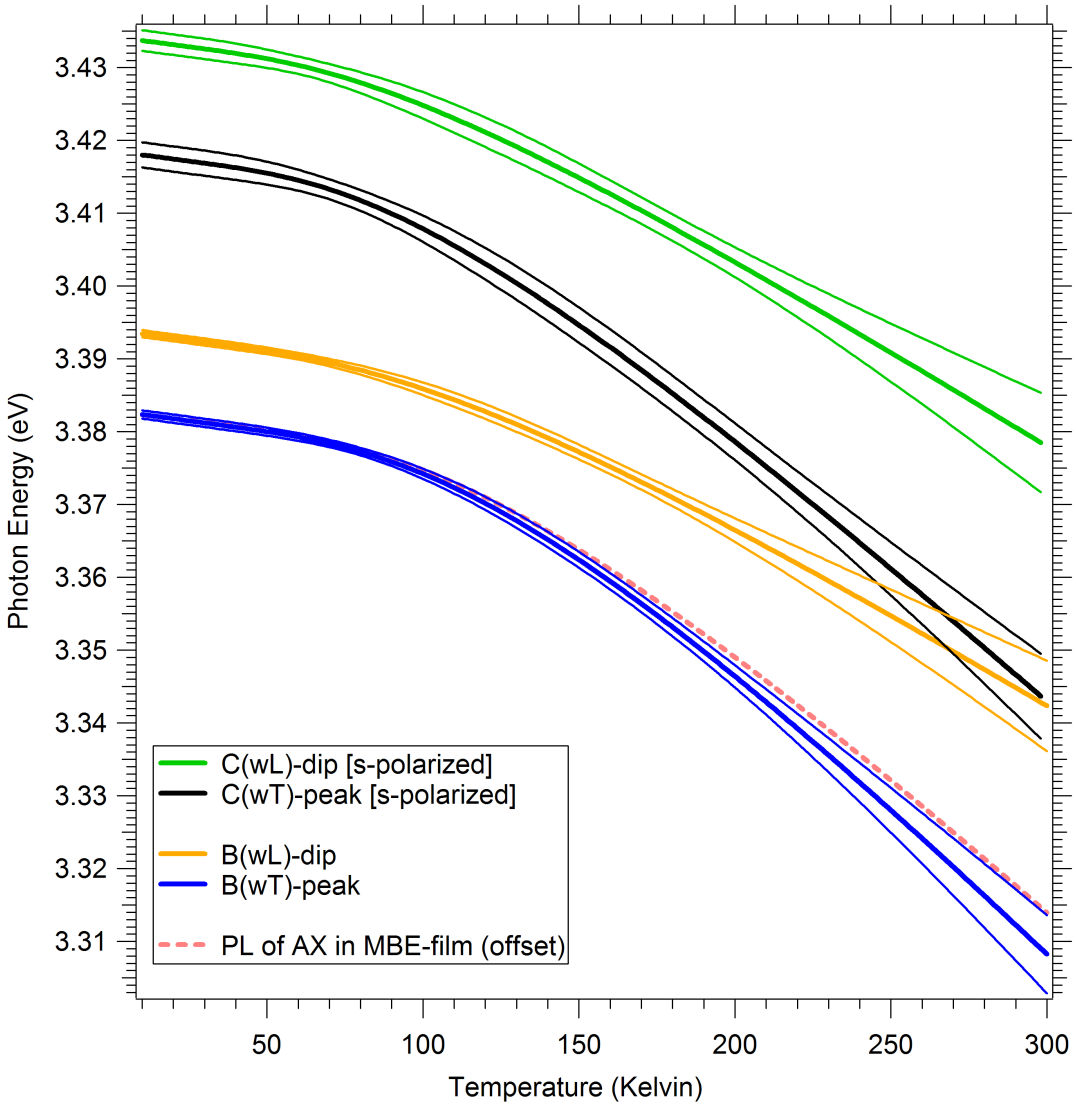

Figure 4.17: Comparison of the fits to temperature dependent reflectivity-peaks and dips of B- and C-free excitons

Table 4.3: Fitting parameters of modified Manoogian fitting procedure [85], see equation 3.20, for the isolated C-free excitonic reflection feature CX of hydrothermally grown bulk ZnO

	B **Peak (c-plane)**		B **Dip (c-plane)**	
Parameter	Value	Uncert. (±)	Value	Uncert. (±)
E_0 $[eV]$	3.3829	0.57×10^{-3}	3.394	0.48×10^{-3}
Θ [K]	402.62	57.8	348.62	97.7
α [eV/K]	-4.01×10^{-4}	0.78×10^{-4}	-2.16×10^{-4}	0.77×10^{-4}
	C **Peak**		C **Dip**	
Parameter	Value	Uncert. (±)	Value	Uncert. (±)
E_0 $[eV]$	3.419	1.8×10^{-3}	3.4343	1.41×10^{-3}
Θ [K]	310.19	94.6	288.41	136
α [eV/K]	-3.40×10^{-4}	0.83×10^{-4}	-2.17×10^{-4}	0.88×10^{-4}

* Values set according to Hamby et al. [22]

and first excited states of Cω_T is plotted in figure 4.18. At room temperature, the C_{n1} peak can be located much more precisely than the dip, with an uncertainty of about 7.5 meV vs 31 meV. For temperatures of 250 K and less, the scenario is similar for both features. It is remarkable that even the position of the peak associated with the first excited state of the C-free exciton can be determined with an error of less than 10 meV for temperatures of up to 180 Kelvin. At higher temperatures it smears out that much that it becomes hard to locate it.

The following protocol was used to take uncertainties of assignment into account: The peak and dip of an excitonic resonance was always read out as the absolute maximum and minimum of the reflectivity spectrum in the region of the resonance investigated, respectively. The error bars of energies of the peak and dip-positions then are deduced from the spectra by estimating the highest and lowest energy within the spectrum where the peak (or the dip) of the resonance in reflection could possibly be positioned within the noise. The error bars were verified by taking several consecutive scans and making sure that the possible peak and dip-positions would lie within the margin of error for all the scans. Additionally, the error bars have to take into account the step size used as well as the uncertainties arising from calibration. The calibration uncertainty though is considerably smaller than the uncertainty arising from the noise in the spectrum. Especially for temperatures above 200 Kelvin it can be difficult to clearly identify the position of the phonon-broadened excitonic peaks and particularly dips. Higher temperatures thus have a bad effect on the identifiability of close lying resonances as well as resonances from the first excited (n=2) or higher states of excitons.

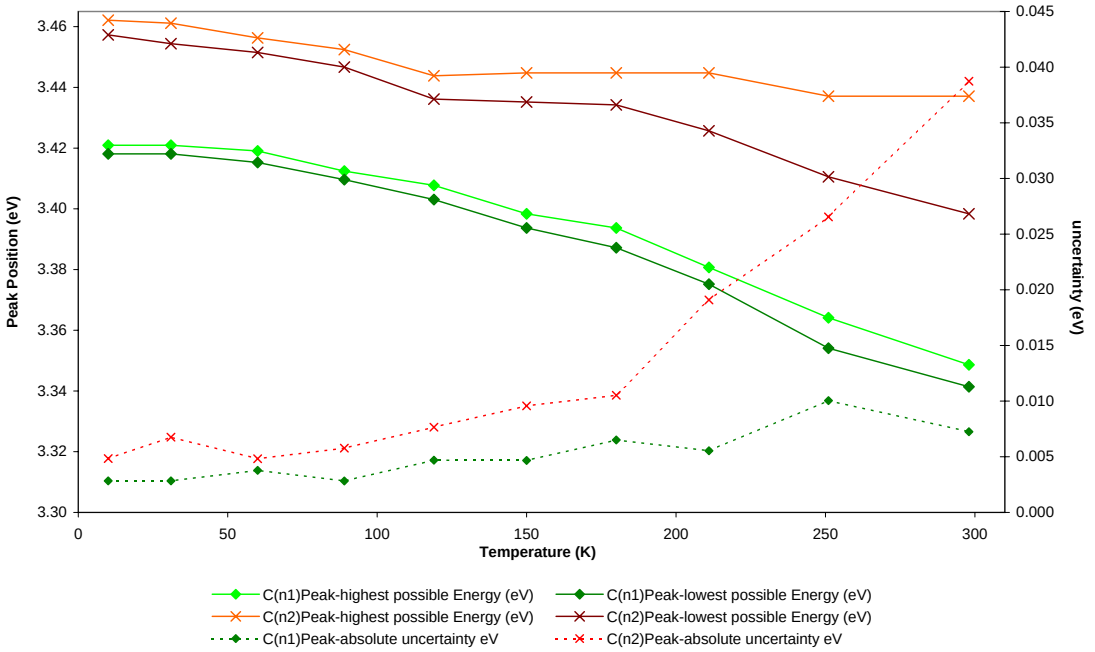

Figure 4.18: Uncertainty in reading the peak position of the peaks related to the C(n1)-free exciton [red lines] and the C(n2)-free exciton [green lines] for the s-polarized reflection scans taken of the a-plane surface of Cermet bulk ZnO crystals

It is important to note that, since the lock-in technique was used, the noise in the reflectivity spectra is not an indication that the measurements are taken at the sensitivity limit of the photo diode (see section 2.5.5). The Lock-in technique much rather allows us to resolve changes in the voltage output of the photo diode that otherwise could not be resolved. To minimize the noise, a higher time constant would be necessary, which in this case would extend the measurement time beyond feasibility. Nevertheless, care has to be taken not to run into the sensitivity limit of the detector, as this would result in an apparent shift of the reflectivity features especially for the dips in reflectivity.

The use of a photon counter is expected to greatly improve results, as the slit-widths of the spectrometer could be reduced significantly with improved sensitivity of the light-sensor, also making measurements using polarization filters much more applicable.

4.5.3 Reflectivity study of PLD-grown films of ZnO

Samples grown by eclipse and standard pulsed laser deposition (sample 'PLD-2' and sample 'PLD-1', respectively) are compared by spectral reflectivity. Eclipse pulsed laser deposition is the name for a pulsed laser deposition process involving

the use of a shadow mask that is placed between the target and the substrate, blocking the large unwanted particulates that are characteristic of the pulsed laser deposition process [51]. The PLD-samples investigated here were grown in our department by R. Mendelsberg. A more detailed description of the general growth procedure can be found elsewhere [51, 127]. The samples consist of an Al_2O_3-substrate with a 60 nm Pt buffer layer. Platinum was used as a buffer layer, since it combines several major advantages over growing straight onto sapphire. Especially as a step towards device structures, platinum is a good material to be used as a backing contact for devices made out of ZnO films. Since Platinum growths on sapphire in the [111] direction, it only has a lattice mismatch of 2% to the lattice of c-plane ZnO. This is much better than the lattice mismatch of 16% between sapphire and c-plane ZnO. Therefore the use of a Platinum buffer layer offers the potential for strongly reduced stress, resulting in less defect creation at the interface of ZnO and its substrate. Defects and stress in the first deposited layers influence the epitaxial growth of the layers grown on top, therefore progressively influencing the quality and morphology of the whole ZnO sample grown. ZnO grown directly onto sapphire with similar growth conditions results in the growth of nanostructures [51].

A shadow mask was used for the growth of sample 'PLD-2'. Its growth therefore is only due to particles that are small enough to be scattered by the gas particles in the HV-chamber. Since the growth is done at an oxygen partial pressure of 8.2×10^{-5} Torr, this might enhance oxidization during the deposition process. Since no shadow mask was used for sample PLD-1, it was grown at a considerably higher growth rate than sample PLD-2. PLD-1 has a resulting thickness of about 600 nm, PLD-2 of about 300 nm. The SEM-images of figure 4.20 and 4.19 show a strong influence of the shadow mask on the surface morphology of the PLD-grown films.

Figure 4.21 relates the low temperature reflectivity of c-plane bulk ZnO to the reflectivity spectra of the two films. For energies below the band gap, the PLD-grown ZnO films are transparent, allowing light to be reflected by the ZnO/Pt-interface. The regular peaks below 3.346 eV are therefore an interference pattern with an energy spacing between the constructive interference-related peaks that is determined by the sample thickness, angle of irradiation and index of refraction for ZnO $\mathrm{Re}(n^*(\omega))$. The thin film interference in the PLD-samples is very strong. The strong damping of the thin film interference at energies just below the A-free exciton energy can only be explained by a strong onset of absorption in that region. Such strong and rapid onset of absorption is a good indication of a high crystal quality of the ZnO layer. The energy interval in which the absorption changes from its low-energy value to highly absorbing is characterized by a temperature dependent change of the position of the interference related peaks and dips in the reflectivity spectra. This band gap related move of the interference features with temperature can lead to their misinterpretation as the *A*- *B*- and *C*-free excitonic reflectivity features [126].

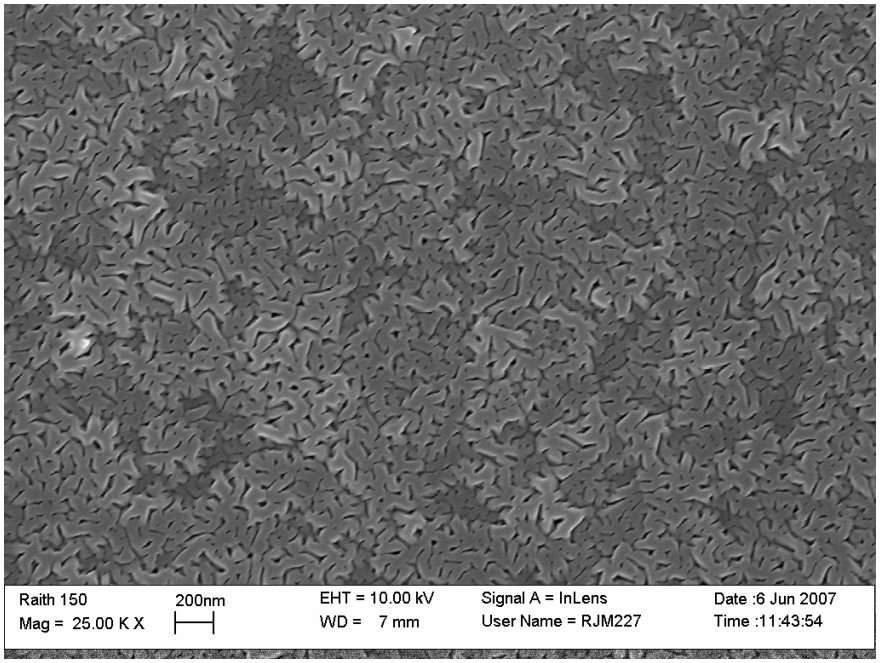

Figure 4.19: SEM-picture of PLD-2: Grown by EPLD, using a square shadow mask

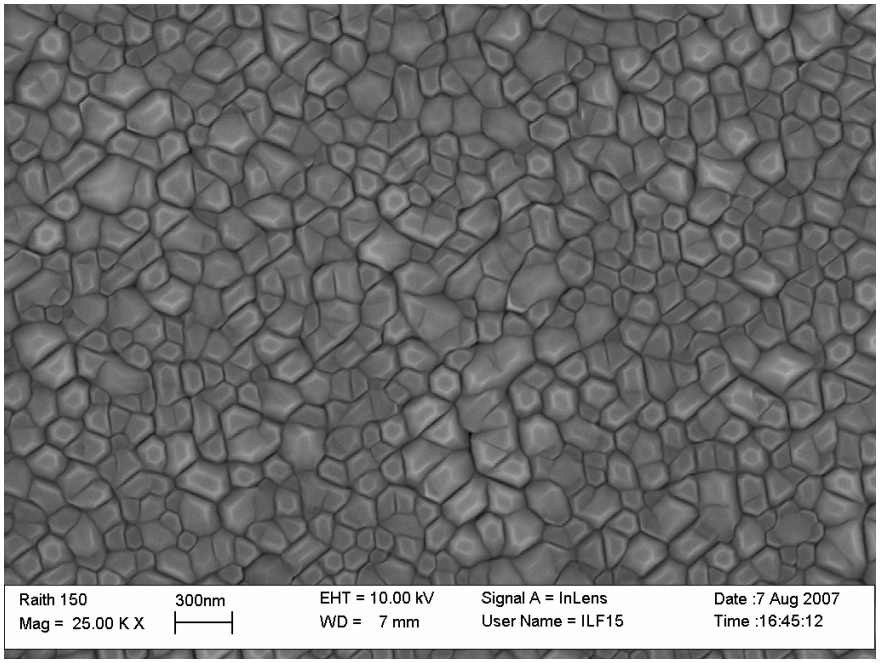

Figure 4.20: SEM-picture of PLD-1: Grown by PLD without the use of a shadow mask

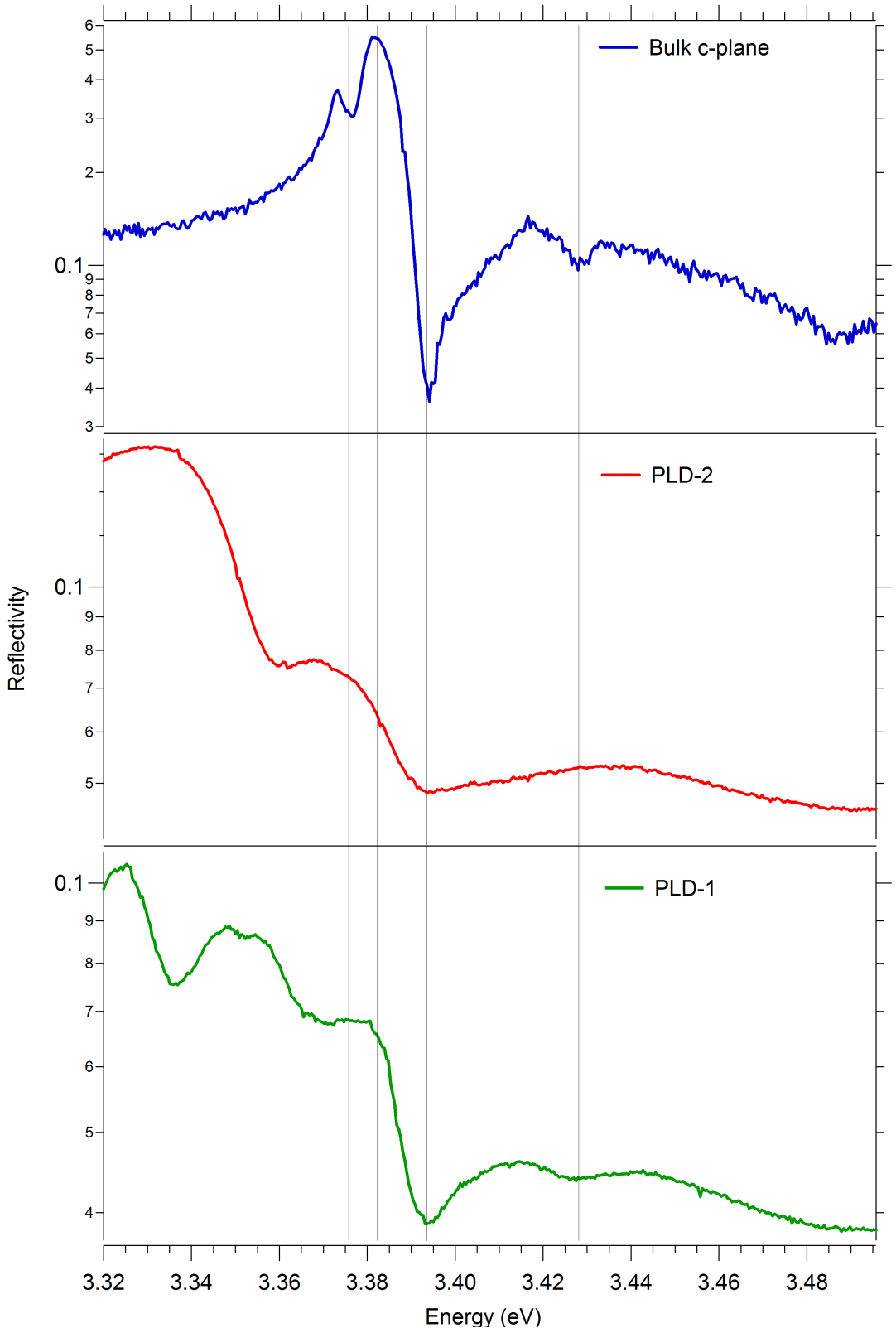

Figure 4.21: Comparison of the reflectivity of bulk ZnO with the excitonic features observed for the two PLD-grown films shown in figures 4.20 and 4.19

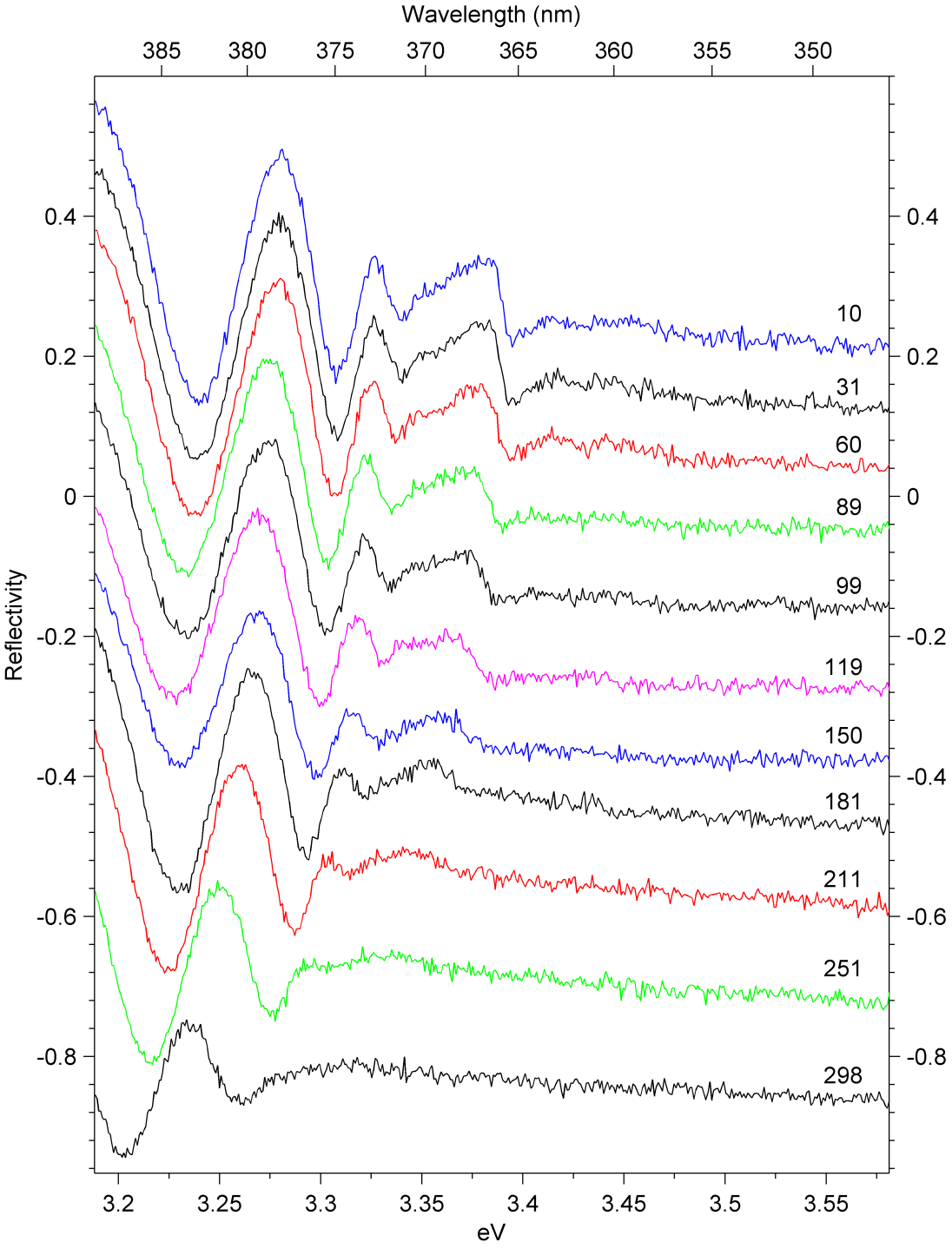

Figure 4.22: Reflectivity spectra of PLD-1 at temperatures ranging from 10 Kelvin to room temperature, of unpolarized light. To avoid the spectra to overlap, the spectra of temperatures above 10 K are plotted with individual constant negative offsets between each other.

The position of the B-excitonic dips associated with $B(\omega_L)$ align very well between all three scans and illustrates that the band structure of the two PLD-films not shifted by lattice strain, although the structure of the surfaces is quite different. The strong difference of the shape of the $B\omega_T$ peak in the reflectivity spectra is expected to be related to the film thickness: As the energy of the dip associated with $B(\omega_L)$ aligns very well between the two films, we conclude that the apparent broadening of the B-excitonic peak is not necessarily a sign of worse crystal quality for PLD-2. Due to its reduced thickness, the film does not fully absorb incoming light for energies above $A(\omega_T)$, leading to an overlap of the interference pattern with the reflectivity spectrum. In addition, this also results in the disappearance of the reflectivity feature at 3.424 eV for PLD-2, that is associated with the first excited state of the A-free exciton.

Figure 4.23 shows the temperature dependent position of the $B\omega_T$ and $B\omega_L$-feature in PLD-1, compared to the temperature dependence of these features in bulk ZnO. It is evident that the band gap shift in the PLD-grown film is matching the band gap shift of the high quality bulk material within the margin of error of our measurement.

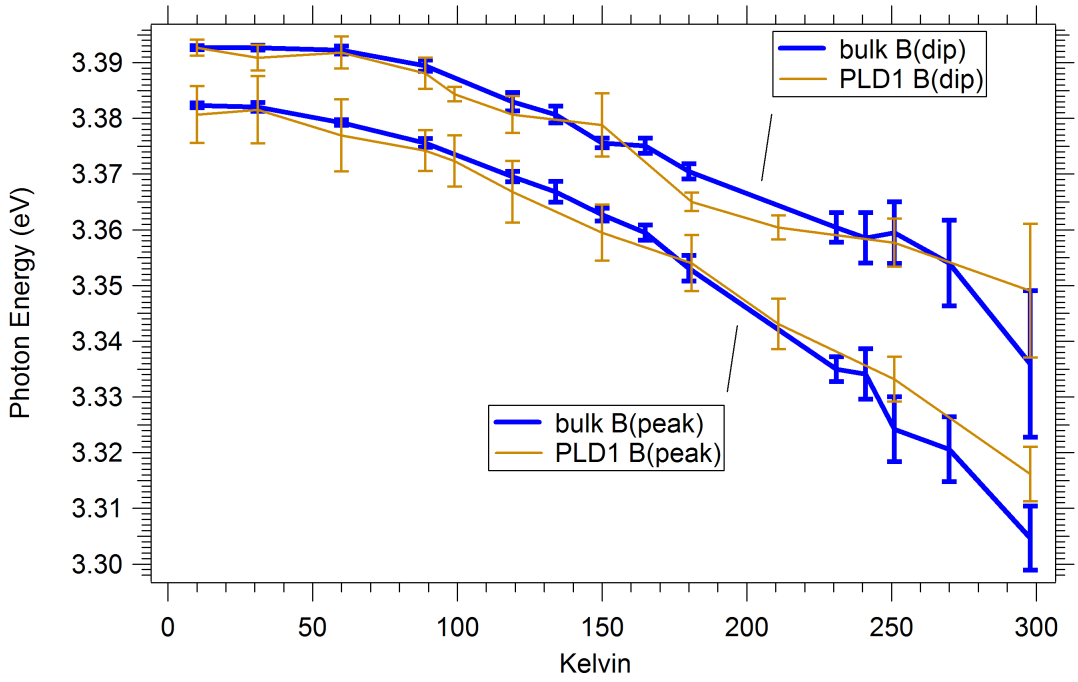

Figure 4.23: Comparison of the temperature dependence of the peak and dip associated with the ω_T and ω_L resonance of the B-free exciton of high quality bulk ZnO with the PLD-grown film PLD-1

Chapter 5

Photoconductive Centres in ZnO

5.1 Introduction

Photoconductivity (PC) is a phenomenon in semiconductors that occurs when the exposure to photons results in increased levels of electrical conductivity. The most simple case is when photons with an energy greater than the band gap energy get absorbed by the semiconductor, causing valence band electrons to be lifted into the conduction band. The resulting mobile electron in the conduction and hole in the valence band increase the conductivity of the material. A classic application of photoconductivity in material research therefore is the investigation of the band gap energy by measuring the conductivity response to the exposure with photons of controlled energy. A strong increase in conductivity, the so-called onset of photoconductivity, is the expected indication that the energy of the photons is sufficient to excite electrons from the valence into the conduction band and therefore is a clear indication of the band-gap energy, which typically is situated at the peak photoresponsivity [30].

The spectral distribution of the photoconductive response is, among other processes, sensitive for energies that electrons can be excited into. This is in contrast to the photon energy emitted in photoluminescence, which is equivalent to the energy gap that electrons and holes cross to recombine. This makes photoconductivity spectroscopy very interesting, as it opens the door to photospectroscopy of energy transitions that are inherently different to those that are involved in the photoluminescence processes. The aim of spectral photoconductivity measurements undertaken as part of this work therefore is to investigate the photon-energy dependent photoresponse for the identification of energy levels involved in the photoconduction process and their relation to the energy transitions responsible for features in photoluminescence and photoreflectance.

There are four possible photoabsorption mechanisms leading to photoconduction [30]: band-to-band transitions, impurity levels to band edge transitions,

ionization of donors and deep level (located in the valence band) to conduction band transitions. In general, photoconduction is an increase in conductivity due to photons being absorbed that create free charge carriers in the conduction and/or valence band. Due to the complex nature of the photoconductive process, there are many more ways in which the energetically resolved photoconductivity response can be affected at particular energies, be it an energy-selective increase or a decrease of the responsivity. Features in the energy spectrum have to be distinguished depending on the nature of the physical process they are related to. A number of effects can strongly influence the photoconductivity at particular energies: (surface)-phonons [32, 108, 112], hot excitons [128], extrinsic processes due to defects and impurities such as trapping of charge carriers [33, 129] and photochemical surface effects [101,130–137]. To avoid confusion, these have to be distinguished from spectral PC features that are caused by processes of intrinsic nature closely connected to the excitonic band structure [107, 138], as found in investigations of the photoconductive response spectrum of ZnO and its relation to exciton transitions that have recently been published [19, 66].

5.1.1 Exciton related features in PC-spectra

Photoconductivity spectra are closely related to absorption spectra due to the simple fact that only absorbed photons can create photo carriers, and excitons are readily observable in low temperature absorption spectra [13]. However, to understand how excitons can cause characteristic features in photoconductivity, one has to answer the question of how electrically neutral exciton complexes can actually contribute to the conductivity of a semiconductor. It is clear that additional processes have to be involved in order for their characteristic energies to influence the intensity of the photoresponse.

A very interesting model is the exciton dissociation through impact ionization with electrons that are accelerated by the applied electric field. This model has been supported by the following observation on epitaxially grown GaAs films [139] and manganese doped CdTe bulk crystals [140,141]: A direct relation can be seen between the electric field dependent rise of the excitonic photoresponse above a certain threshold voltage, and the simultaneous decay of the corresponding PL line. Since the photon energies resulting in a peak in the photocurrent are equivalent to the photon energies of the emission lines associated with the same bound or free-excitons, the energies associated with the dissociation of the exciton complex do not affect these impact ionization related PC-features. This is in contrast to e.g. phonon related dissociation of the excitons, which causes a characteristic shift [111] of the PC-lines by the energy of the phonon involved. The phonon that predominantly is able to resonate with the Coulomb interaction of the exciton in ZnO is the longitudinal optical phonon, with an energy of 72 meV-for other possible phonon-energies see section 5.1.2. Dissociation processes through the interaction of free excitons with defects and

impurities, leading to their ionization and thus conversion into free charge carriers have also been suggested [142].

Intrinsic spectral features in PC-spectra have played an important role in the first understanding of excitons in semiconductors. In 1931, Ya. I. Frenkel published his famous articles developing the theory of excitations of Coulomb-interacting electrons and holes in a crystal lattice, which he called excitons [38, 39]. It was not until about 20 years later in 1951, that E.F. Gross experimentally discovered hydrogen-like series of narrow lines on the absorption edge of Cu_2O crystals, which were attributed to the crystal's optical exciton spectrum [143]. Gross and Novikov then extended their studies by investigating the correlation between the exciton absorption lines and the shape of the photoconductivity curve of a range of 80 monocrystalline samples. A correlation could be established between a high intensity of the photoconductivity signal and the existence of excitonic absorption features in the absorption edge spectrum [144], suggesting that excitons can contribute to the photoconductive process.

The shape of the photocurrent curves and their correlation with absorption lines suggested a differentiation between samples of two types: In the first type, the photocurrent maxima energies correspond to the absorption lines. In samples of the second type, the absorption lines coincide in position with the photocurrent minima. The spectral PC-curves, for crystals of both types, behave according to the polarizations selection rules analogous to the ones outlined in section 4.3.1.

Over the last 50 years, the spectral photoresistive effect at the band edge has been thoroughly investigated, particularly for CdS, by Novikov and Batyrev et al. [114, 115, 145–151]. CdS is similar to ZnO as it is also a II-VI compound with wurtzite crystal structure, with a polarity along the c-axis that is due to a strongly ionic binding between Cd and S. Recently, the spectra were found to be highly sensitive to external factors, namely to IR-illumination [151] or an inhomogeneous surface electric field [152]. The surface electric field with strength of merely 500 V/cm perpendicular to the surface of an in-plane sample at 77 K, is able to change the spectrum of type one into spectra of type two and vice versa, i.e. the exciton related dips in the PC-spectrum could be transformed into exciton related peaks by applying an electric field with $\boldsymbol{E} \perp \boldsymbol{c}$ and $\boldsymbol{k} \perp \boldsymbol{c}$ [114].

5.1.2 Phonon related oscillatory PC

Oscillations in the spectral distribution of the intrinsic photoconductive response at low temperature have been observed in many semiconductors. These oscillations are characterized by a constant period ΔE at energies above a collector level that can be shifted by an external electric field. ΔE is related to the longitudinal optical phonon energy $\hbar\omega_0$ at the centre of the Brillouin zone through the strong interaction of excitons or photoexcited carriers with LO phonons [108,140]. Vanecek et al. [108] summarizes three different relations between ΔE and $\hbar\omega_0$,

depending on the form of interaction between the LO phonons and the carriers or excitons:

In the first case, $\Delta E > \hbar\omega_0$, with the appearance of photocurrent minima according to Stocker et al. [153] at energies

$$E_{\min} = E_0 + n\hbar\omega_0 \left(1 + \frac{m_e}{m_h}\right). \tag{5.1}$$

The collector level E_0 is close to the energy gap, m_e/m_h is the ratio of electron and hole effective masses and n is an integer. The minima are caused by a non-symmetrical loss of momentum that is only possible in a weak external electric field, and if the thermalization of carriers with τ_{AC} takes longer than their lifetime τ_{l} due to rapid cascading of the hot carriers via successive LO phonon emission. Each phonon emission has the lifetime τ_{LO} and the process is thus limited by:

$$\tau_{\mathrm{LO}} < \tau_{\mathrm{l}} < \tau_{\mathrm{AC}}. \tag{5.2}$$

See Stocker et al. [153] for a detailed illustration of the proposed mechanism of oscillatory photoconductivity according to this model.

In case of ZnO it has to be kept in mind though, that the internal electric field resulting from the polarity of the crystal is by magnitudes larger than the external electric field resulting from the driving voltages applied here. The driving voltage is of special interest since it results in the movement of free carriers through the crystal and therefore plays a role in the creation of impact ionization events (see page 128).

The second case with $\Delta E = \hbar\omega_0$ has one of the free or bound exciton transitions as the collector level and the series can be formed either by minima or maxima in the PCR spectrum. This case is most likely the case of hot exciton decay by emission of LO phonons. The hot excitons thus create new recombination and scattering centres that reduce the lifetime and/or mobility of the free carriers at select energies, leading to an oscillatory structure in the PCR spectrum [128]. Bulk ZnO phonon replica were measured to be offset by a multiple of the LO phonon energy, which in the case of ZnO typically is between 71.5 meV for bulk phonon vibrations parallel to the c-axis and 73.1 meV for vibrations normal to the c-axis [32].

The third case of a spacing with $\Delta E < \hbar\omega_0$ has been attributed by Lueth [32] to surface phonons according to the model of Fuchs-Kliewer [109, 154]. The surface phonons in ZnO with a condensed layer of xenon on the surface showed to have an energy of 68±2 meV. This can be calculated from the dielectric constants of the adsorbed layer that the surface-phonons interacts with (see also page 149) [32]:

$$\omega_s^2 = \frac{\epsilon_0 + \epsilon_{ad}}{\epsilon_\infty + \epsilon_{ad}} \omega_{\mathrm{TO}^2}, \tag{5.3}$$

with ϵ_0 as the dielectric constant of the medium and ϵ_{ad} as the dielectric constant of the medium that is adjacent to the surface. Since photoconductivity of ZnO has been shown to be a surface phenomenon [131], a particular sensitivity to surface phonons is not surprising.

5.1.3 Modulated PC

The absolute intensity of unmodulated measurements of photoconductivity is dominated by photoconductive processes with a slow rise and decay time. These slow processes are mostly related to surface gas de- and adsorption processes as well as trapped photo carriers that are slowly released [155]. The slow processes can be indirectly related to the band structure, but are strongly dependent on the history of light exposure, a so called memory effect. To minimize the memory effect on the PC-spectrum, all spectral photoconductivity experiments presented here were carried out using the Lock-In technique with a modulated light source. A closer investigation of the background of the Lock-In Amplifier (LIA) measurements is given in section 2.5.2. Modulated measurements are less influenced by slow photoconductive processes since they only measure the response to repeated short variations of the light exposure and therefore are much more suitable for the identification of the response of energy levels to light of certain energies. The length of light exposure is controlled by the chopping speed, which blocks the light 50% of the time with a frequency that could be varied from 5-5000 Hz. One has to keep in mind that the absolute intensity of the response to short pulses of light can itself be dependent on the underlying amount of excited photocarriers. A sample that has a very low density of excited photocarriers is more light sensitive than a sample which has been exposed to intense light and accordingly has a high density of slow photocarriers. But since the light is only incident on the sample during 50% of the time for the measurement with modulated light, the background photoconductivity is more stable during the measurement than if the sample is continuously exposed to light or no light.

When measuring the response to modulated incident light, a higher background photoconductivity can result in a lower intensity of the spectral features. But, very importantly, this inconsistency in the level of background photoconductivity does in principle not alter the energetic position of spectral features, as would be the case in unmodulated photoconductivity measurements. In unmodulated measurements, the slow drift of the conductivity would overlap with spectral features, leading to an apparent shift of their energy position.

To achieve similar levels of background conductivity between scans, the scans of ZnO were performed from high photon-energy to low photon-energy. Several minutes did pass before the scan reached the spectral regions of interest at the band edge, resulting in a comparable state of excited slow photocarriers, as the preceding history of radiation is dominated by the exposure with photons of above band gap energy for the first part of the scan.

A variation of the chopping speed can also be used to investigate the photon energy dependent transient response of the sample. In general, slow transitions would get filtered out by a fast chopping speed, whereas fast transitions can get drowned out by slow transitions if they have enough time to respond to the incident light, i.e. for slow chopping speeds. Figure 5.8 (see page 148) shows the intensity of the chopping frequency dependent photoconductivity for the case of a slow process. The PCR peaks at 40 Hz, with much lower response to chopping frequencies below and above 40 Hz. The PCR decay with rising frequencies above 40 Hz is exponential, being reduced by a factor of 16 between 40 Hz and 500 Hz. The chopping speed dependent PCR-signal in figure 5.9 essentially follows the same behaviour, but must be connected to a PCR-process with significantly faster response time: the signal increases by a factor of 6 between 160 Hz and 1.8 kHz, to then decay exponentially with chopping frequencies above 1.8 kHz, reaching a signal strength that is reduced by a factor of 1.3 at 5.8 kHz. The difference in response time of different transitions can lead to an apparent shift of peak positions, when slow transitions get filtered out by a fast chopping speed, favouring fast transitions that are at a slightly different energy level. Additionally to the response time of the photoconductor, there is a component in the modulation frequency dependence of the signal intensity that is due to the *RC* low pass filter that is inevitably formed by the capacitance of wires, sample and Lock-in amplifier, in combination with the resistance of these components. Therefore we paid special attention to keep the wiring of the experiment as short as possible to minimize the capacitance related effects.

The response time τ_{res} of a photoconductor is defined as [30]:

$$I(t) = I_0 \times (1 - e^{-t/\tau_{\mathrm{res}}}), \tag{5.4}$$

with I(t) as the photocurrent as a function of time and I_0 as the maximum photocurrent. For time τ_{res}, the photocurrent reaches 63% of its maximum value. For measurements taken with constant current, $I(t)$ and I_0 can be replaced by the time dependent photovoltage $U(t)$ and the maximum photovoltage U_0 respectively. The rise/fall time τ_{rf} is the parameter that describes the time it takes the photocurrent or photovoltage to go from 10% to 90% of its final value. τ_{rf} therefore is most related to the chopping frequency that yields the maximum PCR-signal [30]. Since it is very difficult to acquire more pertinent information about τ_{rf} as well as τ_{res} [30], the time equal to the inverse of the modulation frequency giving the maximum PCR-signal is quoted here as τ_{rf}.

5.2 Spectrally resolved processes in PC

According to the studies of PC-spectra published by Novikov et al. mentioned earlier, there are two types semiconductors: one that has maxima and one that has minima of photocurrent at the position of their exciton absorption lines.

But it is not fully understood what makes a semiconductor crystal have peaks or dips at the position of the excitonic absorption lines, as samples of the same material composition can either show behaviour according to type 1 or type 2 [114]. Theoretically, this variation is attributed to the character of the surface band bending, with the PC-maxima being the result of enriching band bending and the minima being result of depleting band banding. Structureless band-edge photoconductivity is proposed to be due to flat bands near the surface of the semiconductor. It is thus one of the goals of this investigation, to investigate if we see a similar behaviour in ZnO: Do we see excitonic features in the PCR-spectra measured here? Can we establish that they are indeed excitonic, and not due to other effects? Do we see excitonic peaks or dips. In fact, do we only see either peaks or dips in one single sample, or can we see both types in the same spectrum? Finally, can the difference in surface electric field due to different orientations of the ZnO crystal as well as different polarities of the investigated ZnO surfaces influence the nature of the excitonic PCR-features between the two types? Can surface contamination play a role?

To relate the different types of details in the photoconductive spectrum to sample quality, surface effects and polarity, it also has to be considered that many parameters, in particular the electric field strength used to drive the carriers from contact to contact, the illumination intensity, the chopping speed and even the optical illumination geometry of the sample all can potentially influence the spectra observed. Great emphasis was thus placed on the reproducibility of spectra presented here, by varying all of these parameters for each set of scans. This helped us to identify which parameters are related to the spectral response curves investigated. The high number of parameters that can potentially be responsible for a particular PCR spectrum make the investigation of the PCR-spectra relatively complex, and a measure of reliability for the association of features in the PCR-spectra with energies in the electronic structure of the material is needed.

5.2.1 Light penetration depth

First we want to investigate the relation of the absorption of photons with the photogeneration of carriers. The absorption coefficient α introduced in section 4.1 is related to the intensity of the incident light $I(d)$ at a depth d in the crystal through

$$I(d) = I_0 e^{-\alpha d} \tag{5.5}$$

For a depth $d = 1/\alpha$, the intensity is reduced by $I(d) = I_0/e$. Thus a penetration depth β can be defined as the depth at which the light intensity of the incident light is reduced to $1/e$:

$$\beta = 1/\alpha. \tag{5.6}$$

Figure 5.1 shows the penetration depth plotted against the PCR-spectrum of the same c-plane sample that was investigated for its absorptive properties in

section 4.1. The penetration depth is equivalent to the thickness of the sample ($460 \pm 15 \mu m$) at the photon energy of 3.341 eV, marked by (i). This means that for photon energies of 3.341 eV or higher, the sample absorbs more than 63% of the incoming light. Although the PC spectrum does indeed show a rise in its PCR-signal even for energies below (i), this rise is extremely small with less than 1% of the maximum photoresponse which is reached at energies above 3.38 eV. The slow rise of the PCR-signal below (i) can only be made visible by plotting the PCR-spectrum on a logarithmic scale. The PCR-signal only reaches 12% of

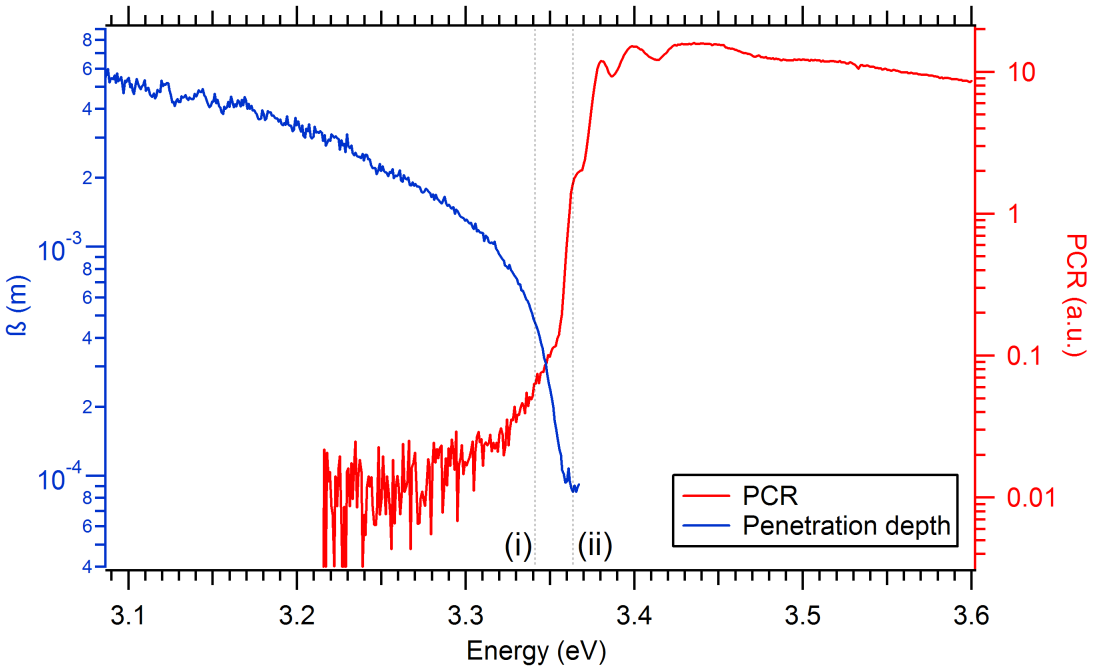

Figure 5.1: The penetration depth in relation to the photoconductivity onset of hydrothermally grown c-plane bulk ZnO, at 10 Kelvin. The vertical line identified with (i) (at 3.341 eV) marks the energy at which the penetration depth β is equal to the sample thickness. (ii) (at 3.364 eV) marks the energy above which the detector could not pick up any light transmitted through the sample. The PCR-spectrum is plotted on a logarithmic scale to emphasize the PCR-response to light of low energy

its peak value at the energy of full absorption of the incoming light at 3.364 eV, marked by (ii). This shows that photons with energies of less than 3.38 eV, although they do get absorbed by the material, do not create free carriers as efficiently as photons of energies of 3.38 eV and above. The photogeneration of carriers is therefore only loosely connected to the absorption of photons. Since their energy is needed to generate free carriers, photons do have to be absorbed in order to create free carriers. But not every absorbed photon does actually create a free charge carrier. The absorption below 3.38 eV involves more processes in the semiconductor that are not creating additional free charge carriers than the absorption at energies of 3.38 eV and above.

Unfortunately the photodetector is not able to pick up any light above 3.364 eV (ii). From literature, we can assume that the penetration depth continues to drop sharply for energies above (ii). For high quality crystalline ZnO, a maximum absorption coefficient of $\alpha > 2 \times 10^5$ cm^{-1}, equivalent to a penetration depth of $\beta < 50$ nm, can be expected above the energy of the A-free exciton at 3.375 eV [7, 156, 157]. At the position of the free excitons itself, the absorption coefficient can even be more than double, with $\alpha > 5 \times 10^5$ cm^{-1}, equivalent to a penetration depth of $\beta < 20$ nm.

The following conclusions can be drawn from the relation between the onset of absorption and the onset of photoconductivity in this ZnO crystal: The PCR spectrum shows fine structure down to the energy of (ii), a photon energy for which the crystal just manages to absorb all the incoming light, as (ii) is the lowest photon-energy at which no light can be detected by the Si-detector. This means that for the fine structure around (ii), the spectral features can still be related to the bulk material. But the fact that light with a very shallow theoretical penetration depth of only 50 nm causes the highest photoconductive response in ZnO means that in ZnO the surface can play a dominant role in the PCR-spectra. A particularly low penetration depth is expected at the energy of the free excitons themselves, making the photoconductive response at the energies of the free excitonic resonances particularly surface sensitive. The band bending at the surface that, according to Novikov et al. determines if the free excitonic features in the PCR-spectrum do have the form of dips or peaks [114], can be caused by adsorbed gases. The polarity of the ZnO crystal in the direction of the c-axis causes the creation of charge compensating surface layers on c-plane surfaces. This results in a face-dependent band bending by adsorbed gas-molecules. According to Hoffmann et al. [120], the concentration of conduction electrons close to the surface is depleted by adsorbed oxygen, and enriched by adsorbed atomic hydrogen. This creates space-charge layers that result in a band bending at the surface as well as a change of the mobility at the surface. A change in the reflectivity has been shown to be related to this process, showing that ZnO has a greater sensitivity to enriching processes by adsorbed atomic hydrogen on the oxygen face, whereas the Zinc-face is more sensitive to depletion through the exposure with oxygen [119, 120]. Although we did not expose the investigated sample with atomic hydrogen or pure oxygen, as this investigation would require an in-situ cleaning procedure of the investigated surfaces, the different sensitivities of the two polar faces to depletion and enrichment, respectively, can be expected to lead to a tendency of different band bending depending on the face investigated. As PCR is expected to be very surface sensitive, we tried to find a relation between the face of the material and the spectral PCR-signal observed. Overall, the high electric field in the space charge layer changes the optical constants and has been experimentally investigated through the reduction of reflectivity that it is connected with [120], see section 4.4.1.

5.2.2 Spectral photoconductivity response of ZnO-thin films at room temperature

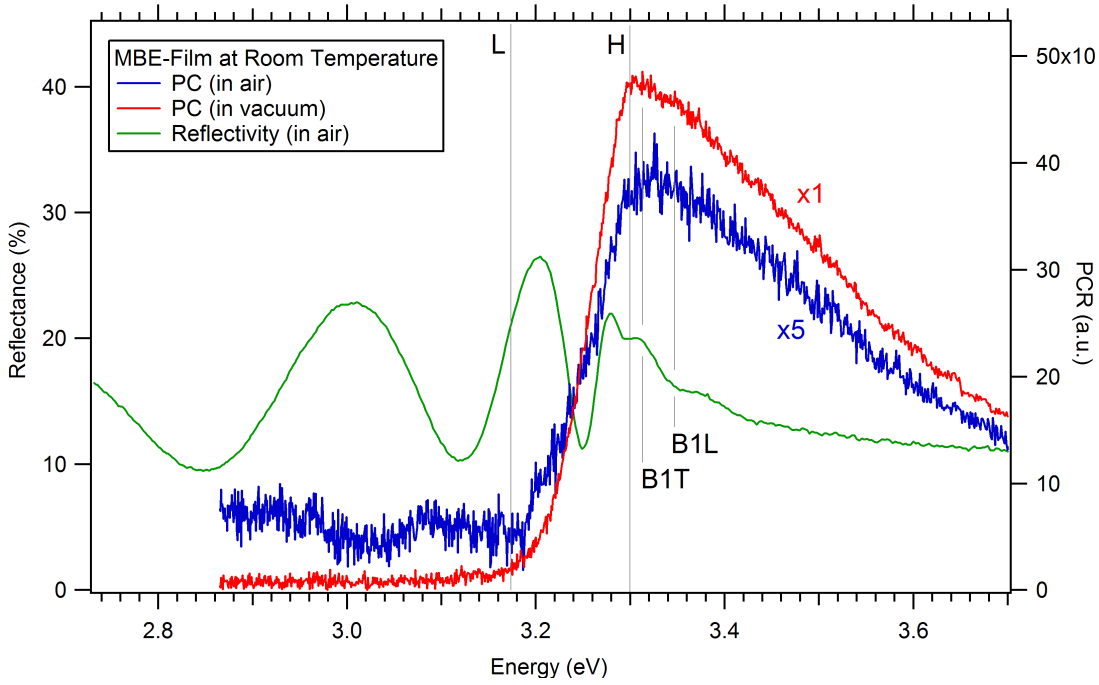

Figure 5.2: Room temperature, normal incidence reflectivity spectrum across the band edge region of an MBE-grown ZnO film, in air, in comparison with the photoconductive response in air and in vacuum. 'B1T' marks the position of the reflection peak associated with the B-free exciton ω_T (n=1), 'B1L' is the reflection dip associated with ω_L (n=1). Faint peaks at these energies can be seen in the PC-spectrum measured in vacuum

The almost purely band gap related onset of photoconductivity of a MBE-grown ZnO film is shown in figure 5.2, for photoconductivity spectra taken in air and in vacuum. The MBE-film was measured using a 4-point contact geometry [62] with 4 equidistant contacts, with a constant current of 5 mA applied to the outer two contacts, and the voltage being measured by the Lock-In amplifier across the inner two contacts. The voltage between the inner two contacts was about 380 mV in dark, and the voltage variation with a chopper frequency of 67 Hz had a maximum of 50 μV in air and 5 μV in vacuum. In figure 5.2, markers are displayed for two significant energies: 'L' at 3.17 eV and 'H' at 3.30 eV. The reflectivity spectrum indicates the onset of strong absorption at 'H', just below the energy of the B-free exciton related reflectivity peak. The onset of strong absorption is evident at 'H', since the regularity of the interference structure in the reflectivity spectrum gets interrupted at this energy and the exciton related reflection features 'B1T' and 'B1L' can be resolved at higher energies. This point in the reflectivity spectrum coincides with the energy where the photoconductivity reaches its peak response value. The peak in photoconductivity is expected to

be marking the energy of the room temperature band gap of the MBE-film [30] and aligns very well with the room temperature band gap energy of ZnO of 3.30 eV [7]. When increasing the photon energy above E_G, the photocarriers get excited more exclusively in the surface region of the semiconductor, due to the reduced penetration depth of light of short wavelengths. Since excited photocarriers at the surface are more likely to recombine, due to the inhomogeneity of the crystal properties at the surface, the photoresponse on the higher-energy side of the main peak goes down. Two very slight peaks can be resolved in the PC spectrum just above 'H', lining up with the peak 'B1T' related to $B\omega_T(n = 1)$ as well as the dip 'B1L' related to $B\omega_L(n = 1)$ in the reflectivity spectrum. Below 'L' at 3.17 eV the photoresponse measured in vacuum is very small, showing no measurable change from the dark conductivity σ_d which the sample shows without incident photons. The transition from low conductivity to high conductivity happens between energies marked as 'L' and 'H' in figure 5.2, an energy range of 130 meV. This transition range is comparable to the transition energy range of 125 meV from low to high absorption seen in thick bulk ZnO crystals in section 4.1.

The photoresponse in air, also shown in figure 5.2 follows a similar spectral dependence as the response measured in vacuum, but the intensity is reduced by a factor of 5.3 against the measurement in vacuum. This clearly shows that surface effects can play a dominant role in the photoconductive process of these epitaxial films, and spectral positions of peaks have to be analyzed carefully, as surface related effects can potentially be strongly energy dependent. In air the PCR continues to vary even for photon energies below 'L', an effect also related to gas adsorption happening on the surface. The reduction of the PCR with exposure to air of the MBE-sample is reversible, therefore no chemical modification of the film but a mere adsorption of molecules from the air is expected to be responsible for the change in the PCR spectrum.

The energetic position of the onset of photoconductivity shows that photonic energies below the band gap can suffice in creating a photocurrent, i. e. donor and acceptor states or defect states near the conduction and valence bands can absorb a photon or hole, increasing the number of free charge carriers [30]. These states can be due to extrinsic dopants as well as intrinsic defects. Extrinsic photoconductivity is a process involving the ionization of an extrinsic dopant with a photon that matches the ionization energy of that dopant. This ionization energy can even be far below the band gap, often in the IR-region. For bulk crystals exposed to ion-beam implantation, resulting in samples with high levels of defects and impurities, we indeed see strong photosensitivity to light of energies far below the band gap. But the onset of strong photoconductivity at the band edge is also observed for these materials.

5.2.3 High detail in low temperature PCR of bulk ZnO

High quality bulk ZnO is very interesting for a better understanding of spectrally resolved photoconductivity of ZnO and of semiconductors in general. The c-plane hydrothermal bulk ZnO crystals purchased from Tokyo Denpa exhibit the lowest defect density of all crystals investigated in this thesis, as supported by the transmission experiments presented in section 4.1. They offer an outstandingly low carrier concentration of 1×10^{14} cm^3 [21] compared to a carrier concentration of 3×10^{18} for the MBE-sample annealed at 850°C, which are investigated in sections 3.2 and 5.4. For a material with such low carrier concentration, free charge carriers created by photoexcitation cause a more substantial change in the conductivity than in materials with higher carrier concentrations such as epitaxially grown films. Also, the bulk samples exhibit a high mobility of about 200 cm^2/Vs (compared to 40 cm^2/Vs in the MBE-films), being related to less trapping of excited charge carriers in defect states. Since trapping is related to slow photoconductive processes [30], it can strongly influence the spectral response curve [19]. This will be investigated through the investigation of the modulation frequency dependent PC-response of these crystals, as with less trapping, the curve is expected to show a smaller influence of the chopping speed on the shape of the spectrum.

Thus here we concentrate on the investigation of the photoconductive response spectra observed from c-plane crystals that were grown by Tokyo Denpa with the hydrothermal method [21]. Since the measurements were not done with an in-situ cleaning process of the surfaces, the various sample surfaces were expected to be in different states of surface contamination and had different compositions of surface adsorbed materials, potentially altering the photosensitive properties of the surface layers. Paying strong attention to reproducibility, this allowed us to investigate the effect the state of the surface can have on the PCR-response spectra, as well as the influence of other measurement parameters that govern photoconductivity.

For the comparison of different surfaces, the scans were taken under as equal conditions as possible. The samples were of quadratic shape and had a size of 0.5×0.5 cm, with 4 electron beam deposited indium contacts in their corners (Hall geometry). The measurements were done in two-point geometry, with a constant current source supplying a constant current of about 1 μAmpere resulting in a voltage of about 1V. It was connected to the electron beam deposited Indium contacts in two corners on one side of the sample. The spectrometer light was then directed onto the sample so that the spectrometer slit imaged between these two contacts in such a way that an illuminated area connected them.

For these high quality crystals, we expected a greater chance to detect photo generated changes in the free carrier concentration that are due to the interaction of the incident light with narrow band energy levels such as bound excitons. Bound excitonic features have been observed in photoconductivity spectra of

other materials, e.g. $Cd_{1-x}Mn_xTe$ [140]. Several groups have investigated the spectral photoconductive response of ZnO. This includes studies of photovoltage spectroscopy of surface states in the energy region below 1 eV [131, 158], studies by Fourier transform infrared photocurrent spectroscopy in the mid infrared wavelength range investigating deep intrinsic defects [129], studies of the photoconductive response of ZnO nanostructures [155,159], studies relating the photoconductive responsivity of annealed ZnO crystals to the number of Zn-interstitials acting as a supplier of shallow donors at 2.8 eV [160], as well as studies relating reduced epitaxial ZnO film thickness to increased photosensitivity due to photoadsorption and photodesorption processes [161]. But only very few studies have recently been published that investigate the relation of the PCR-signal variation in the band gap-region to processes involving the excitonic structure in crystalline ZnO films [19, 106, 129, 162]. Most of these studies only show very broad features that are weakly related to an excitonic origin. Only the study by Tomm et al. [19] investigates temperature dependent excitonic PCR-spectra of ZnO that give feedback about the position of the combined A and B-free exciton in a single PC-peak, giving a precision at room temperature that is comparable to the precision obtained by reflectivity and transmission experiments. They also see a strong onset of defect related photoconductivity at energies just below the A-exciton, very similar to our findings.

We have mentioned the existence of band-edge related fine structure in the PCR-response spectra of ZnO in figure 5.2 and figure 5.1. A similar fine structure can be seen for most high quality ZnO samples and can be described as an intensity variation in the PCR-spectra, apparent at energies starting from the onset of band gap related photoconductivity at about 3.35 eV up to energies of 3.55 eV. Above 3.55 eV, the spectral response becomes featureless for all samples investigated, i.e. there is no photon energy related rise and fall of the photocurrent, no peaks or dips can be seen in the PCR-spectrum for energies above 3.55 eV. The intensity variations observed between 3.35 eV and 3.55 eV often have an apparent oscillatory nature as can be seen in figure 5.1. But the spacings between dips and peaks are not constant and do not seem to follow a regular pattern. The spacing between successive peaks in the PCR-spectra tends to become larger with increasing photon-energy, therefore these peaks can not be expected to be due to interference, as the spacing between interference related peaks has to get smaller with increasing energy due to the associated decrease of wavelength. Of course this is only valid for the case that the interference layer is of constant thickness..

In figure 5.3, the PCR spectrum of figure 5.1 is compared to a to a spectrum taken under the same experimental conditions but with a 5 times smaller slit-width. The reduced slit width has two consequences: the intensity of the incident light on the sample is reduced by a factor of 25, and the spectral FWHM of the incoming light is reduced by a factor of 5. The sample responded to the reduction in linewidth of the incident light with an astonishing amount of fine structure, that could not be detected from any other sample we investigated. In figure 5.3,

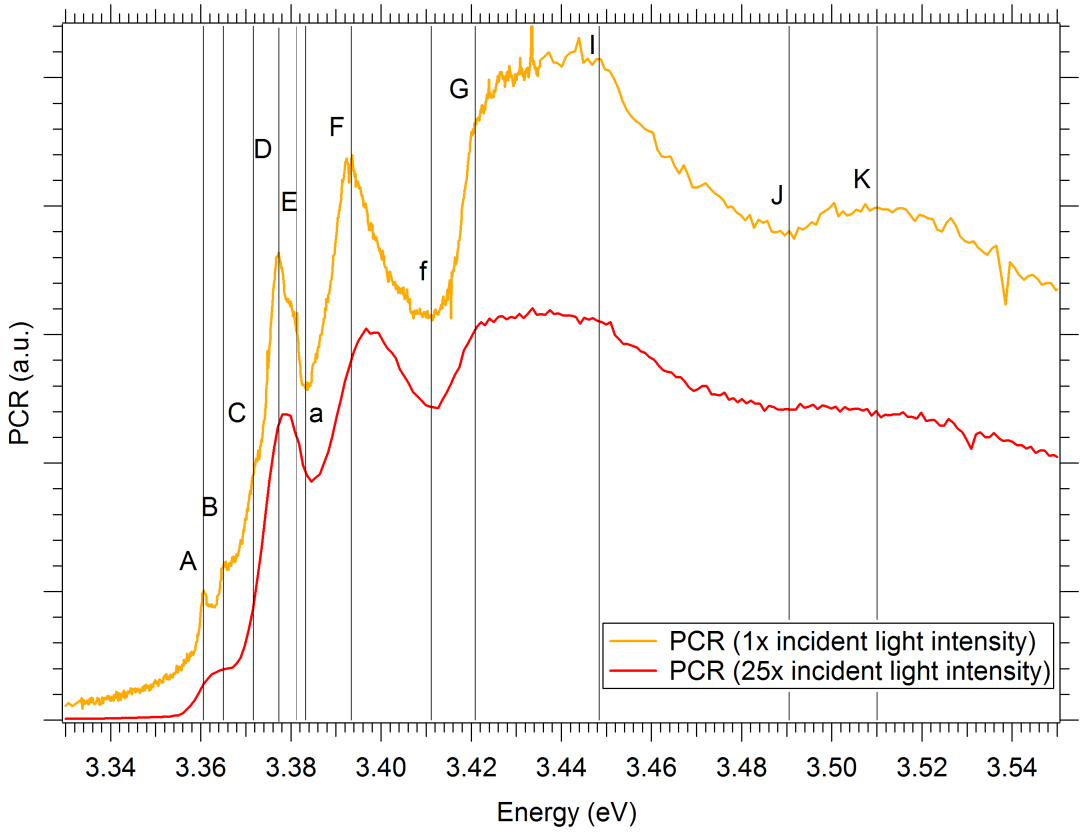

Figure 5.3: PCR-spectrum of sample with the most detailed photoresponse with the response spectrum recorded with a 25 times higher intensity of the incident light. Since the light intensity was increased by opening up the slits of the spectrometer by a factor of 5, the features are broadened. Features are identified with arbitrary letters 'A'-'K' for reference

characteristic PCR-features are marked with arbitrary letters 'A'-'K' for easier reference throughout this chapter, using capital letters for peaks and small letters for dips.

The first step in identifying the origin of features 'A'-'K' in the PCR-spectrum is their direct comparison to better understood spectra of reflectivity for the identification of free excitons, as well as photoluminescence for the identification of bound excitons. This is done in figure 5.4, with a more detailed spectrum of the bound and A-exciton region in figure 5.5. In a rough comparison, figure 5.4 shows very good alignment of free exciton energies to the following spectral features in PCR: Peak 'D' aligns very well with the energy of the A-free excitonic dip and Peak 'F' aligns very well with the energy of the B-free excitonic dip seen in reflection. The broad feature 'G'-'I' corresponds in energy with the C-free exciton.

In the closeup of the energy region of the bound and free *A*-excitons in fig-

ure 5.5, it can be seen that in energy and width peak 'D' in the PCR-spectrum indeed matches very well with the dip in reflectivity that can be associated with A_L. As determined in section 4.4, the positioning of A_L and A_T of our PL and reflectivity experiments matches with the interpretation of Syrbu et al. [16], thus suggesting that peak 'D' is associated with A_L. It is interesting though that the energy associated with A_L by Chichibu et al. [97], marked by a red line in figure 5.5, corresponds to a slight shoulder in our PCR-spectra.

Since the photoconductivity measurements were done at 45 ° to allow the direct comparison of reflectivity and photoconductivity as shown in figures 5.15 and 5.16, the C-free exciton is weakly allowed according to the selection rules. Therefore we show the A-plane reflectivity spectrum here, to show the great match of the C-free excitonic peak in reflectivity and the relative onset of photoconductivity at 'G', with a good alignment of the peak of C_T^1 with the start of the plateau of highest PCR at 'G'. As mentioned before, the A_T^2 transition lies very close to C_T^1. C_L^1 lies right in the middle of the broad PCR-maximum. However, as will be demonstrated by temperature dependent measurements of PCR in section 5.3, the spectral features at the position 'G' to 'I' can also be associated with phonon replica of the neutral and ionized bound A-excitonic transitions 'A' and 'D' in figure 5.5 (see page 158 for details).

In summary there seems to be a good alignment of features in the PCR-spectrum with the energy position of the A- and B-free excitons in reflectivity. But whereas the literature values for energies of the A_T, A_L, B_T and B_L line up pretty well with peaks in the photoconductivity spectrum, there is no distinct peak in the photoconductivity for C_L, and the rise in photoconductivity at the energy of C_T is unlikely to be related to the $A_T^{n=2}$ exciton, as first excited states of excitons are not expected to result in such dominating peaks. If the PC-peaks specified in table 5.1 are indeed due to free excitons, this is what we would expect as a result of the selection rules minimizing the interaction of photons with the C-exciton resonance for the orientation used in this photoconductivity measurement: $\boldsymbol{E} \perp \boldsymbol{c}$, $\boldsymbol{k} \parallel \boldsymbol{c}$. A comparison to the photoconductivity of m-plane bulk ZnO would be interesting for materials with matching low defect density and surface properties.

Photoluminescence is most sensitive to bound excitonic transitions. These strongly dominate its response, therefore it is possible to investigate their nature and clarify their origin via PL-studies. It is remarkable, how well the three fine peaks marked as 'A' 'B' and 'C' in the PCR-spectrum line up perfectly with the emission from A excitons bound to neutral donors I^A, B excitons bound to neutral donors I^B and A excitons bound to ionized donors I_+^A. Peak 'B' matches the position of the emission of neutral donor bound B-excitons with a small offset of about 1 meV, which is very close to the expected uncertainty of 0.5 meV. The energies of the transitions are shown in table 5.1.

The energy of the sharp transition at 3.381 eV ('E') is in great agreement

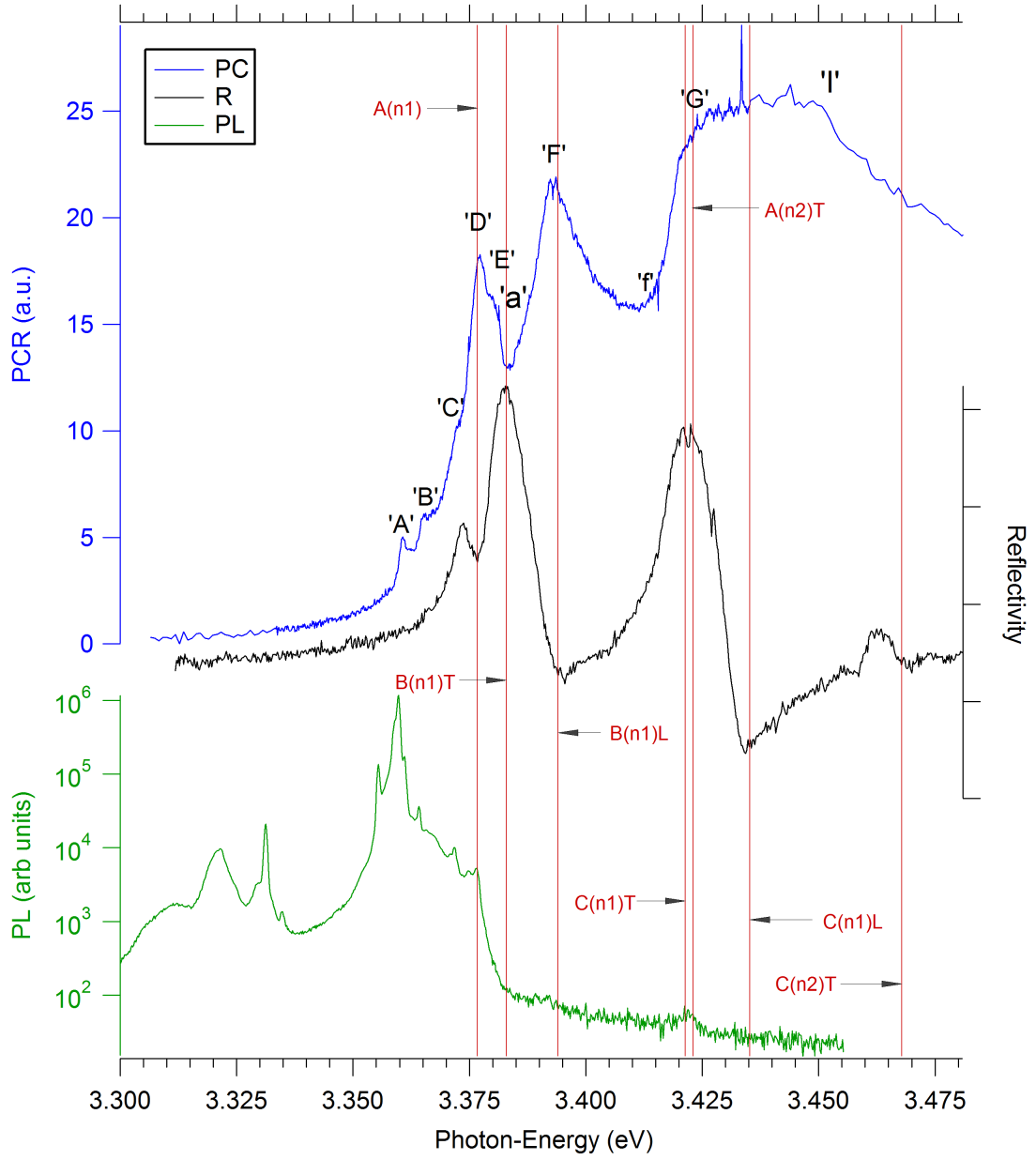

Figure 5.4: The most detailed photoconductivity spectrum observed, measured at low temperature (10K) on hydrothermally grown O-polar c-plane bulk ZnO. The graph shows a comparison with the photoluminescence as measured on a similar bulk ZnO crystal, as well as the reflectivity response as measured on a-plane bulk ZnO (see figure 4.9). For orientation, the red lines show literature values for the ground (n=1) and 1st excited state (n=2) of the free A-, B- and *C*-exciton as measured by photoreflectivity by Chichibu et al. [97], the green lines show the energies measured by photoluminescence spectroscopy by Syrbu et al. [16], see also table 5.1

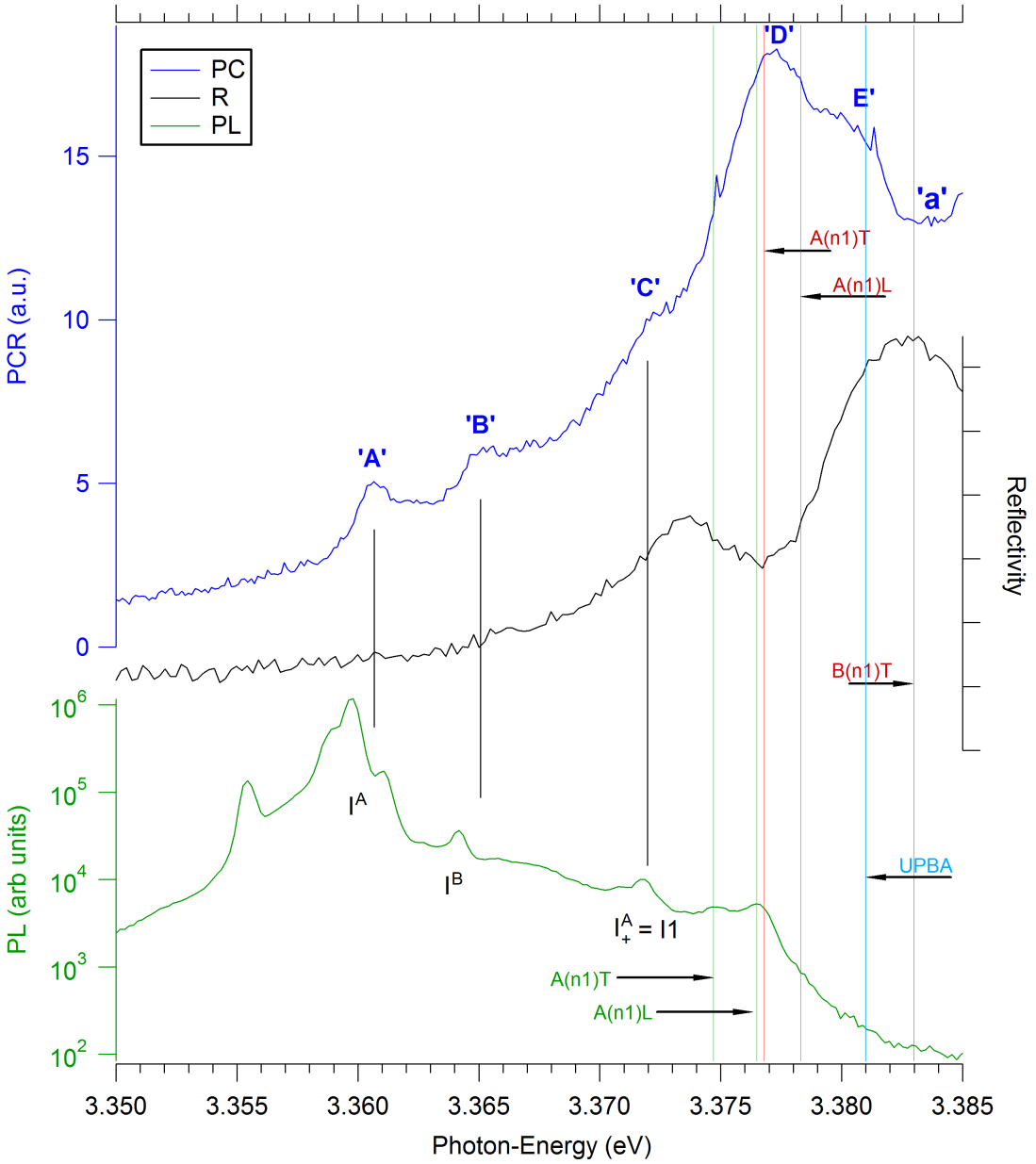

Figure 5.5: Closeup of the energy region of the bound exciton emission lines. For comparison, the red lines show literature values for A_T and A_L, as measured by photoreflectivity by Chichibu et al. [97], whereas the green lines show the energies measured by Syrbu et al. by photoluminescence spectroscopy [16]. A summary of these energies can be found in table 5.1. Peaks 'A', 'B' and 'C' of the photoconductivity spectrum align well with the PL-emission energy of the donor bound A-excitons, the donor bound B-excitons and the ionized donor bound A-excitons, respectively [14, 163]. Peak 'E' lines up very well with the energy associated with the 'upper polariton branch' of the A-exciton (UPBA) in bulk ZnO by Teke et al. [17], indicated in blue

with the energy quoted for the upper polariton branch of 3.3810 eV in bulk ZnO, in a recent publication about bulk ZnO by Teke et al. [17]. Most importantly, the spacing of peak 'E' to peak 'D' is 3.6 meV, exactly matching the spacing observed between the A-free exciton (i.e. A_L) and the upper polariton branch of the A-free exciton UPBA [17, 164].

5.2.4 Characteristic photoconductive response times of resolved features

Besides the change in the PCR-signal intensity with varied chopping speed, the energy of apparent spectral PCR-features may shift significantly. This most often is only an apparent shift, resulting from photoconductive processes with different response times being present at similar photon energies. For example a feature that is associated with a slow process might be dominating an energy region in the response spectrum at low chopping frequencies, to then become filtered out at chopping frequencies that are too high for its response time. Features with a shorter response time can then become stronger than the slow process for high chopping speeds (see figure 5.9 and 5.8). An apparent shift of a feature in the PCR-spectrum with a change in chopping speed results from at least two processes with different response times that are close to each other in the energy spectrum. The result is chopping speed dependent shift of the convolution of the two overlapping PCR-features. The fine features in the response spectrum of the 'high-definition' sample investigated here do not seem to be due to the overlap of features with differing sensitivities to light, as shown in figure 5.3. Here we want to investigate if the features at positions 'A' to 'G' are due to the overlap of processes with different response time. If they are not, this opens the possibility to distinguish differences in the characteristic response times of these features of well defined photon-energies.

Figure 5.6 shows the PCR-spectra as recorded with strongly varying chopping speeds, ranging from 5-3000 Hz. The overall intensity of the photoresponse strongly decreases with increasing chopping speed. But the energy position of features 'A' to 'G' in the photoconductive response spectrum of this Zinc face of c-plane bulk ZnO does not change when the chopping speed is varied. This allows us to assume that the transitions responsible for the fine structure are not due to the overlap of several features that lead to an apparent peak at certain positions, but that transitions of one specific type are responsible for each of the features marked with capital letters 'A' to 'G' in figure 5.6.

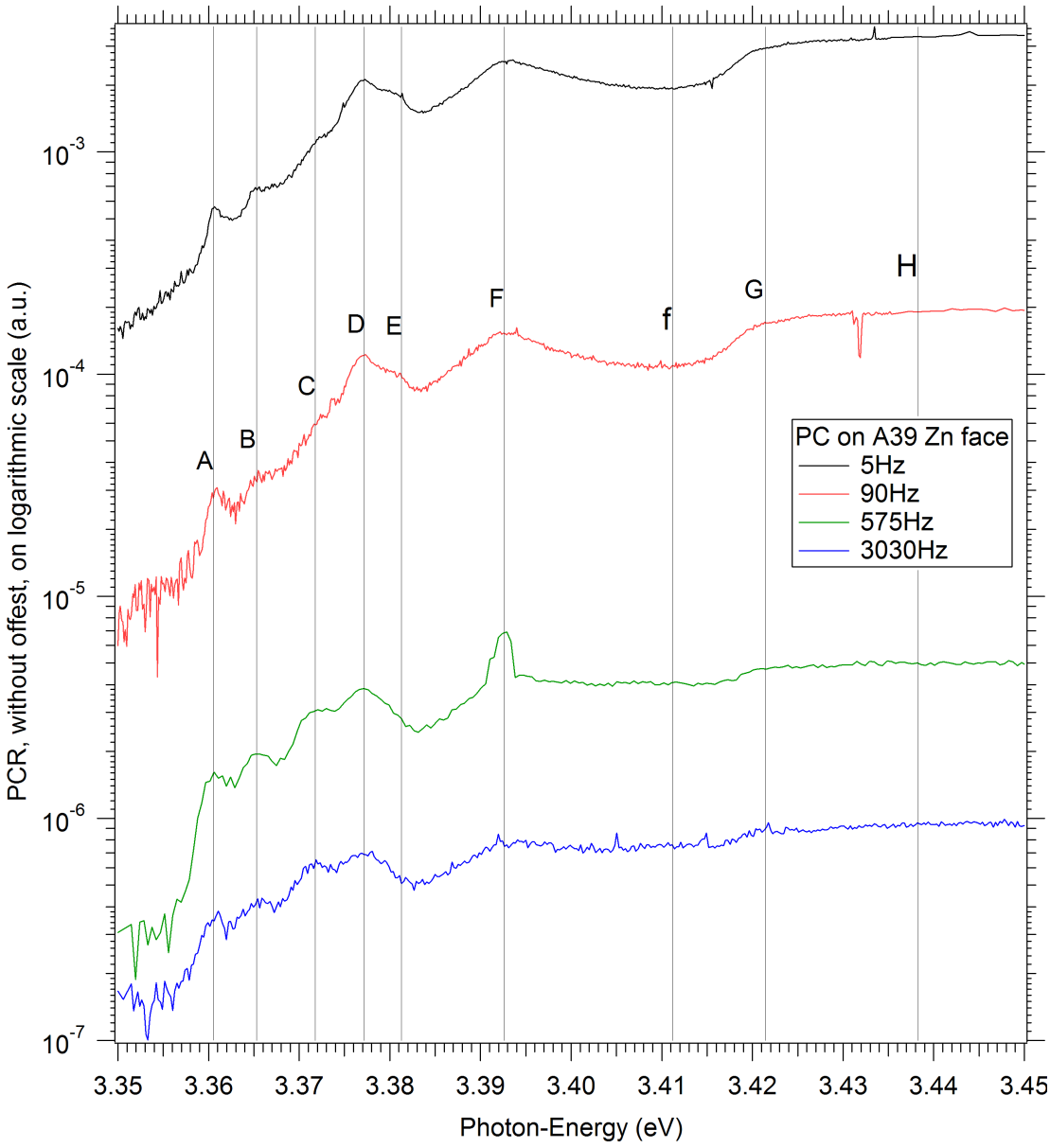

Figure 5.6: Photoconductivity spectra taken at a wide range of chopping speeds in a constant voltage configuration, at 10 Kelvin. The overall PCR-signal decreases strongly with rising chopping speed (no offset used), but peaks at energies marked by 'A' to 'G' respond differently to the variation in chopping speed

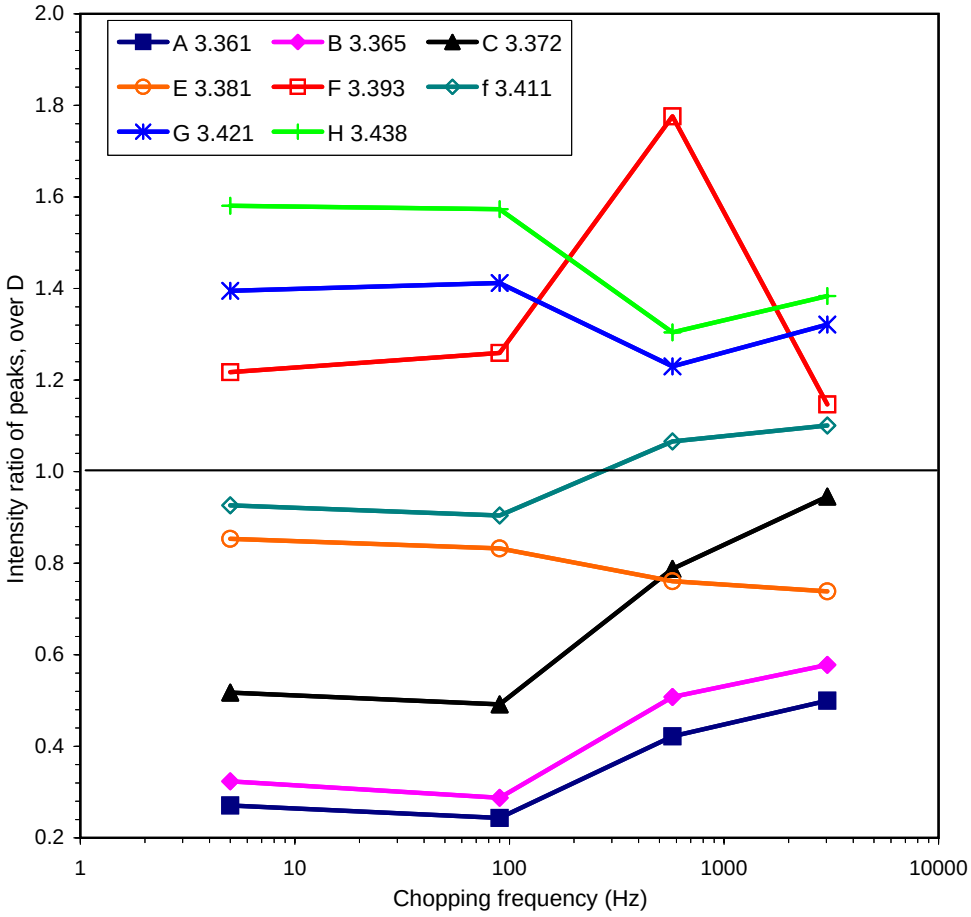

Figure 5.7: PCR-signal of features marked as 'A' to 'G' in figure 5.6, normalized against PCR-signal at 3.377 eV marked as 'D'

Besides bound [140] and free excitons [19], another possible source for a detailed photoconductivity spectrum are phonon related oscillations [140]. The variation of the chopping speed allows us to investigate if the different features each have a characteristic response time, or if they might be phonon-coupled to each other through phonon-interaction.

Figure 5.7 shows the intensity of the features at energies marked as 'A' to 'G', normalized against the intensity of the PCR-signal at 'D' (3.377 eV) which was attributed to $A\omega_L$. For the peaks at energies 'A', 'B' and 'C', the PCR-intensity normalized against the intensity at 'D' decreases from 5 Hz to 90 Hz, to then increase up to 3030 Hz. This behaviour is especially strong for peak 'C', as it is barely distinguishable against the background at 90 Hz and becomes much more pronounced at high chopping frequencies. Of course, the increase of the relative strengths of 'A', 'B' and 'C' in respect to 'D' can also be explained by the fact that 'D' becomes weaker with rising chopping speed above 90 Hz. But in contrast to peaks 'A' to 'C', peak 'E' always loses relative intensity in respect to 'D' when the chopping speed is increased. At 575 Hz, peak 'E' has vanished

in the shoulder of 'D', whereas for 3030 Hz there even is a slight dip at the position of 'E'. This lets us assume that the transition responsible for the peak at 'E' is slower than the transitions responsible for 'A', 'B', 'C' and 'D'. Equally, figure 5.7 lets us assume that the transition responsible for 'D' is slower than the transitions responsible for 'A', 'B' and 'C'.

As follows from the slow PCR transition responsible for the chopping-speed dependence of the PCR-signal in figure 5.8 as well as the fast transition in figure 5.9, the PCR-signal usually has a well defined chopping frequency with maximum PCR-signal. In figures 5.8 and 5.9 this happens at 40 Hz and 1.8 kHz, which is equivalent to a rise/fall time τ_{rf} of 25 ms and 0.55 ms respectively. In figure 5.7, the ratio of the intensities of the various peaks and dips versus the intensity of peak 'D' also does not monotonically increase or decrease, but the intensity ratio shows minima at 90 Hz for peaks 'A' to 'C', as well as minima at 575 Hz for 'G' and 'H'. Also a strong maximum at 575 Hz for the peak at 'F'. These minima and maxima are expected to be related to the maximum PC-response at the frequency that matches the response time of a particular transition. Therefore the A-free excitonic transition 'D' seems to have a response time that matches the chopping frequency around 90 Hz, causing dips for 'A', 'B', 'C', 'G' and 'H' in that region, whereas transition 'F' has a response time that nearly matches the chopping frequency of about 575 Hz, causing a strong peak in its response at this frequency. As a result, peaks 'A', 'B', and 'C' show the fastest response time, matching a chopping speed of more than 575 Hz. They also show a very similar chopping speed dependent intensity relation to peak 'D'. The disappearance of 'C' at 90 Hz can fully be related to the 'D' transition hitting its response time for that chopping speed region.

In conclusion we were able to derive an estimate for the response times of the various features observed in the PCR-spectra of the 'high-definition' sample investigated here. The assumption that features with a different response time are likely to be associated with a different process has been demonstrated through the response of transition 'E', which not only shows a much slower response than features 'A' to 'D', but is also clearly not associated with the same energy coupling. The transitions 'A', 'B' and 'C', that were brought into context with the bound exciton transitions in the PL-spectrum earlier, have shown to possibly be related to $A\omega_L$ through a coupling mechanism that is responsible for the equidistant spacing.

5.2.5 Regularity in the PCR-fine structure

At chopping speeds of 575 HZ and 3030 Hz, the PCR-features 'A', 'B', 'C' and 'D' in figure 5.6 very much look like oscillatory features. At these high chopping speeds they are 'stripped' of the slower surrounding PCR-background, therefore their position is more directly related to the energy of their underlying fast processes. Figure 5.10 shows how it actually is possible to place equidistant

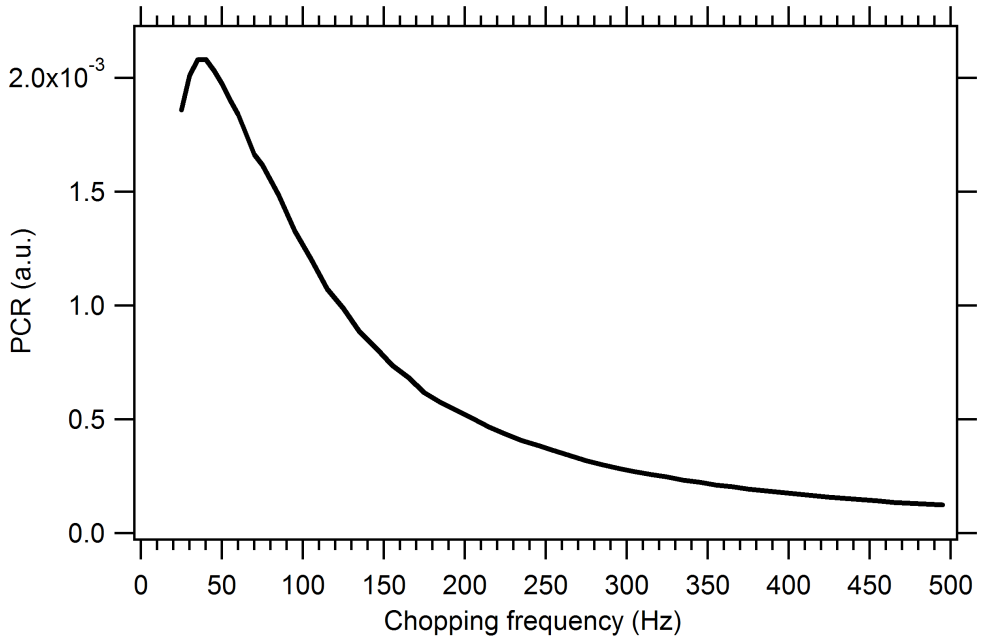

Figure 5.8: Typical influence of chopper speed on PC-intensity for the case that the response time of the sample is slow, with the maximum response at ≈40 kHz (25 ms), as measured on an MBE-thin film

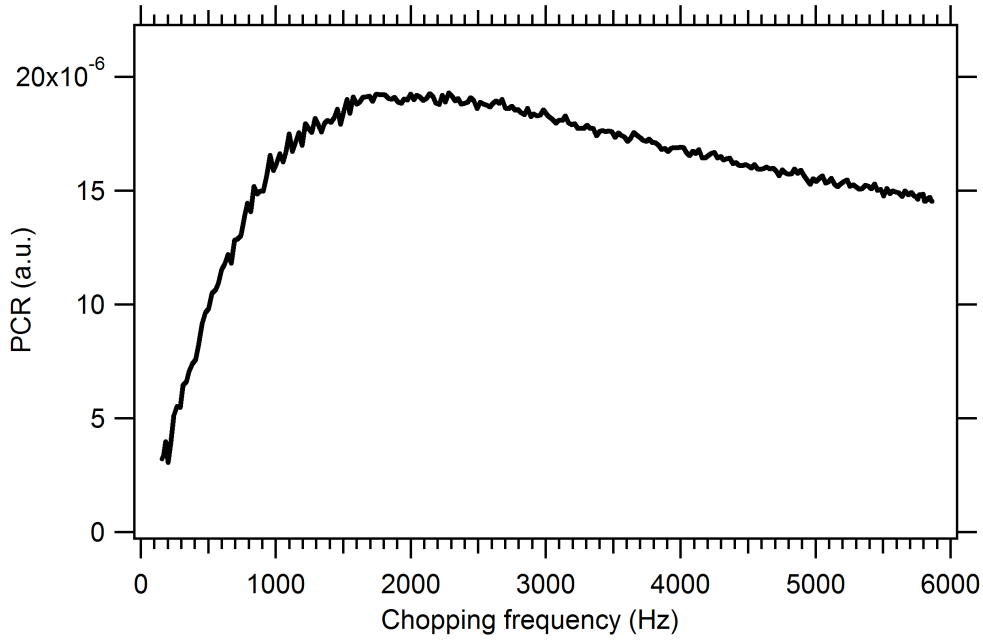

Figure 5.9: Typical influence of chopper speed on PC-intensity for the case that the response time of the sample is fast, with the maximum response at ≈1.8 kHz (0.55 ms), as measured on SnO_2 cluster films on SiN [165]

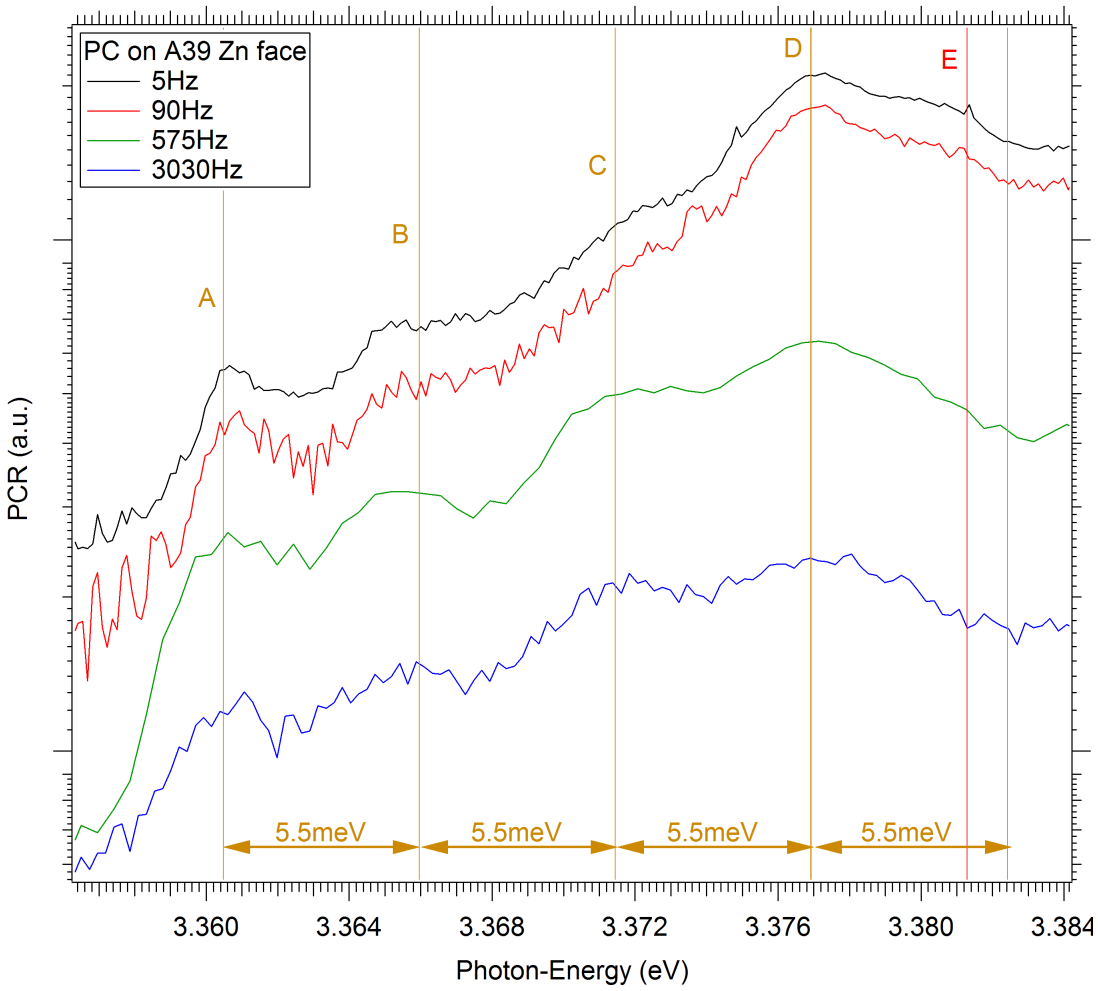

Figure 5.10: Fitting energies at a regular spacing (5.5 meV) to the fine structure in the PCR of bulk ZnO

markers with a spacing of ΔE= 5.5 eV on these four features. The position of the peak energy of the feature marked as 'B' is misleading for the scan taken at 5 Hz. It seems like the PCR is suppressed for the spectra taken at 6 Hz, exactly at the energy where marker 'B' (3.3660 eV) is placed in figure 5.10. It also becomes clear that the transition marked as 'E' can not be due to the same oscillatory relationship, as the energy of transition 'E' is too close to transition 'D'.

If the coupling energy of 5.5 meV is due to phonons, it is of substantially smaller energy than the phonon coupling energy of 72 meV that is associated with the LO-phonon in the ZnO lattice. As described by Vanecek et al. [108], the period of oscillations in the PCR-spectrum is nevertheless always associated with the LO-phonon energy $\hbar\omega_0$ at the centre of the Brillouin zone, as the primary reason for the oscillations is a strong interaction of excitons or (photoexcited carriers) with LO phonons. As discussed in section 5.1.2, the case of phonon related oscillatory photoconductivity at energy intervals smaller than E_{LO} can

be associated with surface phonons via the dielectric constant of the adjacent medium. In the case of the 'high definition' sample the adjacent medium can be expected to be adsorbed air and other contamination such as oil, as only a layer with the thickness of several nanometres interacts with the phonons on the sample surface. This interaction takes place through the dipole moment of the oscillations of the sublattices of Zinc and oxygen against each other [32]: The macroscopic electric field (E_{sph}) of this dipole moment decays exponentially with the wave-vector $\boldsymbol{k}$ of the surface phonon. Therefore a penetration depth of the surface phonon into the adjacent layers of ZnO crystal on one side and the adsorbed layer on the surface on the other side is defined by their dielectric constant. In ZnO a penetration depth of several nanometres can be expected [32]. The electric field E_{ph} interacts with photocarriers in the space charge layer (the layers of the crystal that are close to the surface), as well as with external electrons in the adsorbed layer. The scattering process between the resulting hot electrons and surface phonons influences the energy and momentum of the phonons. As this model is used to describe reductions of the phonon energy from 72 meV down to 68 meV for strong influences from the adjacent layer through adsorbed xenon [32], this only model found in the literature with $E_{ph} < E_{LO}$ does not seem sufficient to explain a phonon-energy of less than 6 meV.

The origin of an oscillatory structure with a spacing of merely 5.5 eV thus has to be investigated more closely. Two approaches seem reasonable at this stage: The first approach is to assume that peaks 'A', 'B' and 'C' are in fact related to the bound excitonic states as suggested by figure 5.5: The localization energy of free excitons to the ionized donors is the energy spacing between peak 'D' and peak 'C'. Since peak 'D' is matching the energy of the free exciton $A\omega_T$ and shows the appropriate temperature dependence in the spectra investigated in section 5.3, we can safely assume that it is related to $A\omega_T$. Peak 'C' matches the energy of the ionized-donor bound A-exciton $I_+^A = I1$ at very high precision, with an offset between the bound exciton emission line $I1$ in the PL-spectrum and the peak in the PCR-spectrum marked as 'C' of merely 0.2 meV. This is well within the uncertainty for the comparison of two measurements taken on two separate equipments, which is expected to be on the order of 1 meV in terms of reproducibility of absolute values. A lower uncertainty is possible for the relative spacing of features within the PL or PCR spectra themselves, which is expected to be of about 0.3 meV. The offset between peaks 'B' and 'A' to I^B and I^A could be accounted for by this uncertainty and the FWHM of Peaks 'A' to 'D', which is about 1.2 meV: The middle of peak 'B' is located 0.9 meV above I^B, and peak 'A' is located in the middle of two strong donor bound PL-emission lines that are spaced by 1.2 meV.

Couturier1989 et al. [140] relate similar fine peaks in their normalized photocurrent spectra with free and bound excitons. They confirmed the 1:1 energy relation to the corresponding PL-lines by applying the impact ionization model: This model relates the dissociation of the free and bound exciton levels into photoconductive carriers with the simultaneous decay of the PL-line. This is

understood to show that electrons accelerated by the applied electric field dissociate the exciton complexes through impact ionization (see also page 128). The measurements of the high quality bulk crystals investigated here were done at a constant current of 40×10^{-6} A, resulting in a typical voltage of ≈ 4 V. Across the distance between the contacts of 0.5 cm, this results in an electric field of $\approx 8\ V/cm$. The according electric field threshold for GaAs was determined to be 0.8 V/cm [139].

Another, more outrageous approach to take account of the similar nature of the PCR peaks 'A'-'D' observed, would be to relate peaks 'B' and 'A' to peak 'C' with the same interaction that relates 'C' to 'D', by fitting a regular spacing between peaks 'A', 'B', 'C' and 'D' in our PCR-spectrum, as shown in figure 5.10. This would introduce a coupling energy of 5.5 meV that is very similar to the energy found to be the localization energy of A_L to an ionized Ga-donor: In photoluminescence, the transitions of A_L and $I1$ are understood to be related to each other through the localization energy of the free exciton to the ionized Ga-donor bound exciton: Meyer et al. [163] have shown that $I1$ can be identified as the ionized version of the donor bound exciton $I8$, which itself can be associated with Ga-donors [14]. They quote a localization energy for $I1$ of 4.1 meV in respect to $A\omega_T$, with an energy spacing between $A\omega_L$ and $A\omega_T$ of 1.3 meV. This results in a localization energy for I_1 in relation to A_L of 5.4 meV. Bertram et al. [166] have shown that the I_1 emission line is associated with domain boundaries in high quality ZnO films: They used highly spatially and spectrally resolved cathodoluminescence, and found that emission lines at the energy of I_0 and I_1 are only found at domain boundaries of the crystallites of their epitaxially grown films, whereas the $I8$ emission is homogeneously observed without correlation with the film morphology. As the energy spacing between $I1$ and A_L is thus related to a surface effect, it might also show as a coupling energy between features in photoconductivity.

Temperature dependent measurements would be a logical next step, to investigate if the localization energies of the respective PL-features correlates with the localization energy of the PCR-features observed here. Unfortunately we did not have a working temperature controller at the time of measurement, and at a later stage could not reproduce these spectra with clean samples of the same material, as is discussed in section 5.2.6. Another good next step for our measurements would be to investigate if the excitonic features observed show a field dependent inverse relation to the intensity of their photo emission lines, as is typical for the impact ionization process. This is an experiment that would give a good indication of the relation between peaks 'A' to 'D' in PCR and the corresponding excitonic lines in PL and would nicely complement temperature dependence investigations of the localization energy associated with peak 'A' to 'D'.

Table 5.2: Position of markers 'A'-'D' in 'high definition' PCR spectra (in eV)

Equidistant spacing of 5.5 meV:			
'A'	'B'	'C'	'D'
3.3605	3.366	3.3715	3.377
Individual peak positions			
3.361	3.365	3.372	3.377
Assigned to:			
I_A	I_B	I_A^+	A_L
Literature values:			
I_6 : 3.3608 [14]	I_A+4.7 meV [163]	3.3718 [14]	3.3772 [14]

Table 5.3: Position of other markers in 'high definition' PCR spectra (in eV) (see e.g. figures 5.3, 5.4 and 5.6)

'E'	'a'	'F'	'G'	'I'	'J'	'K'
3.381	3.383	3.394	*	*	3.434	3.450
Assigned to						
UPBA	B_T	B_L	$1LO_{DAX}$	$1LO_{AL}$		
Literature values:						
A_L+3.6meV	3.3830	3.3941	3.4339	3.4503		
=3.3808 [164]	[97]	[97]				

* Broad feature

5.2.6 Separating slow from fast photoconductive contributions

Figure 5.11 compares the PCR-spectrum of the 'high-definition' Zn-face sample (HD) that was investigated in section 4.4, with the PCR-spectra observed of clean Zn- and oxygen surfaces of the same bulk crystal. The spectra recorded at 90 Hz show a very good match of their energy-positions to 'HD'. However, the difference in Signal to noise (SNR) is striking. The Zn-face shows a substantially better SNR than the O-face. However, even the Zinc-face has a bad SNR compared to HD. The difference in responsivity between the Zinc and oxygen faces should be investigated closer in further studies, for its relation to the band-bending that is expected at the surface of the crystal due to the polarity of the crystal.

The noise level of the 90 Hz measurements of the clean surfaces make it im-

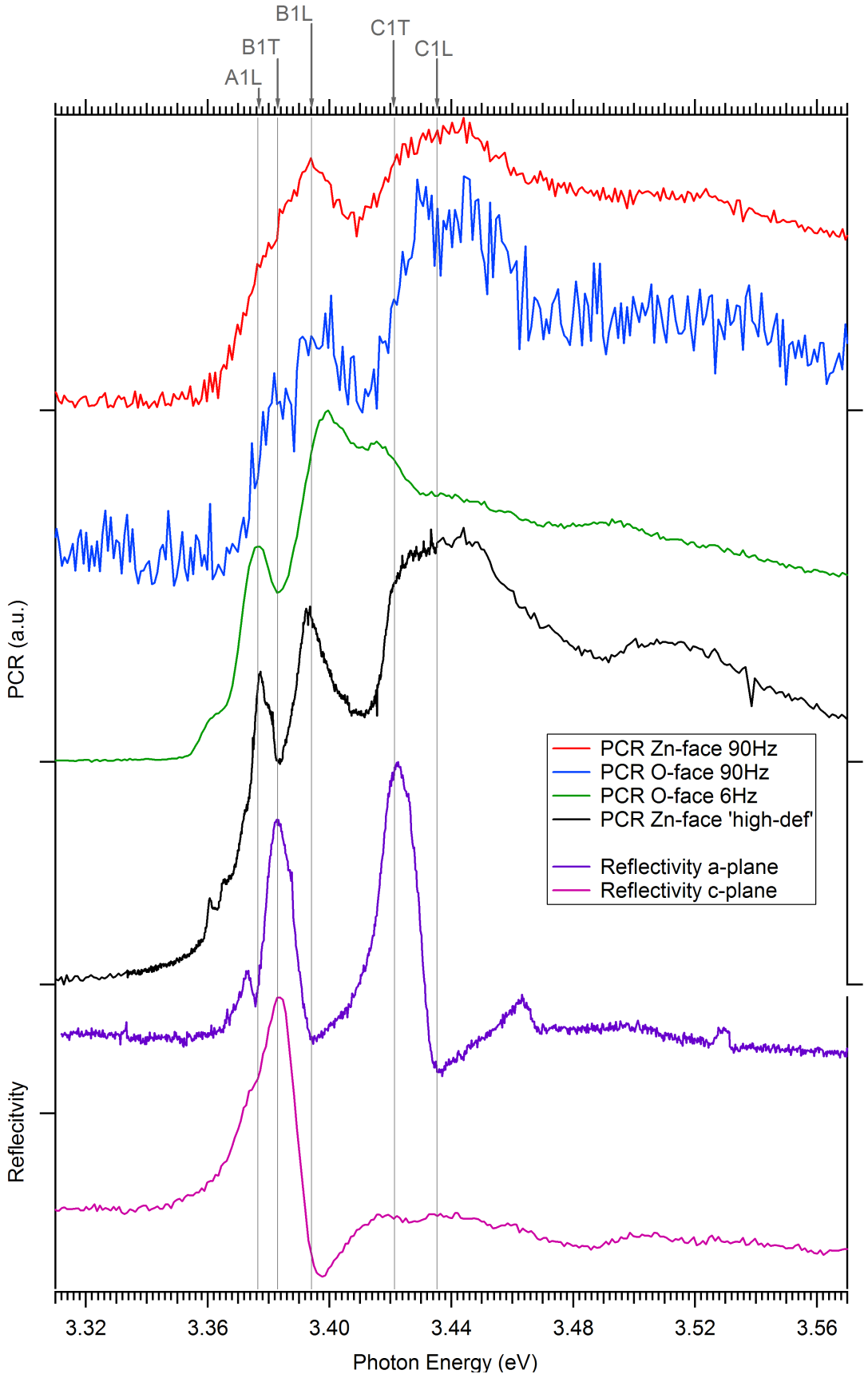

Figure 5.11: A comparison of the photoconductivity and reflectivity response of several hydrothermally grown bulk ZnO crystals, at 10 K. The vertical lines are the literature values for the respective free exciton transition. A good overlap can be seen for the energies of all PCR-spectra with the free excitons, besides the O-face spectrum recorded at 6 Hz, which is found to be distorted by slow photoconductive effects

possible to resolve the bound excitonic features that were investigated in section 5.2.3. Scanning at low chopping speeds substantially improved the SNR, since slow photoconductive processes become allowed to influence the spectrum. The scan at slow chopping speeds shows a much better SNR. However the positions of its spectral features are shifted considerably. This effect that has not been observed for HD, where the energetic position of features in the PCR-spectra were not susceptible to a change of the chopping frequency. The intensity of the PCR-response of HD also was not affected as drastically by a change in chopping speed.

It is important to keep in mind that the photoresponse of semiconductors can be related to processes that are very quick, on the timescale of microseconds [167], as well as deep level processes that can be very slow, in the order of seconds, minutes or even hours [33, 168]. Normally, slow photoconductive processes are strongly related to surface gas de- and adsorption, particularly in ZnO [134–136, 159]. But how does the surface affect the photoconductive spectrum if there is very little ambient gas to be adsorbed, at 10 K?

Tomm et al. [19] showed for PLD-grown films, that the photoresponse of excitonic features can be expected to be much faster than defect related processes at room temperature. They therefore obtained a procedure to filter the slow response from the fast response, by dividing scans taken at increased chopping speeds by scans taken at slow chopping speeds. To get a slightly better understanding of the slow photoconductive response observed for the clean samples at 6 Hz, we investigated its response to a variation in intensity of the incident light. Figure 5.12 shows the 6 Hz scans of the photoconductive response of the O-polar face of clean hydrothermally grown bulk ZnO, with and without the use of a neutral density filter. Instead of changing the slit-widths of the spectrometer to vary the light intensity to investigate the effect of the intensity of the incident light, a neutral density (ND) filter with an optical density (OD) of 0.5 was used here. This avoids the change of spectral and spatial width of the light-beam incident of the sample that is associated with a change of slit-width. The photoconductive response (PCR) spectrum of the scan using the ND filter has been normalized with the response curve of the ND filter. Since the two normalized spectra do not overlap in their PCR-signal, the PCR is not linearly dependent on the intensity of the incident light, but double the intensity for the incident light gives less then double the PCR-response. It is evident from direct comparison of the spectra measured with and without the ND filter, that there are regions in the spectrum that respond more strongly to the change of light intensity than others. This can be related to the slow photoconductive processes dominating this spectrum.

Dividing the normalized response spectrum obtained with ND0.5 by the normalized response spectrum obtained without a neutral density filter reveals a surprising detail: As can be seen by comparing the green curve of this ratio with the black curve of HD in figure 5.12, the spectral features in the ratio-spectrum

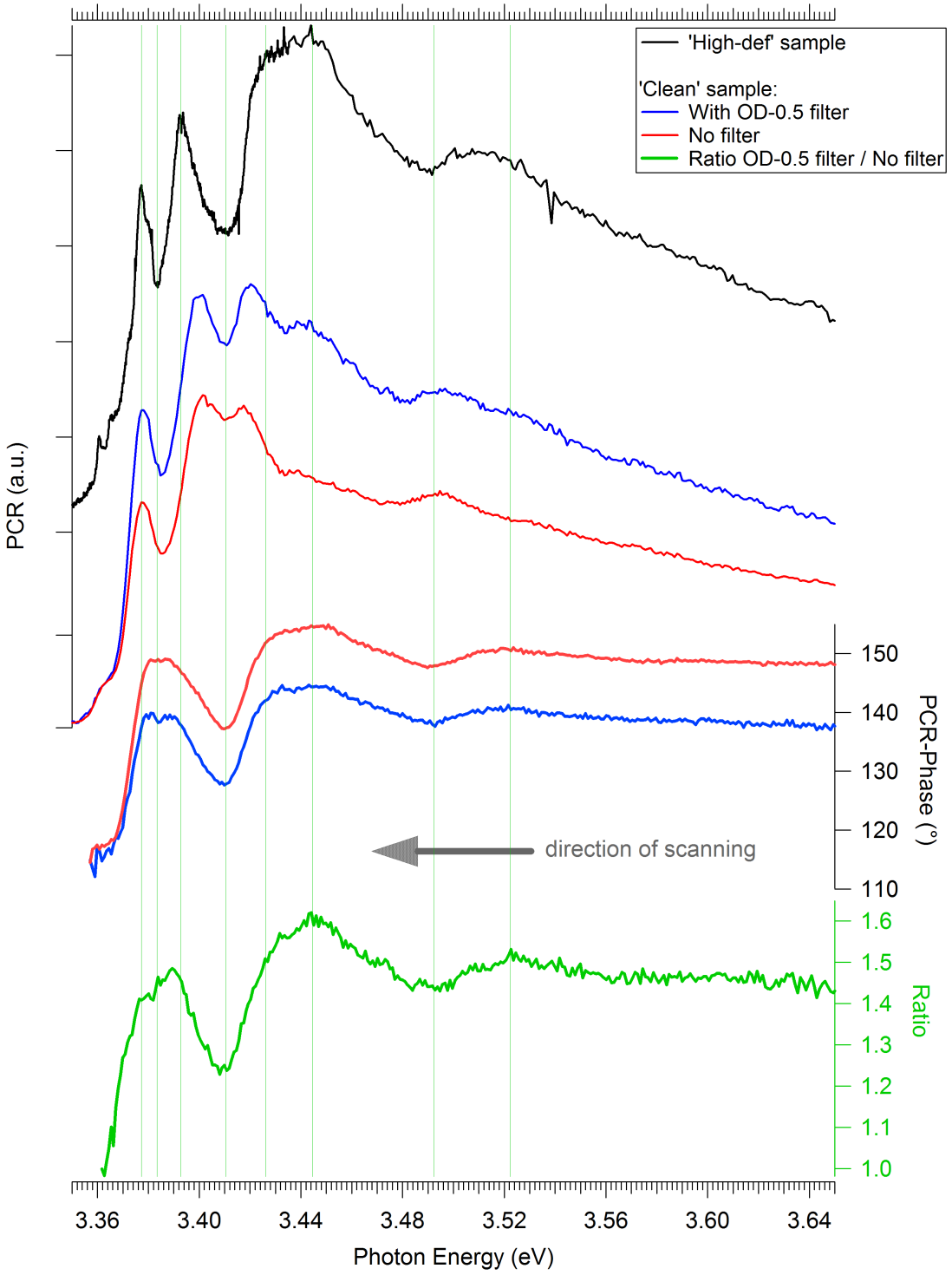

Figure 5.12: Comparison of PCR of 'High-definition' sample with PCR of new (clean) sample, taken at 6 Hz. For the clean sample, two scans normalized against the intensity of the incident light are shown, together with the spectra of the LI-phase for both light intensities. The plot at the bottom of the graph is the intensity of the PCR-spectrum recorded with filter divided by the intensity of the PCR-spectrum recorded without filter, and shows a surprising match with the phase spectra as well as with the spectrum taken of the 'high-definition' sample.

of these two scans taken at different light intensities strongly aligns with HD. The only difference between the ratio spectrum and HD is a different resolution. But all of the dips and peaks of HD can be found in the ratio spectrum, albeit broadened significantly, they are not shifted. This suggests that the change in signal intensity due to the change in light intensity is directly related to the band structure, whereas a persistent effect changes the spectrum related to the bandstructure in an unknown way. This might show why the ratio spectra of scans recorded at different chopping speeds as used by Tomm et al. [19] to avoid slow photoconductive effects was effective: the effect would be similar, particularly since spectra recorded at different chopping frequencies result in different intensities.

In contrast to the light intensity sensitive spectra of the sample investigated in figure 5.12, figure 5.3 shows that the 'high-def' samples shows a good match between the spectra taken at incident light intensities that are changed by a factor of 25. Besides a small shift of the peak marked as 'F', this indifference of the PCR-spectrum to the incident light intensity indicates that the 'high-def' sample is showing the photoresponse of mainly one type of effect, i.e. that the PCR-spectrum is not the result of an overlap of many different PC-processes with a different responsivity to the incident light intensity. Note also that the PCR-response of the HD sample has also shown to be unaffected of chopping speeds as low as 5 HZ (see figure 5.6).

Another way to illustrate the effect slow photoconductive effects have on the measurements taken here is to investigate the spectral response of the Lock-in phase: figure 5.12 shows that the Lock-in phase lines up surprisingly well with the HD-spectrum too. This shows that the change in the transient response observed by the Lock-In amplifier (LIA) is a combination of the slow response and the fast response. With a rise in the fast response, the onset of PCR that the LIA fits a sine to changes its shape, leading to an apparent shift of phase between the sine of the chopper reference wave and the sample signal.

A starting point to understand the peculiar transient response is to take into account that the spectra were recorded point by point, with the spectrometer selecting one wavelength at a time. Due to limitations of the spectrometer control unit, it was only possible to scan from high to low energy. During the time of measurement, which in this case is 23 minutes for 420 steps, the sample is continuously exposed to the chopped light of the wavelength selected by the spectrometer. Thus the PCR-spectrum recorded is influenced at each step by the light history effect that is caused by the radiation the sample was exposed to in the preceding steps of the scan.

In summary, our results indicate a static relationship between fast and slow processes in the photoconductive response spectrum, that can help us to distinguish the PCR-signal that stems from slow processes to the PCR-signal that stems from the band structure in the bulk of the crystal, which is expected to

be very fast. Since the only difference between the HD sample and the clean samples is the state of their respective surfaces, we expect surface effects to be at least partly responsible for the slow effects in PCR. Another important factor might be the quality of the electron deposited Indium contacts used, as the state of the surface during their deposition is also expected to be crucial.

A better SNR does not necessarily allow a better investigation of the intrinsic bandstructure of the material. One has to carefully asses if features in the PCR spectra obtained are in direct relation to characteristic energies of the bandstructure. It is of advantage that the photoresponse due to the intrinsic band structure can be expected to show a very fast response time, and that deep level extrinsic effects can be expected to be slow in comparison [19, 33, 169].

It is important to compare spectra taken at different chopping speeds, to identifying inconsistencies in the spectrum that are due to slower processes. The phase of the Lock-In Signal can also give crucial hints at the change in the transient sample response across the spectrum. In this case we were lucky to have one sample that showed very little change if the chopping speed was altered from 5 Hz to 3000 Hz. Since it also showed the most spectral fine structure, which also aligned very well with the spectra observed in PL, we assume it to be less influenced by slow effects of persistent photoconductivity. Slow changes in the photoresponse have shown to be able to strongly obstruct the spectral investigation of energy states that are important for the opto-electric response of ZnO. It has been found that for slow chopping speeds for the clean samples of hydrothermal bulk ZnO, the response was dominated by the slow change persistent photoconductivity, which might either be due to surface effects or to other traps for charger carriers with a very slow release time, in the order of seconds.

5.3 Temperature dependence of excitonic features in PCR of bulk ZnO

Since we established that for sufficient chopping speeds, both the spectra of the clean Zinc and oxygen faces of hydrothermally grown bulk ZnO essentially have the same spectral response curves as the sample exhibiting the most fine structure, albeit with a much worse SNR, we here can investigate the temperature dependence of the response spectrum of the clean samples at elevated chopping speeds, and relate the findings to the energy spectrum of the 'high-def' sample that was lost.

Figures 5.13 and 5.14 show an overview of the spectra observed from 10 K to room temperature for each face. The markers on the spectra are placed by applying the expected temperature dependence of the bandgap to the markers. We here used the temperature dependence as stated by Hamby et al. [22], which

has been confirmed to be applicable for these crystals in section 4.5.1. The temperature dependence has been applied to the energies of the free excitons that have been observed to play a distinctive role in these spectra in the sections above. Thus we can investigate if the association we made between the PCR-features and free excitons is valid and what types of phonon interaction can be observed.

The temperature dependent spectra of both faces are very similar:

For the Zn-face, figure 5.13 shows that the energies of the free excitonic transitions A_T and B_L are matched by a shoulder and two peaks in the PCR-response across the entire temperature range. The shoulder associated with A_T turns out to be a dip with rising temperatures, as a strong feature at energies below A_T rises strongly with temperature. This feature is expected to be due to defect states that are activated by phonon-interaction with the band edge related onset of photoconductivity [19]. For the energy of B_T, there is no direct relation to a feature in the PCR-spectra, as it is located on the shoulder of B_L that dominates the spectrum in this region.

A very similar temperature dependent behaviour is seen for the O-face, shown in figure 5.14. As was mentioned earlier, the SNR of the O-face is much lower at 10 K, thus the position of the low-temperature PCR-features can not be determined with great confidence, but the markers for B_T and B_L seem to match a distinctive peak, whereas A_T is located within the onset of photoconductivity. With rising temperature, the position of B_L matches the position of a the lowest energy peak in the PCR-spectra that is clearly distinguishable above the defect related broad sub-band gap feature. At the position of B_T, a very weak shoulder can be identified for temperatures of up to 69 K. The A-free exciton can, as on the Zn-face, only be related to a very weak shoulder in the onset of PCR, up to 89 K. For temperatures of 119 K and above, the rise of a strong defect related PCR-peak at energies below A_T creates a dip at the position of A_T.

Up to now we have only tentatively identified the PCR feature at 3.43 eV. It aligns very well with the C-free exciton, as can be seen in figure 5.4. However, the PCR-scans are recorded off a c-plane surface, therefore the C-exciton can not be excited resonantly due to the selection rules investigated in chapter 3. But the C-exciton might be indirectly involved in the creation of a peak in the photoresponse spectrum. Since the spectra were recorded scanning from high to low energies, the levels associated with the C-free excitons can for example be filled by photons of higher energies and result in a higher photoresponse through trapped carriers at the energy of the C-free exciton. Therefore it would be very interesting to investigate the PCR-spectrum of high quality bulk ZnO by scanning from low to high energies.

The temperature dependent PCR-spectra though give a very important clue about the possible origin of this feature, as well as the feature at 3.52 eV: The features at 3.43 eV and 3.52 eV could be related to the first and second order

phonon replica of the combined peaks 'A' and 'D'. The non-Gaussian nature of the peaks positioned between 'G' and 'I' and at 'K' (see figure 5.3) respectively, can thus be explained by their origin in the overlap of two phonon replicas: As indicated by respective markers in figures 5.13 and 5.14, the anti-Stokes phonon replica with ΔE=LO=73.1 meV can be related to the energy of 3.361 eV of the donor bound A-exciton (DAX) that was clearly observed as peak 'A' for the HD-sample (see figure 5.5 and table 5.2), as well as to A_L at 3.377 eV. Towards higher temperatures, the bound excitonic component dies off first, thus leaving a more Gaussian phonon-replica peak that is shifted by the spacing of the two associated zero phonon lines.

The phonon replica indicated by markers in figures 5.13 and 5.14 are kept at a constant spacing to their respective zero-phonon lines and therefore are shifted according to the band gap. No temperature dependent change of the phonon coupling was applied. The shift of the phonon replica, particularly visible for the first phonon replica structure at temperatures around 119 K, is thus brought into connection with the localization energy of the donor bound exciton that is associated with peak 'A' in figure 5.5. This means that indirectly, we are able to investigate the temperature dependence of the fine structure observed for the 'high definition' samples through temperature dependent investigation of the two crystals that show much less detail in the donor bound exciton region due to weaker fast photo response at low temperatures.

The phonon replica associated with DAX dies off above 119 K for both faces, combined with a slight apparent shift to higher energies of the left phonon replica, which only is due to A_L for higher temperatures. This effect is hardly resolved but can be seen most clearly for the scan of the Zinc face at 119 K. The second phonon replica can also be observed at a further offset of 73.1 meV, as indicated by markers labeled with '2LO$_{AL}$' and '2LO$_{DAX}$' in figures 5.14 and 5.13.

The peak associated with B_L can be seen to get phonon broadened by the relation introduced by Hauschild et al. [23], as discussed in section 4.5.1: It can be seen that for the temperature steps between 119 K and 298 K, the peak of B_L gets phonon broadened, with a resulting peak position that is shifted to higher energies according to Γ, according to [23]

$$\Gamma = \Gamma_0 + \alpha * T + \beta/(e^{(E_{LO}/(k_b * T)} - 1), \tag{5.7}$$

with Γ_0=0.65 meV, α=0.016 meV, β=47 meV, E_{LO}=33.0 meV.

The defect related transitions at 150 K can be related to at least two subbands. This is evident for both the Zn- and the O-face.

Figure 5.17 shows the same temperature dependent PCR-measurement of the same surface as is shown in figure 5.13, but scanned at 6 Hz instead of 90 Hz. No temperature dependence could be fitted to the peaks, another evidence that slow effects of different non-excitonic nature dominate the PCR-spectrum of clean

hydrothermal bulk ZnO at low chopping speeds. It is interesting though that the dips at the energies of B_L and C_L can be traced up to room temperature. Although the dip at C_L is not really expected to be associated with the C-free exciton due to the selection rules mentioned above, this shows that dips in PC-spectra that are strongly influenced by slow effects do change according to the bandgap with temperature. Maybe that is a clue as to why some samples show dips at excitonic energies, whereas other samples show peaks [114]. It is also evident that the defect related structure below the energy of A_L gets very strong between 150 K and 250 K. The plateau in the defect related structure is expected to be an experimental artefact.

Simultaneous measurement of PCR and reflectivity

When measuring the PCR and reflectivity response spectra simultaneously, using the same incident light, their relative response in relation to the feature in the electronic structure of the semiconductor can be investigated reliably, as there is no doubt about the state of the sample, its temperature, the calibration and line width of the incident light or other effects such as the electric field resulting from the induced photocurrent. Figure 5.15 shows such spectra as recorded for temperatures ranging from 10 K to 150 K. For temperatures from 180 K up to room temperature see figure 5.16. The temperature dependent change of the width, shape and signal intensities of these free excitonic features can be compared: At 10 K the PCR-peak just below 3.4 eV, as well as the corresponding reflectivity dip are expected to be strongly associated with B_L. As shown before, the reflectivity and PCR features shift according to the band gap shift of high quality ZnO crystals. It is interesting to see that the excitonic features both broaden very similarly with elevating temperature. Especially at temperatures above 180 K, as shown in figure 5.16, it becomes evident that the broadening of the PCR-feature associated with B_L is not due to phonon-interaction that is specific to photoconductivity, but that the reflectivity dip broadens to a very similar extent at these elevated temperatures. Since the method of PCR and reflectivity are so different in their nature, it can be expected that the excitonic state itself broadens accordingly, and that the sensitivity and precision it can be detected with by PCR is very comparable to the sensitivity and precision achieved in our reflectivity measurements. This is remarkable and shows the strength of PCR-spectroscopy to investigate energy levels in ZnO.

5.4 Photoconductivity Study of ZnO Films Grown by Molecular Beam Epitaxy

For samples annealed at close to optimum temperature for improved optical properties as derived from the photoluminescence study in section 3.3, the spectra

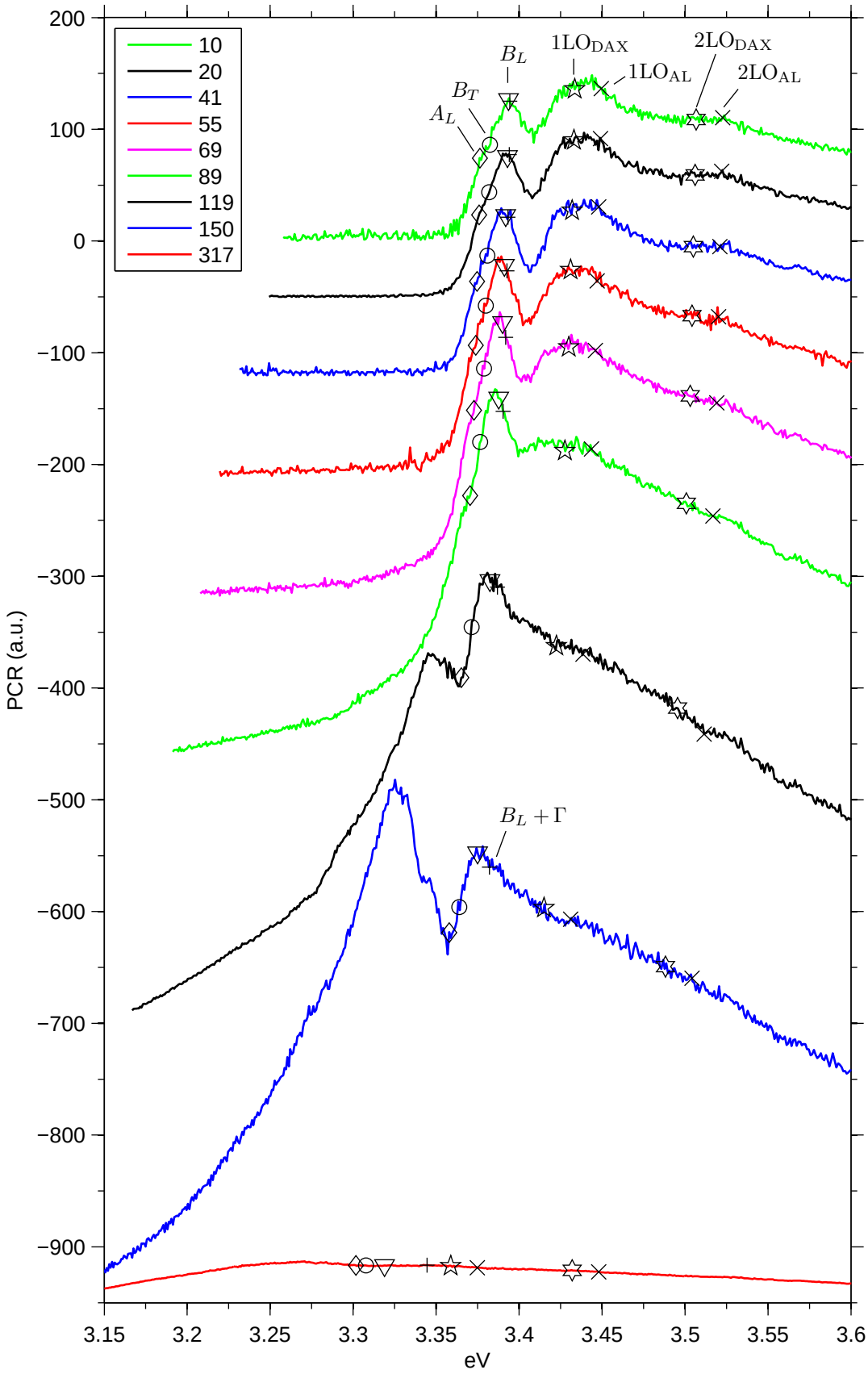

Figure 5.13: PCR of the Zinc face at selected temperatures (Kelvin), at 90 Hz, at an incident angle of light of 45°. The literature values for the energies of the free excitons [97] are indicated on the spectra with symbols. The position of the symbols is shifted according with the temperature dependence of the bandgap [22]

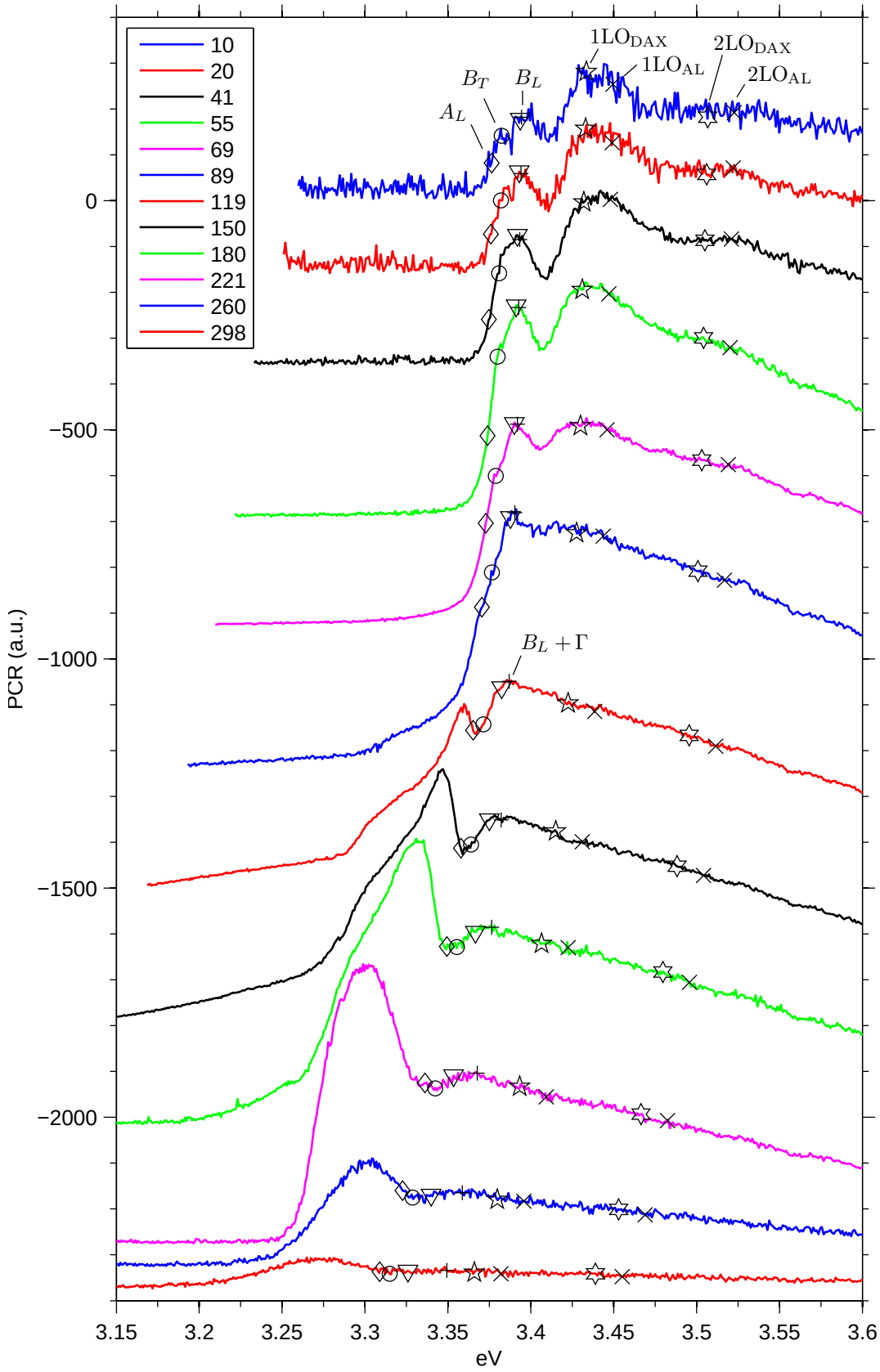

Figure 5.14: PCR of the oxygen face at selected temperatures (Kelvin), at 90 Hz, at an incident angle of light of 45°. The literature values for the energies of the free excitons [97] are indicated on the spectra with symbols. The position of the symbols is shifted according with the temperature dependence of the bandgap [22]

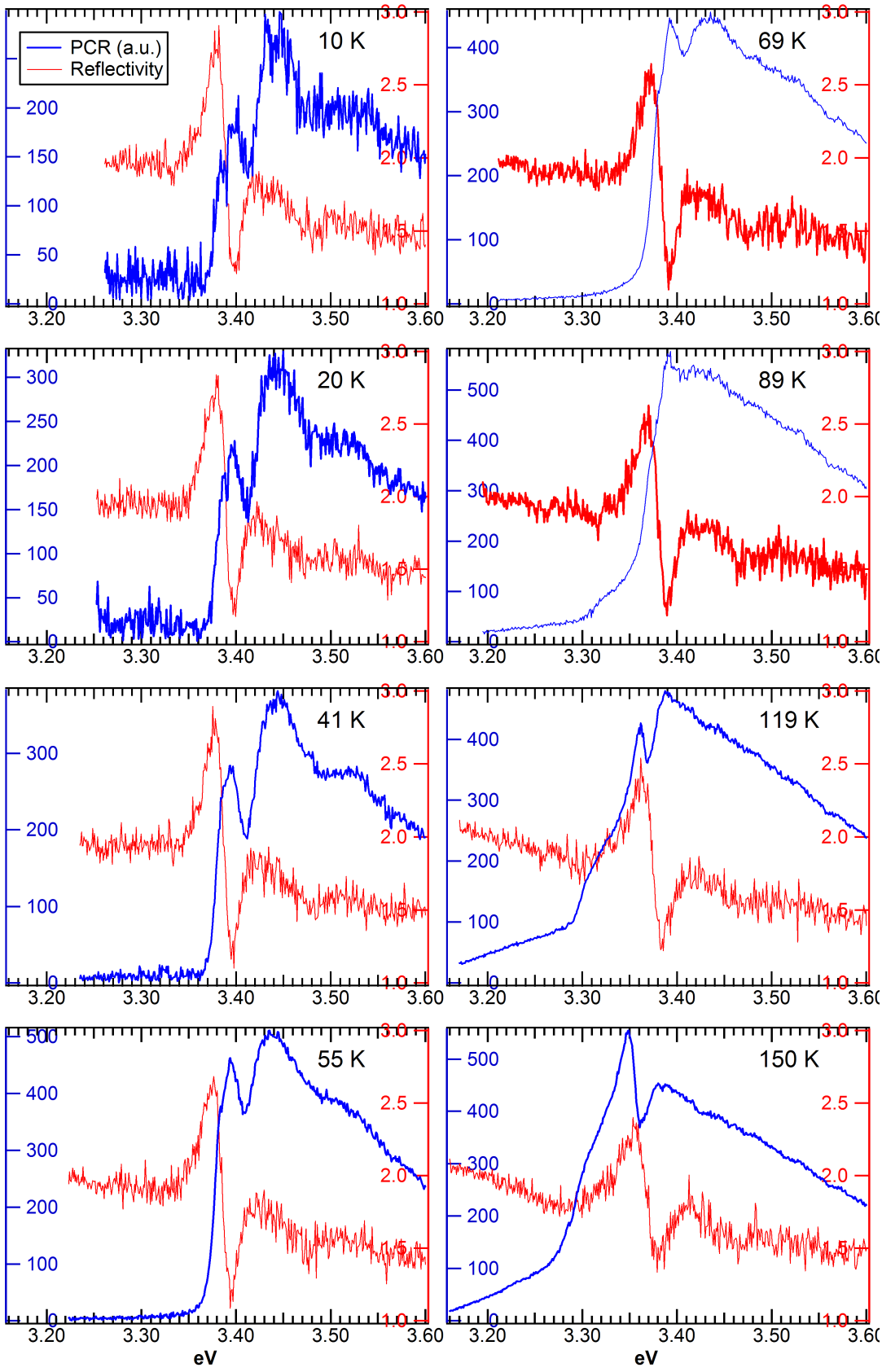

Figure 5.15: Comparison of the PCR-spectra of figure 5.14 with simultaneously recorded reflectivity spectra. At all temperatures, the position of the B-excitonic dip of the reflectivity spectra shows a very good match with the position of the PCR-peak associated with B_L in figure 5.14

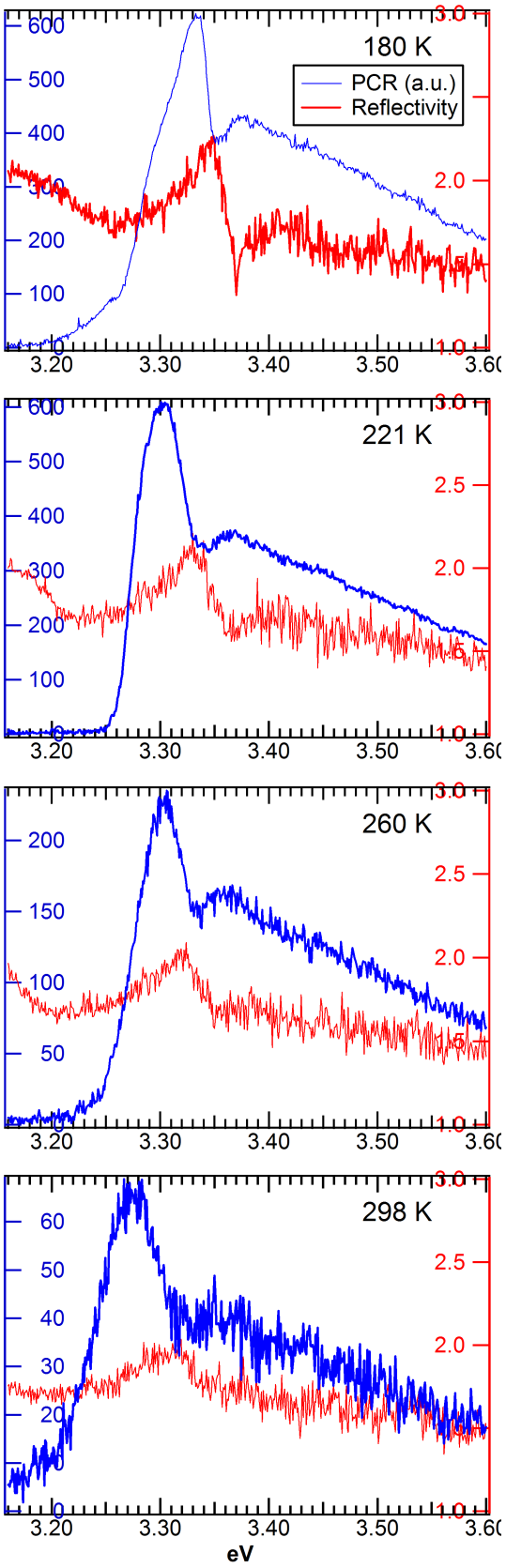

Figure 5.16: continuation of figure 5.15

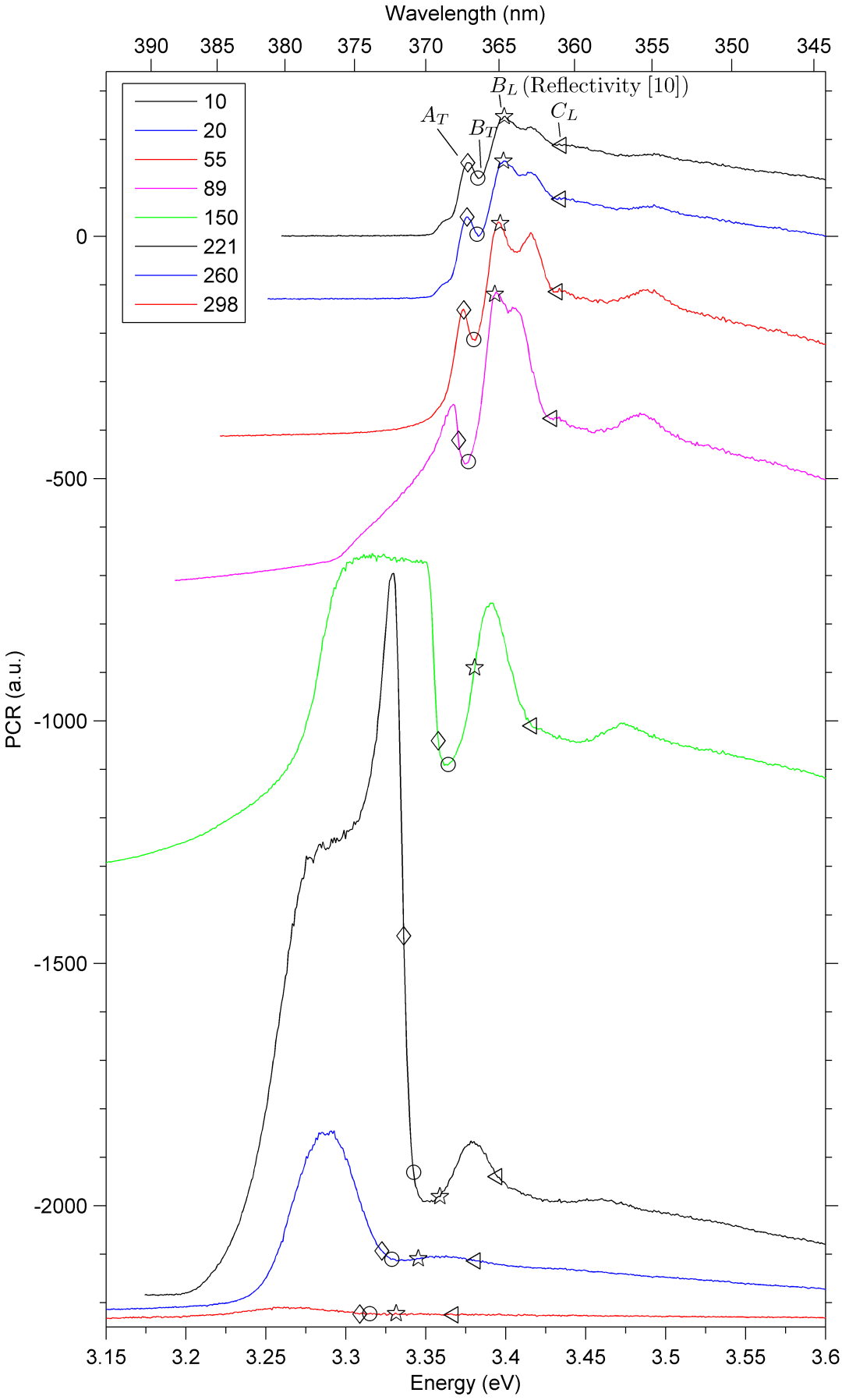

Figure 5.17: Same temperature dependent PCR-measurement of the same surface as is shown in figure 5.13, but scanned at 6 Hz instead of 90 Hz. Only the dips associated with B_L and the dip at the energy of C_L shift according to the bandstructure

of photoconductive responsivity (PCR) reveal strong multi-peak features at the band edge. The dependence of the various spectral PCR features to a variation of temperature give important clues about the different nature of their origins.

The photoluminescence response of the two samples annealed at 750°C and 850°C, as shown in figure 3.3 shows a markedly different photo emission spectrum in the region of the dominating bound exciton emissions around 3.36 eV. For the sample annealed at 750°C, the band edge emission has an intense peak at the position of 'A' and only a very weak should at the position of peak 'B', whereas for the sample annealed at 850°C and 950°C the PL spectrum is dominated by the emission of both energies, 'A' and 'B', as shown in figure 3.3. Despite this difference, the samples annealed at 750°C and 850°C both show by far the strongest PL-emission of all the samples investigated (see figure 3.5).

Figure 5.18 shows the direct comparison of the low temperature PCR-spectra of these two samples, confirming that there is a substantial difference in their (surface?) electronic structure. A difference in film quality is evident in the width of the energy range of the onset of photoconductivity of the two samples. For the sample annealed at 750°C this happens between ≈2.91 eV and 3.39 eV, a range of 470 meV. For the sample annealed at 850°C the onset is more rapid, between ≈3.05 eV and 3.39 eV, a range of 330 meV. For these MBE-samples, the onset of photoconductivity at 10 Kelvin therefore is much less rapid than at room temperature, where this transitions happens across an energy range of only 130 meV, as shown above. Figure 5.1 shows that for high quality bulk ZnO the transition from low conductivity to maximum conductivity happens between 3.245 eV and 3.380 eV, a transition region of 135 meV.

The low temperature PCR-spectra of the two samples annealed at 750 °C and 850 °C are shown in direct comparison with their photoluminescent response in figures 5.23 and 5.24. The phonon replica in the PL-spectra measured for the two samples have a slightly different spacing of 73.4 meV and 72.6 meV respectively. Using this spacing to track the zero phonon line by assuming the same spacing between zero-phonon line and first phonon replica results in a zero phonon transmission at 3.362 eV for the sample annealed at 850°C, the energy of the $I4$-transition that is featuring strongly in the PL-spectrum. For the sample annealed at 750°C, the phonon replicas in the PL are spaced by 73.4 meV, and the zero phonon line therefore is expected at 3.360 eV, exactly in the middle between the $I9$ related peak at 3.357 eV and the very weak $I4$ related shoulder.

For the sample annealed at 750 this lets us assume that the phonon replica is a combination of a replication of $I4$ and $I9$, with a much stronger Huang-Rhys factor [37] for the $I4$-transition, as the weaker PL-shoulder still shows a considerable input into the phonon replica. The zero-phonon line associated with the phonon replica is marked as 'OP' in figure 5.24, and nearly lines up with the energy of the first broad photoconductivity peak at 3.364 eV. The position of the free A-exciton in the PL-spectrum, marked as AX does not line up with the

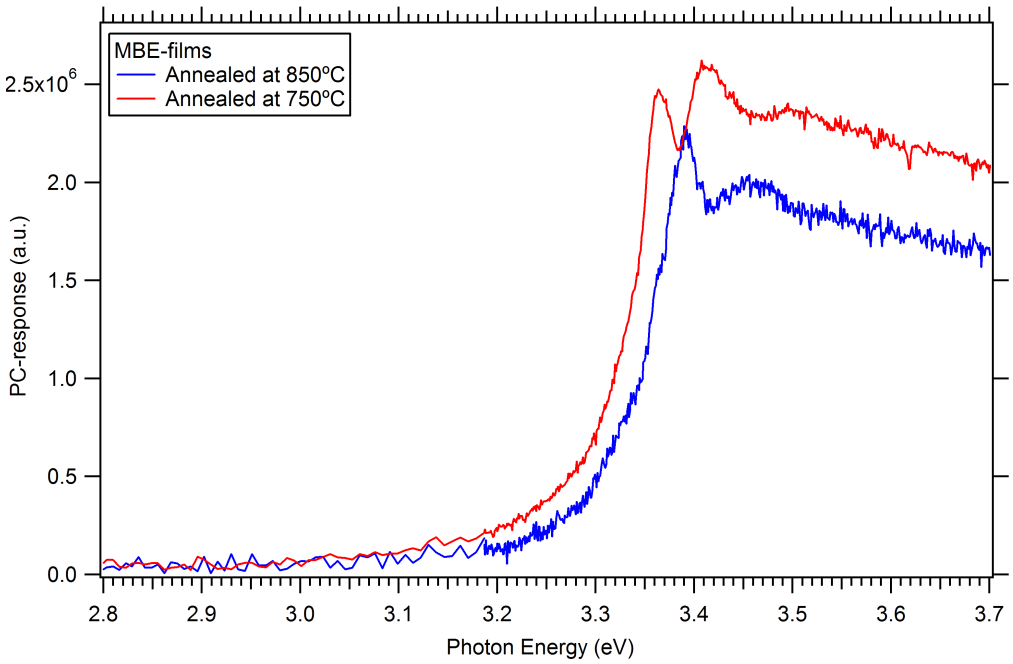

Figure 5.18: Direct comparison of the PCR-spectra recorded at 11 Kelvin, of MBE-films annealed at 850°C and 750°C. The PCR spectra are compared to the photoluminescent emission spectra in figure 5.23 and figure 5.24

PCR-spectrum, but the dip in the PCR-spectrum is located 2 meV above the expected position of the ω_T transition of the B-free exciton.

According to the low temperature spectra, the two MBE-films show a strongly differing photoconductive response. But only through the temperature dependent analysis of the change of the position of the features in PCR did it become possible to find a theory that works for both spectra. The temperature dependent spectra of each sample is shown in figures 5.19 and 5.20. The additional information that can be obtained about the PC-response of these two samples by doing temperature dependent measurements is the characteristic energy dependent shift of the band gap that has to be related to e.g. excitonic features in order to reliably relate them to the band structure. Therefore we tried to apply the temperature dependent shift of the band structure as stated by Hamby et al. [22] to the features of both spectra.

The peaks of the samples annealed at 750 C can not be fitted satisfactorily: Related to the temperature dependence of the band structure, the lowest energy peak appears phonon-broadened to lower energies with rising temperatures, whereas the second peak shifts to higher energies relative to the band gap shift with rising temperatures. Only fitting the dips of the spectrum with the expected temperature dependency of the band structure reveals the true nature of the PC-spectra observed: it is an oscillatory structure with dips at a spacing of

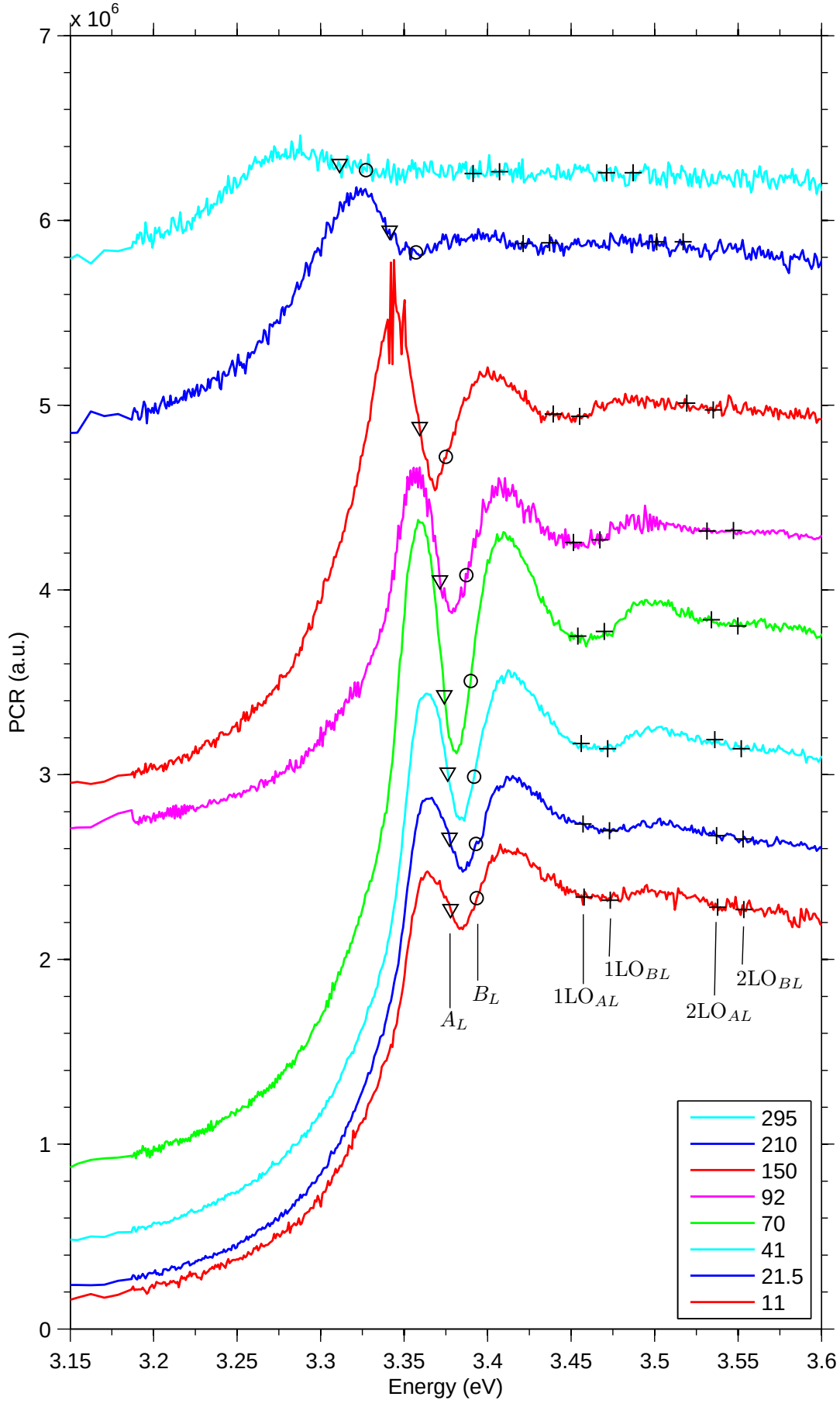

Figure 5.19: Temperature dependent PCR-spectra of MBE-film annealed at 750°C. The temperature in Kelvin for each scan is shown in the legend

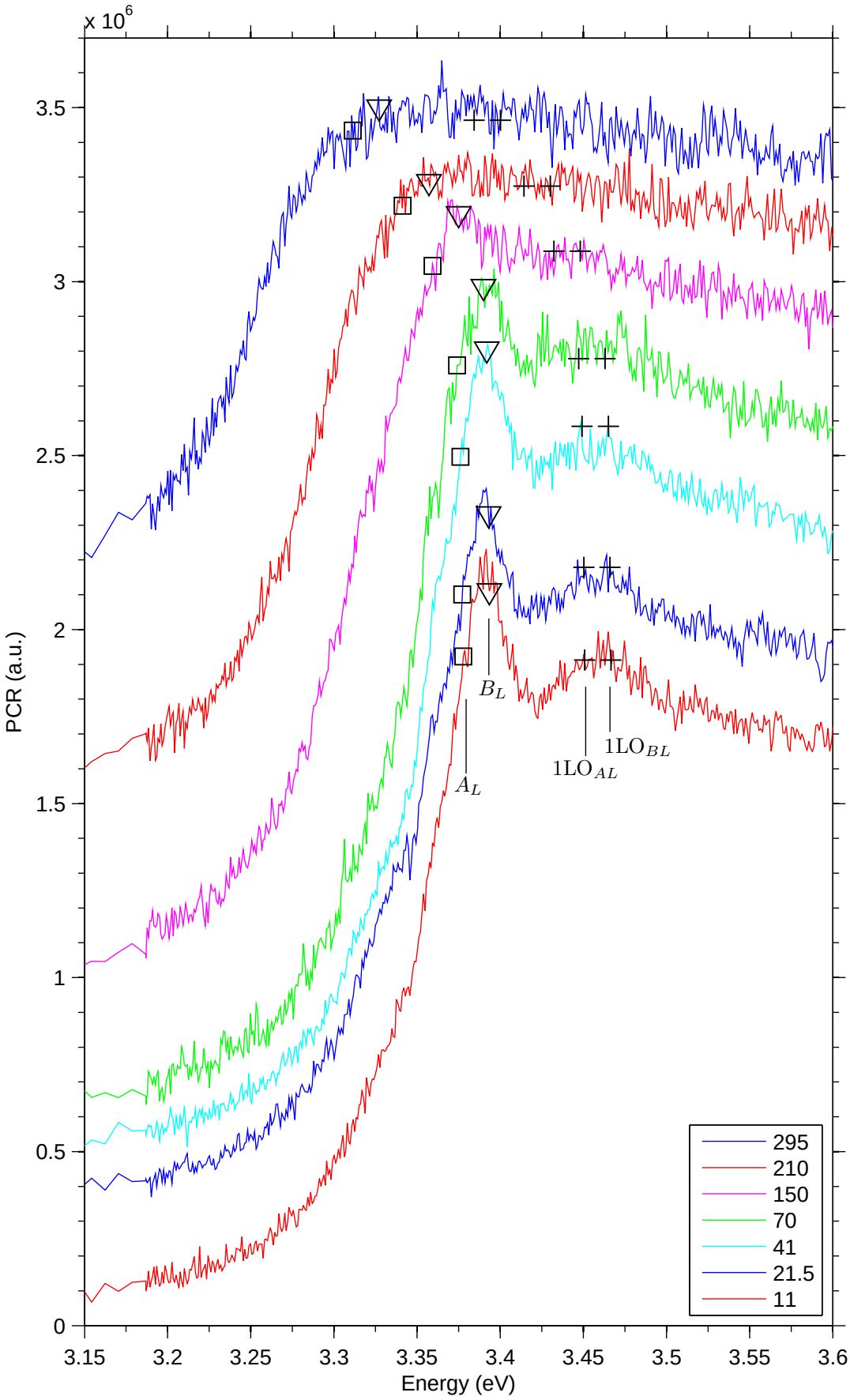

Figure 5.20: Temperature dependent PCR-spectra of MBE-film annealed at 850°C. The temperature in Kelvin for each scan is shown in the legend

80 meV. This is shown by the markers in figure 5.19, that show the literature energies of A_L and B_L. We assume that due to limited resolution, $A_L = 3.3783$ and $B_L = 3.3941$ as found in the literature [97] overlap to create a common dip in the PCR-spectra, that lies in between both levels and acts as an apparent broad collector level. As indicated by '+' markers, the phonon replica of both levels then can be shifted by 80 meV, where they also overlap to create the two visible phonon replica dips at a spacing of 80 meV. All three dips shift very well according to the band structure shift expected, as is seen by the good match of the respective symbols, relative to the three dips in figure 5.19: For all temperatures, the dips are positioned in between the two markers that they are related to. A slight rise of the first peak at higher temperatures is as expected, since a similar behaviour has been seen in the literature [19] and for the bulk crystals investigated in this chapter: A broad defect related PCR-peak just below the bandgap is expected to get activated at higher temperatures.

It is interesting that the oscillatory structure does not start at energies below the first dip (3.37 eV): the onset of PC is very smooth, without a hint of an oscillatory structure. The first dip therefore is expected to be associated with a collector level, the source of the phonon replica levels. Since the dip is positioned at 3.385 eV, it could be associated with B_T, which has an energy of 3.383 eV in unstrained ZnO. Since we see a strong influence of the longitudinal excitons for the bulk PCR-spectra investigated in this chapter, and the MBE-films are not observed to show a strong strain related shift due to crystalline strain, we do prefer the solution described above.

All three dips observed in the spectra in figure 5.19 are spaced at 80 meV. This spacing is substantially larger than the LO-phonon energy of 73.1 meV. As outlined in section 5.1.2, for the case of a phonon replica spacing of $\Delta E_{PR} >$ LO, the oscillatory structure is indeed due to LO-phonons interacting with photoexcited carriers or excitons [108]. The shift is created due to a rapid cascading of the hot electrons to the bottom of the band (and holes to the top of the band) via successive LO-phonon emission. The external field applied to drive the carriers can thus lead to a loss of momentum. For parabolic bands this results in minima at

$$E_{\min} = E_0 + n\hbar\omega_0 \left(1 + \frac{m_e}{m_h}\right). \tag{5.8}$$

Our findings agree very well with the fact that the phonon replica are always expected to create dips for this case [108, 140]. With equation 5.4 and $\Delta E_{PR} = 80\ meV \pm 2\ meV$ we can calculate $m_e/m_h = 0.094 \pm 0.027$, which lies well within the expected value.

Quite a different scenario is observed for the MBE-film annealed at 850 °C. A good fit is seen for the literature value of B_L to the first peak in the PCR-spectrum, see table 5.4. Although A_L can not be resolved as much more than a very slight shoulder (see figure 5.23 it becomes apparent in the position of the phonon replica: Since the phonon replica is a peak, it is suggested that it is

spaced at LO=73.1 meV from the collector level, since it is a special property for the case of ΔE_{PR} = LO, that phonon replica can be observed as peaks in PC [108, 140]. To achieve a good match in the temperature dependent spectra in figure 5.24 with a phonon spacing of 73.1 meV, an overlap of A_L and B_L is assumed in the creation of the broad phonon replica. This works well for all temperatures. Curiously, this sample annealed at 850 C does *not* show the defect related broad peak just below A_L that has been observed in the PCR of all the other samples investigated in this chapter. This might be due to a very good crystal quality. The more likely case though is that the peak is suppressed by a specific property of the sample that maybe should be investigated closer.

It can be observed in figure 5.21 that the peaks of the MBE-sample annealed at 750 C do not behave according to the temperature dependence of the bandgap that is observed for the B_L-related PCR-peak in bulk ZnO (orange line). The first peak of the MBE-sample annealed at 850 C aligns very well with the temperature dependence of the B_L peak observed in bulk crystals. The first peak in PC of the sample annealed at 750 C (green line) also does not align with the defect structure affected peak in bulk ZnO: The red line shows the position of A_L at low temperatures, connected to the energies of the defect structure that becomes apparent at 120 K (see e.g. figure 5.14). Thus the first low energy PC-peak of the MBE-sample annealed at 750 C is unlikely to be related to a combination of A_L at low temperatures that gets shifted to lower energies by the rising defect related PC-peak at elevated temperatures.

The PCR-spectra of the MBE-samples were recorded at 5 Hz, therefore including fast photoinduced effects on the resistivity as well as slow effects that have a rise/fall time τ_{rf} of up to 200 ms.

A very different behaviour was observed for the main peaks of the PC of the samples annealed at 750 °C (750) and 850 °C (850). For sample 750, the amplitudes of the double peak features decrease rapidly as the chopper frequency is increased. At 72 Hz, none of the features is left, besides the onset of photoconductivity. In contrast, sample 850's multi-peak features are not sensitive to increased chopping speeds. At the energy of the first PC peak of the sample annealed at 750 C (750), a much weaker shoulder can be seen in the PC spectrum of sample 850. This brings up the question if the photoconductive response of both samples at this energy is related. Further evidence for the common origin of the dominating peak of sample 750 and the shoulder-peak of sample 850 can be seen in their response times, measured as their sensitivity to higher chopper frequencies. It is remarkable that the shoulder-peak of sample 850 behaves like the peaks in sample 750 and decreases strongly with rising chopping speeds, vanishing at about 140 Hz. The other features in sample 850 can still be detected at chopper frequencies as high as 2 kHz. This result is partly shown in fig 5.22, which shows the change in amplitude for the first dominating peak of samples 750 and 850 as the chopper frequency is varied. The normalized peak-intensity is measured as the difference between the first peak and the first dip, normalized

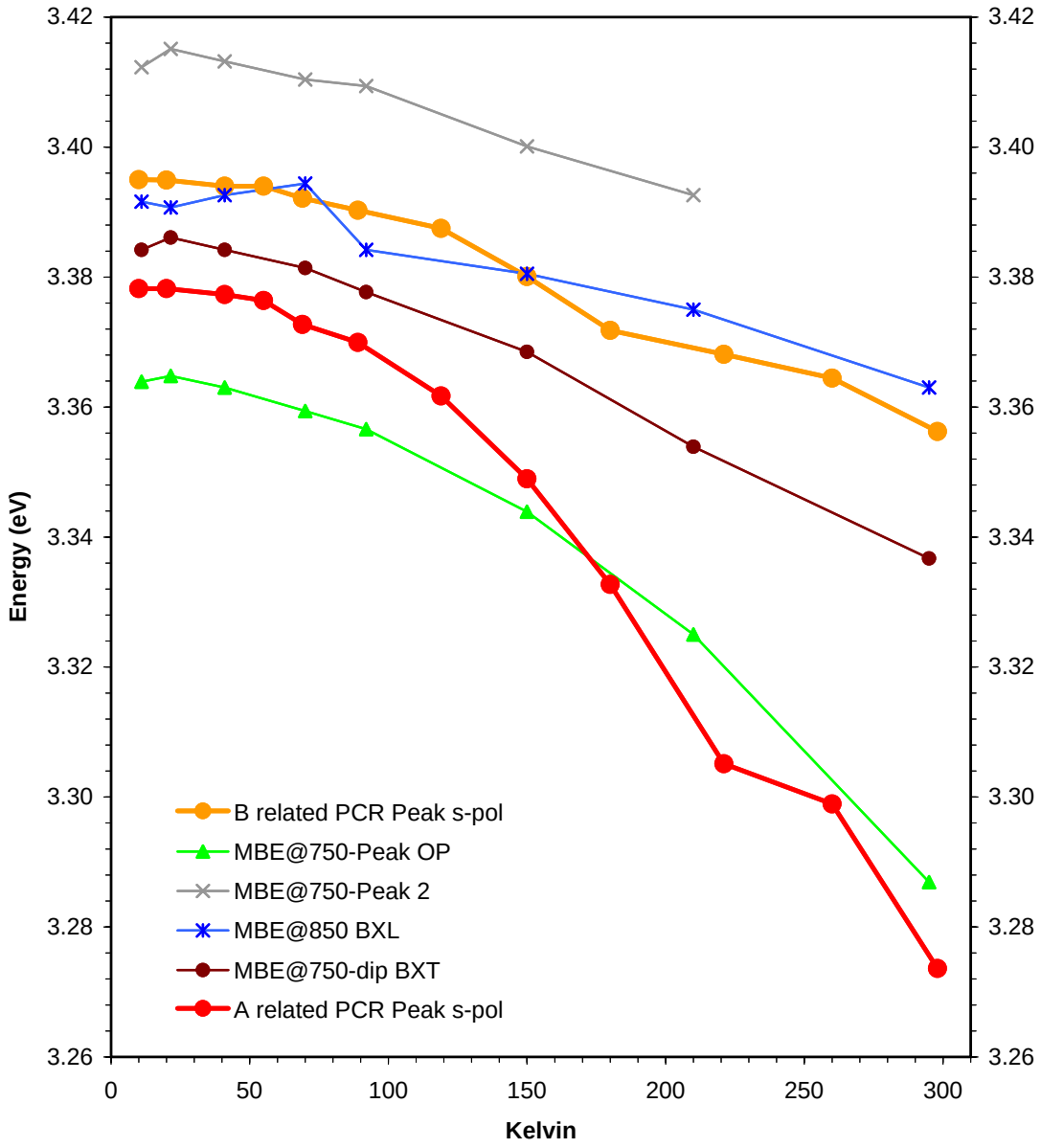

Figure 5.21: Temperature dependent position of features in photoconductivity of bulk ZnO compared to the MBE-sample annealed at 750 C and 850 C

against the background intensity. It can be seen that the relative peak intensity for sample 850 actually increased as the chopper frequency was increased.

This lets us conclude that there is a connection between the response time of the spectra and their relation to the energy structure of the sample: sample 850 with its faster response time shows a more direct relation of its spectra to the bandstructure of the material, as the position of its peaks are reflecting the energy of B_L and the phonon replica of A_L and B_L. In contrast, the slow response time of sample 750 seems to be connected with the fact that the peaks are a rather arbitrary position, whereas the dips in the spectrum move with temperature according to the temperature dependence of the bandstructure.

Of course more samples need to be investigated to generalize these properties.

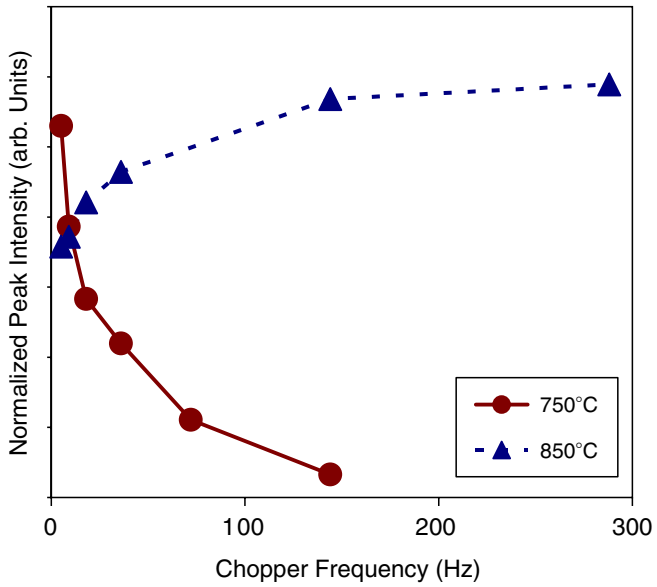

Figure 5.22: The frequency dependency of the intensity of the first dominating PC peak of samples 750 and 850. The peak intensity is normalised to the background photoconductivity at 3.72 eV and is measured as the difference in intensity between the first maximum and the first minimum in the PC spectrum. It can be seen that the peaks behave almost in an opposite fashion [66]

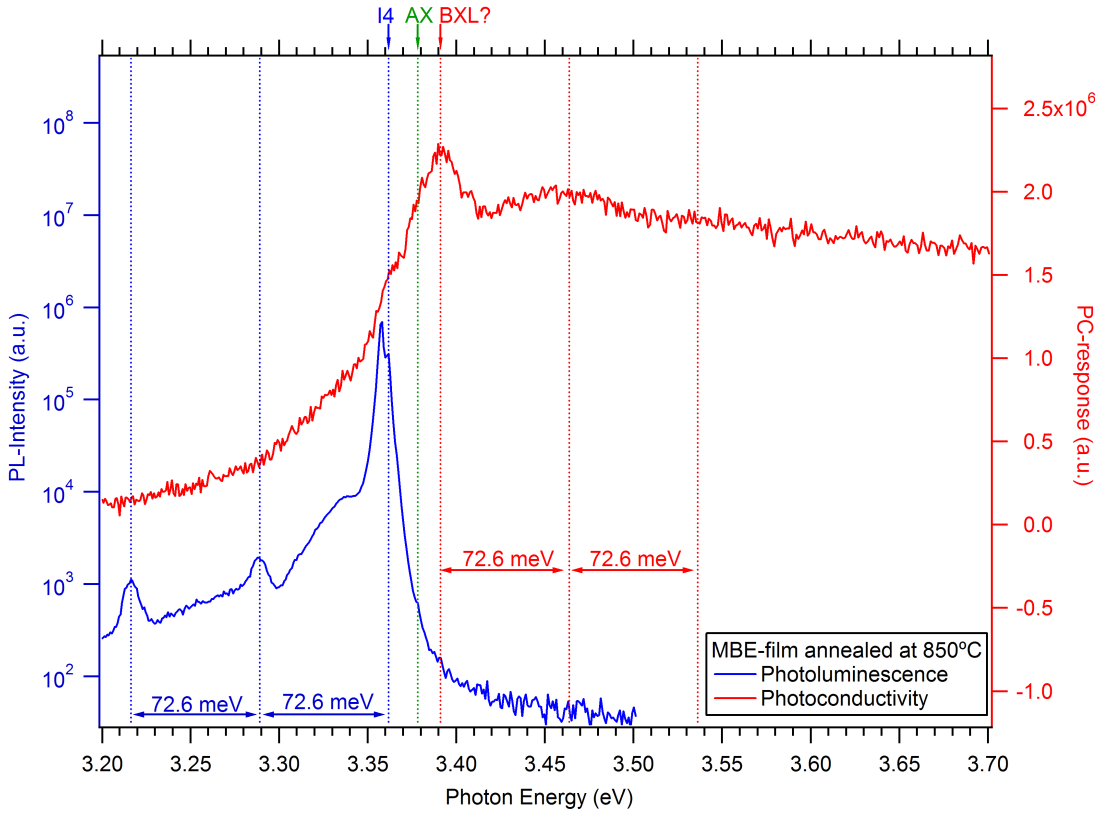

Figure 5.23: 11 Kelvin Photoluminescence and photoconductive response of MBE-grown ZnO film annealed at 850 degC

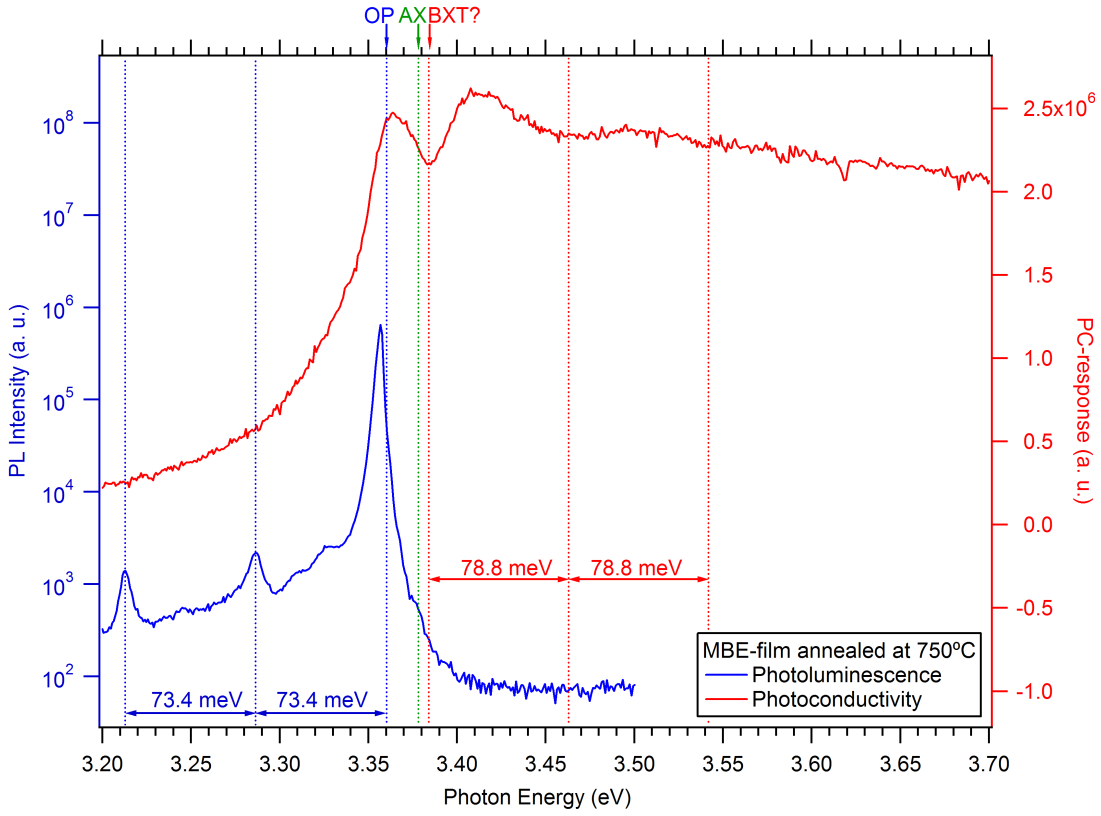

Figure 5.24: 11 Kelvin Photoluminescence and photoconductive response of MBE-grown ZnO film annealed at 750 degC

Table 5.1: Summary of the energy values for free excitonic features in photoconductivity and reflectivity spectra at 10 Kelvin, presented in figures 5.4 and 5.5 as well as figure 4.9, compared to values quoted in recent literature

	n=1		n=1		n=1	
	A_T	A_L	B_T	B_L	C_T	C_L
Values for high quality bulk ZnO quoted in recent literature:						
Photoluminescence [16]	3.3747	3.3765	3.3834	3.3925	–	–
Reflectivity [16]	3.3757	3.3785	3.3835	3.3996	3.4219	3.4338
Photoreflectivity [97]	3.3768	3.3783	3.3830	3.3941	3.4214	3.4353
Spectra in figures 5.4 and 5.5:						
Photoluminescence	3.3746	3.3765	–	–	–	–
Reflectivity at 45 °	Peak	Dip	Peak	Dip	Peak	Dip
	3.374	3.3765	3.383	3.394	3.421	3.434
Photoconductivity		'D'	'a'	'F'	'G'	
		3.377	3.383	3.394	3.421	–

	n=2		n=2		n=2	
	A_T	A_L	B_T	B_L	C_T	C_L
Values of high quality bulk ZnO quoted in recent literature:						
Photoluminescence [16]	3.4239	–	–	–	–	–
Reflectivity [16]					–	–
Reflectivity [47]						3.4700
Photoreflectivity [97]		3.4231				3.4679
Spectra in Figure 5.4:						
PL	–	–	–	–	–	–
R (a-plane)					peak	dip
	–				3.462	3.470
PC					–	–

Table 5.4: MBE-film annealed at 750°C

	PL (eV)	+/- (meV)	PC (eV)	+/- (meV)
BXT? (Dip)	–	–	3.385	0.9
BXT?+1 LO	–	–	3.463	4
BXT?+2 LO	–	–	3.542	8
A-free exciton	3.378	1.2	–	–
OP	3.360	1.4	3.364	2.0
OP-1 LO	3.286	0.7	–	–
OP-2 LO	3.213	0.7	–	–
dE (LO1-LO2)	0.0734	1.4	0.080	2

Table 5.5: MBE-film annealed at 850°C

	PL (eV)	+/- (meV)	PC (eV)	+/- (meV)
BXL? (Peak)	–	–	3.394	1.5
BXL+1 LO	–	–	3.458	6.0
BXL+2 LO	–	–	3.536	10.0
A-free exciton	3.378	0.9	3.378	6
I4	3.362	1.8	3.362	4
I4-1 LO	3.289	0.9	–	–
I4-2 LO	3.217	0.9	–	–
dE (LO)	0.0726	1.8	73	2

Chapter 6

Conclusion and Outlook

6.1 Conclusion

In this work, the opto-electrical properties of ZnO have been studied with a range of different spectroscopic methods. Although all of these methods are well known and basic, they do offer a compelling insight into the crystal and electronic structure of the crystals investigated. Important for this work was the way they complement each other by each giving access to different aspects of the band structure. The high quality bulk ZnO crystals that recently have become available add to this mix and create a great opportunity to relate the opto-electrical response of epitaxially grown films to the properties of almost intrinsic bulk ZnO.

A major question that motivated many experiments in this work were the intriguing spectral details that can be observed in the band edge photoconductivity response of high quality epitaxial ZnO films [66]. These feature are intriguing, since on one hand they seem to be strongly related to the excitonic band structure of ZnO, promising an insight into the charge-carrier transport related energy level, on the other hand however they seemed to be strongly irreproducible between samples with very similar crystal properties. Matters are made worse by a sensitivity of the position of spectral features to differences in parameters such as light intensity, the geometry of light exposure on the sample investigated, the chopping speed or the state of a sample in terms of its history of light exposure, quality of contacting as well as surface contamination. This motivated us to get a better understanding of the intrinsic photoconductive response spectrum of high quality bulk ZnO and the technique necessary to observe it.

Chapter 3 starts the investigation of the band structure of ZnO by showing how photoluminescence measurements can be used to recognize improvements in crystal quality that are achieved by post-growth annealing at various temperatures. Temperature dependent photoluminescence then proves to be a great

technique to get a very direct response of the various energy levels in the band structure that are emitting states, particularly the ones close to the band gap. Due to the identified energy levels of excitons bound to donors of various chemical identity, statements can be made about prevalent defect and impurity levels in the crystal. The intensity variation with temperature can be directly related to activation energies of levels that allow non-radiative decays of the emitting energy levels. The temperature dependence of the free exciton energy can be estimated, although broadening and overlap of emitting states makes the identification of the band gap energy at room temperature difficult.

Chapter 4 adds the techniques of transmission and reflectivity, to allow a more direct analysis of the temperature dependence of the band structure via free exciton levels. The chapter starts by investigating the limits of the applicability of temperature dependent absorption measurements via the inflection method on thick bulk ZnO crystals (d=0.46 mm), as well as the possibility to detect differences in the crystal quality of samples of generally very high crystal quality. A more reliable measurement of the temperature dependence of the band structure is found to be possible by reflectivity measurements. The applicability of reflectivity measurements at an incident angle of 45 ° is investigated, as well as the effectiveness of the application of the selection rules to investigate the temperature dependence one isolated free excitonic transition: the A- and B free excitonic levels can be separated from the C-excitonic levels via the polarization rules, and the temperature dependence of the C-exciton can be separately investigated from any other transitions. However, it has been found that the polarization necessary to isolate the C-free exciton costs more precision through the loss of signal intensity in the polarization filter, than it gains precision by minimizing the influence of the B-free exciton level. The measurement of the temperature dependence of the band structure strongly agreeing with the values found in literature was possible via the B_T-excitonic peak in reflectivity when it was considered that its interaction with the A-free exciton causes a slight shift to lower energies with rising temperatures. The phonon broadening of the free exciton levels has been found to push the reflectivity dip to higher energies, whereas the reflectivity peak is observed to broaden with temperature without a substantial shift of its peak energy. This is the reason why the, in terms of absolute energies, less reliable position of the reflectivity *peak* is more suited for measurements of the temperature dependence of the band structure than the reflectivity dip. In summary it has been found that the utmost simple method of reflectivity at oblique incidence can be a suitable method to get a comparably precise feedback about the temperature dependence of the band structure. In combination with photoluminescence, low temperature reflectivity measurement have also shown to be helpful in determining the spectral position identity and spacing of free exciton levels in high quality bulk ZnO.

Chapter 5 investigates the relation of photoconductive band edge features to the free excitons in ZnO. Apparently contradicting spectra that can be observed for samples with very similar crystal properties lead to the assumption that the

surface might play an essential role in determining the spectral photoconductive response, as surface effects are expected to be slower in their response time than bulk processes. The chopping speed of our light-modulated experiments proved a handy tool to separate the slow from the fast photoconductive processes, showing that the fast photo response of similar crystals indeed is very similar, independent of a modest variation of most measurement parameters. However, dependent on the state of the sample surface, slow photoconductive processes are found to be superimposed on the fast photo response, leading to a spectrum with strongly differing features and energy levels.

Temperature dependent photo response measurements show a strong direct connection of the fast spectral features to the band structure. Particularly a peak at the energy of the $B\omega_L$ resonance is evident for all bulk crystals at faster chopping speeds. Its energy shift in the temperature region ranging from 10 Kelvin up to room temperature matches very well with the expected temperature dependence of the B-free exciton as observed by reflectivity studies in chapter 4.

The incentive of chapter 5 was to establish a connection between spectrally resolved features in the PCR-spectrum of ZnO in today's state of the art bulk ZnO crystals and investigate their relation to energy levels in the material, as up to today no studies have been found in literature that investigate the photoconductive response spectrum of recent high quality bulk ZnO crystals to such spectrally resolved detail.

At low temperatures (10 K), we were able to improve the resolution of our spectra step by step. Finally we were able to not only be the first to resolve separate peaks for the A and B-free exciton resonances of ZnO by PCR, but can even suggest that only the longitudinal branch of the A- and B-free excitons is responsible for the PCR-peaks in our spectra. Precisely at the position of B_T, we see a clear dip in the high resolution low temperature PCR-spectra obtained.

Additionally, fine PCR features were found at the energy of the neutral donor bound A excitons I_A, close to the neutral donor bound B-excitons I_B and at the energy of ionized donor bound A-excitons I_A^+. Finally, we could also resolve a clear feature at 3.6 meV above A_L, suggesting a direct connection to the upper polariton branch of the A-free exciton. If it can be confirmed that the PCR-features are indeed directly related to these PL-features with equivalent energy and spectral width, the new high quality bulk ZnO crystals allow PCR-spectroscopy with a resolution that is closer to the resolution obtained by photoluminescence than expected. This might allow the investigation of transport properties of energy states that have only recently been identified in PL, such as the ionized donor bound exciton line $I1$ and its identification as ionized donor bound exciton [163] as well as the upper polariton branch of the free A-exciton [17]. The role these energy states play in influencing the number of free photo generated charge carriers would be interesting to investigate.

The temperature dependence of the bound exciton levels that could only be

observed for one single bulk ZnO crystal with particularly strong photo response and very little sign of slow effects in the PCR-spectrum could be measured indirectly by investigating the temperature dependence of bulk ZnO crystals of the same crystal quality that however showed much stronger defect related slow photoconductive effects. By detecting the association of a broad peak above the exciton energies with a combination of free excitonic and bound excitonic phonon replica levels the temperature dependent decay of the phonon replica could be indirectly detected. This not only explains the origin of the broad non-Gaussian PCR-feature at 3.43 eV, but also is a good way to get information about the temperature dependent behaviour of the bound excitonic zero phonon levels.

A correlation has been observed between samples that show a temperature dependent association of dips with excitonic features and the dominance of slow photoconductivity in the photoconductive response spectrum. For the investigated bulk ZnO samples as well as the MBE-grown epitaxial films, the samples that exhibited dips instead of peaks at energies that are meaningful in terms of the temperature dependence of the band structure, the photoconductivity away from the dips was strongly correlated with slow effects that blurred the fast photoconductive response that could be observed for higher chopping speeds. All samples with fast photoconductive response showed meaningful peaks that shifted according to the band structure.

In summary the combination of these various optical methods of photoluminescence, reflectivity, photoconductivity and transmission allow us to get a far more complete picture of the temperature dependent energy structure of ZnO as would be possible by just using one technique by itself.

6.2 Outlook

Since the time and manpower available for research and in particular for a PhD-thesis is limited, many ideas could not be realized in the course of this study. Following the logic that the more you learn the more you want to know, here I want to suggest possible next steps in research that would help to solve the most pressing questions following from the work presented in this thesis. Interesting results can therefore be expected from the following studies:

- The PCR-spectra presented in this thesis are exclusively recorded while the incoming light was scanned from high to low photon energies. As a result of the slow dynamics and the trapping states involved in the photoconductive response of ZnO, it would be very interesting to see the changes to the photoresponse spectrum when the experiment is done scanning from low to high energy. In general this would result in a more direct response spectrum, as levels of higher energy than the current scanning point would become excluded from playing a role in the intensity of the photoresponse

at each scanning point.

- The internal electric field in ZnO is oriented parallel to the c-axis. Since in ZnO the internal electric field is expected to play an important role in the creation of free charge carriers from excitonic complexes, it would be very interesting to analyze the impact the orientation of the c-axis has on the photoconductive response spectrum. This can be done by measuring the PC-response on faces of ZnO with the c-axis in-plane or out of plane, i.e. by comparing the spectra obtained on the c-plane surface of a crystal with the spectra obtained on its m- or a-plane surfaces.

- The selection rules in ZnO allow for a strong differentiation of the C-excitonic from the A- and B-excitonic transitions in case they are excited directly. Therefore, after the differences in the response spectrum of surfaces with the c-axis in plane is understood, a polarization study of the photoconductive response of in-plane bulk ZnO would be another imminent next step to solidify the assumption of a direct relation between features in the photoconductive response spectrum and free excitonic states.

- The assumption that the contamination of a sample surface can be responsible for the detectability of the most detailed photoconductive response spectrum of all bulk ZnO crystals investigated could quite easily be experimentally investigated. An approach would be the deposition of insulating capping layers on bulk ZnO, with contacts deposited underneath.

- The face dependency of the reflectivity of new high quality bulk ZnO should be investigated in UHV-systems to allow a controlled exposure of e.g. heat-cleaned sample surfaces to different gases. This would most likely be very helpful for the identification of the involvement of the surface electronic structure with the persistent n-type conductivity that poses the biggest obstacle in ZnO material application [31].

- The temperature dependent analysis of free excitonic resonances by reflectivity can be applied to films with different lattice strains, to investigate the effect of lattice strain on the temperature dependence of the bandstructure.

Since the current efforts in the field of ZnO related research is strong, particular towards ZnO as an optical material for UV-application such as lasers, LED's and photodetectors, the understanding of optoelectrical properties, in particular the room temperature charge transport and its sensitivity to incident light, are of strong interest. The surface of the material is also to be looked at more closely in regard to face dependent band-bending effects due to the polarity of the c-plane faces. This effort might also play an important role in the accomplishment of the major hurdle of persistent p-type conductivity in ZnO.

Appendix A

Publications in peer-reviewed journals

(a) M.J.H. Henseler, W.C.T. Lee, P. Miller, S.M. Durbin, and R.J Reeves, *Optical and photoelectrical properties of ZnO thin films and the effects of annealing*, Journal of Crystal Growth, 287, 48-53, (2006) [66].

(b) W.C.T. Lee, M.J.H. Henseler, P. Miller, C.H. Swartz, T.H. Myers, R.J. Reeves, and S.M. Durbin, *Effect of annealing on the morphology and optoelectrical characteristics of ZnO thin films grown by plasma-assisted molecular beam epitaxy*, Journal of Electronic Materials, 35, 1316-1321, (2006) [79].

(c) E. Boyd, M. Henseler, D. Mackenzie, S. Brown, T*he fabrication and optical characterisation of SnO2 cluster films*, Phys. Status Solidi A Appl. Mater. 206, 931 (2009) [165].

Bibliography

[1] T. Monteiro, C. Boemare, M. J. Soares, E. Rita, E. Alves, *Photoluminescence and damage recovery studies in Fe-implanted ZnO single crystals*, J. Appl. Phys. **93**, 8995 (2003).

[2] W. Benenson, J. W. Harris, H. Stocker, *Handbook of Physics* (Springer, 2002).

[3] C. Klingshirn, M. Grundmann, A. Hoffmann, B. Meyer, A. Waag, *Zinkoxid ein alter, neuer Halbleiter*, Physik Journal **5**, 33 (2006).

[4] R. B. Ellmer K., Klein A, *Transparent Conductive Zinc Oxide: Basics and Applications in Thin Film Solar Cells* (Springer, 2008).

[5] S. Pearton, D. Norton, K. Ip, Y. Heo, T. Steiner, *Recent progress in processing and properties of ZnO*, Prog Mater Sci **50**, 293 (2005).

[6] R. Bhargava, *Properties of Wide Bandgap II-VI Semiconductors*, no. 17 in E M I S Datareviews Series (INSPEC, 1997).

[7] U. Özgür, et al., *A comprehensive review of ZnO materials and devices*, J Appl Phys **98**, 1 (2005).

[8] C. Bates, W. White, R. Roy, *New high-pressure polymorph of zinc oxide*, Science **137**, 993 (1962).

[9] E. Kisi, M. Elcombe, *u Parameters for the wurtzite structure of ZnS and ZnO using powder neutron diffraction*, Acta Crystallogr., Sect. C: Cryst. Struct. Commun. **45**, 1867 (1989).

[10] L. Gerward, J. Olsen, J. Synchrotron Radiat. **2**, 233 (1995).

[11] Z. Alahmed, H. Fu, *Polar semiconductor ZnO under inplane tensile strain*, Phys. Rev. B Condens. Matter Mater. Phys. **77**, (2008).

[12] D. Vogel, P. Krüger, J. Pollmann, *Self-interaction and relaxation-corrected pseudopotentials for II-VI semiconductors*, Phys. Rev. B **54**, 5495 (1996).

[13] D. Thomas, *The exciton spectrum of zinc oxide*, J. Phys. Chem. Solids **15**, 86 (1960).

[14] B. Meyer, et al., *Bound exciton and donor-acceptor pair recombinations in ZnO*, Phys. Status Solidi B Basic Res. **241**, 231 (2004).

[15] D. C. Oh, et al., *Comparative study of photoluminescences for Zn-polar and O-polar faces of single-crystalline ZnO bulks*, Appl. Phys. Lett. **93**, 241907 (2008).

[16] N. Syrbu, I. Tiginyanu, V. Zalamai, V. Ursaki, E. Rusu, *Exciton polariton spectra and carrier effective masses in ZnO single crystals*, Phys B Condens Matter **353**, 111 (2004).

[17] A. Teke, et al., *Excitonic fine structure and recombination dynamics in single-crystalline ZnO*, Phys. Rev. B Condens. Matter Mater. Phys. **70**, 1 (2004).

[18] D. C. Reynolds, et al., *Time-resolved photoluminescence lifetime measurements of the Γ_5 and Γ_6 free excitons in ZnO*, J. Appl. Phys. **88**, 2152 (2000).

[19] J. Tomm, et al., *Optical and photoelectrical properties of oriented ZnO films*, J Appl Phys **87**, 1844 (2000).

[20] H. Fröhlich, *Interaction of Electrons with Lattice Vibrations*, Proceedings of the Royal Society of London. Series A, Mathematical and Physical Sciences **215**, 291 (Dec. 5, 1952).

[21] K. Maeda, M. Sato, I. Niikura, T. Fukuda, *Growth of 2 inch ZnO bulk single crystal by the hydrothermal method*, Semicond Sci Technol **20**, (2005).

[22] D. Hamby, D. Lucca, M. Klopfstein, G. Cantwell, *Temperature dependent exciton photoluminescence of bulk ZnO*, J Appl Phys **93**, 3214 (2003).

[23] R. Hauschild, et al., *Temperature dependent band gap and homogeneous line broadening of the exciton emission in ZnO*, Physica Status Solidi (c) **3**, 976 (2006).

[24] J. Li, H. C. Ong, *Temperature dependence of surface plasmon mediated emission from metal-capped ZnO films*, Appl. Phys. Lett. **92**, 121107 (2008).

[25] Z. Tu, Q. Li, X. Hu, *Theoretical determination of the necessary conditions for the formation of ZnO nanorings and nanohelices*, Phys. Rev. B Condens. Matter Mater. Phys. **73**, 1 (2006).

[26] C. Noguera, *Polar oxide surfaces*, Journal of Physics: Condensed Matter **12**, R367 (2000).

[27] O. Dulub, L. Boatner, U. Diebold, *STM study of the geometric and electronic structure of ZnO(0001)-Zn, (000$\bar{1}$)-O, (10$\bar{1}$0), and (11$\bar{2}$0) surfaces*, Surf Sci **519**, 201 (2002).

[28] T. Becker, et al., *Interaction of hydrogen with metal oxides: The case of the polar ZnO (0001) surface*, Surf Sci **486**, (2001).

[29] M. Kunat, S. Gil Girol, T. Becker, U. Burghaus, C. Wöll, *Stability of the polar surfaces of ZnO: A reinvestigation using He-atom scattering*, Phys. Rev. B Condens. Matter Mater. Phys. **66**, 814021 (2002).

[30] N. Joshi, *Photoconductivity: Art, Science and Technology* (New York: Marcel Dekker, 1990).

[31] S. Chambers, *Surface science opportunities in the electronic structure of ZnO (A perspective on the article, "Quantitative analysis of surface donors in ZnO", by D.C. Look)*, Surf Sci **601**, 5313 (2007).

[32] H. Lüth, *Surface Phonons in the Oscillatory Photoconductivity of Zinc Oxide*, Phys. Rev. Lett. **29**, 1377 (1972).

[33] L. Eaves, P. J. Williams, *Decay of the deep-level extrinsic photoconductivity response of n-GaAs(Cr,Si) at liquid-helium temperature*, Journal of Physics C: Solid State Physics **12**, L725 (1979).

[34] R. H. Bube, *Photoconductivity of Solids* (John Wiley & Sons, Inc, 1960).

[35] J. Mass, A. Lora, T. Rada, J. Jimenez, *Spectrally resolved cathodoluminescence characterisation of ZnO crystal*, Revista Colombiana de fisica **38**, 1122 (2006).

[36] T. Moriyama, S. Fujita, *Epitaxial growth of nonpolar ZnO by MOVPE*, Physica Status Solidi (c) **3**, 726 (2006).

[37] C. Klingshirn, *Semiconductor Optics* (Springer, 2007), third edn.

[38] J. Frenkel, *On the Transformation of Light into Heat in Solids. II*, Phys. Rev. **37**, 1276 (1931).

[39] J. Frenkel, *On the Transformation of light into Heat in Solids. I*, Phys. Rev. **37**, 17 (1931).

[40] B. P. Zakharchenya, *The play of light in crystals*, Semiconductor Science and Technology **23**, 110302 (5pp) (2008).

[41] E. Mollwo, Reichsberichte der Physik **1** (1943).

[42] E. F. Gross, N. Karryev, *Light absorption by cuprous oxide crystal in infrared and visible spectrum*, DAN SSSR (Doklady Academii Nauk **84**, 261 (1952).

[43] P. D. R. Gross, D. A. Marx, Festkörperphysik, Vorlesungsscript, Walther-Meissner-Institut (2004/2005).

[44] U. Rössler, R. Blachnik, *Zinc oxide (ZnO)* (Springer, 1999), vol. 41B, chap. 3.5, pp. 1–27.

[45] A. Mang, K. Reimann, S. Ruebenacke, *Band gaps, crystal-field splitting, spin-orbit coupling, and exciton binding energies in ZnO under hydrostatic pressure*, Solid State Commun **94**, 251 (1995).

[46] W. Lambrecht, A. Rodina, S. Limpijumnong, B. Segall, B. Meyer, *Valence-band ordering and magneto-optic exciton fine structure in ZnO*, Physical Review B - Condensed Matter and Materials Physics **65**, 0752071 (2002).

[47] D. Reynolds, et al., *Valence-band ordering in ZnO*, Phys. Rev. B Condens. Matter Mater. Phys. **60**, 2340 (1999).

[48] Y. Park, C. Litton, T. Collins, D. Reynolds, *Exciton spectrum of ZnO*, Phys. Rev. **143**, 512 (1966).

[49] W. C. T. Lee, Harvesting philosopher's wool: A study in the growth, structure and optoelectrical behaviour of epitaxial zno, Electrical and electronic engineering, University of Canterbury, Christchurch, New Zealand. (2007).

[50] S. Durbin, W. Lee, M. Allen, P. Miller, R. Reeves, *2005 MRS Fall Meeting* (Boston, MA, 2006), vol. 891, pp. 345–350.

[51] R. Mendelsberg, M. Kerler, S. Durbin, R. Reeves, *Photoluminescence behavior of ZnO nanorods produced by eclipse PLD from a Zn metal target*, Superlattices and Microstructures **43**, 594 (2008).

[52] R. Mendelsberg, J. Kennedy, S. Durbin, R. Reeves, *Carbon enhanced blue-violet luminescence in ZnO films grown by pulsed laser deposition*, Current Applied Physics **8**, 283 (2008).

[53] M. Allen, S. Durbin, J. Metson, *Silver oxide Schottky contacts on n-type ZnO*, Appl Phys Lett **91**, (2007).

[54] M. Allen, P. Miller, R. Reeves, S. Durbin, *Influence of spontaneous polarization on the electrical and optical properties of bulk, single crystal ZnO*, Appl Phys Lett **90**, (2007).

[55] C. Tusche, H. Meyerheim, J. Kirschner, *Observation of depolarized ZnO(0001) monolayers: Formation of unreconstructed planar sheets*, Phys Rev Lett **99**, (2007).

[56] S. P. Chennupati Jagadish, *Zinc Oxide Bulk, Thin Films and Nanostructures* (Elsevier, 2006).

[57] B. Kumar, H. Gong, S. Y. Chow, S. Tripathy, Y. Hua, *Photoluminescence and multiphonon resonant Raman scattering in low-temperature grown ZnO nanostructures*, Appl. Phys. Lett. **89**, 071922 (2006).

[58] O. Schmidt, et al., *Effects of an electrically conducting layer at the zinc oxide surface*, Japanese Journal of Applied Physics Part 1 **44**, 7271 (2005).

[59] H. Priller, et al., *Comparison of linear and nonlinear optical spectra of various ZnO epitaxial layers and of bulk material obtained by different experimental techniques*, Physica Status Solidi (b) **241**, 587 (2004).

[60] H. Alves, et al., *Optical investigations on excitons bound to impurities and dislocations in ZnO*, Optical Materials **23**, 33 (2003).

[61] C. Boemare, T. Monteiro, M. J. Soares, J. G. Guilherme, E. Alves, *Photoluminescence studies in ZnO samples*, Physica B: Condensed Matter **308-310**, 985 (2001).

[62] A. Barry, W. Edwards, *Circuit to facilitate the measurement by the four-probe method of the resistivity of silicon in the range 0.002 to 10 000* Ω/cm, Journal of Scientific Instruments **39**, 119 (1962).

[63] SRS, *Model SR830 DSP Lock-In Amplifier*, Stanford Research Systems, 1290-D Reamwood Avenue Sunnyvale, California 94089, second edn. (2005).

[64] D. R. Lide, *CRC Handbook of Chemistry and Physics* (CRC Press, 1990), 71st edn.

[65] PerkinElmer, *Datasheet PE300BF and PE300BUV Cermax Xenon Arc Lamps*, PerkinElmer Optoelectronics (2000).

[66] M. Henseler, W. Lee, P. Miller, S. Durbin, R. Reeves, *Optical and photoelectrical properties of ZnO thin films and the effects of annealing*, J Cryst Growth **287**, 48 (2006).

[67] D. J. Jose Sol, Louisa E. Baus, ed., *An Introduction to the Optical Spectroscopy of Inorganic Solids* (John Wiley and Sons, 2005).

[68] D. R. Vij, ed., *Handbook of Electroluminescent Materials* (CRC Press, Institute of Physics (Great Britain), 2004).

[69] C. H. Swartz, et al., *Investigation of multiple carrier effects in InN epilayers using variable magnetic field Hall measurements*, Journal of Crystal Growth **269**, 29 (2004).

[70] K. Ogata, K. Sakurai, S. Fujita, S. Fujita, K. Matsushige, *Effects of thermal annealing of ZnO layers grown by MBE*, J Cryst Growth **214**, 312 (2000).

[71] J. Ye, et al., *Production of high-quality ZnO films by the two-step annealing method*, J Appl Phys **96**, 5308 (2004).

[72] D. C. Reynolds, et al., *Neutral-donor-bound-exciton complexes in ZnO crystals*, Phys. Rev. B **57**, 12151 (1998).

[73] K. Thonke, et al., *Donor-acceptor pair transitions in ZnO substrate material*, Physica B: Condensed Matter **308-310**, 945 (2001).

[74] A. Janotti, C. Van De Walle, *Native point defects in ZnO*, Phys. Rev. B Condens. Matter Mater. Phys. **76**, (2007).

[75] H. S. Kang, J. S. Kang, J. W. Kim, S. Y. Lee, *Annealing effect on the property of ultraviolet and green emissions of ZnO thin films*, J. Appl. Phys. **95**, 1246 (2004).

[76] A. Wander, et al., *Stability of polar oxide surfaces*, Phys Rev Lett **86**, 3811 (2001).

[77] F. Selim, M. Weber, D. Solodovnikov, K. Lynn, *Nature of native defects in ZnO*, Phys Rev Lett **99**, (2007).

[78] H.-C. Hsu, W.-F. Hsieh, *Excitonic polaron and phonon assisted photoluminescence of ZnO nanowires*, Solid State Communications **131**, 371 (2004).

[79] W. Lee, et al., *Effect of annealing on the morphology and optoelectrical characteristics of ZnO thin films grown by plasma-assisted molecular beam epitaxy*, J Electron Mater **35**, 1316 (2006).

[80] P. Misra, T. Sharma, L. Kukreja, *Temperature dependent photoluminescence processes in ZnO thin films grown on sapphire by pulsed laser deposition*, Current Applied Physics **9**, 179 (2009).

[81] N. Kumar, R. Kaur, R. Mehra, *Photoluminescence studies in sol-gel derived Zno films*, Journal of Luminescence **126**, 784 (2007).

[82] J. Lee, E. S. Koteles, M. O. Vassell, *Luminescence linewidths of excitons in GaAs quantum wells below 150 K*, Phys. Rev. B **33**, 5512 (1986).

[83] T. Li, H. J. Lozykowski, J. L. Reno, *Optical properties of CdTe/Cd1-xZnxTe strained-layer single quantum wells*, Phys. Rev. B **46**, 6961 (1992).

[84] Y. P. Varshni, *Temperature dependence of the energy gap in semiconductors*, Physica **34**, 149 (1967).

[85] A. Manoogian, J. Woolley, *Temperature dependence of the energy gap in seminconductors*, Can J Phys **62**, 285 (1984).

[86] M. Feneberg, et al., *Mahan excitons in degenerate wurtzite InN: Photoluminescence spectroscopy and reflectivity measurements*, Phys. Rev. B Condens. Matter Mater. Phys. **77**, (2008).

[87] R. Pässler, *Dispersion-related assessments of temperature dependences for the fundamental band gap of hexagonal GaN*, J Appl Phys **90**, 3956 (2001).

[88] S. Rudin, T. L. Reinecke, B. Segall, *Temperature-dependent exciton linewidths in semiconductors*, Phys. Rev. B **42**, 11218 (1990).

[89] L. Gupta, S. Rath, S. Abbi, F. Jain, *Temperature dependence of the fundamental band gap parameters in cadmium-rich ZnxCd1-xSe using photoluminescence spectroscopy*, Pramana **61**, 729 (2003).

[90] M. Fox, *Optical Properties of Solids* (Oxford University Press, 2001).

[91] D. Bimberg, M. Sondergeld, E. Grobe, *Thermal dissociation of excitons bounds to neutral acceptors in high-purity GaAs*, Physical Review B **4**, 3451 (1971).

[92] A. Qasrawi, *Refractive index, band gap and oscillator parameters of amorphous GaSe thin films*, Cryst Res Technol **40**, 610 (2005).

[93] J. I. Pankove, *Optical Processes in Semiconductors* (Prentice-Hall, Inc., 1971).

[94] C. Lrez, C. Rincn, *Alloy composition and temperature dependence of the direct energy gap in AlxGa1-xAs*, J Phys Chem Solids **58**, 1111 (1997).

[95] J. Hopfield, D. Thomas, *Theoretical and experimental effects of spatial dispersion on the optical properties of crystals*, Physical Review **132**, 563 (1963).

[96] J. Lagois, *Dielectric theory of interacting excitonic resonances*, Phys. Rev. B **16**, 1699 (1977).

[97] S. F. Chichibu, T. Sota, G. Cantwell, D. B. Eason, C. W. Litton, *Polarized photoreflectance spectra of excitonic polaritons in a ZnO single crystal*, J. Appl. Phys. **93**, 756 (2003).

[98] T. Makino, Y. Segawa, M. Kawasaki, A. Ohtomo, *Analysis on reflection spectra in strained ZnO thin films*, J Cryst Growth **287**, 124 (2006).

[99] A. Tsukazaki, et al., *Emission from the higher-order excitons in ZnO films grown by laser molecular-beam epitaxy*, Appl Phys Lett **84**, 3858 (2004).

[100] D. W. Berreman, *Resonant Reflectance Anomalies: Effect of Shapes of Surface Irregularities*, Phys. Rev. B **1**, 381 (1970).

[101] H. Lüth, *Optical spectroscopy of electronic surface states*, Applied Physics B: Lasers and Optics **8**, 1 (1975).

[102] K. Hümmer, P. Gebhardt, *Angular dependence of the reflection spectra and directional dispersion of the anisotropic exciton polaritons in ZnO*, Physica Status Solidi (b) **85**, 271 (1978).

[103] R. Matz, H. Lüth, *Ellipsometric spectroscopy of the ZnO nonpolar surface*, Applied Physics A: Materials Science & Processing **18**, 123 (1979).

[104] B. Harbecke, B. Heinz, P. Grosse, *Optical properties of thin films and the Berreman effect*, Applied Physics A: Materials Science & Processing **38**, 263 (1985).

[105] R. Ruppin, *Reflectivity of a nonlocal dielectric with an excitonic surface potential*, Phys. Rev. B **29**, 2232 (1984).

[106] V. Harutunian, H. Margarian, V. Melicksetian, J. Panossian, *Surface excitons in ZnO crystals*, Journal of Physics: Condensed Matter **1**, 847 (1989).

[107] M. Sydor, *Intrinsic Photoconductivity of RbI*, Phys. Rev. **163**, 873 (1967).

[108] M. Vanecek, E. Klier, *Intrinsic oscillatory photoconductivity and the band structure of ZnTe and CdTe*, Physica Status Solidi (a) **30**, 441 (1975).

[109] G. Heiland, H. Ibach, H. Lüth, W. Mönch, *Oscillations in photoconductivity due to surface phonons*, Surface Science **35**, 425 (1973).

[110] H. Ibach, W. Mönch, *Surface Phonons in Spectral Oscillations in the Photoconductivity on Silicon (111) Surfaces*, Physica Status Solidi (b) **55**, 243 (1973).

[111] J. C. Ayache, M. Zouaghi, Y. Marfaing, *Oscillatory photoconductivity of n-type CdTe at low temperature*, Physica Status Solidi (a) **2**, 61 (1970).

[112] A. T. Collins, E. C. Lightowlers, P. J. Dean, *Role of Phonons in the Oscillatory Photoconductivity Spectrum of Semiconducting Diamond*, Phys. Rev. **183**, 725 (1969).

[113] R. E. Nahory, *Oscillatory Photoconductivity of Epitaxial GaAs*, Phys. Rev. **178**, 1293 (1969).

[114] A. S. Batyrev, R. A. Bisengaliev, N. V. Zhukova, B. V. Novikov, E. I. Chityrov, *Spectral photoresistive effect of the field in CdS crystals at low temperatures*, Physics of the Solid State **45**, 2060 (2003).

[115] R. A. Bisengaliev, E. D. Batyrev, B. V. Novikov, A. V. Sel'kin, *Photoreflection and photoconduction spectra of CdS crystals: excitons in the electric fields of surface states*, Physics of the Solid State **40**, 806 (1998).

[116] B. Lojek, *Advanced Thermal Processing of Semiconductors, 2002. RTP 2002. 10th IEEE International Conference of* (2002), pp. 21–29.

[117] B. Henderson, G. F. Imbusch, *Optical Spectroscopy of Inorganic Solids* (Oxford Science Publications, 1989).

[118] J. Singh, ed., *Optical Properties of Condensed Matter and Applications*, Wiley Series in Materials for Electronic and Optoelectronic Applications (Wiley, 2006).

[119] G. Heiland, P. Kunstmann, *Polar surfaces of zinc oxide crystals*, Surface Science **13**, 72 (1969).

[120] B. Hoffmann, *"Elektroreflexion" durch Gasadsorption am Zinkoxid*, Zeitschrift fuer Physik A Hadrons and Nuclei **206**, 293 (1967).

[121] L. Wang, N. Giles, *Temperature dependence of the free-exciton transition energy in zinc oxide by photoluminescence excitation spectroscopy*, J Appl Phys **94**, 973 (2003).

[122] S. Tsoi, et al., *Isotopic-mass dependence of the A, B, and C excitonic band gaps in ZnO at low temperatures*, Phys. Rev. B Condens. Matter Mater. Phys. **74**, (2006).

[123] L. Wang, N. C. Giles, *Temperature dependence of the free-exciton transition energy in zinc oxide by photoluminescence excitation spectroscopy*, Journal of Applied Physics **94**, 973 (2003).

[124] X. T. Zhang, et al., *Temperature dependence of excitonic luminescence from nanocrystalline ZnO films*, Journal of Luminescence **99**, 149 (2002).

[125] W. Park, G.-C. Yi, *Photoluminescent properties of ZnO thin films grown on SiO2/Si(100) by metal-organic chemical vapor deposition*, Journal of Electronic Materials **30**, L32 (2001).

[126] Z. Yao, X. Zhang, I. Suemune, S. Huang, *Room-temperature stimulated emission from ZnO thin films grown by radio-frequency magnetron sputtering*, Journal of Luminescence **122-123**, 825 (2007).

[127] R. Mendelsberg, Optical analysis of pulsed laser deposited materials, Ph.D. thesis, University of Canterbury, Department of Physics and Astronomy (2009).

[128] S. Permogorov, *Hot excitons in semiconductors*, Physica Status Solidi (b) **68**, 9 (1975).

[129] H. Frenzel, et al., *Photocurrent spectroscopy of deep levels in ZnO thin films*, Phys. Rev. B Condens. Matter Mater. Phys. **76**, (2007).

[130] D. G. Thomas, J. J. Lander, *Surface conductivity produced on zinc oxide by zinc and hydrogen*, Journal of Physics and Chemistry of Solids **2**, 318 (1957).

[131] G. Heiland, *Photoconductivity of zinc oxide as a surface phenomenon*, Journal of Physics and Chemistry of Solids **22**, 227 (1961).

[132] W. Bauer, G. Heiland, *Spectral sensitization of photoconductivity on the surface of zinc oxide crystals under clean conditions*, Journal of Physics and Chemistry of Solids **32**, 2605 (1971).

[133] N. Beekmans, *Effect of oxygen chemisorption and photodesorption on the conductivity of ZnO powder layers*, Journal of the Chemical Society, Faraday Transactions 1: Physical Chemistry in Condensed Phases **74**, 31 (1978).

[134] J. M. Martn, R. Casanova, N. V. Joshi, *Adsorption-induced enhanced photoconductivity: A reevaluation*, Phys. Rev. B **36**, 9703 (1987).

[135] A. Klimovskii, A. Lisachenko, *Determination of the kinetic parameters for the photoadsorption and photodesorption of oxygen on zinc oxide*, Kinet Catal **32**, 373 (1991).

[136] F. Prado, G. Meyer, J. Saura, *Photocurrents in SnO2 films due to desorption of oxygen*, Journal of Physics: Condensed Matter **5**, (1993).

[137] L. Roman, et al., *Optical band-edge absorption of oxide compound SnO2*, Applied Surface Science **252**, 5361 (2006).

[138] B. V. Novikov, E. F. Gross, M. A. Drygin, *Role of Exciton States in Process of Photocurrent Formation in Germanium*, Jetp Letters-Ussr **8**, 8 (1968).

[139] W. Bludau, E. Wagner, *Impact ionization of excitons in GaAs*, Phys. Rev. B **13**, 5410 (1976).

[140] G. Couturier, D. Kaiser, S. von Molnar, P. Becla, *Oscillatory photoconductivity and photomagnetoresistance in the diluted magnetic semiconductor Cd1-xMnxTe*, Phys. Rev. B **39**, 1663 (1989).

[141] A. Zareba, A. Nadolny, *Photoconductivity originated from dissociation of excitons in* $Cd_{/mathit1-x}/Mn_{/mathitx}/Te$, Physica Status Solidi B **120**, K97 (1983).

[142] G. Mamedov, et al., *Exciton photoluminescence, photoconductivity and absorption in GaSe0.9Te0.1 alloy crystals*, Journal of Luminescence **129**, 226 (2009).

[143] N. A. Gross, E. F. amd Karryew, *Exciton optical spectrum*, DAN SSSR **84**, 471 (1952).

[144] E. F. Gross, B. V. Novikov, *The Fine Structure of the Spectral Curves of Photoconductivity and Luminescence Excitation and Its Correlation to the Exciton Absorption Spectrum*, Journal of Physics and Chemistry of Solids **22**, 87 (1961).

[145] E. F. Gross, A. A. Kaplianskii, B. V. Novikov, *Structure of the Spectral Curve for the Internal Photoeffect in Crystals of Cadmium Sulfide*, Soviet Physics-Technical Physics **1**, 900 (1956).

[146] E. Grillot, B. V. Novikov, E. F. Gross, M. Banciegrillot, *Sur La Diversité Daspect Dés Courbes De Sensibilité Spectrale De Photoconductivité De Cristaux De Sulfure De Cadmium Pur - Influénce De La Polarisation De La Lumiere Excitatrice Et Du Mode De Preparation Des Cristaux Etudies*, Comptes Rendus Hebdomadaires Des Seances De L Academie Des Sciences **252**, 1129 (1961).

[147] E. F. Gross, B. V. Novikov, *The Relation between Background and Fine Structure Maxima of the Spectral Photoconductivity Curves in Cds Monocrystals*, Soviet Physics-Solid State **3**, 906 (1961).

[148] E. F. Gross, K. F. Lider, B. V. Novikov, *Investigation of the Photoconductivity Spectra of Cds Crystals at 77-Degrees-K and 4-Degrees-K in the Absorption Edge Region*, Soviet Physics-Solid State **4**, 836 (1962).

[149] E. F. Gross, Ilyinski.Av, K. F. Lieder, B. V. Novikov, N. S. Sokolov, *Phonon-Assisted Exciton Transitions in Spectral Response of Photoconductivity of Cds Single Crystals*, Physica Status Solidi **34**, K59 (1969).

[150] A. S. Batyrev, B. V. Novikov, A. E. Cherednichenko, *Subsurface Electric-Field Effect on the Excitonic Reflection Spectra of CdSe Single-Crystals*, Fizika Tverdogo Tela **23**, 2989 (1981).

[151] A. S. Batyrev, R. A. Bisengaliev, E. D. Batyrev, B. V. Novikov, V. S. Anbushinov, *Effect of IR illumination on photocurrent spectra in CdS crystals*, Physics of the Solid State **41**, 1075 (1999).

[152] A. S. Batyrev, et al., *Investigation of the excitonic structure in the photoconductivity spectra of CdS crystals*, Physics of the Solid State **40**, 867 (1998).

[153] H. J. Stocker, H. Levinstein, C. R. Stannard, *Oscillatory Photoconductivity in InSb*, Phys. Rev. **150**, 613 (1966).

[154] K. L. Kliewer, R. Fuchs, *Optical Modes of Vibration in an Ionic Crystal Slab Including Retardation. II. Radiative Region*, Phys. Rev. **150**, 573 (1966).

[155] J. Carrey, et al., *Photoconductivity of self-assembled ZnO nanoparticles synthesized by organometallic chemistry*, Semicond Sci Technol **23**, (2008).

[156] W. Liang, A. Yoffe, *Transmission spectra of ZnO single crystals*, Physical Review Letters **20**, 59 (1968).

[157] J. F. Muth, R. M. Kolbas, A. K. Sharma, S. Oktyabrsky, J. Narayan, *Excitonic structure and absorption coefficient measurements of ZnO single crystal epitaxial films deposited by pulsed laser deposition*, J. Appl. Phys. **85**, 7884 (1999).

[158] H. Lüth, G. Heiland, *Surface photovoltage spectroscopy on semiconductor surfaces*, Il Nuovo Cimento B (1971-1996) **39**, 748 (1977).

[159] Z. Fan, et al., *Photoluminescence and polarized photodetection of single ZnO nanowires*, Appl. Phys. Lett. **85**, 6128 (2004).

[160] Y. Sato, H. Kusumi, H. Yamaguchi, T. Komiyama, T. Aoyama, *Photoconductive properties of ZnO crystals with post-growth annealing*, Physica B: Condensed Matter **376-377**, 719 (2006).

[161] S. Mridha, D. Basak, *Thickness dependent photoconducting properties of ZnO films*, Chem. Phys. Lett. **427**, 62 (2006).

[162] H. Kavak, E. SenadIm Tuzemen, L. Ozbayraktar, R. Esen, *Optical and photoconductivity properties of ZnO thin films grown by pulsed filtered cathodic vacuum arc deposition*, Vacuum **83**, 540 (2008).

[163] B. Meyer, J. Sann, S. Lautenschläger, M. Wagner, A. Hoffmann, *Ionized and neutral donor-bound excitons in ZnO*, Phys. Rev. B Condens. Matter Mater. Phys. **76**, (2007).

[164] A. A. Toropov, et al., *Temperature-dependent exciton polariton photoluminescence in ZnO films*, Phys. Rev. B **69**, 165205 (2004).

[165] E. Boyd, M. Henseler, D. Mackenzie, S. Brown, *The fabrication and optical characterisation of SnO2 cluster films*, Phys. Status Solidi A Appl. Mater. **206**, 931 (2009).

[166] F. Bertram, et al., *Microscopic spatial distribution of bound excitons in high-quality ZnO*, Journal of Crystal Growth **272**, 785 (2004).

[167] Q. Xu, J. Zhang, K. Ju, X. Yang, X. Hou, *ZnO thin film photoconductive ultraviolet detector with fast photoresponse*, Journal of Crystal Growth **289**, 44 (2006).

[168] N. Camaioni, G. Casalbore-Miceli, A. Martelli, *Slow transient photoresponse in Schottky-type junctions based on poly(4,4″-dipenthoxy-3′-octyl-2,2′:5′,2″-terthiophene)*, J. Appl. Phys. **89**, 5488 (2001).

[169] G. J. Adriaenssens, S. D. Baranovskii, W. Fuhs, J. Jansen, O. Öktü, *Photoconductivity response time in amorphous semiconductors*, Phys. Rev. B **51**, 9661 (1995).